


1-1-2018

Magneto-Optical Properties of Rare-Earth Doped Semiconductors

Andrew Jacob Helbers

Lehigh University, mathguy7777@gmail.com

Follow this and additional works at: <https://preserve.lehigh.edu/etd>

 Part of the [Biochemistry, Biophysics, and Structural Biology Commons](#)

Recommended Citation

Helbers, Andrew Jacob, "Magneto-Optical Properties of Rare-Earth Doped Semiconductors" (2018). *Theses and Dissertations*. 4286.
<https://preserve.lehigh.edu/etd/4286>

This Dissertation is brought to you for free and open access by Lehigh Preserve. It has been accepted for inclusion in Theses and Dissertations by an authorized administrator of Lehigh Preserve. For more information, please contact preserve@lehigh.edu.

Magneto-Optical Properties of Rare-Earth Doped Semiconductors

by

Andrew J. Helbers

A Dissertation
Presented to the Graduate Committee
of Lehigh University
in Candidacy for the Degree of
Doctor of Philosophy
in
Physics

Lehigh University
August 2017

Copyright
Andrew J. Helbers

Approved and recommended for acceptance as a dissertation in partial fulfillment of the requirements for the degree of Doctor of Philosophy.

Andrew J. Helbers

(Magneto-Optical Properties of Rare-Earth Doped Semiconductors)

Date

Dr. Volkmar Dierolf, Dissertation Director, Chair

Accepted Date

Committee Members

Dr. Gary G. DeLeo

Dr. W. Beall Fowler

Dr. Michael J. Stavola

Dr. Nelson Tansu

Dedication

I would like to thank my committee members, Professors Gary DeLeo, W. Beall Fowler, Michael Stavola, and Nelson Tansu. In particular, I would like to thank Professor Gary DeLeo for his advice on issues ranging from technical aspects of group theory to handling the stress of science.

To my research group members, past and present, thank you for your support and aid, both in ways directly beneficial to the projects described herein, and for indirect ways, such as conversation. In particular, I would like to credit and thank Dr. Keith Veenhuizen for aid in the experiments using Raman Spectroscopy and poling of ferroelectrics, and Dr. Brandon Mitchell for initial training in using the variety of equipment needed to perform these experiments.

To my family and friends, thank you your support and willingness to deal with my numerous ups and downs over the course of this research.

To my advisor, Professor Volkmar Dierolf, thank you for the independence and financial support to conduct this research in an instructive way.

Contents

List of Tables	ix
List of Figures	xiii
Abstract	1
1 Introduction	2
1.1 Motivation	2
1.1.1 Rare-Earths	2
1.1.2 Spintronics	4
1.1.3 Rare-Earth Doped Gallium Nitride	4
1.2 Objectives	6
2 Theoretical Background	7
2.1 Hamiltonian for Rare-Earth Dopants	7
2.1.1 $H_{Coulomb}$ - Coulomb Terms	8
2.1.2 H_{LS} - Spin-Orbit Term	8
2.1.3 H_{CF} - Crystal-Field Terms	10
2.1.4 H_B - Magnetic Field Term	13
2.1.5 H_{other} - Other Terms	14
2.1.6 Consequence of Crystal-Field Terms on Quantum Numbers . .	15
2.1.7 Comments on Relative Magnitudes of Terms	15
2.1.8 Importance of Perturbing Terms	15
2.2 Group Theory for Optical Transitions of Rare-Earth Ions	16

2.2.1	Background	17
2.2.2	Application to Crystal-Field Terms	29
2.2.3	Simplifying Effective g Factors	30
2.2.4	C_{3v}	33
2.2.5	C_1 and C_{1v}	43
2.2.6	SO(2)	49
2.2.7	Magnetic Perturbations	50
2.3	Expected Energy Levels	52
2.3.1	Er^{3+}	52
2.3.2	Nd^{3+}	54
2.4	Host Crystals and Incorporation Sites	55
2.5	Dilute Magnetic Semiconductors	57
2.6	Faraday Effect	59
3	Experimental Methods	60
3.1	Combined Excitation Emission Spectroscopy (CEES)	60
3.1.1	Basic Principle	60
3.1.2	Experimental Setup	61
3.1.3	Magnetic Fields	63
3.1.4	Polarimetry	64
3.2	Equipment Used	65
3.3	Peak Fitting Methods	67
3.3.1	Comments on Broadening Mechanisms	67
3.3.2	Approximated Voigt Profile	69
3.3.3	Zeeman Splitting	70
3.3.4	Ferromagnetic Hysteresis Curves	71
4	Spectroscopic Detection of Ferromagnetic Hysteresis	72
4.1	Motivation	72
4.2	Our Approach	73
4.3	Results	74

4.4	Improving the Detection Threshold	79
4.4.1	Relevant Parameters	79
4.4.2	Estimating Values for Parameters	80
4.4.3	Results	82
4.4.4	Final Comments	85
4.5	Conclusions and Future Advice	86
5	An Investigation of Erbium Doped Lithium Tantalate and Lithium Niobate	87
5.1	Motivation	87
5.1.1	Objectives	88
5.2	Approach	88
5.2.1	Experimental	88
5.2.2	Analysis	90
5.3	Erbium in Lithium Tantalate	91
5.3.1	Sites	91
5.3.2	Polarization	92
5.3.3	Magnetic Splittings	113
5.3.4	Polarization of Zeeman Split Peaks	121
5.3.5	Expected Behavior	121
5.3.6	Conclusions	123
5.4	Erbium in Lithium Niobate	126
5.4.1	Polarization without a Magnetic Field	126
5.4.2	Polarization with a Magnetic Field	132
5.4.3	Magnetic Splittings	135
5.4.4	Conclusions	135
5.5	Suggested Future Work	137
6	Transitions in Erbium Doped Gallium Nitride	138
6.1	Experimental Measurements of Zeeman Splittings as a Function of Applied Field in Erbium Doped Gallium Nitride	138

6.1.1	Introduction	138
6.1.2	Motivation	139
6.1.3	Approach	140
6.1.4	${}^4I_{13/2}$ to ${}^4I_{15/2}$ Emission	140
6.1.5	${}^4I_{15/2}$ to ${}^4I_{11/2}$ Excitation	159
6.2	Polarizations	169
6.2.1	Without a Magnetic Field	169
6.2.2	With a Magnetic Field	171
6.3	Conclusions and Future Work	176
6.3.1	Nonlinear Zeeman Splittings	176
6.3.2	Level Assignments and Properties	177
7	Investigation into an Asymmetry in Zeeman Split Peaks	179
7.1	What is this Asymmetry?	179
7.2	Theoretical Difficulties	181
7.2.1	Transition Probabilities	181
7.2.2	Crystal-Field Distortions	182
7.2.3	Numeric Measure	183
7.3	Results to Date	185
7.3.1	Consistency Issues with Neodymium doped Gallium Nitride	185
7.3.2	Different Effects in Erbium Doped Gallium Nitride Samples	192
7.3.3	Bulk Crystal Hosts	197
7.3.4	Local Symmetry	203
7.3.5	Magnetic Field Magnitude Dependence	204
7.3.6	Polarization Dependence and Magnetic Field Angle Dependence	207
7.3.7	Crystal-Field Numbers	212
7.3.8	Raman Spectroscopy	215
7.3.9	Temperature Dependence	216
7.3.10	Laser Power Dependence	221
7.4	Additional Preliminary Results	221
7.4.1	Appearance in a Crystal with Cubic Symmetry	221

7.4.2	Reversing the c-axis in a Ferroelectric	223
7.5	Possible Mechanisms	224
7.5.1	Faraday Effect	224
7.5.2	Thermal Gradient	225
7.5.3	Strain and Magnetostriction	225
7.5.4	Role of an Additional Electric Field	226
7.6	Suggested Future Work	226
7.7	Conclusions	228
8	Summary	230
8.1	Major Points	230
8.2	Peak Fitting vs. Method of Moments	231
8.3	Uniqueness of Erbium Doped Gallium Nitride	231
8.4	The Asymmetry Effect	232
A	Additional Data for Erbium Doped Lithium Tantalate	233
A.1	Energy Levels	233
A.2	Magnetic Splittings	238
B	Additional Data for Erbium Doped Lithium Niobate	245
B.1	Energy Levels	245
B.2	Magnetic Splittings	248
Vita		258

List of Tables

5.1	Expected electric dipole transition polarizations between levels of given crystal-field number for C_{3v} symmetry and half integer J	93
5.2	Ratios of π to σ polarization for two excitation peaks (involving the ground state and levels of $^4I_{\frac{11}{2}}$) found to be predominantly π polarized for site A.	112
5.3	Shown are fitted g factors for sites A-D.	118
5.4	Shown are fitted g factors for sites E, H1, H2, and I.	119
5.5	Shown are fitted g factors for sites J-M.	120
5.6	Shown are suggested crystal-field number assignments	125
5.7	Fitted effective g factors for site 4, magnetic field parallel to c-axis. .	136
5.8	Suggested crystal-field number assignments for erbium-doped lithium tantalate	136
6.1	Results for the energy levels of the main site in Er doped GaN from various sources. The last two columns are from two different sets of data fitted for this work. The errors in those columns are from estimated 95 percent confidence intervals from the fitting algorithm used, and do not take into account errors from sources such as calibration of the emission axis.	142

6.2	Effective g factors for a magnetic field applied perpendicular to the c -axis. The values in the column corresponding to results obtained here were determined by averaging the g factors determined from each spectrum, using the errors from the fitting algorithm for weighting. Listed errors in that column correspond to one standard deviation. .	147
6.3	Effective g factors for a field applied parallel to the c -axis. Only levels appearing in transitions in the data set used are included. Listed errors in the extrapolated and interpolated columns correspond to a 95 percent confidence interval calculated from a covariance matrix from the fitting algorithm.	152
6.4	Values for apparent effective g factors determined using fits of the fitted energies as a function of fields for the parallel field case (with a small fitted offset for the zero field). Listed errors in the extrapolated and interpolated columns correspond to a 95 percent confidence interval calculated from a covariance matrix from the fitting algorithm.	152
6.5	Values for the g_2 parameters described in this chapter from fits of the fitted energies as a function of fields for the parallel field case (with a small fitted offset for the zero field). Listed errors in the extrapolated and interpolated columns correspond to a 95 percent confidence interval calculated from a covariance matrix from the fitting algorithm.	153
6.6	Comparison of values (in eV) for the assignment of the levels of ${}^4I_{\frac{11}{2}}$.	163
6.7	These are fittings for the effective g factors, energy levels, and g_2 parameters for the parallel field case for excitation from ${}^4I_{\frac{15}{2}}$ to ${}^4I_{\frac{11}{2}}$. g_2 factors which seemed unrealistic are not included here. While fitting g factors given here, it was assumed g_2 values were zero. Errors are 95 percent confidence intervals derived from fitting algorithms. . .	167

6.8	Fittings for the effective g factors, energy levels, and g_2 parameters for the perpendicular field case for excitation from ${}^4I_{\frac{15}{2}}$ to ${}^4I_{\frac{11}{2}}$. Errors are 95 percent confidence intervals derived from fitting algorithms. * For this level (the 1.2585eV peak), while a number with a nonzero error was returned by the fitting, it appeared to be fitting noise for this peak, due to low signal as the field magnitude increased. ** For these levels, visible splittings were not readily apparent in the spectra.	167
6.9	Suggested crystal-field number assignments for the majority site for erbium in gallium nitride. A * indicates that the assignment is in apparent conflict with the effective g factors measured for a magnetic field perpendicular to the c-axis.	178
A.1	Fitted transitions observed for sites A-D. All values are given in eV. Errors are 95 percent confidence intervals derived from the fitting algorithm used.	234
A.2	Fitted transitions observed for sites E, H1, H2, and I. All values are given in eV. Errors are 95 percent confidence intervals derived from the fitting algorithm used.	235
A.3	Fitted transitions observed for sites J-M. All values are given in eV. Errors are 95 percent confidence intervals derived from the fitting algorithm used.	236
A.4	Fitted energy levels for sites A-D. All values are given in eV. Errors are 95 percent confidence intervals derived from the fitting algorithm used.	236
A.5	Fitted energy levels for sites E, H1, H2, and I. All values are given in eV. Errors are 95 percent confidence intervals derived from the fitting algorithm used.	237
A.6	Fitted energy levels for sites J-M. All values are given in eV. Errors are 95 percent confidence intervals derived from the fitting algorithm used.	237
A.7	Fitted level splittings for site A.	239

A.8	Fitted level splittings for site B.	239
A.9	Fitted level splittings for site C.	240
A.10	Fitted level splittings for site D.	240
A.11	Fitted level splittings for site E.	241
A.12	Fitted level splittings for site H1.	241
A.13	Fitted level splittings for site H2.	241
A.14	Fitted level splittings for site I.	242
A.15	Fitted level splittings for site J.	242
A.16	Fitted level splittings for site K.	243
A.17	Fitted level splittings for site L.	243
A.18	Fitted level splittings for site M.	244
B.1	Fitted transitions for sites 2-5. All values are given in eV. Errors are 95 percent confidence intervals derived from the fitting algorithm used.	246
B.2	Fitted transitions for sites 6-9. All values are given in eV. Errors are 95 percent confidence intervals derived from the fitting algorithm used.	246
B.3	Fitted transitions for sites 10-11. All values are given in eV. Errors are 95 percent confidence intervals derived from the fitting algorithm used.	247
B.4	Fitted splittings for sites 2, 3, 4 and 9, for a magnetic field applied parallel to the c-axis, with an expected magnitude of 740mT. All values are given in meV. Errors are 95 percent confidence intervals derived from the fitting algorithm used.	249

List of Figures

1.1	The f-block elements are indicated. The row of elements of these labeled as the Lanthanides are known as rare-earths.	3
2.1	Mixing of states with m_j value differing by integer multiples of three (for C_{3v} symmetry) produces three groups of crystal-field quantum numbers, of which two groupings must be identical under time reversal.	43
2.2	The energy levels of erbium most important to this work are shown. Note that final states do not have m_j as a good quantum number, but the number of states shown with each crystal-field number is valid. The relative ordering of energies may also differ.	53
2.3	For C_{3v} symmetry for half integer J multiplets, the selection rules are expressed neatly in this diagram. These rules apply to both Nd^{3+} and Er^{3+}	54
2.4	The energy levels of erbium most important to this work are shown. Note that final states do not have m_j as a good quantum number, but the number of states shown with each crystal-field number is valid. The relative ordering of energies may also differ.	55
2.5	A portion of the wurtzite crystal structure, applicable to the gallium nitride samples used in this work. The marked polyhedra are meant to show how this structure can result in C_{3v} symmetry.	56
3.1	Example CEES data for an erbium doped gallium nitride epitaxial film sample with one majority incorporation site.	61
3.2	A typical setup for the CEES spectroscopy used for this work.	63

3.3	Example CEES data in the vicinity of one peak which splits with the application of a magnetic field, for a transition of site A in an erbium doped lithium tantalate bulk crystal sample.	64
3.4	Example CEES data for a peak exhibiting fluorescence line narrowing for the majority site in erbium doped gallium nitride.	69
3.5	Diagram of the three parameters used for fitting Zeeman splitting for a transition between two doubly degenerate levels.	70
4.1	Example expected behavior for peak splitting or width measures with hysteresis, assuming an arctangent function approximation for the hysteresis.	74
4.2	Taken from Ref. [75], second moment of an emission peak near 1.353eV from Nd ³⁺ in GaN as a function of applied magnetic field. . .	75
4.3	Fitted widths as a function of applied field. Field was cycled prior to this measurement, so there is no virgin material portion. Sample E185-R1-J, GaN:Nd epitaxial film	76
4.4	Fitting of the fitted widths using an approximate arctangent function to model ferromagnetic hysteresis, from an experiment using a magnet expected to have its own hysteresis. Sample E185-R1-J, GaN:Nd epitaxial film	77
4.5	Older data from the author of Ref. [75] analyzed by the same method as used for Figure 4.4, with two different approaches to assign field values.	78
4.6	Detection threshold for error model using initial parameters as a function of applied magnetic field.	83
4.7	Dependence of the detection threshold as a function of peak photon count, with all other parameters held constant.	84
4.8	Modeled detection threshold for a 0.1T applied field as a function of energy range per pixel, with all other parameters held constant, with the caveat that total photon count per range of energy is kept constant, rather than peak photon count.	85

5.1	Fitted amplitudes as a function of excitation polarization for several transitions for Site A. 0 degrees corresponds to π polarization, assuming correct angling of the sample and setup.	93
5.2	Fitted amplitudes as a function of emission polarization for several transitions for Site A, all thought to involve the lowest level of the ${}^4I_{\frac{11}{2}}$ multiplet, C1. 0 degrees corresponds to π polarization, assuming correct angling of the sample and setup.	95
5.3	Fitted amplitudes as a function of emission polarization for several transitions for Site A, all thought to involve the lowest level of the ${}^4I_{\frac{13}{2}}$ multiplet, B1. 0 degrees corresponds to π polarization, assuming correct angling of the sample and setup.	96
5.4	Fitted amplitudes as a function of excitation polarization for several transitions for site C. 0 degrees corresponds to π polarization, assuming correct angling of the sample and setup.	97
5.5	Fitted amplitudes as a function of emission polarization for several transitions for site C. 0 degrees corresponds to π polarization, assuming correct angling of the sample and setup.	98
5.6	Fitted amplitudes as a function of emission polarization for several transitions for site C. 0 degrees corresponds to π polarization, assuming correct angling of the sample and setup.	99
5.7	Fitted amplitudes as a function of excitation polarization for several transitions for site B. 0 degrees corresponds to π polarization, assuming correct angling of the sample and setup.	100
5.8	Fitted amplitudes as a function of emission polarization for several transitions for site B. 0 degrees corresponds to π polarization, assuming correct angling of the sample and setup.	100
5.9	Fitted amplitudes as a function of emission polarization for several transitions for site B. 0 degrees corresponds to π polarization, assuming correct angling of the sample and setup.	101

5.10	Fitted amplitudes as a function of polarization for several transitions for site D. 0 degrees corresponds to π polarization, assuming correct angling of the sample and setup.	102
5.11	Fitted amplitudes as a function of polarization for several transitions for site H1. 0 degrees corresponds to π polarization, assuming correct angling of the sample and setup.	103
5.12	Fitted amplitudes as a function of polarization for several transitions for site H2. 0 degrees corresponds to π polarization, assuming correct angling of the sample and setup.	104
5.13	Fitted amplitudes as a function of polarization for several transitions for site I. 0 degrees corresponds to π polarization, assuming correct angling of the sample and setup.	105
5.14	Fitted amplitudes as a function of excitation polarization for several transitions for site M. 0 degrees corresponds to π polarization, assuming correct angling of the sample and setup.	106
5.15	Fitted amplitudes as a function of polarization for several transitions for site J. 0 degrees corresponds to π polarization, assuming correct angling of the sample and setup.	107
5.16	Fitted amplitudes as a function of polarization for several transitions for site K. 0 degrees corresponds to π polarization, assuming correct angling of the sample and setup.	108
5.17	Fitted amplitudes as a function of polarization for several transitions for site L. 0 degrees corresponds to π polarization, assuming correct angling of the sample and setup.	109
5.18	Fitted amplitudes as a function of polarization for several transitions for site E. 0 degrees corresponds to π polarization, assuming correct angling of the sample and setup.	110
5.19	These show scaled intensity as a function of excitation polarization angle for a transition believed to be the same transition for all identified sites. 0 degrees corresponds to π polarization, assuming correct angling of the sample and setup.	111

5.20	Fitted Zeeman split peaks from an excitation spectrum for sites A and B.	115
5.21	Fitted Zeeman split peaks from an excitation spectrum for sites A and B.	115
5.22	Fitting of splitting of a level for site A as a function of magnetic field angle relative to the c-axis. Error bars represent a 95 percent confidence interval from the fitting algorithms used, and in the second case, an inclusion of an estimate of possible field magnitude error. . .	116
5.23	Fitted excitation polarizations for the Zeeman split transitions for a field parallel to the c-axis. This is for the lowest doubly degenerate level of ${}^4I_{\frac{15}{2}}$ to the lowest doubly degenerate level of ${}^4I_{\frac{11}{2}}$. The shown transitions were σ polarized in the zero magnetic field case.	122
5.24	Fitted excitation polarizations for the Zeeman split transitions for a field parallel to the c-axis. This is for the lowest doubly degenerate level of ${}^4I_{\frac{15}{2}}$ to the second lowest doubly degenerate level of ${}^4I_{\frac{11}{2}}$. The shown transitions were π polarized in the zero magnetic field case. . .	123
5.25	Fitted amplitudes as a function of polarization for several transitions for site 2. 0 degrees corresponds to π polarization, assuming correct angling of the sample and setup.	127
5.26	Fitted amplitudes as a function of polarization for several transitions for site 3. 0 degrees corresponds to π polarization, assuming correct angling of the sample and setup.	128
5.27	Fitted amplitudes as a function of polarization for several transitions for site 4. 0 degrees corresponds to π polarization, assuming correct angling of the sample and setup.	129
5.28	Fitted amplitudes as a function of polarization for several transitions for site 7. 0 degrees corresponds to π polarization, assuming correct angling of the sample and setup.	130
5.29	Fitted amplitudes as a function of polarization for several transitions for site 9. 0 degrees corresponds to π polarization, assuming correct angling of the sample and setup.	131

5.30	Fitted excitation polarizations for the Zeeman split transitions for a field parallel to the c-axis. These are the transitions which were σ polarized for the zero magnetic field case. This is for the lowest doubly degenerate level of ${}^4I_{15/2}$ to the lowest doubly degenerate level of ${}^4I_{11/2}$	133
5.31	Fitted excitation polarizations for the Zeeman split transitions for a field parallel to the c-axis. These are transitions which were π polarized for the zero magnetic field case. This is for the lowest doubly degenerate level of ${}^4I_{15/2}$ to the second lowest doubly degenerate level of ${}^4I_{11/2}$	134
6.1	Emission transitions for Er^{+3} observed in the data used for this work.	141
6.2	Fitting of an emission spectrum from the majority site in erbium doped gallium nitride. Five parameters are used to describe the positions of nine emission peaks.	143
6.3	Result of fitting the splitting of a transition near 0.8032eV. In this case, the field was applied parallel to the c-axis. The linear fits shown in green for the splittings were not forced to have a particular intercept. Error bars are from 95 percent confidence intervals from the fitting algorithm.	144
6.4	Spectra for a parallel applied field in the vicinity of what is believed to be an avoided crossing. Portions of spectra in this region were fitted using two peaks for each field. The results of that fitting are overlaid here. Error bars are from 95 percent confidence intervals from the fitting algorithm.	145
6.5	This is data for A2373 showing spectra as a function of applied field, with lines indicating the transitions centers as predicted by the initial guesses obtained to this point.	146
6.6	Fitted energy levels for A2373 with a magnetic field applied perpendicular to the c axis. Error bars correspond to a 95 percent confidence interval, using values from the fitting algorithm.	148

6.7	Fitted energy levels for A2373 with a magnetic field applied parallel to the c axis. Error bars shown correspond to a 95 percent confidence interval, using values from the fitting algorithm.	149
6.8	Calculated apparent effective g factors for the ground state of the majority site, using a linear dependence for the splitting on the applied field magnitude, depending on which levels are used for the calculation. The errors are from 99 percent confidence intervals derived from Monte Carlo error estimation, using a covariance matrix from the fitting algorithm, as well as an estimate for the error in field magnitude.	154
6.9	This is an illustrative example showing approximately where level (anti)crossings including the ground state are expected to occur. Note that the first plot has a logarithmic scale while the second does not. .	156
6.10	Fitted center energies as a function of applied field strength. Note that the ground state center is fixed to be zero.	158
6.11	The transitions which were observed in this data set are indicated, with corresponding levels. The level scheme corresponds to the one used in this work.	159
6.12	Excitation profile taken from CEES data collected by the author of [44], believed to be from sample A2373, using the level scheme suggested in that work. The arrow indicates the peak not assigned. . . .	160
6.13	Excitation spectra as a function of platform temperature. The 1.2550eV peak is marked with an arrow. Scaling is accomplished by dividing by the amplitude of the highest intensity peak.	161
6.14	Fitted excitation spectrum with transition assignments labeled. Solid lines involve A1, dashed lines involve A2, and dotted lines involve A3.	162
6.15	Fitted energies vs. platform setpoint temperature, with errors taken from the fitting algorithms used	164
6.16	Fitted energy levels for A2373 with a magnetic field applied parallel to the c axis. Error bars correspond to a 95 percent confidence interval, using values from the fitting algorithm.	166

6.17	Fitted energy levels for A2373 with a magnetic field applied perpendicular to the c axis. Error bars correspond to a 95 percent confidence interval, using values from the fitting algorithm.	168
6.18	Emission polarizations for some of the transitions observed in Er doped GaN. Labels indicate assigned transitions. σ polarization corresponds to 90 degrees, and π to 0 degrees.	170
6.19	Excitation polarizations for some of the transitions observed in Er doped GaN. Labels indicate assigned transitions. σ polarization corresponds to 90 degrees, and π to 0 degrees.	170
6.20	Fitted spectra for four excitation polarization angles for the A2373 sample. The magnetic field is parallel to the c-axis. This shows transitions involving from the lower levels of ${}^4I_{\frac{15}{2}}$ to the levels of ${}^4I_{\frac{11}{2}}$	172
6.21	Fitted spectra for four excitation polarization angles for the A2373 sample. The magnetic field is parallel to the c-axis. This shows four split peaks from the level assigned as A1 to C6.	173
6.22	Excitation polarizations for the four peaks originating from magnetic splitting of the A1 to C6 and A1 to C1 transitions for the majority site for Er in GaN. These are expected to be π and σ polarized.	173
6.23	Excitation polarizations for the four peaks originating from magnetic splitting of the A1 to C3 transition for the majority site for Er in GaN. These are expected to be π and σ polarized.	174
6.24	Excitation polarizations for the four peaks originating from magnetic splitting of the A1 to C4 transition for the majority site for Er in GaN. These are expected to be π and σ polarized.	174
6.25	Excitation polarizations for the four peaks originating from magnetic splitting of the A1 to C5 and A1 to C2 transitions for the majority site for Er in GaN. These are expected to be π polarized.	175
7.1	Comparison of spectra taken for a Nd doped GaN sample with a magnetic field applied parallel and antiparallel to the c-axis. The figure is taken from Ref. [75].	180

7.2	Typical difference in spectra for a field applied in one direction, and then reversed. Data fitted to determine a measure of the asymmetry. Spectra from Site A in erbium doped lithium tantalate.	184
7.3	Comparison of scaled excitation profiles taken from CEES data for +4T and -4T magnetic fields applied parallel to the c-axis, using the the Janis brand cryostat and helium immersion superconducting magnet, thought to be at helium vapor temperatures (tens of K). Samples are Nd doped GaN epitaxial films. Emission energy was 1.355eV. Data shown was taken from three different samples in the same run of the experiment on the same day.	186
7.4	Excitation profiles from CEES data for sample E185-R1-N, for fields applied both parallel and anti-parallel to the c-axis with the indicated magnitudes. The two sets with lower field values were conducted on the Montana Instruments Cryostation setup, and the remaining two with the Janis brand cryostat setup.	188
7.5	Comparisons of the asymmetry effect in excitation profiles from CEES data for two GaN:Nd samples.	189
7.6	Comparisons of the asymmetry effect in emission profiles, taken from the same CEES data as the excitation profiles in Figure 7.5.	190
7.7	Portion of CEES under applied magnetic field from data taken by the author of [75]. Emission axis is approximate. Neodymium doped gallium nitride, but specific sample unknown.	191
7.8	Comparison of portion of CEES for magnetic field applied parallel and antiparallel to the c-axis for sample E176-R2-J.	191
7.9	Comparison ratios of amplitudes of magnetically split emission peaks expected to experience changes in relative amplitude due to the previously observed asymmetry effect, as a function of approximate relative spatial location on the sample.	192
7.10	CEES data differences of CEES data for application of a magnetic field parallel and antiparallel to the c-axis. The sample used is the GaN:Er on sapphire substrate sample used in Ref. [74].	194

7.11	CEES data differences of CEES data for application of a magnetic field parallel and antiparallel to the c-axis. The sample used is the GaN:Er on AlN substrate sample used in Ref. [74].	195
7.12	CEES data and differences of CEES data for application of a magnetic field parallel and antiparallel to the c-axis. The sample used is the GaN:Er on 111 plane Si substrate sample used in Ref. [74].	196
7.13	CEES data and differences of CEES data for application of a magnetic field parallel and antiparallel to the c-axis. The sample used is the GaN:Er on GaN substrate sample used in Ref. [74].	197
7.14	Comparison of excitation profiles from CEES data for GaN:Er on [111] Si sample	198
7.15	Comparison of two sets of CEES data for GaN:Er on [111] Si sample, with difference of 50mT in applied field magnitude, in same direction	199
7.16	CEES data and differences of CEES data for application of a magnetic field parallel and antiparallel to the c-axis. The sample used is A2373, also a GaN:Er epitaxial film on a sapphire substrate.	200
7.17	Differences in CEES data for a magnetic field applied parallel and antiparallel to the c-axis for σ and π emission polarizations, and for flipping of the sample in the mount relative to the the magnetic field for LiTaO ₃ :Er	201
7.18	Differences in CEES data for a magnetic field applied parallel and antiparallel to the c-axis for π and σ polarized emission in erbium doped lithium niobate.	202
7.19	Comparison of asymmetry effect for three different sites (A, B, and C) for Er in LiTaO ₃ . Results were obtained by comparing the Zeeman split transitions corresponding to the assigned transition from B1 to A2.	204
7.20	Numeric measure of asymmetry vs. applied field magnitude for an excitation peak for the E176-R2-J sample, which is a neodymium doped gallium nitride sample. Error bars correspond to one standard deviation.	205

7.21	Modified numeric measure of asymmetry vs. applied field magnitude for an emission peak for an unknown Nd doped GaN sample. Error bars correspond to one standard deviation.	206
7.22	Modified numeric measure of asymmetry vs. applied field magnitude for an emission peak for an unknown Nd doped GaN sample. Error bars correspond to one standard deviation.	207
7.23	Numeric measure of asymmetry vs. polarization angle for several orientations of the magnetic field relative to the c-axis for the B1 to A2 transition for site A in LiTaO ₃ :Er. Dotted lines are added to give an indication of the change in sign of the data. The angle axes indicate the angle of the linear polarizer, and the magnetic field is always applied at an angle corresponding to zero degrees. The sample is rotated relative to these for each experiment. Thus, in the parallel case, the c-axis of the crystal is also along zero degrees (with some error), and in the perpendicular case, the c-axis of the crystal is along 90 degrees.	208
7.24	Example fitting of sums and differences of spectra for one Zeeman split peak, using a Malus' Law type form to describe amplitudes and differences for positive and negative magnetic fields. The data is identical to the data used to produce the plot for the parallel case in Figure 7.23. The sums and differences refer to combining spectra for positive and negative magnetic fields.	210
7.25	Maximum magnitude (signs removed) of asymmetry measure for both overall asymmetry numerical measure and measures for individual peaks as a function of applied field angle. Values with unusually high errors in the fitting are omitted. Error bars correspond to a 95 percent confidence interval.	211
7.26	Example fitting of +/- magnetic field spectra and their difference for 45 degrees between the c-axis and the magnetic field. Note the rather large effect.	212

7.27	Fitted emission polarization for the B1 to A2 transition for site A in erbium doped lithium tantalate without an applied magnetic field. Here, 0° corresponds to the c-axis of the crystal.	213
7.28	Comparison of polarizations of Zeeman split peaks for the B1 to A2 transition for site A in erbium doped lithium tantalate for an angle of 45° between the c-axis and the magnetic field. Here, 0° corresponds to the orientation of the magnetic field, and the c-axis of the crystal is oriented along 45° . The angles show data as a function of polarization angle.	214
7.29	Plots demonstrating asymmetry effect for site A in LiTaO3 for the transitions assigned as B1 to A1 and B1 to A2, with an overlapping pair of peaks from site B appearing to the right in the former.	214
7.30	Plots demonstrating asymmetry effect for site C in LiTaO3 for the transitions assigned as B1 to A1 and B1 to A2	215
7.31	Comparison of Raman spectra for an applied magnetic field parallel and perpendicular to the c-axis, as well as without an applied magnetic field, for erbium doped lithium tantalate.	217
7.32	Differences in CEES for applied magnetic fields parallel and antiparallel to the c-axis for higher temperatures.	218
7.33	Fitted differences in emission spectra of erbium lithium tantalate as a function of emission polarization angle for select temperatures. The magnetic field was applied along 0° , while the c-axis was aligned along 45° . The fitting model assumes that the amplitudes of the peaks can be described using a Malus' law type dependence, with the same offset angle for both peaks. This also assumes this portion of the spectra can be accurately modeled with only two peaks.	219
7.34	Values of the asymmetry measure for π and σ polarized emission from erbium doped lithium tantalate as a function of platform temperature. Error bars correspond to 95% confidence intervals.	220
7.35	A measure of the asymmetry vs. excitation power for two emission polarizations.	221

7.36	Difference in CEES data for an applied magnetic field and an applied magnetic field in the opposite direction, for erbium doped Cs_2NaYF_6 , with unknown orientation.	222
7.37	Difference in CEES data for an applied magnetic field parallel and antiparallel to the c-axis of erbium doped lithium tantalate, for what are believed to be two differently ferroelectric poled regions of erbium doped lithium tantalate.	223

Abstract

There is interest in magnetic properties of doped semiconductors for possible applications in spintronics and for gaining further insight into the incorporation sites of the dopants. To this end, optical spectroscopy was conducted on several rare earth doped systems subject to a magnetic field. In particular, several important results were obtained for erbium doped gallium nitride. The results provide insight into states of the dopants, effective g factors, and site symmetry, and some of the difficulties inherent in performing measurements of those properties. Additional results were obtained regarding a previously observed effect in which reversing the orientation of an applied magnetic field seems to change transition probabilities of rare-earth dopants in some cases.

Chapter 1

Introduction

1.1 Motivation

1.1.1 Rare-Earths

The term *rare-earths* refers to the first row of the f-block of the periodic table (sometimes with the addition of yttrium and scandium), characterized by partially filled 4f shells, with completed 5s and 5p shells. The larger radial extent of the $n = 5$ shells means that the partially filled 4f shells are shielded from local electric fields by this outer shell. This leads to similar intra-4f transitions for a given rare-earth element (in a given charge state) in a variety of different host materials. [13] [77] In practice, of course, not all host materials may work well for a given application and transition. Some of these difficulties will be described in 1.1.3.

Rare-earths are already used in a variety of existing technologies. Triply ionized erbium has transitions corresponding to the best wavelengths for transmission in silica glass ($1.54\mu m$), and is used in fiber communications, such as in erbium-doped fiber amplifiers. [21] Neodymium has a transition near $1.06\mu m$ which can be frequency doubled to give green light, as is done for some green lasers, based on Nd:YAG. [69] Lasers based on Nd:YAG are used for many purposes, including applications in medicine, [42] dentistry [46], and manufacturing. [12] Europium has a transition around $630nm$, in the red part of the spectrum, and is used in phosphors

Group→	1	2	3	4	5	6	7	8	9	10	11	12	13	14	15	16	17	18	
↓Period																			
1	1 H																		2 He
2	3 Li	4 Be											5 B	6 C	7 N	8 O	9 F	10 Ne	
3	11 Na	12 Mg											13 Al	14 Si	15 P	16 S	17 Cl	18 Ar	
4	19 K	20 Ca	21 Sc	22 Ti	23 V	24 Cr	25 Mn	26 Fe	27 Co	28 Ni	29 Cu	30 Zn	31 Ga	32 Ge	33 As	34 Se	35 Br	36 Kr	
5	37 Rb	38 Sr	39 Y	40 Zr	41 Nb	42 Mo	43 Tc	44 Ru	45 Rh	46 Pd	47 Ag	48 Cd	49 In	50 Sn	51 Sb	52 Te	53 I	54 Xe	
6	55 Cs	56 Ba		72 Hf	73 Ta	74 W	75 Re	76 Os	77 Ir	78 Pt	79 Au	80 Hg	81 Tl	82 Pb	83 Bi	84 Po	85 At	86 Rn	
7	87 Fr	88 Ra		104 Rf	105 Db	106 Sg	107 Bh	108 Hs	109 Mt	110 Ds	111 Rg	112 Cn	113 Nh	114 Fl	115 Mc	116 Lv	117 Ts	118 Og	
Lanthanides			57 La	58 Ce	59 Pr	60 Nd	61 Pm	62 Sm	63 Eu	64 Gd	65 Tb	66 Dy	67 Ho	68 Er	69 Tm	70 Yb	71 Lu		
Actinides			89 Ac	90 Th	91 Pa	92 U	93 Np	94 Pu	95 Am	96 Cm	97 Bk	98 Cf	99 Es	100 Fm	101 Md	102 No	103 Lr		

Figure 1.1: The f-block elements are indicated. The row of elements of these labeled as the Lanthanides are known as rare-earths.

for converting light to red light. [34] Host crystals already containing rare-earths, such as yttrium in the already mentioned YAG, or Yttrium Aluminum Garnet, allow for easy incorporation of other rare-earth dopants. Outside optics, rare-earth magnets are another application. [48]

Some optical applications for rare-earths could be improved with different crystal host materials. For example, for a solid state laser, excess heating is a common engineering problem. If a host material with higher thermal conductivity and similar other characteristics is identified, it may be possible to use greater pump intensities (and presumably greater power output), or to achieve similar powers with fewer engineering problems due to cooling requirements. For applications using phosphors, such as solid-state white lighting, there may be efficiency gains to be made in changing from phosphors to a technology in which the dopant is directly excited, as in an LED, in terms of the amount of rare-earth material needed. Ideally, if a set of rare-earths producing several visible colors, such as red, green, and blue, can be made into LEDs with the same host material, it would be possible to produce these colors without phosphors on a single substrate. [70] Erbium (green), europium (red), and thulium (blue) might permit such a system. [25] Determining how to make devices

with a cheaper host material, such as silicon, without sacrificing too much performance, may translate into cheaper products. These applications require work in identifying and improving performance in candidate host materials.

1.1.2 Spintronics

Rare-earths tend to have unpaired spins, making them useful for magnetic applications. One goal of research along these lines is to develop a cheap, conventional semiconductor with ferromagnetic properties, which maintains those properties at and above room-temperature. This would allow biasing of electron spins in a semiconductor, allowing both magnetic and electric properties of an electron to be exploited. Further, if this can be accomplished by doping semiconductors, in principle, the degree of this biasing might be controlled in a way similar to carrier concentration. Such materials may allow applications such as spin-polarized LEDs, as demonstrated in Mn doped GaAs, albeit only at cryogenic temperatures. [55] This use and transport of the spin of electrons in electronic devices is part of a field called Spintronics.

There exist claims of room-temperature ferromagnetism in gallium nitride samples doped with various rare-earths, including erbium doped gallium nitride [1] [47] [74], gadolinium doped gallium nitride [8], and neodymium doped gallium nitride. [37] This provokes interest in understanding the magnetic properties of these materials.

1.1.3 Rare-Earth Doped Gallium Nitride

In a process known as thermal quenching, photoluminescence emission intensities for rare-earth dopants decrease as temperature increases. It is empirically known that the degree of thermal quenching decreases with increasing band gap. [13] [70] One paper examining Pr, Eu, Tb and Tm doped AlN provides a model which could explain the degree of thermal quenching, based upon a model for how energy is transferred to the dopant. [36] It proposes that energy is transferred to the rare-earth dopant by aid of a local defect which can trap carriers, which in turn creates

a charge imbalance which attracts a carrier of opposite charge. This leads to a trapped exciton which can transfer energy to the dopant. At elevated temperatures, the carriers are not trapped for as long a period of time, and thus, energy transfer to the dopant is less likely. Another paper studying Er doped InGaP came to the conclusion (by varying the ratio of In to Ga and studying the resulting thermal quenching) that there exists a trapping level which exists at constant offset from the vacuum level, with largely similar reasoning to the previous paper. [49] A wider band gap would correspond to greater average differences in energy between trapping levels inside the band gap and the conduction and valence bands, suggesting a higher temperature may be needed for carriers to escape the trapping levels.

Whatever the mechanism, in an extreme case, this may make obtaining a desired optical emission from a rare-earth dopant only reasonably efficient at cryogenic temperatures, rendering the material useless for room-temperature applications. This causes several problems. First, many common and well understood host materials, such as silicon, may not be usable host materials for optical applications. Second, insulators, with huge band gaps, while experiencing less of this thermal quenching effect, may have significant trade-offs, such as poor thermal conductivity, or difficulty in producing PN junctions. While not the only possible solution, this is the argument in favor of gallium nitride. It has a comparatively wide band gap (3.4eV) without being an insulator, and facilities and technologies already exist for its production. [70]

With regard to the spintronics applications, gallium nitride and zinc oxide have both been suggested as good candidate materials for room-temperature ferromagnetic semiconductors. [10] Some results using samples which were also examined in this work suggested ferromagnetism in strained epitaxial erbium-doped gallium nitride films. Specifically, hysteresis loops appeared for some samples. [74] The possibility of ferromagnetic behavior in rare-earth doped gallium nitride also inspired a prior attempt to determine whether hysteresis curves could be measured spectroscopically in neodymium doped gallium nitride. [75] It has been suggested that, due to a number of factors which can lead to false positives in detecting ferromagnetism in small samples, multiple types of experiments are required to verify its

presence. [51] This led to revisiting the question of whether spectroscopic detection of ferromagnetic hysteresis is feasible.

In particular, erbium doped gallium nitride has been suggested as a possible basis for a laser diode for applications in optical fiber communication, owing to little thermal quenching and the light emission from erbium near $1.5\mu m$, near the optimum wavelength for transmission in silica glass. [78]

1.2 Objectives

- Reexamine whether hysteresis loops can be observed spectroscopically, suggesting ferromagnetism, in neodymium doped gallium nitride. [75]
- Verify level and crystal-field number assignments for the majority site in erbium doped gallium nitride.
- Investigate a previously observed effect in which changing the sign of an applied magnetic field oriented along the c-axis led to different emission spectra in both neodymium and erbium doped gallium nitride samples, despite an expectation of time-reversal symmetry. [75] [44]
- Develop and apply a technique for examining nonlinear level splittings for the application of magnetic fields to erbium doped gallium nitride.
- Develop an experimental setup for examining polarization of transitions in detail, while also applying magnetic fields. Determine the behavior of the polarization of split transitions. Use this technique to verify crystal-field number assignments in several host materials.

Chapter 2

Theoretical Background

The results presented in this work involve measuring relative transition probabilities and energy levels. Interpreting and understanding these results requires a framework for predicting energy levels and selection rules.

The two rare-earth ions considered, Nd^{+3} and Er^{+3} , have the electron configuration for Xenon ($1s^2 2s^2 2p^6 3s^2 3p^6 3d^{10} 4s^2 4p^6 4d^{10} 5s^2 5p^6$), with the addition of $4f^3$ for the former and $4f^{11}$ for the latter. Similar structures occur for other triply ionized rare-earths. [77] This implies three valence electrons for the former, and three holes for the latter.

2.1 Hamiltonian for Rare-Earth Dopants

The first step in developing a framework for understanding the states of the rare-earth dopants in a crystal is to consider the Hamiltonian for the system. As was implied in the previous chapter, rare-earth ions in a crystal can be considered using perturbed version of the Hamiltonian for the in-vacuum case.

$$H = H_{Coulomb} + H_{LS} + H_{CF} + H_{Zeeman} + H_{other}$$

2.1.1 $H_{Coulomb}$ - Coulomb Terms

Since this work is concerned only with transitions between electrons in the same configuration, energies corresponding to changes in configuration are not considered, such as energies from a change in the principal quantum number n . However, electron-electron interactions must still be considered.

Energies for electrostatic portions of 4f configurations can be written in terms of Slater radial integrals. In practice, it may be difficult to obtain enough experimental data to determine these integrals empirically, and it may also be difficult to calculate them directly without knowledge of the wavefunctions. Thus, it is common to calculate the ratios of Slater integrals for hydrogenic wavefunctions, which are well known, and assume the ratios are similar for other systems. This leaves this term in the Hamiltonian with one free parameter. [77] Of course, with sufficient data, more of them could be left as fitting parameters. The following gives an expression for a Slater integral between two electrons, labeled a and b , with each having values of n and l .

$$F^k(n_a l_a, n_b, l_b) = e^2 \int_0^\infty \int_0^\infty \frac{r_{<}^k}{r_{>}^{k+1}} R_i^2(n_a l_a) R_j^2(n_b l_b) dr_i dr_j$$

R is the radial eigenfunction for each electron. $r_{<}$ and $r_{>}$ refer to the lesser and greater of r_i and r_j at each point being integrated, respectively. e is the fundamental charge.

How exactly these integrals are summed to give energies in an LS basis set is tabulated in Ref. [52], under the electrostatic matrices portion. It includes information on how to relate its results in terms of E^i values to the F^k integrals described here. The E^i values, or electrostatic parameters, are linear combinations of F_k integrals which may appear in other works.

2.1.2 H_{LS} - Spin-Orbit Term

For the cases in this work, LS coupling is taken as the dominant term for the rare-earth dopants after the Coulomb interaction terms, and associated terms are used

to label levels. For the dopants considered, which take on f^N configurations in the charge state expected, this involves coupling electrons in the same configuration, with only the number of electrons changing for the different dopants considered in this work. Rare-earth ions typically have large LS coupling energies. [77]

$$H_{SO} = \sum_{i=1}^N \xi(r_i)(\mathbf{s}_i \cdot \mathbf{l}_i)$$

where

$$\xi(r_i) = \frac{\hbar}{2m^2c^2r_i} \frac{dU(r_i)}{dr_i}$$

$U(r_i)$ refers to the spherically symmetric potential one obtains by assuming that one can envision each electron as being affected by a sum of a potential from a fixed nucleus and time-averaged positions of all the other electrons. The spin-orbit term requires a sum over all the electrons of the configuration. It is assumed that interactions with other configurations can be ignored. If it is found that the spin-orbit interaction term is quite large compared to electrostatic terms, it is possible to calculate matrix elements for both in a basis set of states determined from LS coupling and then diagonalize the matrix to find a new basis set. The spin-orbit radial integral,

$$\zeta_{nl} = \int_0^\infty R_{nl}^2(r)\xi(r)dr,$$

is a constant for a given configuration, and is called the spin-orbit radial integral. The product term, $\mathbf{s}_i \cdot \mathbf{l}_i$, is given by

$$\left(l^N \alpha SL \left| \sum_{i=1}^N (\mathbf{s}_i \cdot \mathbf{l}_i) \right| l^N \alpha' S' L' \right) = \sqrt{l(l+1)(2l+1)} (l^N \alpha SL || \mathbf{V}^{11} || l^N \alpha' S' L')$$

Note that α as used here in discussions of the Hamiltonian refers to any additional quantum numbers not indicated. Values are tabulated in [52] for the reduced matrix element on the right hand side, $\langle l^N \alpha SL || \mathbf{V}^{11} || l^N \alpha' S' L' \rangle$, for a variety of configurations. \mathbf{V}^{11} is a unit tensor operator introduced by Racah in [59], and can be

thought of as a linear combination of spherical tensor operators, \mathbf{u}^k , weighted by spin operators.

Having done this, it becomes apparent that this term adds one parameter to be determined, ζ_{nl} , in addition to the Slater integrals.

2.1.3 H_{CF} - Crystal-Field Terms

Definition

The crystal-field term includes corrections that result from taking the rare-earth ion in question from the vacuum to a particular location in a crystal. This term should be the only term so far which varies for different incorporation sites and host materials. Typically, this term is expressed in terms of spherical harmonics, or, more correctly when referring to terms in the Hamiltonian operator, operators transforming like the spherical harmonics. This is similar to performing an expansion of the electric field in terms of spherical harmonics. Here, however, quantum mechanical features, such as exchange interactions, also contribute. These are the tensor operators, \mathbf{C}_q^k , [77] which appear in the expression

$$H_{CF} = \sum_{k,q,i} B_q^k (\mathbf{C}_q^{(k)})_i$$

The k and q indices correspond to similar indices for spherical harmonics. The i refers to a particular electron. Symmetries associated with an incorporation site in the crystal should also apply to the crystal-field terms, which results in certain values of B_q^k being zero, as will be discussed later in the portion on group theory.

The Spherical Tensor, $\mathbf{C}_q^{(k)}$, can be expressed in terms of spherical harmonics, Y_{lm} .

$$C_q^{(k)} = \sqrt{\frac{4\pi}{2k+1}} Y_{kq}$$

Unfortunately, it is difficult to calculate the B_q^k coefficients *a priori*, as the expansion is ultimately taking into account both classical and quantum mechanical features. Recall that this term is treated as the only term with dependence on the

choice of crystal host. Thus, it is common to treat these as fitting parameters after assuming a particular symmetry to limit their number. [50] The group theory section will discuss how many nonzero, relevant parameters are present for relevant symmetries.

Calculation

Calculations of the crystal-field term between the energy levels for the vacuum case involve using various properties of angular momentum operators to simplify calculations. The Wigner-Eckart Theorem allows calculation of spherical tensors acting between states with a basis in terms of quantum numbers j and m_j in a way that removes dependence on m_j values.

$$\langle \alpha j m | C_q^{(k)} | \alpha' j' m'_j \rangle = (-1)^{j-m_j} \begin{pmatrix} j & k & j' \\ -m_j & q & m' \end{pmatrix} \langle \alpha j || C^{(k)} || \alpha' j' \rangle$$

The portion containing six elements in parentheses is a Wigner 3j symbol. Below is a similar result for removing dependence on J , using a variant of the same theorem. The portion in brackets below is the Wigner 6j symbol.

$$\langle \alpha S L J || C^{(k)} || \alpha' S' L' J' \rangle = (-1)^{s+K+j+L'} \sqrt{(2J+1)(2J'+1)} \begin{Bmatrix} L & J & S \\ J' & L' & k \end{Bmatrix} \langle \alpha S L || C^{(k)} || \alpha' S' L' \rangle$$

For a single electron, ignoring spin, this last element in the former expression is calculated rather easily, using

$$\langle \alpha l || C^{(k)} || \alpha' l' \rangle = \delta_{\alpha\alpha'} (-1)^l \sqrt{(2l+1)(2l'+1)} \begin{pmatrix} l & k & l' \\ 0 & 0 & 0 \end{pmatrix}$$

However, none of the systems considered in this work can be considered as single electron systems. To perform these multiple electron system calculations is rather difficult, and was considered by Racah for several configurations of electrons in a series of papers. [59] [60] [61] It is common to refer to tables of tabulated values

to determine these. [52] However, typically, the tables are expressed in terms of a different tensor, $U_q^{(k)}$, than the $C_q^{(k)}$ tensors described so far. If all electrons are members of the same configuration, the following expression is valid.

$$\langle l^N SLJm_j | C_q^{(k)} | l^N S'L'J'm'_j \rangle = (-1)^l (2l+1) \begin{pmatrix} l & k & l' \\ 0 & 0 & 0 \end{pmatrix} \langle l^N SLJm_j | U_q^{(k)} | l^N S'L'J'm'_j \rangle$$

Here, l refers to the orbital angular momentum for one of the electrons, presumed to be the same for all the electrons (which is the case in systems considered in this work). The earlier expressions using the Wigner-Eckart theorem also apply to the unit tensor operator.

$$\langle LSJm_j | U_q^{(k)} | LSJ'm'_j \rangle = (-1)^{J-m_j} \begin{pmatrix} J & k & J' \\ -m_j & q & m' \end{pmatrix} \langle LSJ || U^{(k)} || \alpha' J' \rangle$$

$$\begin{aligned} & \langle \alpha SLJ || U^{(k)} || \alpha' S' L' J' \rangle = \\ & (-1)^{s+K+J+L'} \sqrt{(2J+1)(2J'+1)} \begin{Bmatrix} L & J & S \\ J' & L' & k \end{Bmatrix} \langle \alpha SL || U^{(k)} | \alpha' S' L' \rangle \end{aligned}$$

The values for $\langle \alpha SL || U^{(k)} | \alpha' S' L' \rangle$ are given in [52].

Crystal-Field Numbers

As will be discussed further in the portion on group theory, for a given symmetry, crystal-field numbers are assigned to levels, grouping them by their transformation properties. Put differently, these numbers categorize states by symmetry. They are relevant insofar as these properties can be used to predict whether the matrix elements of certain operators will yield zero when operating between two states. The crystal-field number assigned to a particular group of levels which are part of a multiplet with J angular momentum is determined by the value of m_j closest to zero sharing the same representation as the levels.

2.1.4 H_B - Magnetic Field Term

The Zeeman interaction term is taken as

$$B\mu_B (\mathbf{L} + g_s\mathbf{S})$$

where μ_B is the Bohr magneton, B the applied magnetic field, and g_s the gyro-magnetic ratio for the electron. \mathbf{L} and \mathbf{S} correspond to the summed orbital and spin angular momenta, respectively, for the electron configuration. Other coupling schemes may be more relevant when examining electron configurations not considered in this work, such as $f^N s$, the situation in which one electron is in an incomplete s shell and N electrons are in an incomplete f shell. [77]

By application of the Wigner-Eckart theorem, and evaluation of the resulting terms, it can be shown that the diagonal terms result in a simple expression for LS coupling.

$$\langle \alpha SLJm_j | \mathbf{L} + g_s\mathbf{S} | \alpha SLJm_j \rangle = m_j g$$

$$g = 1 + (g_s - 1) \frac{J(J+1) - L(L+1) + S(S+1)}{2J(J+1)}$$

g is the Landé g factor for the multiplet. The non-zero off diagonal elements are given by

$$\langle \alpha SLJm_j | \mathbf{L} + g_s\mathbf{S} | \alpha SL(J-1)m_j \rangle =$$

$$(g_s - 1) \sqrt{(J^2 - m_j^2)} \sqrt{\frac{(S+L+J+1)(S+L+J-1)(L+J-S)(S+J-L)}{4J^2(2J+1)(2J-1)}}$$

Ignoring the off diagonal terms for the moment, this means that the magnetic term simplifies to

$$E_B = B\mu_b m_j g,$$

where g is the Landé g factor, B is the applied magnetic field, and μ_B is the Bohr magneton. In this work, since crystal-field splittings are expected to mix states of differing m_j , this is simplified to an effective g factor, which corresponds to some weighted average of m_j and g in the previous equation. This gives

$$E_B = B\mu_B g_{eff}$$

Of course, since levels in half-integer spin systems come in pairs, as will be discussed later, this means that pairs of levels must exhibit opposite signs for the effective g factor given above. Thus, in this work, effective g factors, when given for a doubly degenerate level, are the value one would obtain using the above equation, if E_B gives the difference in energy between the two levels as a function of applied field.

The above makes an assumption that the magnetic field is along the same direction as that indicated by m_j . The effective g factor has angular dependence, and thus, the direction of B is relevant. It is a rank 2 tensor, considering a linear relation between each orientation of \mathbf{B} and each orientation of $\mathbf{L} + g_s\mathbf{S}$. As will be discussed later, symmetry permits simplification of the number of levels required for fitting.

2.1.5 H_{other} - Other Terms

It must be noted that there are other terms that must be handled in order to develop precise models for calculating energy levels of the rare-earths. These include relativistic corrections, spin-spin and orbit-orbit interactions, as well as terms approximating multibody interactions for electrons. [77]

LS Coupling

Ultimately, because there are other terms in the Hamiltonian which are nonzero, the LS coupling labels may be more or less valid depending on the particular system. That is, an energy level labeled with particular values for L and S , even in vacuum, may have differing actual values for those quantities. [77]

2.1.6 Consequence of Crystal-Field Terms on Quantum Numbers

For LS coupling, in the absence of a crystal-field term, the Zeeman interaction term can be expressed neatly in terms of a good quantum number, corresponding to J_z . However, once the crystal-field interaction is applied, energy levels corresponding to differing J_z values are mixed, meaning that m_j ceases to be a good quantum number. It is convenient to consider the resulting levels as being derived from combinations of states for which m_j is a good quantum number. Discussion of these and related difficulties in definitively labeling states can be found in [77].

2.1.7 Comments on Relative Magnitudes of Terms

As will be discussed later, multiplet splittings in Er^{3+} considered in this work are typically on the order of tenths of electron volts to electron volts. This is the relative magnitude of the H_{LS} term. For crystal splittings occurring in this work, the magnitude is thousandths to hundredths of electron volts. This justifies applying the crystal-field term as a perturbation of the LS coupling levels. However, the magnetic field terms, in at least one case described in this work, can exceed the magnitude of the crystal-field splittings at magnitudes which are reasonably experimentally accessible. From a theoretical standpoint, this means that the magnetic field term cannot be applied as a perturbation of the crystal-field split levels, but needs to be applied simultaneously. Fortunately, this task can be handled by available software packages, such as described in Ref. [4].

2.1.8 Importance of Perturbing Terms

Typically, intra 4f transitions are electric dipole forbidden because the parity of the initial and final states are identical, and the electric dipole operator has odd parity. This means that the transition probability is proportional to an integral over all space of an odd integral, which is zero. Putting the rare-earth into a crystal perturbs this symmetry. This also presents the possibility that less symmetric local

environments may be an advantage to luminescence efficiency.

2.2 Group Theory for Optical Transitions of Rare-Earth Ions

There is an important link between the way in which terms split and the symmetry of the perturbation that causes the splitting. The symmetry determines how many levels split and in which way those energy levels are mixed to form the new set of energy levels. Group Theory provides a framework for determining this sort of information, given some information about the term being split and the symmetry of the perturbation to the Hamiltonian. While the full framework of group theory can be quite complex, and is not described in full detail here, the basic ideas behind this approach are rather simple. For example, consider the following differential equation for ψ as a function of x , with $V(x)$ some fixed function.

$$\psi'' + (\lambda - V(x))\psi = 0$$

If $V(x)$ is even, for any solution $\psi(x)$, it can be seen by applying the transformation $x \rightarrow -x$, that $\psi(-x)$ also satisfies this differential equation for the eigenvalue λ . By writing out the above for both solutions, subtracting them, and removing common factors, it is possible to obtain

$$\psi(x)\psi''(-x) - \psi(-x)\psi''(x) = 0$$

Integrating the above yields

$$\psi(x)\psi'(-x) - \psi(-x)\psi'(x) = \text{constant}$$

However, this constant is presumably the same for every point in space. If the solutions are now interpreted to refer to actual, normalizable wavefunctions in quantum mechanics, the wavefunctions and their derivatives must be zero or tending to zero asymptotically far away. This implies that this constant is zero.

$$\begin{aligned}
\psi(x)\psi'(-x) - \psi(-x)\psi'(x) &= 0 \\
\left(\frac{f}{g}\right)' &= \frac{gf' - fg'}{g^2} \\
\Rightarrow \left(\frac{\psi(x)}{\psi(-x)}\right)' &= 0 \\
\psi(x) &= c\psi(-x)
\end{aligned}$$

Applying the above twice,

$$\psi(x) = c\psi(-x) = c^2\psi(x) \Rightarrow c^2 = 1$$

If it is assumed that the ψ functions are real, this means solutions to this equation are forced to be either even or odd functions, because $c = \pm 1$. This also allows classifications of eigenfunctions for the equation based on this value of c . Knowing the parity of the wavefunctions also allows computing whether an operator placed between two states will produce zero due to symmetry if the parity of the operator is known. In some sense, this amounts to also classifying operators using this distinction.

Group theory, in its application here, is essentially a formalized way of making the above argument, in potentially much more complicated situations. In some cases, such as complicated molecules, it is much more difficult to make simple arguments of the type given above, and even more difficult to solve for the wavefunctions analytically, making group theory quite valuable. The above example is largely taken from Ref. [22].

2.2.1 Background

It is not possible to give an overview of group theory which is at the same time concise, mathematically rigorous, and sufficient to perform the calculations described here. Far more thorough treatments are available, and should be referenced for claims asserted here. [22] [72] The goal of this portion is to demonstrate a practical approach to performing the relevant calculations, and to show the results of those calculations.

Some Basic Definitions

A group is a set of elements with an operation, group multiplication (which may be distinct from arithmetic multiplication), which links ordered pairs of the elements to a third element in that set. That third element, or the product, must always be in the set if the two operands are in the set. The operation must be associative, but need not be commutative. The set must include a unit element, E , such that for any element A in the set, $A \cdot E = E \cdot A = A$. The dot here represents the group multiplication operation. Finally, for each element A in the set, there must exist an inverse element A^{-1} also in the set, with the property that $A^{-1} \cdot A = A \cdot A^{-1} = E$. If the group multiplication happens to be commutative for the group elements, the group is also said to be Abelian.

Many examples of groups exist. The set of all integers form an Abelian group under addition, as adding any two integers yields a third integer, addition is both commutative and associative, zero acts as a unit element, and positive and negative integers form pairs for inverses. Relevant to this work are groups of symmetry operations. Rotations, for example, by multiples of a quarter of a complete turn along one axis, could be said to form a group, with a group multiplication representing the net effect of performing the two rotations in order as another rotation. The rotations about a given axis are associative and commutative, because the only thing that matters is the sum of the rotated angles when applying the operation. Rotating by an angle of zero gives an identity element. Inverses can be found by finding the number of additional quarter turns required to form a full rotation, the net result being equivalent to no rotation at all.

The aforementioned symmetry operations can be represented as square matrices acting on coordinates (vectors). This allows an easy representation of symmetry operations as groups consisting of matrices, with matrix multiplication being group multiplication. Two groups are said to be isomorphic to one another if a one-to-one mapping of their elements makes their group multiplication tables identical. A subgroup is a group whose elements are all present in a larger group, using the same group multiplication rules for its elements. All groups have two improper subgroups,

the first being the set consisting of just the identity element, and the second being identical to the group of which it is a subgroup. Proper subgroups are any other valid subgroups.

A class is a set of elements in a group which can be related to one another using a similarity transformation. That is, if elements A , B , and C are all in group G , and $CAC^{-1} = B$, then A and B are said to be part of the same class. A class must include all elements in the group which can be related by this sort of transformation. Classes may not be groups themselves. Classes tend to have physical significance in the context of symmetry groups. For example, pure rotation operators may form a class separate from reflection operators. Note that the identity element always forms a class by itself, as any such transformation results in $CEC^{-1} = CC^{-1} = E$ for any C . For the finite groups considered here, it is possible to determine these from a group multiplication table, and simply exhausting the possibilities. The order of a group is the number of elements in the group.

If this group is mapped homomorphically to operators in a vector space of dimension n , this is called an n -dimensional representation of the group. If the mapping is also isomorphic, it is called a faithful representation of the group, and the orders of the group of operators and the original group are equal. Representations (D) are called equivalent if they can be related to one another using another operator (C) such that

$$D'(R) = CD(R)C^{-1}$$

$D(R)$ indicates a particular operator, corresponding to a particular element, R , in the original group. If these operators are written as matrices, it can be shown that the trace of each operator in D is left invariant by the above transformation. This value is called the character of the group element R in the representation D . Equivalent representations result in the same values for the characters of the group elements. It can be shown that elements of the original group belonging to the same class will all have the same character in a given representation.

Fortunately for physical symmetries, it is often obvious how to represent symmetry group elements in a three-dimensional vector space as matrices. Unfortunately, it may be possible to construct representations in a number of different numbers of dimensions. In Ref. [22], there is an example for representing the group of the identity and inversion operators in two dimensions. This is done by considering writing functions as linear combinations of $f(x)$ and $f(-x)$, in which case, the identity operator can be represented as a 2x2 identity matrix, and the inversion operator by a 2x2 matrix with zeros on the diagonal, and ones on the off diagonal. If a lower dimensional representation can be found, the representation is called reducible. An irreducible representation has the smallest dimensionality possible. There exist criteria, such as Schur's lemma, for determining whether a representation is reducible, which can be found in several texts on group theory.

Representations can be added. This is accomplished in the matrix example by combining matrices from each representation in block diagonal form. If the representation matrices share the same block diagonal form, or if there exists a similarity transformation which makes this the case when applied to all group element matrices, then the representation is reducible, to the sum of representations corresponding to each block. An irreducible representation cannot be broken down in this way.

Symmetry Groups

Fortunately, the types of groups relevant to the work presented here are quite limited. Typically, three types of symmetry operations appear in solid-state physics, reflections, translations, and rotations. Since the work here deals with dopants thought to be isolated, rather than repeating crystals of rare-earths, only reflections and rotations are relevant. To avoid translations over successive operations, these operations must all leave one point in space unchanged. These are referred to as the point groups. Rotations about an axis by $\frac{2\pi}{n}$ radians are represented by C_n . These clearly form a group because n such operations gives the identity element (labeled as E) and any number of such rotations will yield some other number of rotations, from which multiples of 2π in angle can be added or subtracted to limit the number

of elements in the group to n . Reflections are denoted by σ , with a subscript v or h indicating a vertical or horizontal axis containing the reflection, where vertical implies the same axis as that used for rotations. Complicating this somewhat is the possibility of combining such operations. By combining a half turn, C_2 , and a reflection, σ_h , it is possible to generate an operation called an inversion, I , whose effect on coordinates can be described as $x, y, z, \rightarrow -x, -y, -z$.

For groups consisting only of the rotational symmetries along one axis, the groups are labeled as C_n , with n indicating the fraction of a full rotation producing the symmetry. n is selected to be the largest possible value. D_n groups have the rotational operations of C_n , with the addition of a rotation of π along an axis orthogonal to the rotation axis associated with C_n . The addition of an h or v subscript to C_n , such as in C_{3v} , indicates the addition of a mirror symmetry corresponding to the σ_v or σ_h operation with matching subscript. The h subscript for D_{nh} indicates the same addition. S_n is defined as the group of rotation reflections, such that the element C_n is combined with σ_h to produce symmetry elements. Additionally, T indicates the symmetry of a tetrahedron, O that of an octahedron, and Y that of an icosahedron (not relevant to these applications). T may have a subscript d added, indicating a diagonal mirror plane, and O may have a subscript h. n is typically restricted to 1,2,3,4, and 6. A time reversal operator, R , is sometimes considered, indicating changes in the flows of current and magnetic field direction, and increases the number of possible groups.

Before continuing, it is important to note that the tables required to perform analysis of level splitting, such as multiplication tables, character tables, and representations, are readily available in books for the 32 crystallographic point groups. [31]

Constructing a Character Table

The dimensionality theorem can be used to indicate the number of irreducible representations. If the order of the group being represented is h , and l_i gives the

dimensionality of the irreducible representation numbered i , then

$$\sum_i l_i^2 = h$$

Further, it can be shown that the number of irreducible representations is equal to the number of classes in the group.

The characters for the classes in each irreducible representation are often of use for further applications without any direct need of the irreducible representations as actual matrices. Character tables give this information, with entries corresponding to the classes and the representations, and are available in books and online. The rows give information for each representation, and the columns for each class. Simple rules apply to the character tables, which may be sufficient to determine them without using or knowing the actual representations.

- Since the identity element is always represented by a unit matrix, the character (trace) of the identity element is always equal to the dimensionality of the representation. This gives one column of the character table.
- There is always a one-dimensional representation corresponding to a one-dimensional group in which all elements are one. This is because all group multiplication tables can be satisfied by multiplying one by itself to obtain one for every entry. This is typically given in the first row of the character table, meaning the first row is filled with ones for each class.
- The rows of the table must be orthogonal and normalized to the order of the group, if each character entry is weighted by the number of elements in the corresponding class.
- The columns of the table must be orthogonal and normalized to the order of the group divided by the number of elements in the class, if each character entry is weighted by the number of elements in the corresponding class.
- While not a rule, characters for symmetry groups are typically integer valued.

There are multiple conventions for labeling the irreducible representations. For the Mulliken labels,

Label	Meaning
A	Symmetric under C_n , One-dimensional
B	Antisymmetric under C_n , Two-dimensional
E	Two-dimensional
T	Three-dimensional
F	Four-dimensional
'	Symmetric under σ_h
"	Antisymmetric under σ_h
1	Symmetric under C_2 rotation perpendicular to the C_n rotation
2	Antisymmetric under C_2 rotation perpendicular to the C_n rotation
<i>g</i>	Symmetric under inversion (g for gerade)
<i>u</i>	Antisymmetric under inversion (u for ungerade)

Another common scheme labels the irreducible representations as Γ with subscripts distinguishing them, perhaps with a superscript preceding the Γ indicating dimensionality.

Character tables are typically combined with information on which common operators correspond to each irreducible representation. To determine how x, y, and z transform, consider a three-dimensional representation for spatial coordinates. Calculate the characters for each class using this representation. Now, it must be possible to represent this new representation as a linear combination of irreducible representations, whose characters are added according to this linear combination to form the characters of the representation. This indicates which of the irreducible representations correspond to x, y, and z. For irreducible representations of dimension 2 or greater, combinations of a number of basis functions equal to the number of dimensions are needed. In the examples which will follow, it is obvious which coordinates must go with each irreducible representation, because block form matrices are achieved, with dimensions corresponding to the dimensions of the irreducible representations. If this is the case, the coordinates corresponding to each block are associated with the irreducible representation corresponding to each block.

The basis functions for a representation can be thought of as a set of functions which can be used to create that representation by mapping out how each operator changes the functions. To determine the irreducible representations of a set of basis functions, one must find a way to describe the action of the various operators mapping these functions to each other using matrices, compute the trace of these matrices (characters), and then express these traces as a combination of the characters for the irreducible representations in the tables. Then, one must determine how to break up the matrices into the irreducible representations indicated by this linear combination by placing them all in block diagonal form. The basis functions correspond to the functions for each block diagonal form. Examples will be given later for a few symmetry groups of interest.

Constructing Multiplication Tables for Irreducible Representations

There is a rule for determining whether an operator acting between two states will yield zero for symmetry reasons based upon multiplying irreducible representations by one another. In summary, the characters for the classes of the product are identical with the products of the characters for the classes. After performing this operation, the product representation is decomposed into a linear combination of the irreducible representations by finding such a linear combination for the characters producing the product's characters. This resulting linear combination of representations is the product of the two representations used.

Extending to Double Groups

The above framework is complicated by the property of representations of half-integral values of J . The character of a rotation class for rotation angle ϕ for such a representation is given by

$$\frac{\sin\left((2J+1)\frac{\phi}{2}\right)}{\sin\left(\frac{\phi}{2}\right)}$$

For integer J , the above has the desirable property that adding 2π to the angle gives the same value. For half-integer J , this expression changes sign under such a

rotation. In order to resolve the issues that this produces, one solution corresponds to imagining that the crystal is symmetric under rotation by 4π rather than 2π radians, and adds an operator, R , corresponding to rotation by 2π . This element is applied to each of the already existing elements of the group to create a new group with twice as many elements. It is important to note that there may be cases in which this does not double the number of classes, if, for example, rotation by π is already an operator. Every class besides a rotation by π produces two classes in the double group. More details on the rotation by π and the rules which will soon follow can be found in Ref. [56]. In short, rotation by π shares a class with this added set of operators if and only if there is another rotation by π along an axis perpendicular to the rotations for the first rotation operator.

A set of rules can be applied to derive the double group character table.

- First, determine the number of classes and the order of the double group, which generally creates adds a new class for each single group class, with the exception of the π rotation case already mentioned.
- Then, the sum of squares of the dimensions of the classes should still equal the order of the overall group. The representations which appeared without considering the double group should still be present.
- The portion of the table corresponding to the original operators and representations should be identical to the single group entries.
- For the original representations for the single group, the characters for corresponding classes differing only by the R operator are identical.
- For the added representations unique to the double group, the characters for each original and corresponding added class (that is, class differing only by this R operator) must be the same value with opposite signs.
- The rules about the entries for the identity representation (first row) being one and the entries for the identity operator class being the dimension of the representation still apply, as this is still a character table.

- The rules about normalizing the rows and columns also still apply, as do the rules about orthogonality.

Kramers Theorem

Time reversal symmetry has a consequence for half-integer spin that is not present for integer spin. Specifically, if a state is a solution of the Hamiltonian, its time reversed state is also a solution. Time reversal changes the sign of angular momenta. For a half-integer spin system, this requires that no state can be its own equivalent time reversed state (since there is no possible zero spin state). This forces states in a half-integer spin system to exist in pairs with identical energy. However, the addition of a magnetic field breaks this time reversal symmetry.

In the original paper, it is stated that in systems where the number of electrons is odd affected by purely electric (not magnetic) fields, the energy levels must be doubly degenerate. [32]

Since the group theory predictions here do not explicitly include time reversal, when calculations involving such systems are shown later, this property is included after the fact.

Determining Level Properties

The next step is to apply these character tables to determine how multiplets split into levels with symmetries corresponding to these irreducible representations. This problem turns out to be similar to the problem of decomposing sets of basis functions. A representation for the group of levels is needed which can be broken up into a linear combination of the irreducible representations for symmetry group under consideration. The case considered here will be that of calculating splittings of multiplets of given J .

Fortunately, the number of splittings for a multiplet of given J for a given symmetry has already been determined in Ref. [64], which will be useful for verifying the results. The result is as follows, for J values up to 8.

Set of Point Groups	Point Groups
Cubic	O_h, O, T_d, T_h, T
Hexagonal	$D_{6h}, D_6, C_{6v}, C_{6h}, C_6, D_{3h}, D_3, C_{3v}, C_{3h}, C_3, D_{3d}, S_6$
Tetragonal	$D_{4h}, D_4, C_{4v}, C_4, D_{2d}, S_4$
Lower Symmetry	$D_{2h}, D_2, C_{2v}, C_{2h}, C_2, C_s, S_2, C_1$

J	0	1	2	3	4	5	6	7	8
Cubic	1	1	2	3	4	4	6	6	7
Hexagonal	1	2	3	5	6	7	9	10	11
Tetragonal	1	2	4	5	7	8	10	11	13
Lower Symmetry	1	3	5	7	9	11	13	15	17

J	$\frac{1}{2}$	$\frac{3}{2}$	$\frac{5}{2}$	$\frac{7}{2}$	$\frac{9}{2}$	$\frac{11}{2}$	$\frac{13}{2}$	$\frac{15}{2}$
Cubic	1	1	2	3	3	4	5	5
Any Other Symmetry	1	2	3	4	5	6	7	8

To be clear, the entries in the second two of these tables give the number of distinct energy levels, not the degeneracy of any of those distinct energy levels. In order to determine irreducible representations for each J value, the character for each class needs to be calculated.

By considering properties of spherical harmonics, it is possible to derive the following expressions for the character of a multiplet with J for its combined angular momentum. The representation of J is labeled as D_J . χ is used to indicate character. Justification for these relations is discussed in a set of lecture notes available online. [11] To briefly describe the method, one can imagine a set of m_j states to represent a multiplet of J , and then calculate characters from matrices for how these states are changed by the operators. This representation makes the character for the identity operator equal to the number of valid m_j states, which is equal to $2J + 1$.

$$\chi^{(J)}(E) = 2J + 1$$

$$\chi^{(J)}(C_n) = \frac{\sin\left((2J + 1)\frac{\pi}{n}\right)}{\sin\frac{\pi}{n}}$$

$$\chi^{(J)}(i) = (-1)^J (2J + 1)$$

$$\chi^{(J)}(S_n) = (-1)^J \frac{\sin\left((2J + 1)\frac{\pi}{n}\right)}{\sin\frac{\pi}{n}}$$

$$\sigma_h = C_2 \times i = S_2$$

$$\chi^{(J)}(\sigma_h) = (-1)^J \sin\left((2J + 1)\frac{\pi}{2}\right)$$

Ultimately, the irreducible representations themselves become the crystal-field quantum numbers. That said, it may be the case that one such quantum number refers to more than one such representation.

The above expression for the character of a rotation is valid for any axis, meaning that any reflection operator can be expressed as a product of the inversion operator and a rotation about some axis by π . Thus, the above expression for the character for mirror operators applies to any such mirror operator, not just σ_h . The above expression leads to the interesting property that for half-integral J , the character is proportional to the sine of an odd number times π , meaning that the character of a mirror operator for half-integral J is always zero. Additionally, for integral J , the character of the mirror operator reduces to $+1$.

Application to Selection Rules

Once we have a multiplication table for the irreducible representations, representations for the levels, and representations for some basic operators, it is possible to determine whether those operators are expected to yield zero for symmetry reasons when acting between two levels. In general, for $\langle \Psi_1 | A | \Psi_2 \rangle$ to be non zero, the product of the representation for Ψ_1 with the representation for A must contain the representation for Ψ_2 . Using this simple principle, it is possible to use existing resources with precomputed tables. [31]

For an electric dipole, one checks whether x , y , or z as operators in place of A can yield nonzero results. Also, the unit directions associated with each of those

operators corresponds to the polarization associated with the electric dipole transition. For splitting under applied magnetic fields, one follows a similar procedure. Assuming higher order terms are negligible, this is reduced to calculating $\langle \Psi | H_B | \Psi \rangle$. If the H_B operator for a given orientation (suppose along the z axis) is proportional to a term like $L_z + gS_z$, it is expected that this will transform, in terms of symmetry operations, identically to combinations of the x , y , and z operators (in this example, only z). This also implies that the rules for magnetic splitting (for this low order term) act similarly to selection rules for electric dipole transitions.

2.2.2 Application to Crystal-Field Terms

It can be shown that the Hamiltonian conforming to a given symmetry group is equivalent to the symmetry operators commuting with the Hamiltonian. This allows simplification of the crystal-field terms which are permitted. The following table is taken from Ref. [50], and indicates the values of q for which B_q^k may be nonzero for various symmetry operations.

Symmetry Operations	Permitted q
C_2, σ_h	$0, \pm$ even number
C_3	$0, \pm$ multiples of 3
C_4	$0, \pm$ multiples of 4
C_6	$0, \pm$ multiples of 6
σ_v, U_2	0 , any positive number

Further, Ref. [77] explains that for f electron configurations, terms with $k > 6$ do not contribute. If the electrons are equivalent (as is the case in this work), only terms with even k are needed. Since q must be bounded inclusively by $-k$ and k , this enables a tabulation of a finite number of elements for the symmetries already discussed in some detail. The term for $k = 0$ is ignored, as its predominant effect is a uniform shifting of levels.

For C_{3v} , the nonzero terms are $B_2^0, B_4^0, B_4^3, B_6^0, B_6^3$, and B_6^6 , for a total of six terms. For C_{1v} , there are three nonzero terms for $k = 2$, five for $k = 4$, and seven

for $k = 6$, giving a total of fifteen terms. For C_1 , essentially no symmetry, $k = 2$ gives five, $k = 4$ gives nine, and $k = 6$ gives thirteen, for a total of twenty-seven terms. It can be seen that symmetry has a great effect on reducing the number of crystal-field terms. This large number of terms for low symmetry groups requires a large amount of experimental data to fit them.

When acting on a multiplet with angular momentum J , a crystal-field operator with a particular value of q can be nonzero only when acting between states whose difference in m_j is equal to q . This property, combined with the table above, gives rise to the notion of grouping states by crystal-field number. For example, for C_3 symmetry, m_j states can be mixed only into one of three groups by the crystal-field, because there will be no off-diagonal elements connecting states whose m_j values differ by a value other than an integral multiple of three. The practice for assigning a crystal-field quantum number is to use the m_j value of the set of mixed states closest to zero.

2.2.3 Simplifying Effective g Factors

The effective g factor can be represented as a tensor.

$$g = \begin{bmatrix} g_{xx} & g_{xy} & g_{xz} \\ g_{yx} & g_{yy} & g_{yz} \\ g_{zx} & g_{zy} & g_{zz} \end{bmatrix}$$

However, in order to have C_{3v} symmetry (which should be valid for the case in which the magnetic fields are not large enough to dominate the symmetry of the system), this tensor needs to have threefold rotational symmetry. The z axis is the rotation axis.

Consider first the application of a magnetic field along the z axis. The following quantity must be invariant under the rotation.

$$(L_x + g_s S_x)g_{xz} + (L_y + g_s S_y)g_{yz} + (L_z + g_s S_z)g_{zz}$$

The last term has this symmetry guaranteed, as it is unaffected. Note that a

multiplication by a rotation matrix for the xy plane will not change the column and row of g_{ij} corresponding to z . Thus, for any rotation, $L_x + g_s S_x$ and $L_y + g_s S_y$ change, while g_{xz} and g_{yz} do not.

$$(L_x + g_s S_x)g_{xz} + (L_y + g_s S_y)g_{yz} =$$

$$(\cos(\theta)(L_x + g_s S_x) + \sin(\theta)(L_y + g_s S_y))g_{xz} + (-\sin(\theta)(L_x + g_s S_x) + \cos(\theta)(L_y + g_s S_y))g_{yz}$$

$$g_{xz} = \cos(\theta)g_{xz} - \sin(\theta)g_{yz}$$

$$g_{yz} = \sin(\theta)g_{xz} + \cos(\theta)g_{yz}$$

$$g_{yz} = \frac{1 - \cos(\theta)}{\sin(\theta)}g_{xz} = \frac{\sin \theta}{1 - \cos(\theta)}g_{xz}$$

Either $g_{xz} = 0$ or

$$\frac{1 - \cos(\theta)}{\sin(\theta)} = 1,$$

of which the second requires $\sin(\theta + \frac{\pi}{2}) = \frac{1}{\sqrt{2}}$. However, if a system has a rotational symmetry of $\frac{\pi}{4}$, which satisfies this, it also has one of $\frac{\pi}{2}$. Thus, it appears that for any rotational symmetry about the z axis, these values of the tensor must be zero. Further, a similar argument applies to g_{zx} and g_{zy} by rotating a magnetic field in the xy plane, and requiring the coefficients of $(L_z + g_s S_z)$ to remain unchanged.

All that remains is to examine the elements containing only x and y . First, to simplify this process further, it is possible to select axes x' and y' by rotating x and y about the z axis such that $g_{yx} = 0$ for the new coordinates. This is accomplished by rotating by an angle θ such that $\tan \theta = \frac{g_{yx}}{g_{xx}}$. This rotation leaves the results for entries containing z unchanged. From here on, it is assumed that x and y now represent these primed axes.

Consider a magnetic field along the x axis, and the result of rotating the field.

$$g_{xx}(L_x + g_s S_x) + (L_y + g_s S_y)g_{xy} =$$

$$(g_{xx} \cos \theta)((L_x + g_s S_x) \cos \theta + (L_y + g_s S_y) \sin \theta) +$$

$$+(g_{xy} \cos \theta - g_{yy} \sin \theta)(-(L_x + g_s S_x) \sin \theta + (L_y + g_s S_y) \cos \theta)$$

This reduces to two equations by forcing the coefficients of the operators to be equal.

$$g_{xx} = g_{xx} \cos^2 \theta + (-g_{xy}) \sin \theta \cos \theta + g_{yy} \sin^2 \theta$$

$$g_{xy} = g_{xy} \cos^2 \theta + (g_{xx} - g_{yy}) \sin \theta \cos \theta$$

Continuing, one must make an assumption about whether $\sin \theta$ is equal to zero. The only group with rotational symmetry which will be discussed in detail for this work is C_{3v} , so for this group, it can be assumed $\sin \theta$ is non-zero.

$$g_{xx} \sin \theta = g_{xy} \cos \theta + g_{yy} \sin \theta$$

$$g_{xy} \sin \theta = (g_{xx} - g_{yy}) \cos \theta$$

$$g_{xx} \sin \theta = (g_{xx} - g_{yy}) \cos^2 \theta + g_{yy} \sin \theta$$

$$0 = (g_{xx} - g_{yy})(\cos^2 \theta - \sin \theta)$$

Solutions for $\cos^2 \theta - \sin \theta$ do not occur for any angles in the 32 crystallographic point groups, which means that $g_{xx} = g_{yy}$, which in turn means that $g_{xy} = 0$.

Thus, the above is sufficient to show that groups with C_{3v} symmetries produce a symmetric effective g tensor, with the xx and yy elements being identical when diagonalized (if z is the rotation axis). This means that the effective g factors for C_{3v} can be expressed using only two numbers, g_{\perp} and g_{\parallel} , for fields perpendicular and parallel to the z -axis, respectively.

2.2.4 C_{3v}

Constructing Single Group Tables

As will be discussed later in this chapter, a reasonable guess for the symmetries of the incorporation sites for the systems examined in this work is C_{3v} symmetry. This makes both this symmetry, and slight breakings of it, of particular interest. First, there are six group elements, the identity element, E, two rotation operators, C_3 and C_3^2 , a mirror operator, σ_v , and two other mirror operators corresponding to two other planes obtained by rotating the first mirror plane by C_3 . This means the order of the group is six. The identity element forms a class, the pure rotation operators form a class, the operators involving reflection form a class. This indicates that this group must be represented by three irreducible representations with each a dimension l_i , satisfying

$$l_1^2 + l_2^2 + l_3^2 = 6$$

However, since the dimensions must be positive integers greater than zero, the only solution to the above requires that there are two irreducible representations of dimension one, and one representation of dimension two. Using this information, we begin to fill out the first row and the first column of the character table, with four unknown entries.

	E	$2C_3$	$3\sigma_v$
A_1	1	1	1
A_2	1	a	b
E	2	c	d

Orthogonality between the first row and the other two gives

$$1 + 2a + 3b = 0$$

$$2 + 2c + 3d = 0$$

Orthogonality with the first column gives

$$1 + a + 2c = 0$$

$$1 + b + d = 0$$

Combining some of these gives

$$a + 3b = -2 \Rightarrow 1 + a = 2 \Rightarrow a = 1$$

which then allows straightforward determination of all the other entries.

$$b = -1$$

$$d = 0$$

$$c = -1$$

	E	$2C_3$	$3\sigma_v$
A_1	1	1	1
A_2	1	1	-1
E	2	-1	0

Note that this character table was constructed without explicit knowledge of the matrix representations of the operators. For this next portion, x, y, and z will be identified with these representations. Consider matrices for an operator in each class.

$$E = \begin{bmatrix} 1 & 0 & 0 \\ 0 & 1 & 0 \\ 0 & 0 & 1 \end{bmatrix}$$

$$C_3 = \begin{bmatrix} -\frac{1}{2} & -\frac{\sqrt{3}}{2} & 0 \\ \frac{\sqrt{3}}{2} & -\frac{1}{2} & 0 \\ 0 & 0 & 1 \end{bmatrix}$$

$$\sigma_v = \begin{bmatrix} -1 & 0 & 0 \\ 0 & 1 & 0 \\ 0 & 0 & 1 \end{bmatrix}$$

The characters are 3, 0, and 1. Comparing this to the character table, this can be achieved by adding the characters for A_1 and E . Inspecting the above matrices, and noting that none of the operators should change z , it can be seen that this representation is already in a block diagonal form combining a one-dimensional and a two-dimensional representation. The z coordinate appears in the block corresponding to the one-dimensional representation, meaning that z corresponds to A_1 . By similar reasoning, x and y correspond to E .

This process can be continued for other basis functions. Consider the operators acting on the sum $x^2 + y^2$. This should be unaffected by rotations or reflections, meaning that all the matrices corresponding to this should simply be the number one, in a one-dimensional matrix. Comparing the traces of this to the character table, it can be seen that this corresponds to A_1 . By extension, any basis function left unchanged by the operations of the symmetry group must correspond to the first group in the table.

Rotations about the various axes, R_x , R_y , and R_z , can also be considered. R_z does not change into another type of rotation under the action of the operators of the symmetry group, but reflection reverses the direction of the rotation. This would result in one-dimensional matrices equal to one for the identity and rotation classes, but negative one for the reflection classes. This implies R_z corresponds to A_2 . R_x and R_y , however, form various linear combinations with one another under these operations, and this implies a two-dimensional representation. This leaves only the possibility of identifying these with E . Continuation of this process gives all the information typically displayed in character tables.

	E	$2C_3$	$3\sigma_v$	Linear Functions and Rotations	Quadratic Functions
A_1	1	1	1	z	$x^2 + y^2, z^2$
A_2	1	1	-1	R_z	
E	2	-1	0	$(x,y), (R_x, R_y)$	$(x^2 - y^2, xy), (xz, yz)$

Next, there is the matter of the products of the irreducible representations.

	E	$2C_3$	$3\sigma_v$	
A_1	1	1	1	
A_2	1	1	-1	
E	2	-1	0	
$A_1 \times A_1$	1	1	1	A_1
$A_2 \times A_1$	1	1	-1	A_2
$E \times A_1$	2	-1	0	E
$A_2 \times A_2$	1	1	1	A_1
$A_2 \times E$	2	-1	0	E
$E \times E$	4	1	0	$E + A_1 + A_2$

Integer J

For integer values of J , the above is sufficient to make predictions about splitting of multiplets. Recall the earlier expression for the character of a rotation operator.

$$\chi(C_n) = \frac{\sin\left((2J+1)\frac{\phi_n}{2}\right)}{\sin\left(\frac{\phi_n}{2}\right)}$$

Setting $\phi = \frac{2\pi}{3}$, this gives rise to a repeating cycle of 1,0, and -1 as J increases. The character of the identity element is equal to the number of states for a given J , which means this is equal to $2J+1$. For the mirror operator, the operation is considered as a product of a particular rotation by π , which gives a character of $(-1)^J$ for integer J , and an inversion operator, which gives a character of $(-1)^J$. This means that the character of the mirror operator is always $+1$ for integer J . It is important to note a discrepancy with [77], which treats the character of a mirror operator as identical to the character of a rotation by π , which is incorrect when discussing C_{3v} symmetry, which has no such symmetry.

These rules give the characters for integral J . To find the representations in terms of irreducible representations, these characters are expressed as a linear combination of the characters of those representations.

J	E	$2C_3$	$3\sigma_v$	Linear Combination
0	1	1	1	A_1
1	3	0	1	$E + A_1$
2	5	-1	1	$2E + A_1$
3	7	1	1	$A_1 + (A_1 + A_2) + 2E$
4	9	0	1	$A_1 + (A_1 + A_2) + 3E$
5	11	-1	1	$A_1 + (A_1 + A_2) + 4E$
6	13	1	1	$A_1 + 2(A_1 + A_2) + 4E$
7	15	0	1	$A_1 + 2(A_1 + A_2) + 5E$
8	17	-1	1	$A_1 + 2(A_1 + A_2) + 6E$
9	19	1	1	$A_1 + 3(A_1 + A_2) + 6E$

In the linear combination column, each unit instance of a representation corresponds to a number of levels equal to the number of dimensions in the representation. The choice to write a unit of A_1 separately was made in order to denote that A_1 seems to correspond to $m_j = 0$, but for nonzero even m_j , levels appear to be added in pairs of A_1 and A_2 , or in adding E , as J increases. Unlike the half-integer j case, in which two one-dimensional representations are treated as parts of a two-dimensional representation to preserve Kramer's degeneracy, here each distinct representation above must represent a level. This means that the number of representations needed for each J gives the number of split groupings of levels, and can be shown to reproduce the level splittings given earlier for hexagonal symmetry. The degeneracy of each grouping with the same energy must correspond to the dimensionality of the corresponding irreducible representation.

As noted earlier, for threefold rotational symmetry, m_j levels are mixed within groups whose members have differences in m_j equal to an integral multiple of three. This leads to two quantum numbers being assigned for these representations. ± 1 for E , and 0 for A_1 and A_2 .

Using the product rules developed earlier, polarization selection rules can be found. For $\langle \Psi_1 | A | \Psi_2 \rangle$ to be non zero, the product of the representation for the state Ψ_1 by that for A must contain the representation for Ψ_2 . In the crystals of interest

in this work, the dipole operator for z will give π polarization, and x and y will give σ . z is identified with A_1 , and x and y with E .

	A_1	A_2	E
A_1	π		σ
A_2		π	σ
E	σ	σ	$\pi\sigma$

For magnetic fields, consider the operators $L_z + g_s S_z$ and $L_x + g_s S_x$. The former is unaffected by rotations around the z axis, but reverses sign under reflection. This behavior corresponds with A_2 . The latter should rotate and transform like x and y , and thus corresponds with E . A parallel magnetic field in this work is considered as being along the z axis, so nonzero elements for this operator acting between two states are given by essentially the same table, marked by *parallel* and \perp . Note that actually forming a basis for E with $L_x + g_s S_x$ requires including $L_y + g_s S_y$, so like x and y , these operators are considered identical in symmetry properties.

	A_1	A_2	E
A_1	\parallel		\perp
A_2		\parallel	\perp
E	\perp	\perp	$\parallel \perp$

If off-diagonal terms are ignored, it can be seen that a parallel magnetic field should always split degenerate levels, while a perpendicular field should only split degenerate levels with the symmetry of E .

Constructing Double Group Tables

C_{3v} has no rotations by π , so the procedure here is straightforward. Each class in the original group now is joined by a corresponding class multiplied by R . The number of classes is now six, and the number of elements is twelve. This is solved easily for the number and dimensionality of irreducible representations if another set of irreducible representations is added with the same dimensions as the original,

as $2(1^2 + 1^2 + 2^2) = 12$. Applying rules for the first row and column, as well as some rules for extending values in the table, the following is obtained. Justification for the labels of the new representations will become more apparent once results for the level splittings are obtained.

	E	$2C_3$	$3\sigma_v$	RE	2 R C_3	3 R σ_v
A_1	1	1	1	1	1	1
A_2	1	1	-1	1	1	-1
E	2	-1	0	2	-1	0
$E_{\frac{1}{2}}$	2	a	b	-2	-a	-b
$E_{\frac{3}{2}}$	1	c	d	-1	-c	-d
$E'_{\frac{3}{2}}$	1	e	f	-1	-e	-f

Note that only six variables remain after this.

At this point, it should be noted that strictly speaking, multiplying elements for checking for normalization and orthogonality requires taking the complex conjugate of one of the two rows or columns of characters. In the previous portion for the single group, this was not needed, because the characters were all real, but technically speaking, this should have been done there as well.

From the row orthogonality and normalization

$$2 + 2ac^* + 3bd^* = 0$$

$$2 + 2ae^* + 3bf^* = 0$$

$$1 + 2ce^* + 3df^* = 0$$

$$2a^*a + 3b^*b = 2$$

$$2c^*c + 3d^*d = 5$$

$$2e^*e + 3f^*f = 5$$

From the column orthogonality and normalization

$$2a + c + e = 0$$

$$2b + d + f = 0$$

$$a^*b + c^*d + e^*f = 0$$

$$a^*a + c^*c + e^*e = 3$$

$$b^*b + d^*d + f^*f = 2$$

It can be shown that the three row normalization equations above can be derived from the others. Rather than solve the above equations in full, a shortcut is added, by observing that these added representations must include a way to represent the group corresponding to $j = \frac{1}{2}$ which was not present in the original representations. As discussed earlier, the character for a rotation operator for a given J has a simple expression, and $2J + 1$ gives a value of 2 for the identity operator character. This neatly fits with the added dimension two representation. This can be considered as a guess, which turns out to satisfy all the above equations.

Applying this, $a = 1$, the value for the character of the rotation of $J = \frac{1}{2}$ by C_3 , which from the fourth equation gives $b = 0$. From the seventh equation, $c + e = -2$. Using the ninth equation, one obtains $c - e = 0$. This means $c = e = -1$. Using the tenth equation, this gives $d^*d + f^*f = 2$. From the eighth equation, $d = -f$. Next, from the last equation, $d^*d = 1$. From the third equation, $df^* = -1$. Since d and f are of unit magnitude, the only solution is if one of the two is the imaginary number and the other its negative. This uncertainty reflects the symmetry in the equations under a swap of the last two rows of the table. It can be verified that all these characters satisfy all the above equations.

	E	$2C_3$	$3\sigma_v$	RE	2 R C_3	3 R σ_v
A_1	1	1	1	1	1	1
A_2	1	1	-1	1	1	-1
E	2	-1	0	2	-1	0
$E_{\frac{1}{2}}$	2	1	0	-2	-1	0
$E_{\frac{3}{2}}$	1	-1	i	-1	1	-i
$E'_{\frac{3}{2}}$	1	-1	-i	-1	1	i

The multiplication table is worked out similarly to before. Only the final result is given below.

	A_1	A_2	E	$E_{\frac{1}{2}}$	$E_{\frac{3}{2}}$	$E'_{\frac{3}{2}}$
A_1	A_1	A_2	E	$E_{\frac{1}{2}}$	$E_{\frac{3}{2}}$	$E'_{\frac{3}{2}}$
A_2	A_2	A_1	E	$E_{\frac{1}{2}}$	$E'_{\frac{3}{2}}$	$E_{\frac{3}{2}}$
E	E	E	A_1+A_2+E	$E_{\frac{1}{2}} + E_{\frac{3}{2}} + E'_{\frac{3}{2}}$	$E_{\frac{1}{2}}$	$E_{\frac{1}{2}}$
$E_{\frac{1}{2}}$	$E_{\frac{1}{2}}$	$E_{\frac{1}{2}}$	$E_{\frac{1}{2}} + E_{\frac{3}{2}} + E'_{\frac{3}{2}}$	A_1+A_2+E	E	E
$E_{\frac{3}{2}}$	$E_{\frac{3}{2}}$	$E'_{\frac{3}{2}}$	$E_{\frac{1}{2}}$	E	A_2	A_1
$E'_{\frac{3}{2}}$	$E'_{\frac{3}{2}}$	$E_{\frac{3}{2}}$	$E_{\frac{1}{2}}$	E	A_1	A_2

Half-Integer J

The crystal-field splitting for half-integer J multiplets is considered. Character calculations were already discussed. Half-integer angular momenta require double valued characters, so it is expected that these states must be represented only by the added irreducible representations (as there are no issues with overlapping classes), which have different values for the extended operators. In this case, then, it is adequate to be concerned only with expressing characters using the first three classes for the new three representations.

J	E	$2C_3$	$3\sigma_v$	Linear Combination
$\frac{1}{2}$	2	1	0	$E_{\frac{1}{2}}$
$\frac{3}{2}$	4	-1	0	$E_{\frac{1}{2}} + \left(E_{\frac{3}{2}} + E'_{\frac{3}{2}} \right)$
$\frac{5}{2}$	6	0	0	$2E_{\frac{1}{2}} + \left(E_{\frac{3}{2}} + E'_{\frac{3}{2}} \right)$
$\frac{7}{2}$	8	1	0	$3E_{\frac{1}{2}} + \left(E_{\frac{3}{2}} + E'_{\frac{3}{2}} \right)$
$\frac{9}{2}$	10	-1	0	$3E_{\frac{1}{2}} + 2 \left(E_{\frac{3}{2}} + E'_{\frac{3}{2}} \right)$
$\frac{11}{2}$	12	0	0	$4E_{\frac{1}{2}} + 2 \left(E_{\frac{3}{2}} + E'_{\frac{3}{2}} \right)$
$\frac{13}{2}$	14	1	0	$5E_{\frac{1}{2}} + 2 \left(E_{\frac{3}{2}} + E'_{\frac{3}{2}} \right)$
$\frac{15}{2}$	16	-1	0	$5E_{\frac{1}{2}} + 3 \left(E_{\frac{3}{2}} + E'_{\frac{3}{2}} \right)$
$\frac{17}{2}$	18	0	0	$6E_{\frac{1}{2}} + 3 \left(E_{\frac{3}{2}} + E'_{\frac{3}{2}} \right)$

Considering Kramer's degeneracy, and that the dimension of each representation is the number of states it represents, it appears that the energy levels for this symmetry are naturally separated into levels corresponding to $E_{\frac{1}{2}}$ and a combination of $E_{\frac{3}{2}}$ and $E_{\frac{3}{2}'}$, suggesting two groupings of levels. The above also suggests that every third increment of J adds a doubly degenerate state represented by $E_{\frac{3}{2}}$ and $E_{\frac{3}{2}'}$, starting with $m_j = \pm\frac{3}{2}$. A similar thing can be said for adding a state represented by $E_{\frac{1}{2}}$ if one considers every third value of m_j starting from either $+\frac{1}{2}$ or $-\frac{1}{2}$. This idea is used to assign the crystal-field numbers. Levels corresponding to $E_{\frac{1}{2}}$ are given crystal-field number $\pm\frac{1}{2}$, and levels corresponding to $E_{\frac{3}{2}}$ and $E_{\frac{3}{2}'}$ are given $\frac{3}{2}$. This also explains the choice of labels. Recall that E refers to a two-dimensional representation. The rationale for labeling two one-dimensional representations as $E_{\frac{3}{2}}$ and $E_{\frac{3}{2}'}$ is that the levels that result here always appear as combinations of equal parts of the two. The subscripts refer to the crystal-field numbers that result for each.

All that remains is determining the selection rules. Since the basis functions developed for the single group still apply, and still correspond to the same representations, these can be derived from the multiplication table using just the portion corresponding to the products of new and old representations. The results are tables virtually identical to the integer J results. Note that higher order moments for transitions can be determined by the same process. A doubly degenerate level with crystal-field number $\frac{3}{2}$ is not expected to split under a magnetic field applied perpendicular to the c-axis (z axis) of the crystal, but all other splittings are expected. These rules will be a great importance later in this work.

	$E_{\frac{3}{2}}$	$E_{\frac{3}{2}'}$	$E_{\frac{1}{2}}$
$E_{\frac{3}{2}}$	π		σ
$E_{\frac{3}{2}'}$		π	σ
$E_{\frac{1}{2}}$	σ	σ	$\pi\sigma$

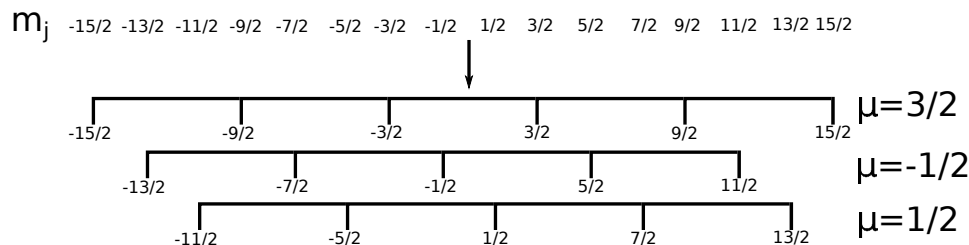


Figure 2.1: Mixing of states with m_j value differing by integer multiples of three (for C_{3v} symmetry) produces three groups of crystal-field quantum numbers, of which two groupings must be identical under time reversal.

	$E_{\frac{3}{2}}$	$E_{\frac{3}{2}'}$	$E_{\frac{1}{2}}$
$E_{\frac{3}{2}}$			⊥
$E_{\frac{3}{2}'}$			⊥
$E_{\frac{1}{2}}$	⊥	⊥	⊥

2.2.5 C_1 and C_{1v}

Constructing Tables

Unfortunately, if the rotation and reflection symmetries are both broken, the symmetry group that results contains only one element, E. If the reflection remains, there is one other symmetry operation available. These groups are considered primarily because they give an indication of what might happen if the symmetry of C_{3v} breaks slightly.

For C_{1v} , there are two elements, identity and reflection, with one class for the identity element, and one class for the reflection. This means there must be two irreducible representations of each dimensionality one, so that $1^2 + 1^2 = 2$, as had to be the case for C_{3v} . Note that C_s is essentially the same group, except the mirror plane is oriented differently.

For C_1 , there is only the identity element, which implies one irreducible representation of dimension one by similar reasoning. For C_1 , this also means that the

character table has only one entry, unity. For C_{1v} , it is only slightly more complicated.

	E	σ_v
A_1	1	1
A_2	1	a

It is easily seen by inspection that the only way to maintain orthogonality for rows and columns is if $a = -1$.

	E	σ_v
A_1	1	1
A_2	1	-1

For C_1 , since the only operator is the identity operator, the action of the operators on any possible basis functions can be represented with a single one-dimensional matrix equal to one, which implies all basis functions are identified with A .

For C_3 , some functions may change. Since the mirror axis has been selected as vertical, z is left unchanged, and is identified with A_1 . For the correct rotation of the x and y axes, one of these axes should be changed in sign by the reflection operator, and the other not. This implies that x and y are expressed as a combination of the A_1 and A_2 , with some rotation allowing them to be considered separately, so that x' is identified with A_1 and y' with A_2 . Similarly, all functions can be classified according to whether they change sign under this reflection to determine their irreducible representation.

	E	σ_v	Linear Functions and Rotations	Quadratic Functions
A_1	1	1	x, z, R_y	x^2, y^2, z^2, xz
A_2	1	-1	y, R_z, R_x	xy, yz

For C_1 , there is only one representation corresponding to an identity, so the product table for the irreducible representations is simply $A \times A = A$. For C_{1v} ,

	E	σ_v	
A_1	1	1	
A_2	1	-1	
$A_1 \times A_1$	1	1	A_1
$A_2 \times A_1$	1	-1	A_2
$A_2 \times A_2$	1	1	A_1

Integer J

For C_1 , because all levels and all operators must have the same representation, whose product with itself is itself, all operators acting between states may have nonzero value, so the selection rules are essentially that there are no rules imposed by the symmetry of the crystal-field, and therefore, no way of distinguishing symmetries of crystal-field split levels by use of group theory.

For C_{1v} , for splitting of multiplets with integer J , the procedure is the same as for C_{3v} . First, the characters of the multiplets are determined.

J	E	σ_v	Linear Combination
0	1	1	A_1
1	3	1	$A_1 + (A_1 + A_2)$
2	5	1	$A_1 + 2(A_1 + A_2)$
3	7	1	$A_1 + 3(A_1 + A_2)$
4	9	1	$A_1 + 4(A_1 + A_2)$
5	11	1	$A_1 + 5(A_1 + A_2)$
6	13	1	$A_1 + 6(A_1 + A_2)$
7	15	1	$A_1 + 7(A_1 + A_2)$
8	17	1	$A_1 + 8(A_1 + A_2)$
9	19	1	$A_1 + 9(A_1 + A_2)$

Because all levels may be mixed and grouped for both of these symmetries, the crystal-field quantum number for all these levels is 0.

Next, the selection rules. Unfortunately, these are of less use experimentally, because experimentally, the orientation of the remaining mirror plane (since it is

assumed that the relevance of this is breaking symmetry) is not typically controlled. Thus, the treatment of y as distinct from x is a problem.

	A_1	A_2
A_1	$x, z, L_x + g_s S_x, L_z + g_s S_z$	$y, L_y + g_s S_y$
A_2	$y, L_y + g_s S_y$	$x, z, L_x + g_s S_x, L_z + g_s S_z$

Thus, the primary result of this exercise for C_{1v} is that rotations in the xy plane may produce different dipole moments and magnetic fields. From the perspective of experimentally derived results only controlled for magnetic fields and polarizations parallel and perpendicular to the c axis of a crystal (taken to be the z axis), this does not yield any certainties of zero for particular operator elements. Further, if the relevance of this is to examine breaking of C_{3v} symmetry, this suggests that in an actual crystal, for a given defect, there could be three different so-defined x and y axes, depending on which mirror symmetry is preserved. This implies that multiple versions of the same site with identical energies could exist simultaneously, complicating selection rules.

Constructing Double Group Tables

For C_1 , the process of extension is trivial. Initially, only the representation and operators corresponding to identity were available. Now, there is one additional class of operator, for R. Two classes with order 2 of the group can have only two one-dimensional representations. Following the rules for extending a character table,

	E	R
A	1	1
\bar{A}	1	-1

The multiplication table is essentially identical to the single group results for C_{1v} , which makes sense, considering that rules for constructing character tables permit only one valid table for two one-dimensional representations. Constructing representations of the values of J is trivial, as they must be made of only \bar{A} , as it is

the only double valued representation, and the number of these required is simply equal to $2J + 1$. This implies that there is only one crystal-field quantum number, which will be assigned as $\frac{1}{2}$, the lowest (positive, since there is a choice) m_j for this representation. Since all possible functions are mapped to the identity representation, this means group theory places no restrictions on any transition moments or magnetic terms. Still, from Kramer's degeneracy, the levels must still be doubly degenerate.

For C_{1v} , there are now four operators, in a group of order four, implying four one-dimensional representations. Following through the procedure for constructing this table gives

	E	σ_v	R	R σ_v
A_1	1	1	1	1
A_2	1	-1	1	-1
$E_{\frac{1}{2}}$	1	a	-1	-a
$E_{\frac{1}{2}'}$	1	b	-1	-b

Orthogonality of columns requires

$$a + b = 0$$

$$2 + a^*a + b^*b = 0$$

Following through,

$$a^*a = -1$$

$$b = -a$$

This allows assigning either $a = i$ and $b = -i$, or $a = -i$ and $b = i$.

J	E	σ_v	Linear Combination
$\frac{1}{2}$	2	0	$\left(E_{\frac{1}{2}} + E'_{\frac{1}{2}} \right)$
$\frac{3}{2}$	4	0	$2 \left(E_{\frac{1}{2}} + E'_{\frac{1}{2}} \right)$
$\frac{5}{2}$	6	0	$3 \left(E_{\frac{1}{2}} + E'_{\frac{1}{2}} \right)$
$\frac{7}{2}$	8	0	$4 \left(E_{\frac{1}{2}} + E'_{\frac{1}{2}} \right)$
$\frac{9}{2}$	10	0	$5 \left(E_{\frac{1}{2}} + E'_{\frac{1}{2}} \right)$
$\frac{11}{2}$	12	0	$6 \left(E_{\frac{1}{2}} + E'_{\frac{1}{2}} \right)$
$\frac{13}{2}$	14	0	$7 \left(E_{\frac{1}{2}} + E'_{\frac{1}{2}} \right)$
$\frac{15}{2}$	16	0	$8 \left(E_{\frac{1}{2}} + E'_{\frac{1}{2}} \right)$
$\frac{17}{2}$	18	0	$9 \left(E_{\frac{1}{2}} + E'_{\frac{1}{2}} \right)$

The representations for half-integer J values are essentially identical to the result for the C_{3v} , but with the states of crystal-field number $\frac{3}{2}$ replaced by states of crystal-field number $\frac{1}{2}$. Similarly, the labels were chosen to reflect that the splittings almost act as if there is a two-dimensional representation. Kramer's degeneracy suggests that only one crystal-field quantum number is needed, $\frac{1}{2}$, since the two representations must lead to the same energies under time reversal. The multiplication table is updated below.

	A_1	A_2	$E_{\frac{1}{2}}$	$E'_{\frac{1}{2}}$
A_1	A_1	A_2	$E_{\frac{1}{2}}$	$E'_{\frac{1}{2}}$
A_2	A_2	A_1	$E_{\frac{1}{2}}$	$E'_{\frac{1}{2}}$
$E_{\frac{1}{2}}$	$E_{\frac{1}{2}}$	$E'_{\frac{1}{2}}$	A_2	A_1
$E'_{\frac{1}{2}}$	$E'_{\frac{1}{2}}$	$E_{\frac{1}{2}}$	A_1	A_2

As noted before, x and y are distinguished by the mirror symmetry, so the following table simply gives selection rules in terms of x , y , and z , which also applies to the magnetic operators along the same direction.

	$E_{\frac{1}{2}}$	$E'_{\frac{1}{2}}$
$E_{\frac{1}{2}}$	x, z	y
$E'_{\frac{1}{2}}$	y	x, z

The same discussion at the end of the portion on integer J for these symmetries is also relevant here.

2.2.6 SO(2)

Considering the case of a magnetic field separately, a magnetic field along a particular direction, selected as z for now, has rotational symmetry in the xy plane, but no mirroring or other rotational symmetries. This is referred to as SO(2), the rotation group for rotations around a line (which could also be considered as C_∞). This presents a complication not present in the previous two symmetry groups, in that there are an infinite number of symmetry options, and so the group is of infinite order. Rather than consider the details, the results of finding the irreducible representations are simply presented and used here. The character table is given below, in a form which differs from that of the previous tables. It can be also be found in [28]. Specifically, the character of a rotation by angle ϕ is given in a functional form, and the single row details all the irreducible representations as a function of $m \in \mathbb{Z}$.

	Function	E	R(ϕ)
$A_{\pm m}$	$(x \pm iy)^m$	1	$e^{\pm im\phi}$

Fortunately, the m values here neatly correspond to the m_j values for the splitting of an LS coupled multiplet with total angular momentum j . This implies the expected result for the splitting of levels in a magnetic field, that all will split according to their m_j value. Note that all the irreducible representations are of dimension one, implying that all levels of a multiplet will be singly degenerate under this axial symmetry.

In order to determine electric dipole selection rules, one must have a representation for z and for x and y (the last two should be indistinguishable). Note that the effect of multiplying characters for the representations of the above form is to add and subtract m values, implying that selection rules will be of a form involving differences in m_j values.

For a representation of z , which does not explicitly appear in the above, note that its behavior under rotations in the xy plane is to remain unchanged. Thus, z is identified with the $m = 0$ case, which is the only representation which gives ones for its two characters for any angle ϕ .

Since the procedure of taking a product of two such representations is to add the m values for each, and the transition rule that a product of the initial state and transition element representations must contain the final state representation, this implies electric dipole transitions along the direction of the magnetic field are allowed for $\Delta m_j = 0$.

A representation for x or y is slightly more difficult, because there is no way to form such a representation without a linear combination of two irreducible representations. The two representations are for $m = 1$ and $m = -1$. Following a similar reasoning, this implies electric dipole transitions polarized in the xy plane are allowed for $\Delta m_j = \pm 1$.

The combined result is familiar, that electric dipole transitions require $\Delta m_j = 0, \pm 1$.

Electric Dipole Polarized along z	$\Delta m_j = 0$
Electric Dipole Polarized along x,y	$\Delta m_j = \pm 1$

A similar procedure would apply to higher dipole moments. In the case of a magnetic field whose effects on the states are significantly larger than the effects of the crystal-field terms, the symmetry group described here is what is expected. In such a case, m_j is expected to be a good quantum number, and all levels in LS coupled multiplets are expected to be singly degenerate. Note that the z axis here refers to the magnetic field direction, not the c -axis of a crystal.

2.2.7 Magnetic Perturbations

In order to add the effects of a perturbation of a different symmetry than the original, the procedure is to start with the representations identified for the more significant symmetry, and determine the irreducible representations for these in terms of the perturbing symmetry. [22]

The result discussed for SO(2) symmetry, that only one-dimensional representations appear, suggests all levels will be singly degenerate. Unfortunately, it is difficult to identify the new representations (which are in terms of m_j values, no longer a good quantum number) without knowing more about the particular case. The electric dipole selection rules are also complicated by states being composed of multiple m_j states. For example, if all states in a multiplet contain some proportion of all m_j labeled states, then any transitions between those states would have no restrictions on polarization relative to the magnetic field (as there would always exist an allowed electric dipole transition both for polarizations parallel and perpendicular to the magnetic field axis).

Still, in some cases, this may be possible without additional information, such as a multiplet with $j = \frac{3}{2}$ split mostly by C_{3v} symmetry. In such a case, the $m_j = \pm\frac{1}{2}$ states cannot mix with any other state, including one another (although the $m_j = \pm\frac{3}{2}$ states can mix with one another).

The result also suggests that it is conceivable that electric dipole moments could change as a function of applied magnetic field magnitude and direction. Of course, the question of degree depends on the relative effects of the magnetic field's symmetry and the crystal-field's symmetry. The results for the selection rules determined here are identical if the sign of the magnetic field is reversed (a point which will be relevant to chapter 7).

In short, it is not possible in general to discuss how selection rules for a dopant in a crystal change as a result of an applied magnetic field without more information, because selection rules for the crystal-field are given in terms of the crystal-field quantum numbers, μ , and in terms of axes determined by the crystal, whereas the rules for an applied magnetic field are given in terms of m_j , and in terms of axes given by the magnetic field. The two are not, in general, simultaneously good quantum numbers.

In principle, fitting energy levels in terms of the parameters discussed earlier may make it possible to determine the makeup of states in terms of m_j values (which must also produce the correct Zeeman splittings at low field when compared to experimental values) as a function of applied magnetic field, and carrying out

rotations between the two axes for m_j values may make some of this analysis feasible.

2.3 Expected Energy Levels

Triply ionized erbium and neodymium have the convenience of having similar electronic structure, with three holes or electrons involved in the L-S coupling. Their both having half-integer J values leads to an essentially identical analysis in terms of crystal-field numbers and selection rules.

For three electrons or holes in a 4f configuration, there are only two possible sums for S , $\frac{1}{2}$, and $\frac{3}{2}$. The sum for L can be valued from 0 to 8 (9 is excluded due to the Pauli exclusion principle), in integer increments. The number of combinations of S and L are limited by symmetry requirements for equivalent electrons (or holes), leading to the terms 4S , 2P , 2D , 4D , 4F , 2F , 2G , 4G , 2H , 4I , 2I , 2K , and 2L . Four of these occur twice, 2D , 2F , 2G , and 2H .

For each combined value of L and S from this set, there are values for J going from $|l - s|$ to $|l + s|$ in increments of one. It can be shown that the term with the greatest multiplicity is 4I , so the lowest energy multiplet will always be from that term, by Hund's first rule. For neodymium, $4f^3$ is less than half-filled, so the lowest energy multiplet is $^4I_{\frac{9}{2}}$, by Hund's third rule. For erbium, $4f^{11}$ is more than half-filled, so $^4I_{\frac{15}{2}}$ is lowest.

2.3.1 Er^{3+}

It should be noted that energies of many multiplets for this ion in its free state have been measured experimentally. [43] The lowest energy LS coupled multiplets considered in this work, in order of increasing energy, are expected to be $^4I_{\frac{15}{2}}$, $^4I_{\frac{13}{2}}$, $^4I_{\frac{11}{2}}$, and $^4I_{\frac{9}{2}}$. These are the multiplets predominantly used in the experiments in this work. The two lowest multiplets have a separation corresponding to $1.54\mu m$, an ideal wavelength for transmission in silica glass fibers. Thus, these lower levels are of particular interest for applications.

Results for C_{3v} symmetry for multiplets of odd J have already been discussed

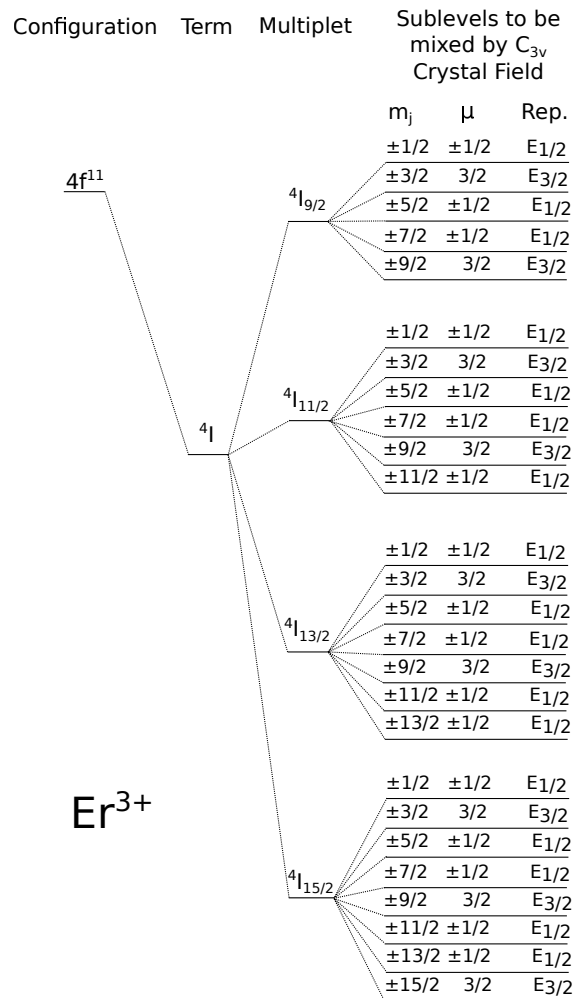


Figure 2.2: The energy levels of erbium most important to this work are shown. Note that final states do not have m_j as a good quantum number, but the number of states shown with each crystal-field number is valid. The relative ordering of energies may also differ.

in some depth. For the majority of materials in this work, it is expected that this symmetry group, or something close to it, is applicable to sites.

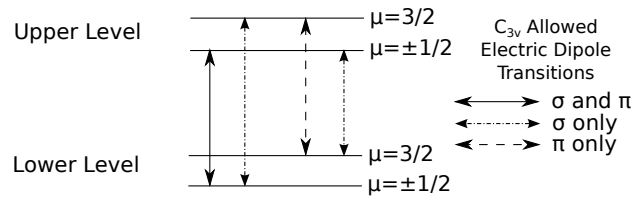


Figure 2.3: For C_{3v} symmetry for half integer J multiplets, the selection rules are expressed neatly in this diagram. These rules apply to both Nd^{3+} and Er^{3+} .

2.3.2 Nd^{3+}

As alluded to earlier, the situation is very similar for neodymium, but with different ordering of multiplets. It should be noted that the energies for the multiplets have been measured for the free ion. [76] Fewer of the results presented in this work involve neodymium, and only a specific set of multiplets was used, ${}^2G_{7/2}$, ${}^2G_{5/2}$, ${}^4F_{3/2}$, and ${}^4I_{9/2}$.

The same results for crystal-field numbers and numbers of levels should apply for both C_{3v} and C_{1v} .

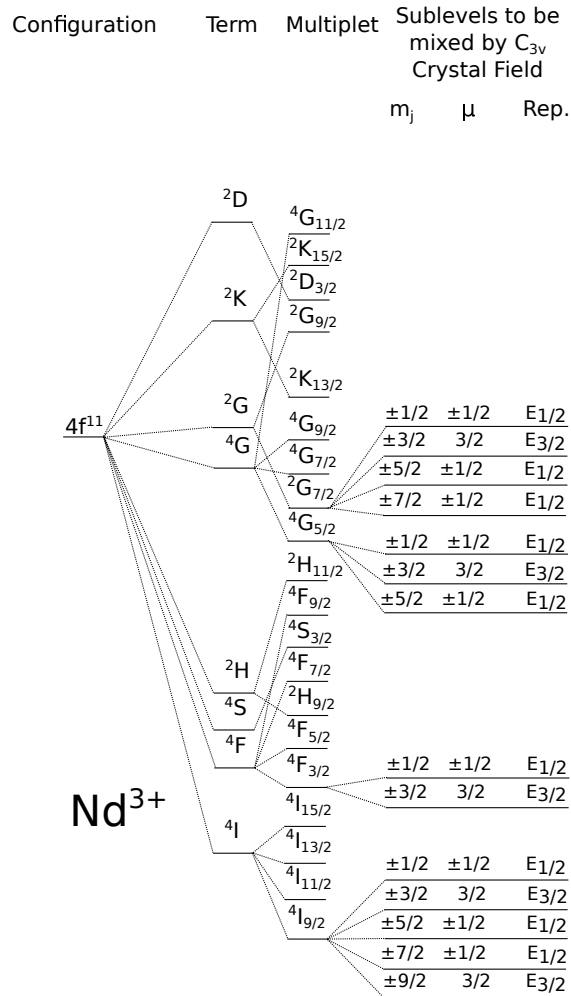


Figure 2.4: The energy levels of erbium most important to this work are shown. Note that final states do not have m_j as a good quantum number, but the number of states shown with each crystal-field number is valid. The relative ordering of energies may also differ.

2.4 Host Crystals and Incorporation Sites

The gallium nitride samples used in this work are in the wurtzite crystal structure, a hexagonal crystal structure which is constructed by an overlap of two fcc lattices for two different types of atoms.

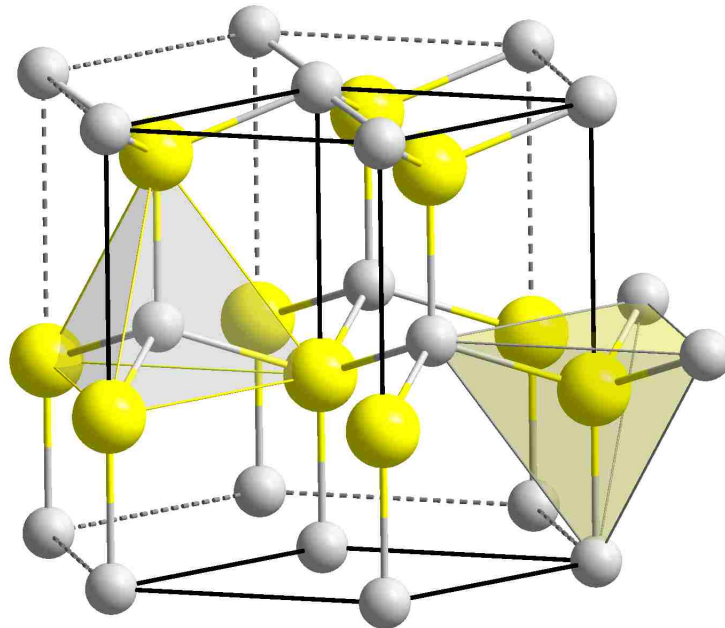


Figure 2.5: A portion of the wurtzite crystal structure, applicable to the gallium nitride samples used in this work. The marked polyhedra are meant to show how this structure can result in C_{3v} symmetry.

For wurtzite GaN, a reasonable guess as to the incorporation site for a positively charged rare-earth ion is that it replaces a positively charged gallium ion in the crystal. This substitutional gallium site would have C_{3v} symmetry, assuming nothing changes significantly besides this exchange. Translation along the c axis does not break this symmetry, and is what makes this differ from tetragonal symmetry. This is the justification for guessing that C_{3v} , or a slightly broken version of it, may be a good framework for analyzing the energy levels of the rare-earth dopants in gallium nitride. The same argument applies to rare-earth doped wurtzite GaAs. Density Functional Theory calculations exist which suggest that rare-earth dopants in GaN substitute for gallium, with a number of possible local defects, such as nearby

nitrogen and gallium vacancies. [66]

A similar argument applies to LiNbO_3 and LiTaO_3 , that either the lithium or the niobium (tantalum) is replaced by the dopant. Previous experimental work showed substitution of the lithium site for erbium doped LiNbO_3 [20] and for iron doped LiNbO_3 . [19] In the former case, an offset along the c axis was observed. Similar behavior for erbium in lithium tantalate and the similar crystal structure of the host has been used to argue that the incorporation sites for LiNbO_3 and LiTaO_3 are similar. [45] The lithium site has C_{3v} symmetry, even if slightly displaced along the c axis, if the c axis is identified with z .

Once a dopant is placed in a particular location in the lattice, a variety of local defects can increase the number of apparent incorporation sites. In this way, one substitutional site can be modified to generate several distinct incorporation sites. In III-nitrides, nitrogen vacancies are suggested as one such defect. [54] Charge compensation may also play a role in some hosts, in which a substitution of a rare-earth dopant for an ion in the crystal of differing charge leads to a variety of local deformations, such as in lithium tantalate. [45]

It has been proposed that defects might be helpful in increasing intensity of transitions in either creating so-called trap levels, which increase the chance of an exciton in the host material being close enough to the rare-earth dopant to transfer its energy, [36] or in promoting the mixing of 4f states with other states of differing parities. [77] In the case of codoping GaN with Er and Mg, it was found that a particular site had significantly enhanced luminescence, suggesting that this may have added a trapping mechanism to improve energy transfer. [29]

2.5 Dilute Magnetic Semiconductors

As mentioned in the introductory chapter, one motivating factor for this research is the search for ferromagnetic semiconductors. Dilute magnetic semiconductors would accomplish this by using dopants to introduce ferromagnetic properties, and would presumably have the advantage of control of the magnetic properties via

the concentration of the dopant. More specifically, this would hypothetically allow control of the degree of spin polarization of the carriers in the material.

To date, Mn doped GaAs has been demonstrated to have these properties, with a working device dependent on the effect having been demonstrated. Unfortunately, it has a cryogenic Curie temperature (the temperature below which the material exhibits ferromagnetic properties, and above which it does not). [55]

A paper by Dietl *et al.* suggested that Mn doped GaN and ZnO might be more promising host materials for increasing the Curie temperature, possibly exceeding room-temperature. [10] However, a later paper using a percolation theory model to remove the mean field approximation used by Dietl suggests much lower Curie temperatures than room-temperature for those materials at reasonable doping concentrations, 103K for 5 percent doping of Mn into GaN, as opposed to in excess of room-temperature. [68] This is relevant because the mean field approximation used is based upon nearest neighbor interactions, and assuming that all dopants can be considered as a typical, and giving a similar contribution to the overall behavior. At achievable doping concentrations, a significant proportion of dopants will have different numbers of nearest neighbor dopants, potentially none. For percolation, a feature in which a sufficiently high, randomly distributed concentration guarantees the existence of chains connected by nearest neighbors traversing the entire system, via nearest neighbors in an fcc lattice (the sublattice for either Ga or N in wurtzite GaN), about 20 percent of the lattice points (of the sublattice) must be the dopant. At lower concentrations, dopants form isolated groups if only nearest neighbor interactions are considered. Complicating this further is that the percolation theory model does not consider the possibility that the dopants may tend to cluster together in regions of the crystal, rather than being uniformly randomly distributed. [67]

There are claims of having achieved Curie temperatures in excess of room-temperature with transition-metal and rare-earth doped GaN, but without a device being demonstrated, these claims are questioned. [51] It has been suggested that SQUID magnetometry, a common method for measuring magnetic hysteresis curves of samples, may be susceptible to experimental artifacts, especially when the

amount of material being measured is quite small. This implies that demonstration of hysteresis curves by SQUID should be considered a necessary, but not sufficient criterion for determining whether doped GaN samples are ferromagnetic, rather than paramagnetic. To date, no device based upon dilute magnetic semiconductors has been demonstrated to function at room-temperature, despite the predictions by Dietl *et al.* having been made nearly two decades ago. This also casts some doubt on the validity of these claims. [51] This is a motivating factor for determining additional experimental methods for measuring ferromagnetic properties, and any effects which might be related to ferromagnetism are of interest for this reason.

A further complication is a claim that a significant part of the magnetic moment in rare-earth doped GaN may not come from the dopants directly, but from gallium vacancies. [79]

2.6 Faraday Effect

This effect is discussed here because it is considered as a possible explanation for another effect to be discussed later. Discovered by Michael Faraday, it is an effect in which linearly polarized light traveling through a material experiences rotation in its polarization proportional to the magnitude of an applied magnetic field applied parallel to the light propagation. It is present in many dielectric materials, including water. It is characterized by a material specific Verdet constant, ν , which gives the degree of rotation per unit of magnetic field per unit of length traveled by the light. It is explained by changes in the index of refraction for left and right circularly polarized light. [23]

$$\theta = \nu B d$$

θ is the angle of rotation, B is the magnitude of the magnetic field, and d is the distance traveled by the light in the material.

Chapter 3

Experimental Methods

3.1 Combined Excitation Emission Spectroscopy (CEES)

3.1.1 Basic Principle

The ability to distinguish energy levels for differing incorporation sites of a dopant is useful for finding differences between them. In this work, materials with wide band gaps are employed, allowing the use of laser wavelengths that can directly excite particular transitions in the dopants resonantly for a variety of multiplets.

In CEES, a tunable laser is used to excite dopants resonantly, and a subsequent emission is measured with a spectrometer. Emission spectra are recorded for a range of excitation wavelengths by repeating a process of adjusting the tunable laser wavelength and recording a new emission spectrum. Typically, the initial excitation corresponds to a significantly higher energy than the emission that is measured, enabling straightforward separation of the excitation light from the emission. Since similar possible emission energies are expected for all excitations (perhaps with different relative intensities) for one incorporation site, if the energy levels of different sites are significantly different, it is possible to distinguish sites by the appearance of a "grid" in the collected data. That is, each excitation energy corresponding

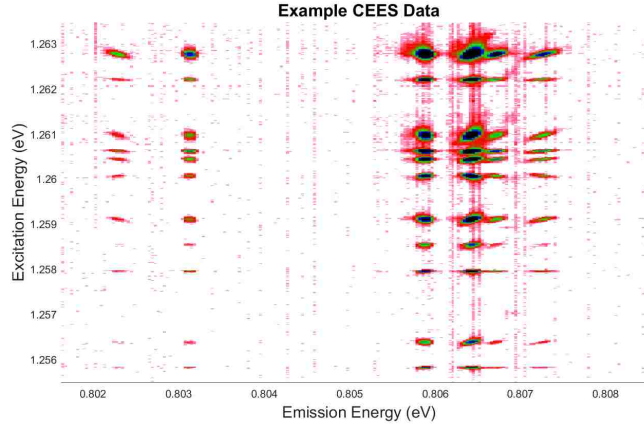


Figure 3.1: Example CEES data for an erbium doped gallium nitride epitaxial film sample with one majority incorporation site.

to the same site should produce similar emission spectra. If one plots intensity as color, for example, on a two dimensional figure, where one linear axis is the excitation energy, and the orthogonal linear axis is the emission energy, one should observe high intensity colors in a grid-like pattern. An example of this is shown in Figure 3.1. It should be noted that there are complications to this assumption, which will be relevant to erbium doped lithium tantalate, in which it is possible that two sites may exhibit some sort of energy transfer mechanism. In cases where this is suspected, peaks are typically assigned to the two sites based on relative strength.

Further discussion and some prior results obtained using this measurement can be found in chapter 8 of Ref. [53].

3.1.2 Experimental Setup

First, a tunable laser is coupled into an optical fiber. This fiber is used to direct light into a structure containing a dichroic mirror, selected to reflect the excitation wavelengths and transmit the emission wavelengths (or beam splitter). The dichroic mirror reflects the excitation light into an objective, which is aimed at a sample,

which is typically cooled to cryogenic temperatures in a cryostat both to reduce thermal quenching and to simplify spectra (as this biases the dopants towards their lower energy levels). Emission light from the sample which passes back through the objective passes through the dichroic mirror, and is coupled into another optical fiber. This fiber leads to the monochromator, which uses gratings and mirrors to split the emission light by wavelength and allows imaging of spectra by a CCD array.

A piece of glass is used to reflect a portion of the light from the laser into a fiber coupler. An optical fiber then directs this light into one of two wavelength meters, enabling recording of excitation wavelengths or feedback loops to tune the excitation wavelength to a particular value. An optical power meter is set either to measure this redirected light, or at another point in the setup. All of the measurement instruments and the tuning of the tunable laser are controlled by a computer. A rough diagram is shown in Figure 3.2. A brief list of steps once the setup is prepared and focused onto a sample is given below.

1. Adjust excitation wavelength to a desired new value
2. Simultaneously record emission spectrum, excitation wavelength, and excitation power
3. Repeat until the desired set of excitations is complete

The same experimental setup for CEES was also used for other types of measurement, using a non-tunable laser in place of the tunable laser. This was done for ultraviolet excitation and Raman spectroscopy.

Occasionally, the process and experimental setup were modified to combine additional measurements with CEES. For example, when certain additional variables were considered, such as emission polarization, or measuring magnetic splittings for one excitation wavelength, only one excitation wavelength, or a non-tunable laser was employed. In this case, the process was often similar, with the adjustment of an excitation wavelength being exchanged with the adjustment of some other parameter. The measurement of the excitation wavelength also allowed for the addition of

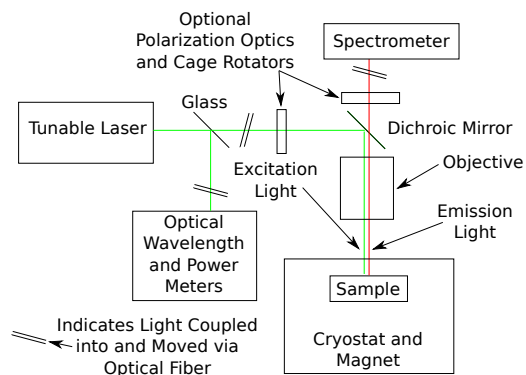


Figure 3.2: A typical setup for the CEES spectroscopy used for this work.

feedback loops to correct this wavelength in cases where this value tended to drift over time.

3.1.3 Magnetic Fields

In this work, the transitions studied are between at least doubly degenerate levels. For data in this work, all of the levels were doubly degenerate levels, with one exception, in erbium doped Cs_2NaYF_6 .

Thus, upon the application of a magnetic field, a given transition between such levels can split into as many as four new levels. For one peak in CEES data, since such a peak corresponds to a combination of a distinct excitation and an emission transition, this one peak can become sixteen new peaks arranged in a four by four grid. An example of this is shown in Figure 3.3.

Magnetic fields were applied by either using an Oxford brand helium-immersion superconducting magnet capable of fields in excess of 6.6 tesla in conjunction with a Janis brand cryostat, or the electromagnet included in the Magneto-Optic Option of a Montana Instruments Cryostation, capable of maximum fields in somewhat in excess of 1 tesla, depending on the spacing of adjustable probe tips and sample geometry considerations. Control of the latter could be accomplished by a computer,

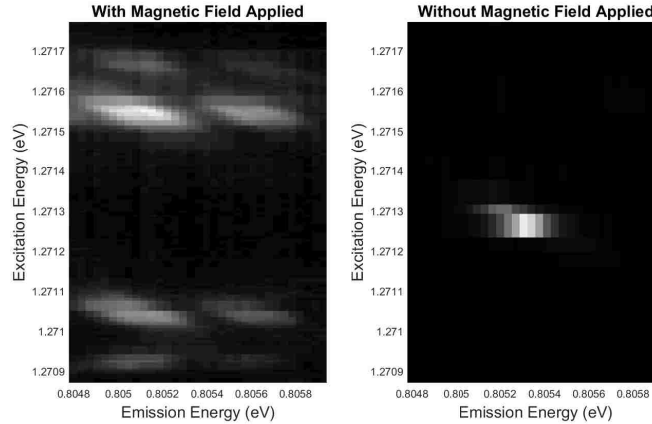


Figure 3.3: Example CEES data in the vicinity of one peak which splits with the application of a magnetic field, for a transition of site A in an erbium doped lithium tantalate bulk crystal sample.

whereas the former was controlled using a power supply and function generator to perform linear ramping of the magnetic field.

In order to determine splitting for a variety of incorporation sites, CEES was combined with the application of a field. In some cases, where the behavior of the splittings as a function of magnetic field was of interest, the Montana Instruments Cryostation’s network interface was used to control ramping of the magnetic field for each excitation wavelength, enabling recording of emission spectra for each of a set of excitation wavelengths and magnetic field values.

3.1.4 Polarimetry

In order to examine the role of polarization, a motorized cage rotator from Thor Labs (model number K10CR1) was fitted with a linear polarizer to measure polarization of transitions in an automated way. Both emission and excitation light polarization could be controlled in this way (with the help of additional optics or measurements to mitigate the issue of changes in power as the excitation polarization is changed). Similar to the case for magnetic fields, the ability to control

polarization was sometimes used in conjunction with the ability to control excitation wavelength to produce data sets of emission spectra as a function of both of those variables.

In some cases, it was relevant to control magnetic fields, polarization, and excitation wavelength together. This produced sets of emission spectra as a function of all three variables. This was accomplished by adjusting the magnetic field and polarization at each excitation before advancing to the next wavelength. This was considered a desirable approach for some of the experiments in this work because it prevented issues arising from returning the tunable laser to precisely the same wavelength and power for an additional measurement of another variable. Unfortunately, as might be surmised, the addition of each variable adds significantly to the time required to conduct a complete set of measurements.

3.2 Equipment Used

In the case of CEES for erbium doped samples, the excitation laser was typically chosen to be either one of two Sacher brand diode lasers, both model number TEC500, (one tunable near 970nm, the other near 800nm), or a 1.5 micron laser and Erbium Doped Fiber Amplifier. One other non-tunable E-TEK brand diode laser was used on occasion, with excitation near 980nm, with wider spectral range and higher power than the aforementioned Sacher brand laser near the same wavelength output. For neodymium doped samples, a Coherent brand dye laser, model 590, was used to achieve wavelengths in the range of 600 to 630nm. For the dye laser and the Sacher brand diode lasers, tuning of the wavelength was accomplished with computer controlled stepper motors. For ultraviolet light (about 351nm), to excite a GaN host material, a Coherent Innova 300 laser was used, which was not tunable.

A variety of instruments were used for power measurement. Typically, these measurements were used either to verify consistent power output, or to correct spectra for any variation. All of them had a computer interface to communicate

with the computer controlling all the equipment. The devices used were the Thorlabs PM100D with S121C or S120VC attachment, the ILX OMM-6810B Optical Multimeter, HP 8163A Lightwave Meter, and the Newport 1830-C Optical Power Meter. The selection of device for each experiment was determined by wavelength and power considerations, as well as availability in a laboratory with shared equipment.

Two wavelength meters were used, one primarily for infrared light, an HP 86120B, and one primarily for visible light, a Coherent Wavemaster. The former has a rated accuracy of 3ppm, and the latter has a rated accuracy of $\pm .005$ nm, but both report resolution to .001nm or better.

For measuring spectra, an Acton SpectraPro 500i monochromator was used, with one of two CCD (charge-coupled device) arrays, both with computer interfaces. The first, a Princeton Instruments LN/CCD 1340/100 E1, as implied by the model number, was liquid nitrogen cooled, and had 1340 by 100 pixels, of which only the portion of the 100 pixel axis with greatest signal was used. This was used for all spectra with wavelengths up to and including roughly one micron. A second array, a Hamamatsu C8061-01, gave a 512 pixel output, and was used for all the spectra with wavelengths near 1.5 microns (although it can be used for a wider range). This second array had thermoelectric cooling, and had the unfortunate issue of a dead pixel, which is removed in the data presented in this work.

Calibration of the emission axis was accomplished in several different ways, depending on the wavelength range. For visible light, a series of spectral lamps with known spectra was used to perform calibration. For emission in the range of 920nm to 1000nm, the aforementioned Sacher brand tunable diode laser was used in conjunction with the optical wavelength meters to produce spectra for a series of measured wavelengths. For 1.5 micron emission, a Photonetics brand tunable external cavity laser was used to produce similar spectra.

While performing various experiments, occasionally additional pieces of equipment were required for some specific task. In order to investigate possible spatial variation in a parameter, and to change samples while using the Janis brand cryostat, Attocube brand linear steppers were used, which had a computer controlled

interface for automated control of the stepping.

Programs for control of experiments were written using LabVIEW version 5.1, and run on a personal computer using Microsoft Windows XP. A variety of interfaces were used to communicate with equipment, including GPIB, RS-232, USB, and PCI expansion cards.

3.3 Peak Fitting Methods

The experiments conducted in this work all ultimately result in sets of peaks in spectra, which must be analyzed. This requires a formal approach more sophisticated than visual inspection to find the pixel with the highest intensity. The approach selected in this work was to develop specific numerical models for the shapes of spectral peaks, and use nonlinear fitting algorithms in order to fit these models to actual data. This is in contrast to the method of moments used in the past for similar data, [75] in which moments of the data are collected without making assumptions about the specific distribution of the data. As will be discussed, complicated broadening mechanisms make developing an exact model for the lineshapes in CEES data likely impossible (which is what makes the method of moments an attractive approach). Still, an approximate numerical model has important advantages, such as the ability to perform fitting. This can take advantage of redundancy in optical spectra in order to determine parameters which may have otherwise been difficult to extract.

3.3.1 Comments on Broadening Mechanisms

Multiple mechanisms broaden peaks in spectra, which may not have the same behavior. They are broadly classified into two groups, homogeneous if the mechanism affects everything producing the peak in an identical way, and inhomogeneous if the mechanism affects them in different ways. For example, Doppler broadening when conducting spectroscopy on molecules in a gas would affect molecules differently, depending on their relative motion, and would be classified as an inhomogeneous broadening mechanism.

First, there is an uncertainty principle relation requiring an inverse relationship between the lifetime of a state and the uncertainty in energy of that state, $\Delta t \Delta E \geq \hbar$. This implies that states which are observed (due to finite lifetimes) will always have some uncertainty in energy. This yields homogeneous broadening. It can be shown using a damped oscillator model that the intensity of radiation follows a Lorentz distribution.

$$I = I_0 \frac{\frac{\Delta\nu}{2\pi}}{(\nu - \nu_0)^2 + \left(\frac{\Delta\nu}{2\pi}\right)^2}$$

For a set of dopants at what might otherwise be identical sites, small differences may arise, such as differences in distant defects, or variations in local strain. This means that for what is labeled as a single site, there is effectively a distribution of sites which may have slightly different energy levels. This leads to what is known as fluorescence line narrowing, an inhomogeneous broadening mechanism. Suppose that as a function of strain along some axis which varies in the host crystal, there exists a site with a peak appearing in CEES data whose excitation and emission energies both vary roughly linearly with this strain. The result is something that looks like a diagonally oriented peak, as seen in experimental data shown in Figure 3.4.

The appearance of these features is sometimes taken to imply strain is present in the host crystal due to the above argument. In order to handle these cases in fitting for centers of levels, a linear relation between excitation and emission energy is assumed, and a peak in CEES data is assumed to be representable as a product of profiles for emission and excitation. Observation (and an argument about the result if each of these similar sites had essentially identical magnetic splittings) led to justifying using the same linear relation for the excitation and emission energies for magnetically split peaks in fitting. Further discussion of this and related experimental results can be found in the eighth chapter of [53].

If this variation in energies for dopants at the same site is modeled using a Gaussian distribution, the Voigt profile for the line shape arises very naturally. If each of the individual dopant ions corresponding to one site produces a similar Lorentz profile, but with differing center energy values described by a Gaussian

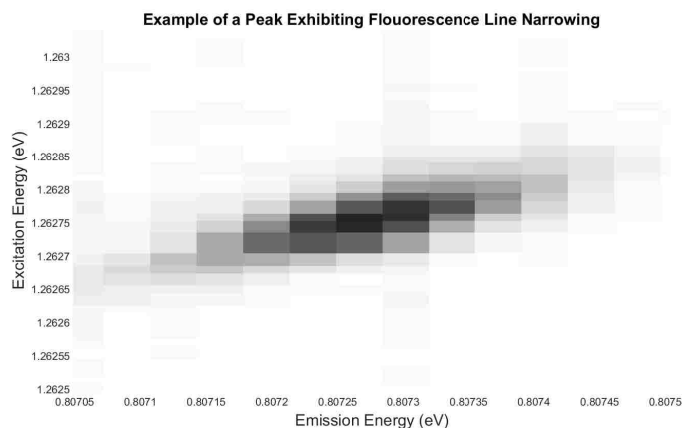


Figure 3.4: Example CEES data for a peak exhibiting fluorescence line narrowing for the majority site in erbium doped gallium nitride.

profile, the operation that describes the overall emission is a convolution of a Lorentz and a Gaussian line shape, which is the definition of a Voigt profile. Of course, the flaw in this argument is that a distribution of energies for similar sites is not certain to be Gaussian. Still, this is used as a starting point for making an approximate model.

3.3.2 Approximated Voigt Profile

The convolution of Lorentzian and Gaussian line profiles can become computationally expensive. Thus, in this work, peak fitting was accomplished with an approximation to the Voigt profile taken from Ref. [35]. This expresses this profile in terms of a weighted average of Gaussian and Lorentzian profiles, significantly reducing computational difficulty, with a tradeoff of some small loss in accuracy in the profile shape. It is assumed in most fitting in this work that the parameter corresponding to how Gaussian or Lorentzian the profile is is identical for all peaks in a particular spectrum. This is somewhat inaccurate on some level, particularly when comparing spectra with peaks of significantly different lifetimes, but this is another tradeoff

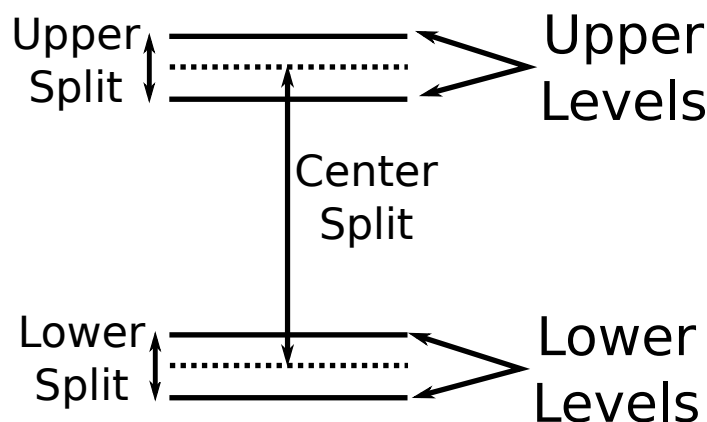


Figure 3.5: Diagram of the three parameters used for fitting Zeeman splitting for a transition between two doubly degenerate levels.

made for simplifying fitting.

3.3.3 Zeeman Splitting

Zeeman splitting can produce difficulties in fitting due to the number of possible peaks. As discussed earlier, this process may cause four times as many peaks as originally present. To simplify the process, as few parameters as possible are used. In analyzing the splitting of an individual peak due to a transition between two doubly degenerate levels, the parameters used are the (two) differences in energy for each of the lower and upper levels, and a parameter corresponding to the average difference between the upper and lower energies. Because these parameters can describe any relative shift of the four levels (and only three are needed, because the absolute position is lost by taking differences to give transition energies), they are adequate to describe the level splitting. This is shown in Figure 3.5. Allowing the center of the split peaks to vary from the zero field case also allows analysis of how this might change as a function of applied field.

For spectra with large numbers of peaks with small splittings, this idea is extended. First, one must determine a correct level assignment for the peaks. This

process is discussed later in specific cases, but is aided by noting whether the former process here yields level splittings which seem to be shared between peaks. Once this is established, it is argued that one can fit these peaks by defining the center of the ground state split level as zero, assigning relative position parameters to all the centers of the other levels, and assigning a parameter for the splitting of each level. Thus, for n doubly degenerate levels, there are $2n - 1$ parameters needed to describe their relative positions for Zeeman splittings. Reducing this number of parameters also aids in cases where one particular peak is not easily fit for one of these parameters, but another peak is.

To aid in reducing the number of parameters, in both the cases above, it is argued that the Zeeman split peaks likely have similar widths, and so only one width parameter is used for each of four grouped split peaks.

3.3.4 Ferromagnetic Hysteresis Curves

As will be discussed later, it became important to develop an approximate model for ferromagnetic hysteresis to determine whether hysteresis was present in a experimentally derived quantity that revealed the magnitude, but not the sign of an applied magnetic field. One computationally simple suggestion found in the literature [58] was to model hysteresis with two offset arctangent functions. This was the approach used in that portion of this work.

Chapter 4

Spectroscopic Detection of Ferromagnetic Hysteresis

4.1 Motivation

As discussed earlier, there is significant interest in transition-metal and rare-earth doped GaN for possible ferromagnetic properties. Work in this field has had some issues with consistency. There are a number of conflicting reports on the transition temperatures for rare-earth and transition-metal doped nitrides, including reports of values exceeding room-temperature. [3] There is also a controversial paper on Gd doped GaN in which a magnetic moment per Gd was found to be 4000 times the Bohr magneton, compared to an atomic moment of 8 times the Bohr magneton. [7]

These problems need to be addressed. As mentioned earlier, it was proposed in the literature that additional methods of verification of these properties are needed to confirm ferromagnetic behavior. [51] Since even members of our own research group have reported ferromagnetic hysteretic behavior in rare-earth doped (in this case, erbium) gallium nitride, [74] it seems important that multiple methods of measuring ferromagnetic properties be used and developed.

A proposal which was considered in the past [75] was to use optical spectra to measure the total magnetic field experienced by a sample, and compare this to the

magnetic field applied to that sample. This would enable measurement of magnetic fields inside the sample, as opposed to simply adjacent to the sample. It should be noted, however, that this particular method may be susceptible to similar issues that were mentioned for SQUID magnetometry, namely that of other, external sources of hysteresis.

4.2 Our Approach

The idea was to find whether the splitting of a peak in spectra could be used in order to determine the magnetic field magnitude that a sample experiences, and compare that to the applied magnetic field. If one cycles the applied magnetic field between a large positive and a large negative value several times, one ideally should see if there are signs of a remnant field. If the splitting depends only on the magnitude of the applied field (if we confine the situation to the field being applied along one axis), we should see signs that the field the sample experiences "lags" behind the field that is applied. Using the offset arctangent model for ferromagnetic hysteresis, and assuming an approximately parabolic behavior for peak splitting measures as a function of applied magnetic field, Figure 4.1 shows an expected result, for a full cycle of the applied magnetic field (not starting from a virgin material state).

There are multiple means for extracting information about Zeeman splittings, but we specifically are interested in ones that work well at lower applied fields. Performing a fit for each individual peak can run into issues, namely, that adjustments in both the width and splittings can accomplish similar results in tweaking a model to match the data. One metric used by a previous student [75] was calculating the second moment of the peak. This was convenient, in that it incurs negligible computational difficulty. However, this metric had difficulties returning to the same value at zero applied field, both in data from that work and in new data presented here. A proposed alternative is to model the Zeeman split peak as a single peak, and use the fitted width as a measure of the splitting. Clearly, this method should not work well for well-split, resolved Zeeman split peaks, but it happened to avoid

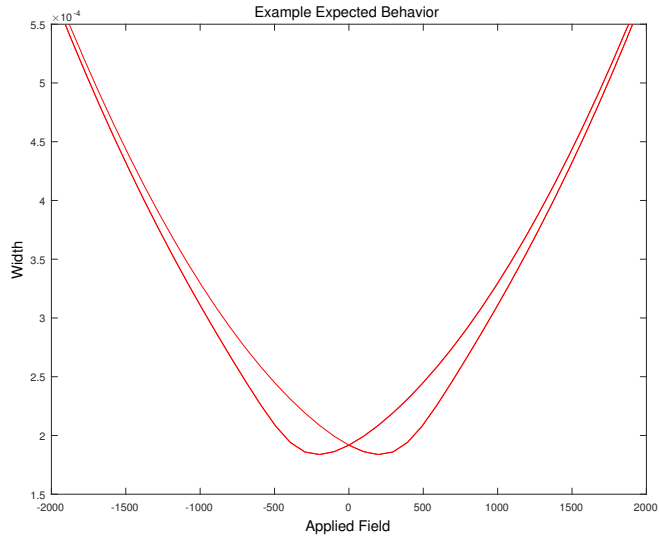


Figure 4.1: Example expected behavior for peak splitting or width measures with hysteresis, assuming an arctangent function approximation for the hysteresis.

much of the aforementioned problem in returning to the same value at zero applied field.

The growth conditions for the samples used in this work are given in Ref. [62]. The primary samples used in this portion are E176-R2-J and E185-R1-J. Some of the data presented here were previously described in Ref. [75].

4.3 Results

In all experiments, the dopant was resonantly excited with a wavelength near 600nm. In the experiments I performed and present here, 603.041nm was set as the target wavelength for a feedback loop using a Coherent Wavemaster and a stepper motor used to rotate a birefringent crystal in a dye laser. Both experiments involved cooling in a cryostat and the application of a magnetic field. For more details, see

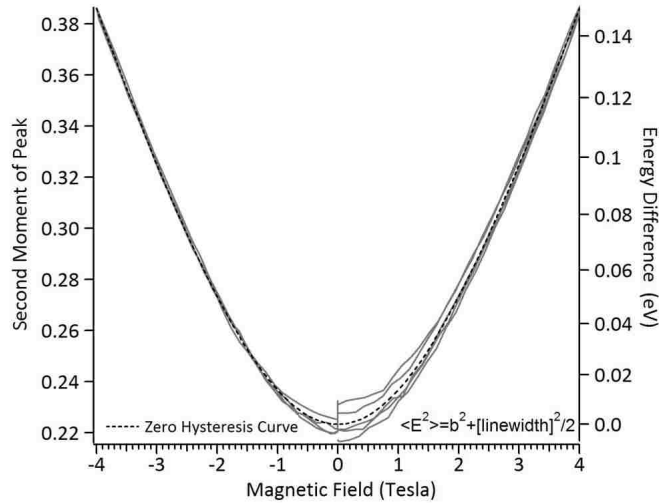


Figure 4.2: Taken from Ref. [75], second moment of an emission peak near 1.353eV from Nd^{3+} in GaN as a function of applied magnetic field.

Chapter 3.

As discussed, taking the second moment of the peak yielded issues in reproducing the same value at zero applied field. There may be several reasons for this, such as noise, or a lack of stability in the laser excitation used to trigger the emission. It should also be noted that a feedback loop was employed to keep the excitation wavelength constant during my own experiments. By using a Montana Instruments Cryostation with an optional Magneto-Optic module, we were able to conduct these sorts of experiments using a magnet which has a hysteresis of its own, typically on the order of 0.1 tesla (depending on the probe configuration used). This allowed testing this approach in a situation in which hysteresis is certain to be present. The result was separation between the curves for increasing and decreasing applied field, in line with the general prediction made.

As discussed in the Chapter 3, an approximate model for ferromagnetic hysteresis based on arctangent functions was employed. This was used only for the purpose of an approximate model which would allow data fitting in a straightforward way.

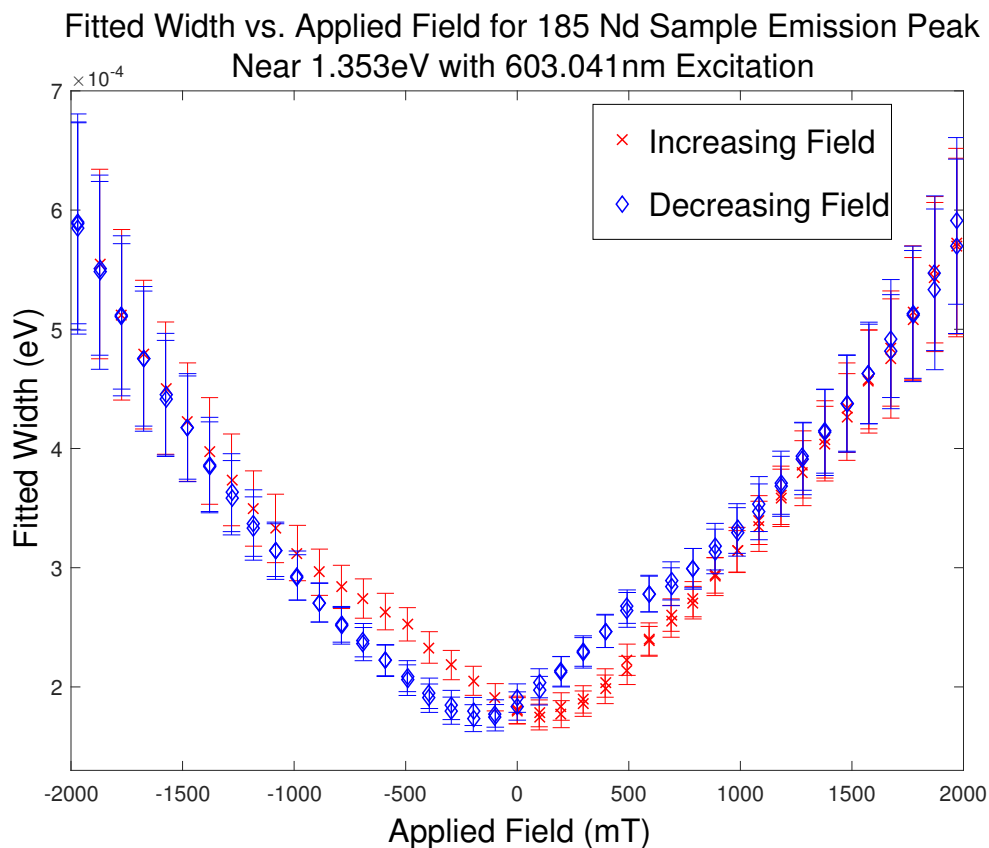


Figure 4.3: Fitted widths as a function of applied field. Field was cycled prior to this measurement, so there is no virgin material portion. Sample E185-R1-J, GaN:Nd epitaxial film

Ideally, if this were to be used as a method for detection of hysteresis, something more physical should be used.

The result was that the confidence interval for the parameter giving the remnant field did not include zero, and included a range in the vicinity of the expected value. Having established a method for doing this analysis, it was thought to be valuable to reuse old data to reexamine the question of ferromagnetic hysteresis. The experiments described in Ref. [75] were conducted using a helium immersion superconducting magnet not expected to have any inherent hysteresis. While I

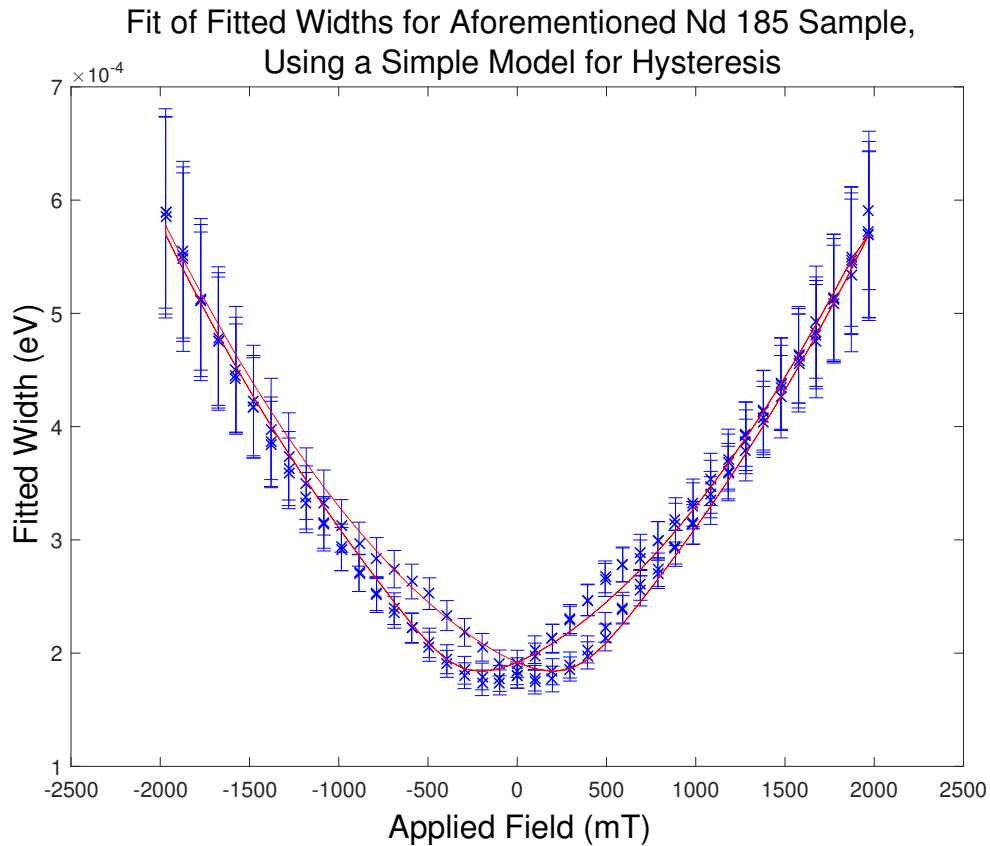


Figure 4.4: Fitting of the fitted widths using an approximate arctangent function to model ferromagnetic hysteresis, from an experiment using a magnet expected to have its own hysteresis. Sample E185-R1-J, GaN:Nd epitaxial film

was able to find the original data, assignment of applied field values was somewhat ambiguous. I used two methods to assign field values, and both led to a similar result.

The first approach leads to a fitted remnant field of 42mT, with a 95% confidence interval of -63mT to 148mT. The second leads to 25mT, with 95% a confidence interval of -780mT to 830mT. Neither of these results is persuasive in demonstrating ferromagnetic hysteresis.

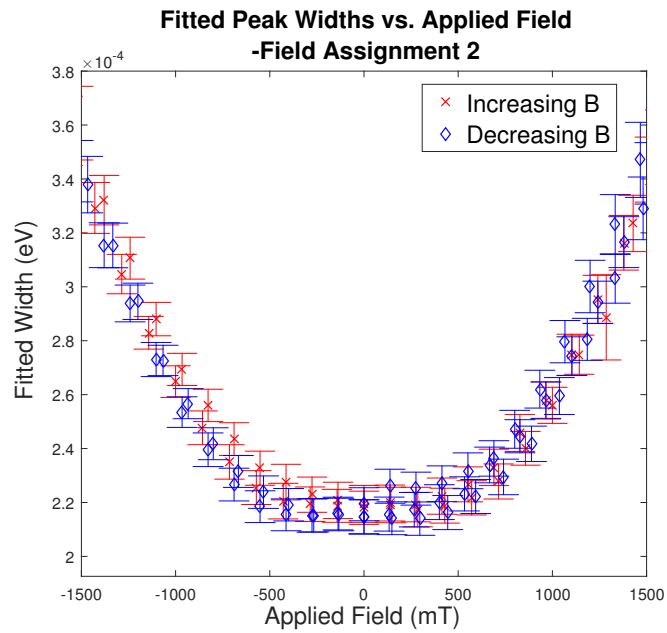
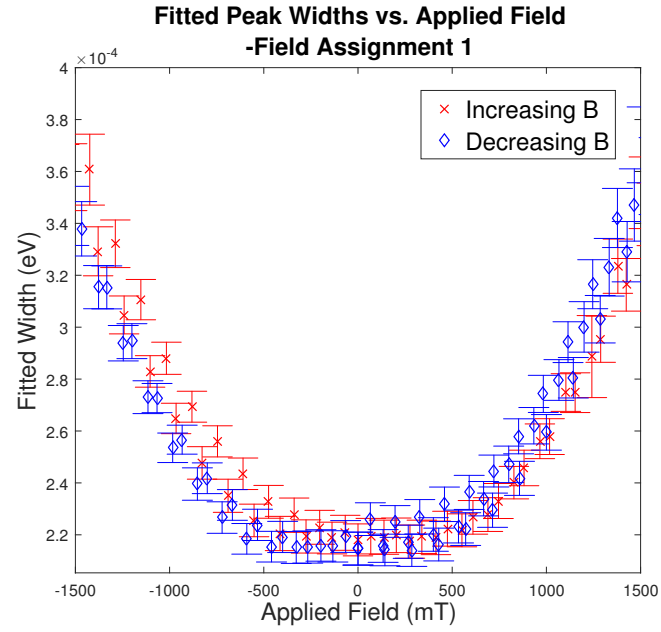


Figure 4.5: Older data from the author of Ref. [75] analyzed by the same method as used for Figure 4.4, with two different approaches to assign field values.

4.4 Improving the Detection Threshold

4.4.1 Relevant Parameters

Several parameters are not easily adjusted. For example, significantly larger effective g factors would generally require larger angular momenta, which is limited for a given number of 4f electrons. The relevant parameters for which large changes are likely difficult or impossible are

- The saturation magnetization of the sample- specific to the sample
- The effective g factor for the level used for detection- limited by the possible effective g factors of the dopant used
- The linewidth of the transition used for detection- specific to the site and the sample
- To some extent, the temperature, as one likely goal is to use this technique to study behavior as a function of temperature, and second, there is a strict lower limit to the temperature

The following parameters are much more reasonably adjusted, perhaps with changes in instrumentation.

- Resolution of the spectra- depends on specifics of the spectrometer optics and CCD array used
- Intensity- can be improved via reductions in losses, increases in laser power, and increases in exposure time
- Improvements in accuracy of labeled field strengths- might be improved by implementing alternate control techniques

As can be seen in the example spectra, the ultimate question of whether ferromagnetism in the sample can be observed requires the detection of a separation of

curves showing widths as a function of applied magnetic field just adjacent to the zero field point. If there is more than one source of hysteresis, and the unwanted source is quite large compared to the other source, this requires the ability to reduce errors such that error in measuring the precise magnitude of the unwanted source is much smaller than the magnitude of the wanted source.

4.4.2 Estimating Values for Parameters

The first, and arguably most important parameter to develop any sort of analysis of required precision, is the magnitude of the remnant magnetic field. To estimate this, results from Ref. [74] were considered, which refer to erbium doped gallium nitride, with an erbium concentration of $6 \times 10^{19} \text{ cm}^{-3}$. From inspection of the plots, an upper estimate of $0.01 \frac{\text{emu}}{\text{cm}^3}$ for the volume magnetization corresponding to a remnant field is made. Assuming a relative permeability of unity, this leads to an estimate of 0.01mT. This is drastically smaller than any result suggested above. Considering that the magnet for the Montana Instrument Cryostation has a radial spatial variation on the order of parts in ten thousand within a millimeter, and a hysteresis on the order of 100mT, even if the hysteresis of the magnet itself is completely consistent from run to run and no error appears in the measurement of the hysteresis curves (which is itself doubtful), having adequate precision to subtract two curves requires submillimeter positioning for the sample and the laser relative to the magnet. This suggests that improving the detection threshold adequately will require a different magnet system, with either no ferromagnetic hysteresis of its own, or hysteresis that is consistent and measurable to a precision corresponding to something less than 0.01mT.

It is assumed that a magnetic field magnitude of about 1 tesla is more than sufficient to reach saturation for this hysteresis behavior. It should be noted that saturation in this behavior means that an increase in field magnitude will not improve the detection threshold, and may indeed cause other issues involving stability if this higher magnitude corresponds to a longer period of time to perform the measurement. Of course, this magnitude may be higher.

Next, an effective g factor for some transition needs to be selected. This is approximately limited by the possible combined angular momentum of three 4f electrons or holes if this is limited to erbium or neodymium. For order of magnitude estimates, an effective g factor of 10 is selected for one level (which is somewhat more than twice the largest j value for the multiplets involved in the emission and excitation schemes for the data shown earlier), and 2 for another (an arbitrary estimate for the ${}^4F_{\frac{3}{2}}$ multiplet, which was involved in the peak mentioned earlier).

The linewidth is difficult to determine as well, and is sample dependent, but for some data presented in a later chapter on erbium-doped gallium nitride from a sample believed to have rather sharp transition lines, a width of about 3×10^{-5} eV was found for some peaks. This is taken as a best-case scenario estimate.

For the precision of the magnetic field axis, if the applied field axis varies by an amount much greater than the residual magnetic field, since the width depends on the sum of the residual and applied fields, it will not be possible to observe separations in width due to the residual field. This places a requirement that precision for the applied magnetic field axis must be less than about 0.01mT.

The next step is to determine how the error in this fitted hysteresis varies as a function of the adjustable parameters listed, resolution and intensity. To do this, a model was created, using the aforementioned analysis methods of fitting with a single peak and calculating second moments, considering Poisson distributions for intensity for each pixel. This was done using an approximated lineshape which was used to fit data to be shown later for Er doped GaN.

The point at which the maximum difference is observed for the increasing and decreasing magnetic field appears to be near the zero field point. Assuming a quadratic dependence for the width on the total field (plus a constant term), the difference is given by

$$\Delta w = a(B_{\text{applied}} + B_{\text{residual}})^2 - a(B_{\text{applied}} - B_{\text{residual}})^2 = 4aB_{\text{applied}}B_{\text{residual}}$$

B_{residual} corresponds to the difference between the upper and lower hysteresis curves, and is expected to be zero at the turning point of the applied field, and at a

maximum at zero applied field. Since the question of this chapter is to determine the point at which this value can be determined to be non-zero, this can be rearranged to give the residual field in terms of the observed width difference. Taking this further, to detect such a field, a difference in widths must be larger than the error in widths, implying that this equation can be used to give a detection threshold as a function of the applied field, the quadratic term constant a , and the error in the widths.

$$B_{threshold} = \frac{\Delta w}{4aB_{applied}}$$

Of course, the relation between measures of width and the applied field are not guaranteed to be quadratic, but this is used to develop an approximate model for the detection threshold. In Ref. [74], it appears that the coercive field may be on the order of a few tenths of a tesla.

A typical maximum intensity for the experiments and equipment in this chapter, about twenty thousand photons in a one second exposure, was used for an initial estimate of intensity. An estimate for resolution was determined by using that of the specific CCD array and optics used to obtain that peak maximum intensity, 3×10^{-5} eV per pixel. Monte Carlo error estimation was used in order to determine the errors in widths, leading to the possibility of variations from run to run of the model.

4.4.3 Results

The initial estimates for parameters suggest that the detection threshold, if the coercive field is close to 0.2 tesla, is likely on the order of 50mT. This is somewhat higher than the magnetic field adjacent to a typical refrigerator magnet, suggesting that if such a large residual field were present, simpler tests of ferromagnetism may be more suitable at this detection threshold. This estimate is also expected to be a lower estimate for the threshold in the actual setup used here, owing to ignoring additional sources of errors.

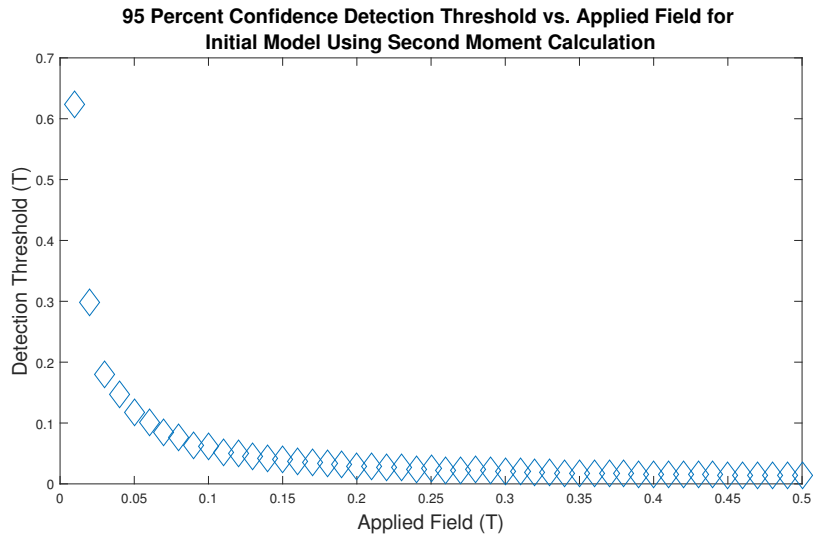


Figure 4.6: Detection threshold for error model using initial parameters as a function of applied magnetic field.

Photon Count

Results for adjusting the peak intensity (or more correctly, the number of photons recorded), and nothing else, suggest that increasing the photon count by a factor of ten almost halves this detection threshold. However, it should be noted that exceptionally long exposure times may lead to the increasing importance of other issues not accounted for in this model, such as misfiring of a pixel, or drift in laser wavelength and power, or perhaps worst of all, if a conventional electromagnet is used, temperature changes which cause slight variations in the applied magnetic field.

The result of comparing the peak detection threshold at $0.1T$ was that if the photon count is increased by a factor of 10^{15} , that is, fifteen powers of ten, the residual field detection threshold becomes close to the desired value. A plot with logarithmic axes in Figure 4.7 shows several modeled points. This seems to be highly impractical to achieve, and for the reasons mentioned already, simply summing up more exposures over much more time (assuming that this is an option for practical

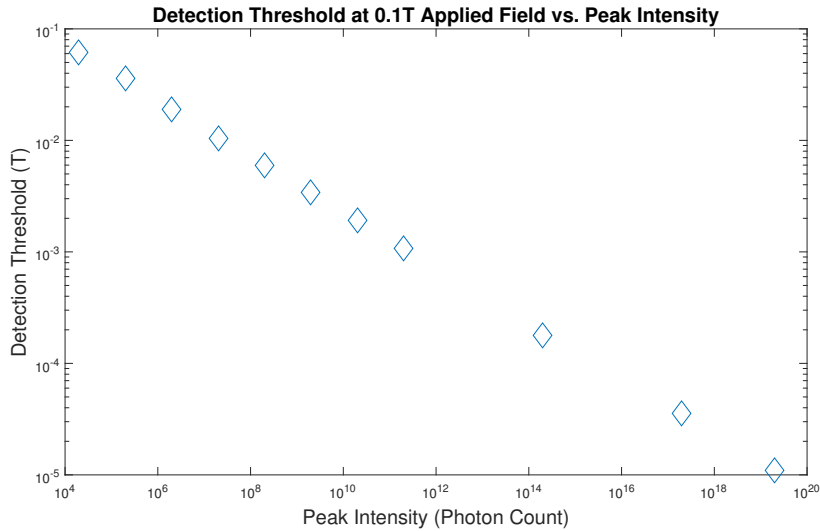


Figure 4.7: Dependence of the detection threshold as a function of peak photon count, with all other parameters held constant.

reasons) is subject to its own flaws which are not considered here. If even possible, it would likely require radical redesign of the experimental apparatus.

Spectral Resolution

In order to normalize for the effects of intensity change, for each run of the model, the intensity was scaled by the change in resolution, to keep the same number of photons per range of spectrum.

Unfortunately, after a certain threshold (corresponding to at least 10 pixels), it appears that this process did not cause a sufficiently significant decrease in the detection threshold to be discernible from fluctuations due to the model including Monte Carlo estimation. This is seen in Figure 4.8. It is suggested that the resolution of the experiments conducted here is likely adequate for these measurements, in the sense that increasing this by a factor of about 30 does not seem to yield any improvement.

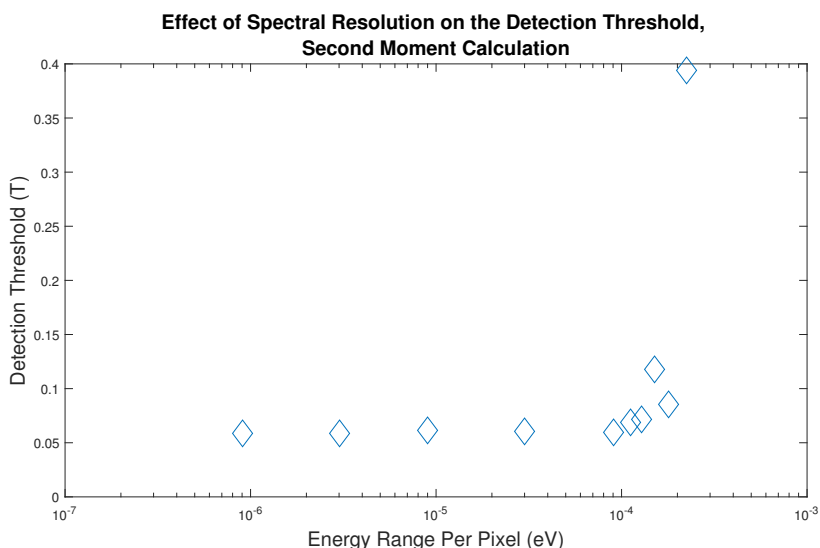


Figure 4.8: Modeled detection threshold for a 0.1T applied field as a function of energy range per pixel, with all other parameters held constant, with the caveat that total photon count per range of energy is kept constant, rather than peak photon count.

4.4.4 Final Comments

It seems that it is unlikely that this method could be improved in any straightforward way to permit this measurement, unless the sample itself has a dramatically (several orders of magnitude) higher residual magnetic field than was estimated. But, this is the most important question that must be answered in order to determine whether this technique could be used. In the end, it appears that the only way to improve the detection threshold is to drastically improve the signal to noise ratio beyond what is currently the case.

Also, there is an issue that must be resolved- the precision of the applied field needs to be smaller than the value of the residual field. This likely precludes the Montana Instruments Cryostation with Magneto-Optic option for the field magnitudes which were discussed. The Oxford Brand liquid helium immersion superconducting magnet used for some of the prior data shown here also would likely need to

be computer controlled in order to improve this, as for the experiments in Ref. [75], a computer was simply set to record spectra at regular intervals while a separate function generator was operated by hand.

In any case, this method is likely still susceptible to the same issues as SQUID, in that when an exceptionally small magnetic field is under investigation, alternate sources of observed ferromagnetic behavior become plausible. [51]

4.5 Conclusions and Future Advice

We were not able to establish ferromagnetic hysteresis, although some of the results look qualitatively like such hysteresis could be present. The older experiments conducted using the Janis cryostat could conceivably be improved upon, however. The addition of a feedback loop to stabilize the excitation laser wavelength, and measures taken to improve precision in the applied field strength are expected to help. Still, it seems unlikely that this method, with the equipment our group currently has, could easily detect remnant fields significantly smaller than several tens of millitesla.

Regardless, success in the experiments using a magnet with its own hysteresis has proven that it is at least feasible to measure ferromagnetic hysteresis via this method, provided the fields produced by the hysteresis are sufficiently large.

Chapter 5

An Investigation of Erbium Doped Lithium Tantalate and Lithium Niobate

5.1 Motivation

Other projects described in this work led to an interest in a close examination of site symmetries, and developing an experimental setup to examine this in detail. As will be discussed in a later chapter, the presence of an unusual asymmetry in Zeeman split peaks in optical spectra in several erbium doped host crystals was perhaps the most important of these. This sparked an interest in determining whether this effect had any dependence on the properties of the levels involved in the transition. This motivates identifying crystal-field numbers for several of these hosts.

Erbium doped lithium tantalate and lithium niobate were known from prior work to have a large number of spectroscopically distinguishable incorporation sites [45] [16], and samples available gave excellent signal and very sharp transition peaks in comparison to gallium nitride samples which were available. This made these materials interesting as model systems for applying such a setup.

In principle, if a large number of incorporation sites are present (greater than

ten or so), it would be surprising if all these sites had the same symmetry group. That said, it may be possible that slight perturbations from a perfect symmetry may not be distinguishable, depending on the ability of an approach to determine this. The ultimate question we wished to answer was, can combined excitation-emission spectroscopy (CEES) be combined with control of applied magnetic fields and polarization of excitation and emission light to identify these differences in symmetry?

It should be noted that simultaneous analysis of polarization and magnetic splitting of peaks will be examined in a later chapter, due to its arguably greater relevance to that chapter.

5.1.1 Objectives

- Identify a variety of incorporation sites in erbium doped lithium niobate and lithium tantalate
- Compare polarization and magnetic data to selection rules for C_{3v} symmetry to identify both the crystal-field numbers for the levels, and the sites which best conform to the selection rules (indicating higher degrees of symmetry).
- Determine crystal-field numbers for erbium doped gallium nitride in the same way, but for the majority site.

5.2 Approach

5.2.1 Experimental

The changes to a typical CEES setup were fairly minimal. The Montana Instruments Cryostation with Magneto-Optic option was used both as a cryostat, and as a means for applying a magnetic field with variable magnitude. Mounting the sample at different angles relative to this field in different experiments permitted some control of magnetic field angle relative to the c-axis. In principle, this could be improved

with a rotational stage. Polarization and magnetic field control were accomplished as described in Chapter 3.

Unfortunately, each additional variable significantly increases the amount of time required. In practice, this led to a preference for looking at as few variables simultaneously as possible. Still, many relevant group theory predictions allow comparison for such limited data sets, such as polarization of transitions without an applied magnetic field, or which levels are split under magnetic fields applied parallel and perpendicular to the *c*-axis.

As discussed earlier, it is expected that in their host crystals, both neodymium and erbium will take a charge state (+3) such that their levels will have odd *J*. In the host materials described here, as well as in wurtzite gallium nitride in Chapter 6, it is expected that the majority incorporation site for the rare-earths will have C_{3v} symmetry. This leads to the levels for both of these dopants (which are split from multiplets with particular *L*, *S*, and *J*) which can be classified with a crystal-field number of either $\pm\frac{1}{2}$ or $\frac{3}{2}$. These numbers represent some symmetry of the levels involved. Doubly degenerate levels with a crystal-field number of $\frac{3}{2}$ are expected not to split under a magnetic field applied perpendicular to the *c*-axis, while levels with a number of $\pm\frac{1}{2}$ are. All doubly degenerate levels are expected to split under a magnetic field applied parallel to the *c*-axis. The electric dipole transition rules have already been discussed in Chapter 2, and are summarized in Table 5.1.

Thus, the most important goal appears to be identification of these crystal-field numbers for each level, and comparing how well the associated rules apply for each site. For a large number of sites, it seems unlikely that all would have perfect or nearly perfect C_{3v} symmetry. Unfortunately, if one imagines a simple reduction in symmetry, such as breaking the threefold rotation, but keeping a mirror symmetry, the same predictions for C_{1v} predict all doubly degenerate levels will have the same polarization and field splitting behavior. Thus, if the perturbation of symmetry is slight, this might lead to a situation in which rules for C_{3v} symmetry appear to hold mostly, with some slight errors. This could cause an issue with a detection threshold, which will be complicated by things like higher order transition terms, precision in mounting and polarization angles, detection of splittings in spectra,

and higher order terms for magnetic splitting. So, even if the results for one of these materials suggests all the sites have C_{3v} symmetry, there may exist errors which mask C_{1v} symmetry. This complication, however, gives all the more reason to examine whether this approach can work. Fortunately, it will be shown that there are clear differences between particular sites.

5.2.2 Analysis

Magnetic splittings were analyzed using the procedures for peak fitting discussed in Chapter 3. When possible, several split peaks with shared levels were used to improve error estimates. Otherwise, individual split peaks were fitted. Polarizations were analyzed in two steps. First, amplitudes were determined for each of a number of polarization angles. For the data presented in this section, this was determined by simply summing the intensities near the center of a peak in CEES data for each polarization angle. In the next chapter, there will be a portion in which amplitudes are obtained by peak fitting. Second, these are fitted to the following function, with the parameters, a , b , and θ_0 , with the polarization angle represented by θ .

$$I(\theta) = (a + b \cos^2(\theta - \theta_0))$$

In the data presented here, the raw data and a fitted function of this form are shown together.

It should be pointed out that the scheme used to identify levels in a concise way here is duplicated from [44]. That is, the levels of ${}^4I_{\frac{15}{2}}$ are labeled with the letter A, followed by a positive integer starting from one, and ascending to eight, in order of increasing energy. For ${}^4I_{\frac{13}{2}}$, the letter is B, and the number cannot exceed seven, and for ${}^4I_{\frac{11}{2}}$, the letter is C, and the number cannot exceed six. Not all of these levels were observed for the materials and sites discussed in this chapter.

5.3 Erbium in Lithium Tantalate

Samples used for this work were single-crystal erbium doped stoichiometric lithium tantalate samples commercially available from the OXIDE Corporation.

5.3.1 Sites

While prior work on erbium doped lithium tantalate using CEES to identify sites does exist, [45] experiments showed that the list of identified sites was incomplete. Thus, an important first step was in identifying these sites by their transitions. Labels for sites here are largely taken from the labels in Ref. [45]. An additional five sites were assigned the letters I, J, K, L and M, without particular reasoning for the additional letter assignments.

As described in Chapter 3, the process of identifying sites consists of identifying grids within CEES data, that is, identifying sets of emission peaks that appear with particular excitation peaks, and vice versa. The first step is to identify these sites and their transitions. Tables of all transitions observed in data used for this work are included in Appendix A. Some peaks involving other multiplets for this system were reported in Ref. [45], as well as some of the same energy levels discussed here.

Next, level assignments are made. If we assume that states are roughly thermally populated within a multiplet before a transition, there should be a tendency for transitions to include the lowest levels of the starting multiplet. This implies different peaks may be seen in excitation and in emission for transitions between the same two multiplets. If two sets of transitions sharing one multiplet in common have similar differences in peaks, it is reasonable to ascribe those differences to level spacings in the shared multiplet. Using this reasoning, the levels are identified. For reasons which will be described later, some of the transitions are thought to involve interactions with phonons in the host lattice. Assuming that the erbium dopants are all in roughly similar incorporation environments, it is reasonable that similar level assignments should appear for all or most of the sites.

Comparison of different schemes suggested that the temperature was low enough

relative to the level spacings (that is, kT was smaller than the level spacings) that only the lowest level of the starting multiplet was involved in transitions. This greatly reduces the effort in the analysis to follow, because each set of transitions should only differ in one level. Appendix A also includes the result of fitting the observed transitions with a model for the energy levels.

5.3.2 Polarization

Site A

First, the site with the greatest emission intensity, here labeled site A, was examined in detail. As the majority site, it is easy to extract information from it, providing a standard of comparison for other sites. First, comparison of transitions for two excitation and emission schemes was done to verify a level assignment. Next, polarizations were determined by fitting intensities in spectra as a function of polarization angle using a simple model

$$I(\theta) = a + b^2 \cos^2(\theta + \theta_0)$$

Next, visual inspection of the fit and comparison of the magnitudes of a and b parameters were used to determine if a given transition was likely linearly polarized. After so doing, θ_0 was used to determine the precise angle. It should be noted that an offset in this angle is expected (due to issues such as imperfect mounting angles), but if this offset is constant, it is expected that polarized transitions within the same experiment should cluster around two angles orthogonal to one another.

In doing this, it usually appeared that the expected number of levels in several multiplets seemed to have behavior as predicted by group theory results for C_{3v} symmetry.

Comparison of results for excitation and emission transitions between the ${}^4I_{\frac{15}{2}}$ and ${}^4I_{\frac{11}{2}}$ multiplets and magnetic splitting results shown later suggested that six of these transitions could reasonably be ascribed to a transition involving the doubly

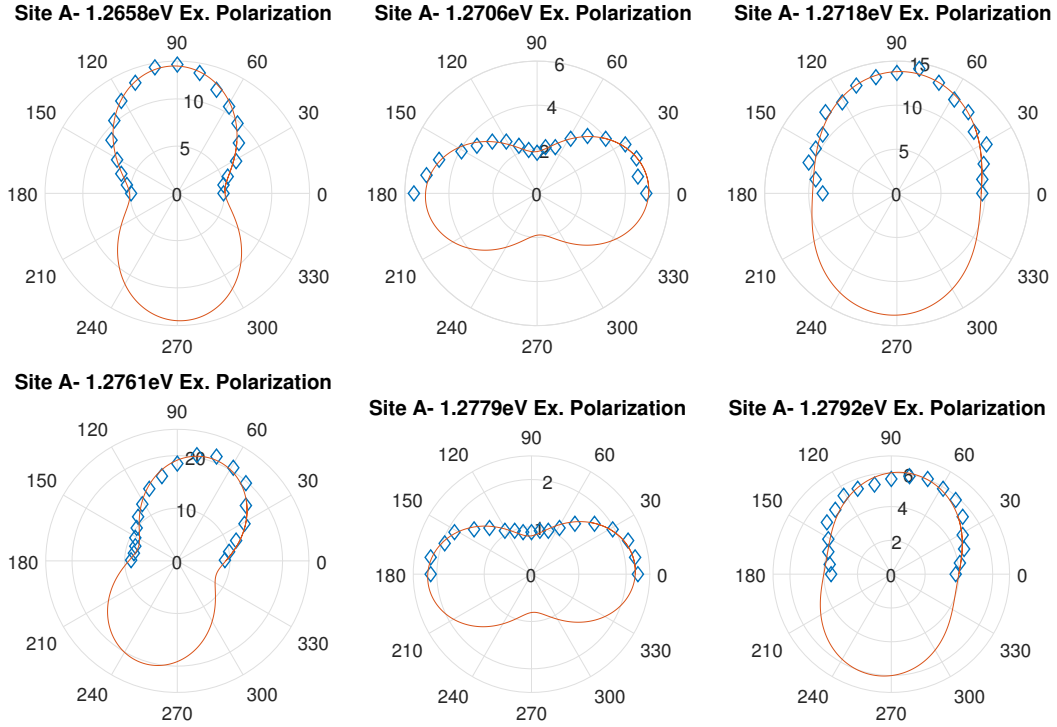


Figure 5.1: Fitted amplitudes as a function of excitation polarization for several transitions for Site A. 0 degrees corresponds to π polarization, assuming correct angling of the sample and setup.

Table 5.1: Expected electric dipole transition polarizations between levels of given crystal-field number for C_{3v} symmetry and half integer J .

	$\pm \frac{1}{2}$	$\pm \frac{3}{2}$
$\pm \frac{1}{2}$	$\pi \sigma$	σ
$\pm \frac{3}{2}$	σ	π

degenerate ground state. In excitation polarization, it appears that two such transitions are somewhat π polarized, and the remaining four somewhat σ polarized. Assuming C_{3v} symmetry, this suggests a crystal-field quantum number of $\frac{3}{2}$ for the ground state, and similar assignments for all the levels in the ${}^4I_{\frac{11}{2}}$ multiplet.

Similar differences in energy appear for four transitions in the ${}^4I_{\frac{11}{2}}$ to ${}^4I_{\frac{15}{2}}$ emission and the ${}^4I_{\frac{13}{2}}$ to ${}^4I_{\frac{15}{2}}$ emission. This suggests that these differences correspond

to the spacing of levels in the ${}^4I_{\frac{15}{2}}$ multiplet. Unfortunately, these results appear less strongly polarized than for the excitation polarizations already described, and not all levels of the multiplet are known, making it more difficult to judge the results.

If the assignment of $\pm\frac{1}{2}$ crystal-field quantum number is kept for the lowest level of ${}^4I_{\frac{11}{2}}$, it might be reasonable to claim that the next three observed levels in ${}^4I_{\frac{15}{2}}$ above the ground state should be assigned $\pm\frac{1}{2}$. However, from this evidence alone, it might be reasonable to claim that the first three levels could be assigned $\pm\frac{3}{2}$ due to a bias towards σ polarization. In fact, magnetic splitting results to be shown later suggest that the second doubly degenerate level of ${}^4I_{\frac{15}{2}}$ has negligible splitting under a perpendicular magnetic field, suggesting this $\pm\frac{3}{2}$ assignment. It is therefore difficult to make a definitive claim about these levels.

If only the emission starting from the ${}^4I_{\frac{11}{2}}$ level is considered, the implication is that the lowest level of that multiplet has a crystal-field number of $\pm\frac{1}{2}$, and the ground level has $\pm\frac{3}{2}$, which agrees with the results for the excitation involving this same upper multiplet. Continuing, the second doubly degenerate level is likely $\pm\frac{1}{2}$, and the third $\pm\frac{3}{2}$. This is complicated by the next emission, which appears to be π polarized. The spacing of this level from the highest energy transition appears in emission from ${}^4I_{\frac{11}{2}}$ and from ${}^4I_{\frac{13}{2}}$, suggesting that this transition still involves the same lowest level of ${}^4I_{\frac{11}{2}}$ as the first three. The group theory transitions cannot explain how three possibilities, π , σ , and both, are possible from two possible combinations of crystal-field numbers (as the first four emissions all involve the same starting level, implying the same starting crystal-field number, and there are only two possibilities for the final crystal-field number).

Still, knowing that none of the transitions have been completely σ or π polarized, it is not unreasonable to assert that this π biased polarization may be best interpreted as a transition for which both polarizations are allowed, but in this particular situation, the moment for π polarized transitions is greater.

Complicating the assignment of the emission peaks is the possibility of phonon assisted transitions. One phonon mode observed in Raman spectroscopy in LiTaO_3 with an energy of 140 cm^{-1} has been reported, which corresponds to the spacing of this emission (about 17 meV). [63] This corresponds to the difference between the

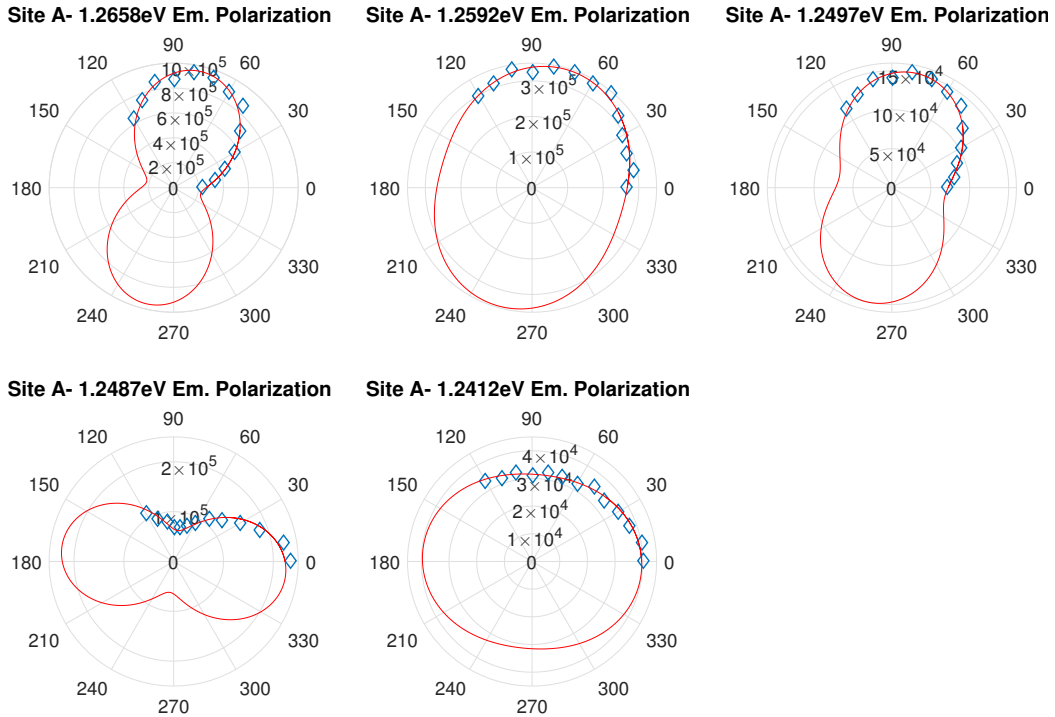


Figure 5.2: Fitted amplitudes as a function of emission polarization for several transitions for Site A, all thought to involve the lowest level of the ${}^4I_{\frac{11}{2}}$ multiplet, C1. 0 degrees corresponds to π polarization, assuming correct angling of the sample and setup.

highest energy emission and the peak that was just discussed. However, if this were due to a phonon assisted transition, it would be difficult to explain why identical spacings do not seem to appear for the other sites. Other phonon modes exist with energies close to other differences in emission energies, including some closely spaced near 25 meV. There exist prior results involving another emission scheme which when combined with emission peaks found in this work produces too many energy levels for the ground multiplet. [45] Clearly, not all of these transitions can be ascribed to a simple decay from one initial state to one of eight final states, so something in one of these assignments for higher levels of the ${}^4I_{\frac{15}{2}}$ multiplet must be wrong. For now, it is assumed that levels corresponding to spacings appearing

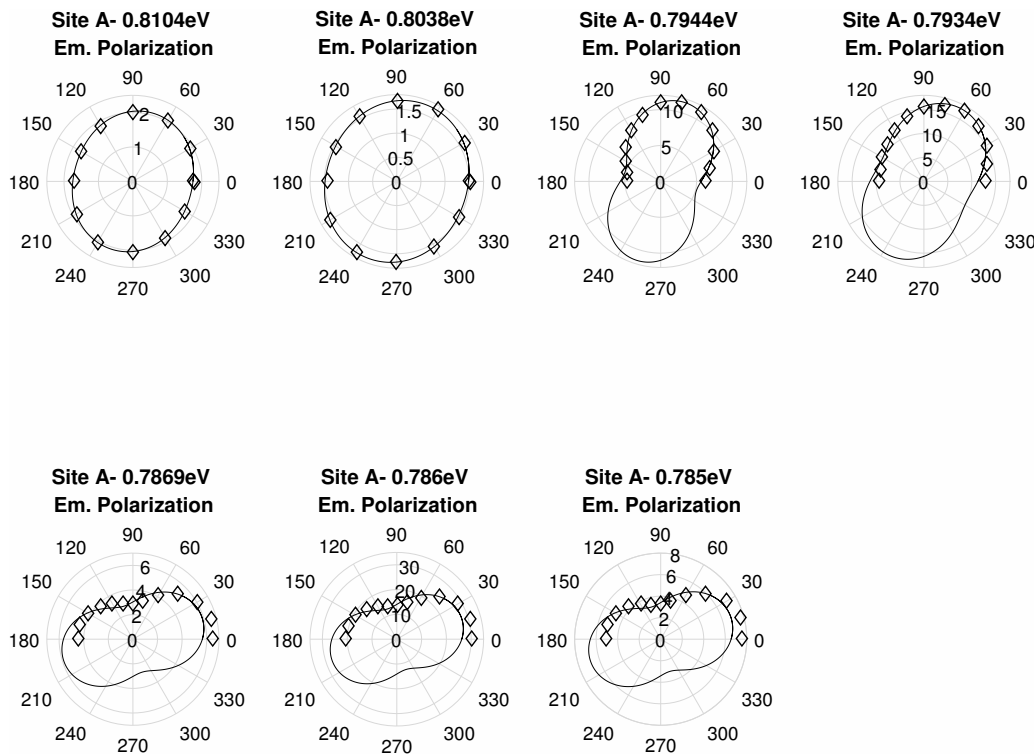


Figure 5.3: Fitted amplitudes as a function of emission polarization for several transitions for Site A, all thought to involve the lowest level of the ${}^4I_{\frac{13}{2}}$ multiplet, B1. 0 degrees corresponds to π polarization, assuming correct angling of the sample and setup.

in two or more emission schemes ending with the lowest energy multiplet are likely to be valid.

Other Sites

This led to the next step, applying this to the other sites. This initial level assignment also gave an initial guess for which levels had which crystal-field numbers, by assuming the energy levels should be roughly similar. Also, there is now the issue of determining which sites have a breakdown of rules prescribed by C_{3v} symmetry. Assuming the assignments for the ground state and the levels of ${}^4I_{\frac{11}{2}}$ are essentially

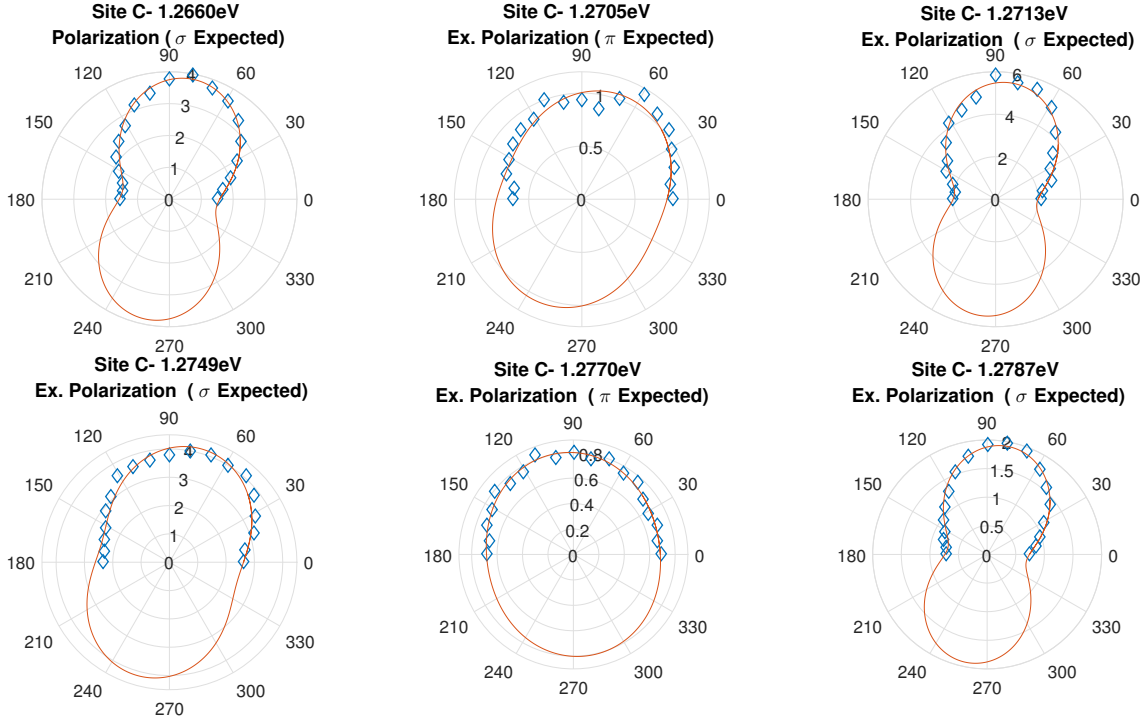


Figure 5.4: Fitted amplitudes as a function of excitation polarization for several transitions for site C. 0 degrees corresponds to π polarization, assuming correct angling of the sample and setup.

correct, we can compare how well different sites adhere to these rules. Ideally, a numeric measure should be made, but this is not straightforward to apply to every site, due to complications which will be discussed shortly.

Consider first, site C, which is easily separated from more closely spaced sites. Subjectively, the 980nm excitation polarization experiments, while still showing a difference between the second and fifth levels of ${}^4I_{\frac{11}{2}}$ and the others, seems to have resulted in a loss of the predominance of π polarization. The magnetic splittings associated with the ground state seem to suggest no perceptible splitting under a perpendicular magnetic field, so it seems unlikely that this is due to an entirely different ordering of levels. This suggests that site C is somehow much more perturbed from C_{3v} symmetry than site A is. The emission results look similar to the results

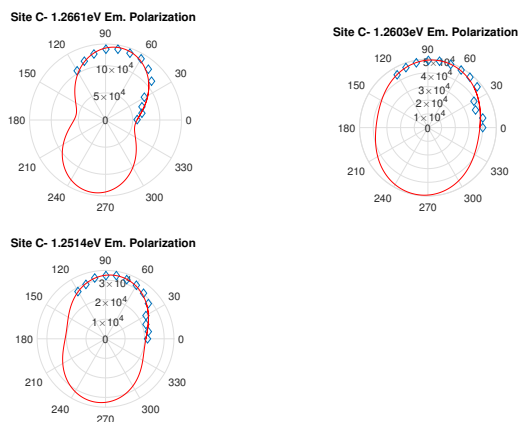


Figure 5.5: Fitted amplitudes as a function of emission polarization for several transitions for site C. 0 degrees corresponds to π polarization, assuming correct angling of the sample and setup.

for site A, but with the σ polarized emissions starting from the ${}^4I_{\frac{11}{2}}$ multiplet less pronounced.

Site B, however, shows no obvious π polarized excitations in the same experiment that revealed them for site A. Since all the transitions appear to be mostly σ polarized, it is not entirely obvious that C_{3v} symmetry applies. Magnetic results, also to be shown later, suggest negligible splitting for the ground state. This may suggest a significant departure from this symmetry. The emission from the ${}^4I_{\frac{11}{2}}$ ${}^4I_{\frac{15}{2}}$ multiplet transitions show less strongly polarized σ emissions, while the emissions starting from the ${}^4I_{\frac{13}{2}}$ multiplet look qualitatively almost identical to the site A results. This result, that sites B and C are likely of lower symmetry than site A, has been previously reported. [45]

Complicating the issue of developing a numeric measure is that some sites have not had enough transitions identified to determine whether they have the same polarizations as for site A. For example, only four excitation transitions for the ${}^4I_{\frac{15}{2}}$ to ${}^4I_{\frac{11}{2}}$ multiplets have been identified with site M. For several sites (D, H2, I, M), it is the case that one identified transition is biased towards π , but for whatever reason, a second excitation of this polarization has not been identified. For site H1,

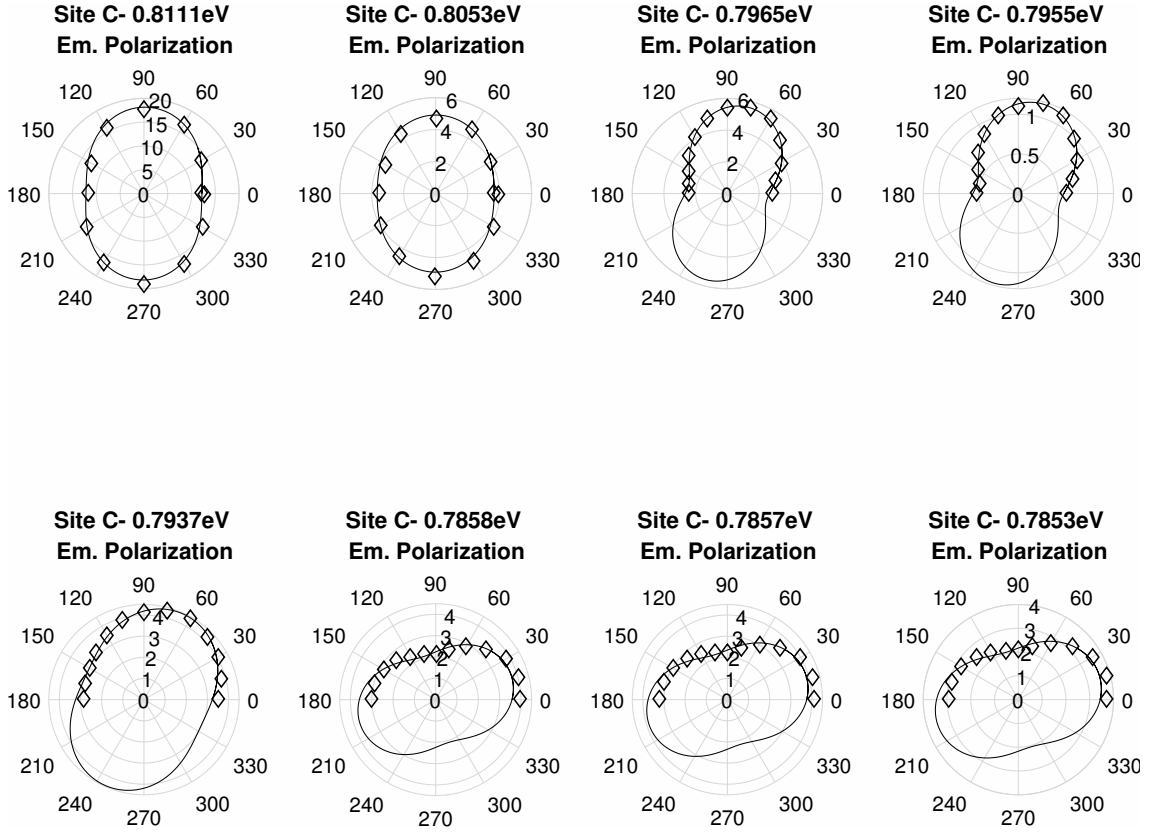


Figure 5.6: Fitted amplitudes as a function of emission polarization for several transitions for site C. 0 degrees corresponds to π polarization, assuming correct angling of the sample and setup.

it is unclear whether to include this in this category, due to problems of signal to noise ratio. It appears that the second peak is not observable in the data set used, creating ambiguity. Still, the remaining transitions for that site appear strongly σ polarized.

When considering the emissions between the same two multiplets for these four sites, all sites seem to follow a pattern of the highest energy emission being slightly more σ polarized, and the next lower energy ones being more even. Site H2 seems to be a bit more pronounced in this polarization for the first transition. Emission transition polarizations for ${}^4I_{\frac{13}{2}}$ to ${}^4I_{\frac{15}{2}}$ seem to show essentially the same result as

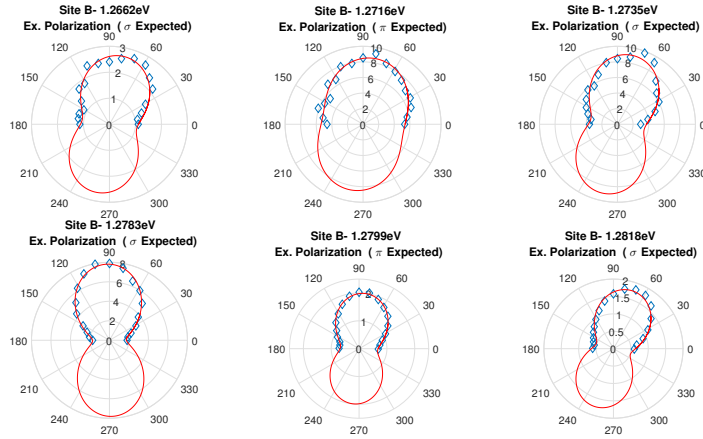


Figure 5.7: Fitted amplitudes as a function of excitation polarization for several transitions for site B. 0 degrees corresponds to π polarization, assuming correct angling of the sample and setup.

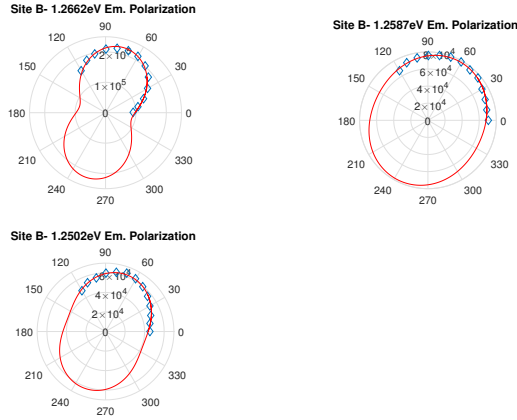


Figure 5.8: Fitted amplitudes as a function of emission polarization for several transitions for site B. 0 degrees corresponds to π polarization, assuming correct angling of the sample and setup.

for site A.

Several other sites (J, K, L) show similar results as for sites B and C. Specifically, the second and fifth excitation energies which were π polarized for site A appear to have little to no particular bias towards π polarization. Site K was not identified

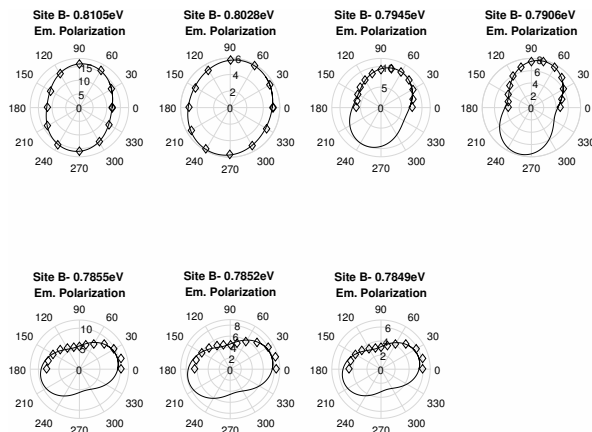


Figure 5.9: Fitted amplitudes as a function of emission polarization for several transitions for site B. 0 degrees corresponds to π polarization, assuming correct angling of the sample and setup.

in the emissions for the ${}^4I_{\frac{11}{2}}$ to ${}^4I_{\frac{15}{2}}$ multiplet decay, but these results for site J and L also show little means of distinction between them. Emissions from ${}^4I_{\frac{13}{2}}$ to ${}^4I_{\frac{15}{2}}$ also show little distinction.

Site E appears to be an intermediate case, that is, while one excitation transition (for ${}^4I_{\frac{15}{2}}$ to ${}^4I_{\frac{11}{2}}$) is clearly π polarized, a second transition appears with a distinct polarization that is not obviously π polarized, but appears to be polarized differently from the σ polarized excitations. A numeric measure which relies on examining the two π polarized transitions would have trouble distinguishing this site from site D because only one such transition has been identified for site D. The highest energy emission observed for ${}^4I_{\frac{11}{2}}$ to ${}^4I_{\frac{15}{2}}$ is more σ polarized than for some other sites, but generally, the emission transition data looks much more similar to that for the other sites here.

So far, just from the excitation polarizations (and assuming similar crystal-field number assignments for all the sites), site A appears to most obviously adhere to expectations for C_{3v} symmetry. Sites D, E, H1, H2, I, and M may also adhere fairly well, with some of those having uncertainties as discussed. Sites B, C, J, K, and L appear to adhere poorly, in terms of lacking clear π polarized excitations, and

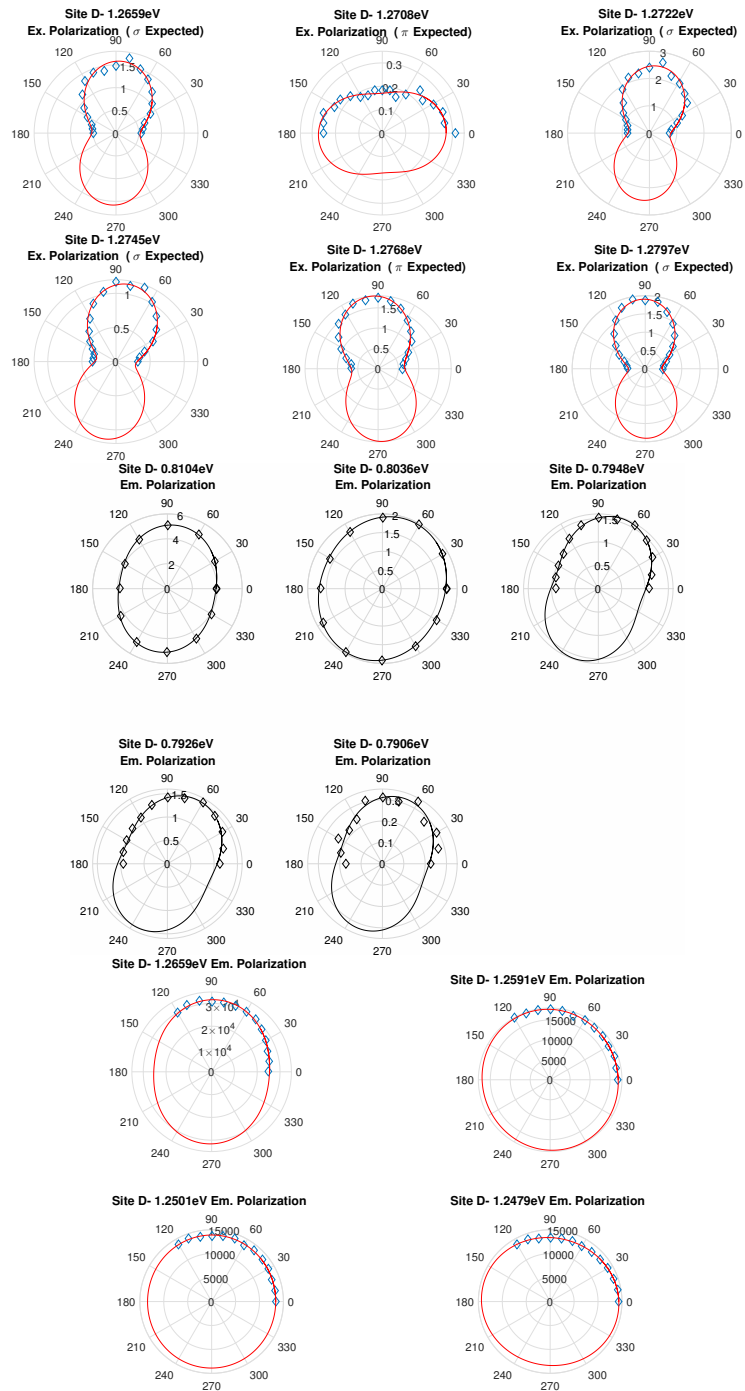


Figure 5.10: Fitted amplitudes as a function of polarization for several transitions for site D. 0 degrees corresponds to π polarization, assuming correct angling of the sample and setup.

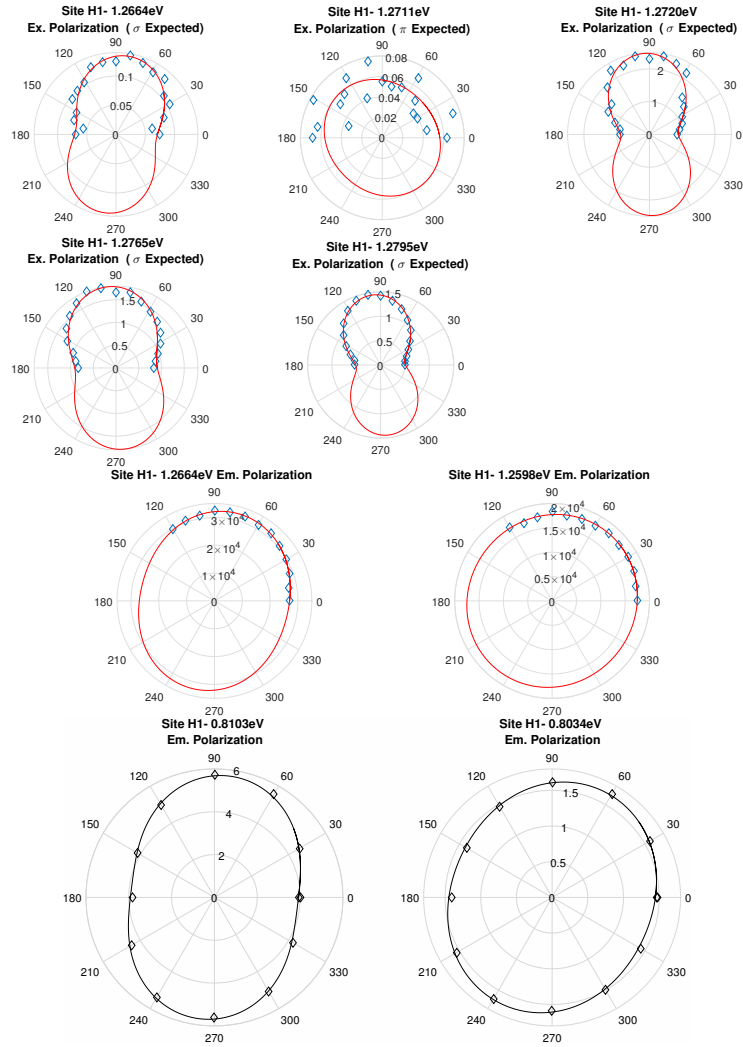


Figure 5.11: Fitted amplitudes as a function of polarization for several transitions for site H1. 0 degrees corresponds to π polarization, assuming correct angling of the sample and setup.

having several more evenly polarized transitions.

For the emission data, it appears that the highest energy emission observed for ${}^4I_{\frac{11}{2}}$ to ${}^4I_{\frac{15}{2}}$ varies somewhat between sites, but that most of the polarizations for the two emission schemes look qualitatively very similar. The most distinguishing characteristics appear to be the two excitation transitions from ${}^4I_{\frac{15}{2}}$ to ${}^4I_{\frac{15}{2}}$ which

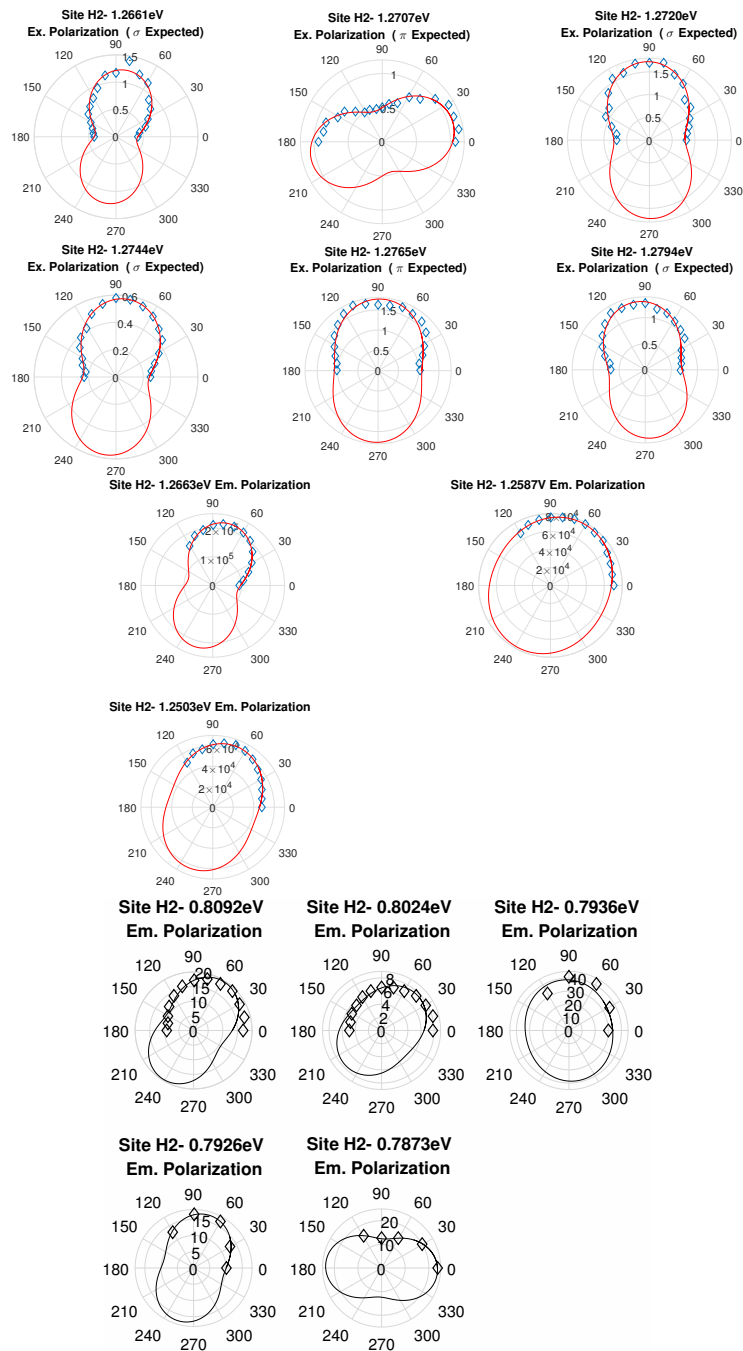


Figure 5.12: Fitted amplitudes as a function of polarization for several transitions for site H2. 0 degrees corresponds to π polarization, assuming correct angling of the sample and setup.

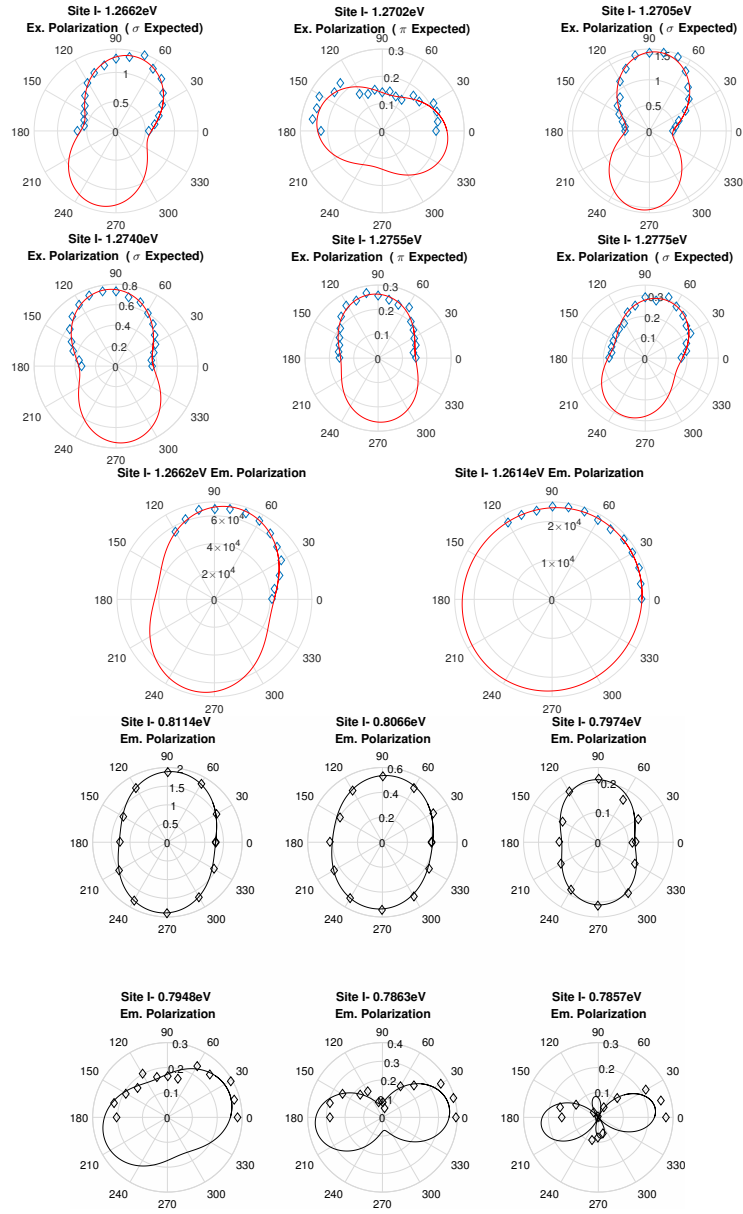


Figure 5.13: Fitted amplitudes as a function of polarization for several transitions for site I. 0 degrees corresponds to π polarization, assuming correct angling of the sample and setup.

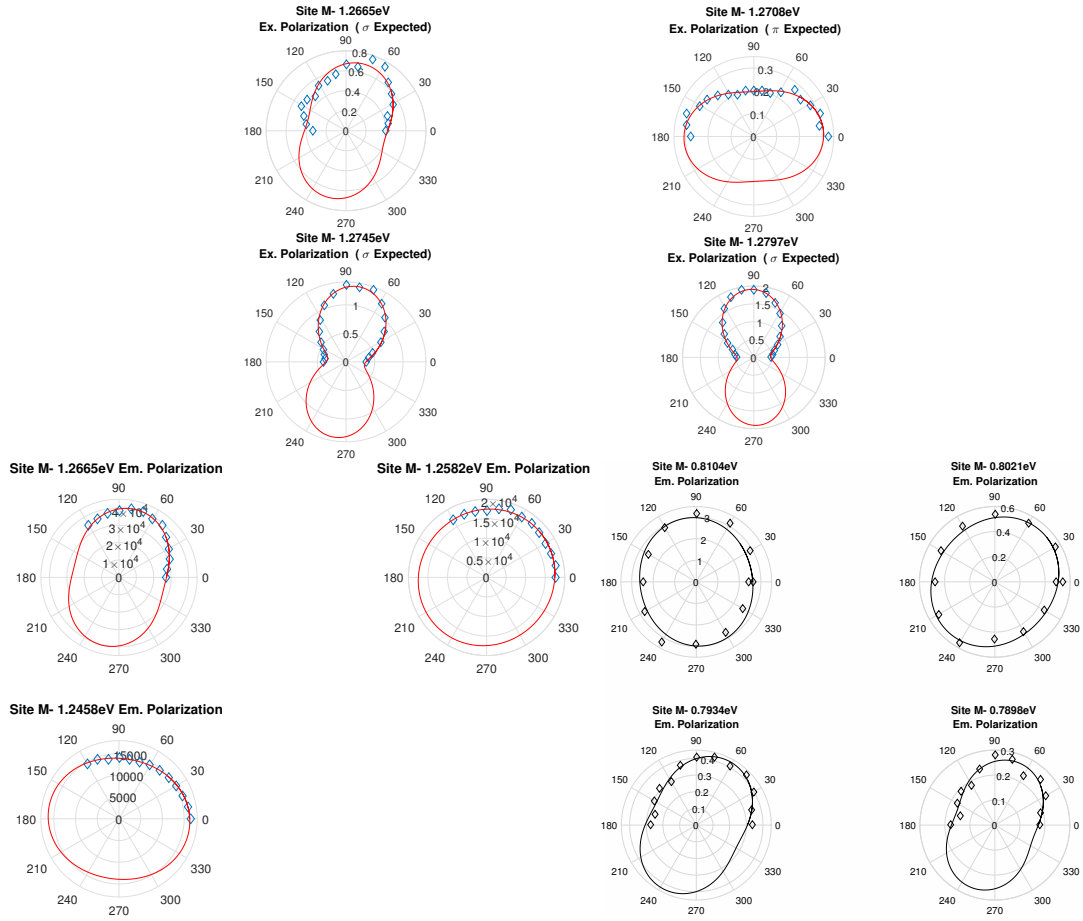


Figure 5.14: Fitted amplitudes as a function of excitation polarization for several transitions for site M. 0 degrees corresponds to π polarization, assuming correct angling of the sample and setup.

are expected to be π polarized, and the aforementioned σ polarized emission involving those same multiplets. This survey has also given information on crystal-field assignments and the identification of several possible phonon-coupled transitions.

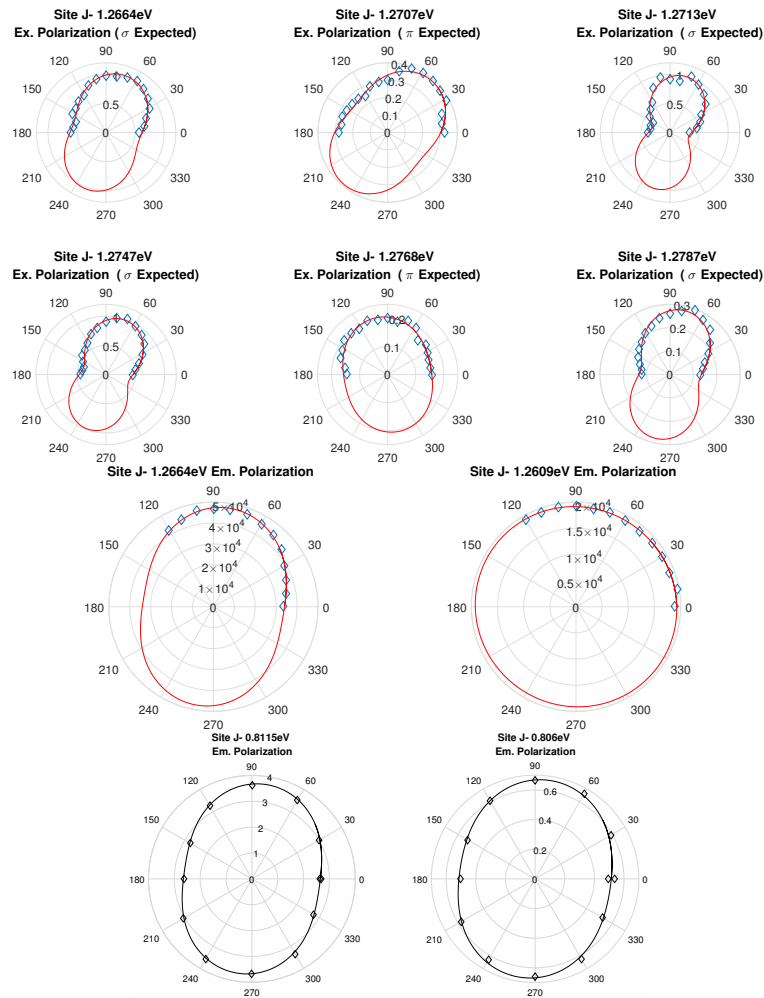


Figure 5.15: Fitted amplitudes as a function of polarization for several transitions for site J. 0 degrees corresponds to π polarization, assuming correct angling of the sample and setup.

Direct Comparison

Despite the aforementioned difficulties, one attempt at a comparison of degree symmetry of incorporation sites was made by comparing a number of polarization amplitude results within the same figure. Because all the sites have different relative intensities, this required a scaling. One particular (sometimes) π polarized peak

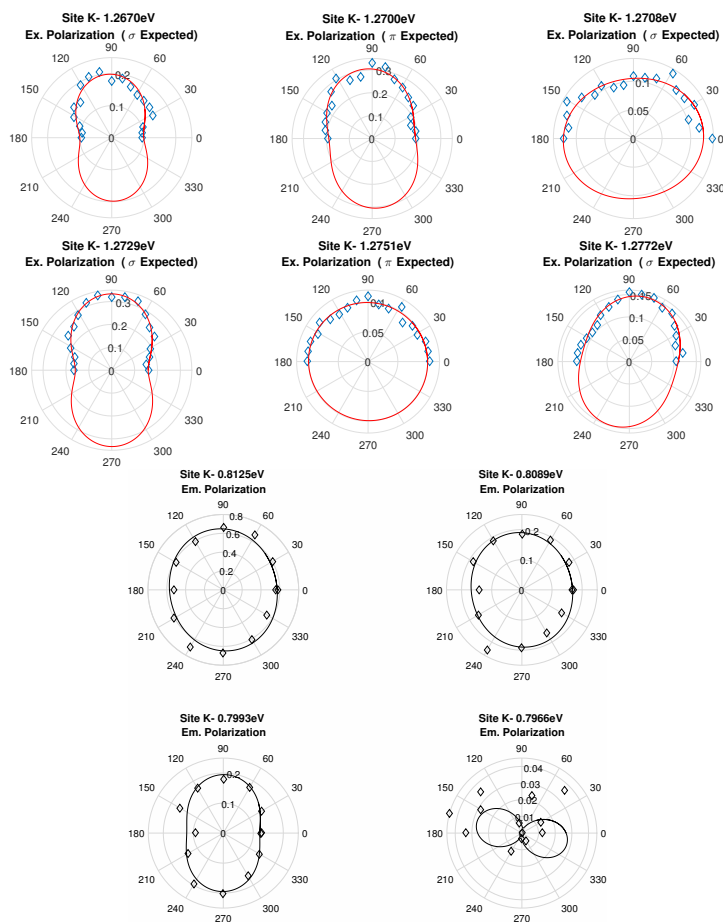


Figure 5.16: Fitted amplitudes as a function of polarization for several transitions for site K. 0 degrees corresponds to π polarization, assuming correct angling of the sample and setup.

seemed to be identifiable for all the peaks, corresponding to a transition from the ground state to the second doubly degenerate level of ${}^4I_{11/2}$. While some information can be gleaned from examination of these plots, significant overlap made this difficult.

This led to an alternate approach. Using the fits of the polarization data, the ratio of the values these fitted functions give for 0 and 90 degrees was used as a measure of how π polarized the transition was. It is not entirely clear how these

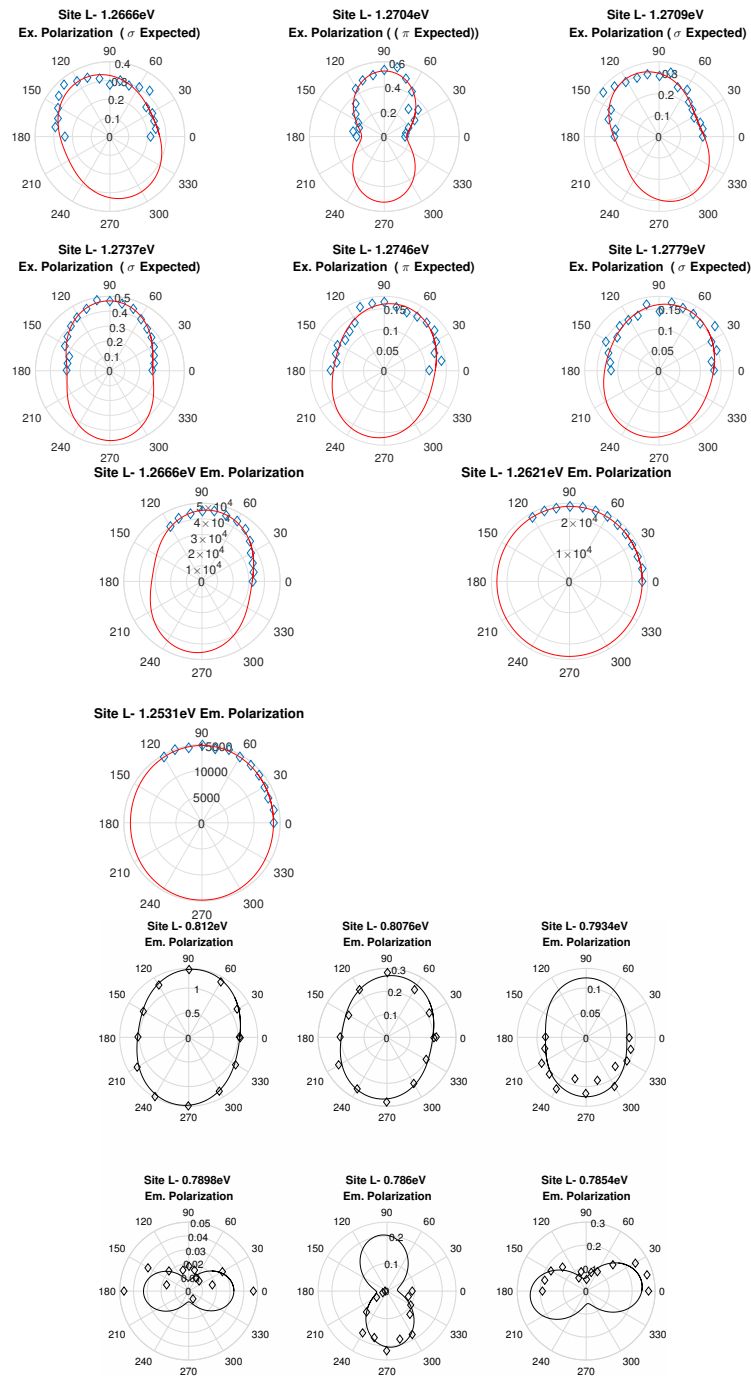


Figure 5.17: Fitted amplitudes as a function of polarization for several transitions for site L. 0 degrees corresponds to π polarization, assuming correct angling of the sample and setup.

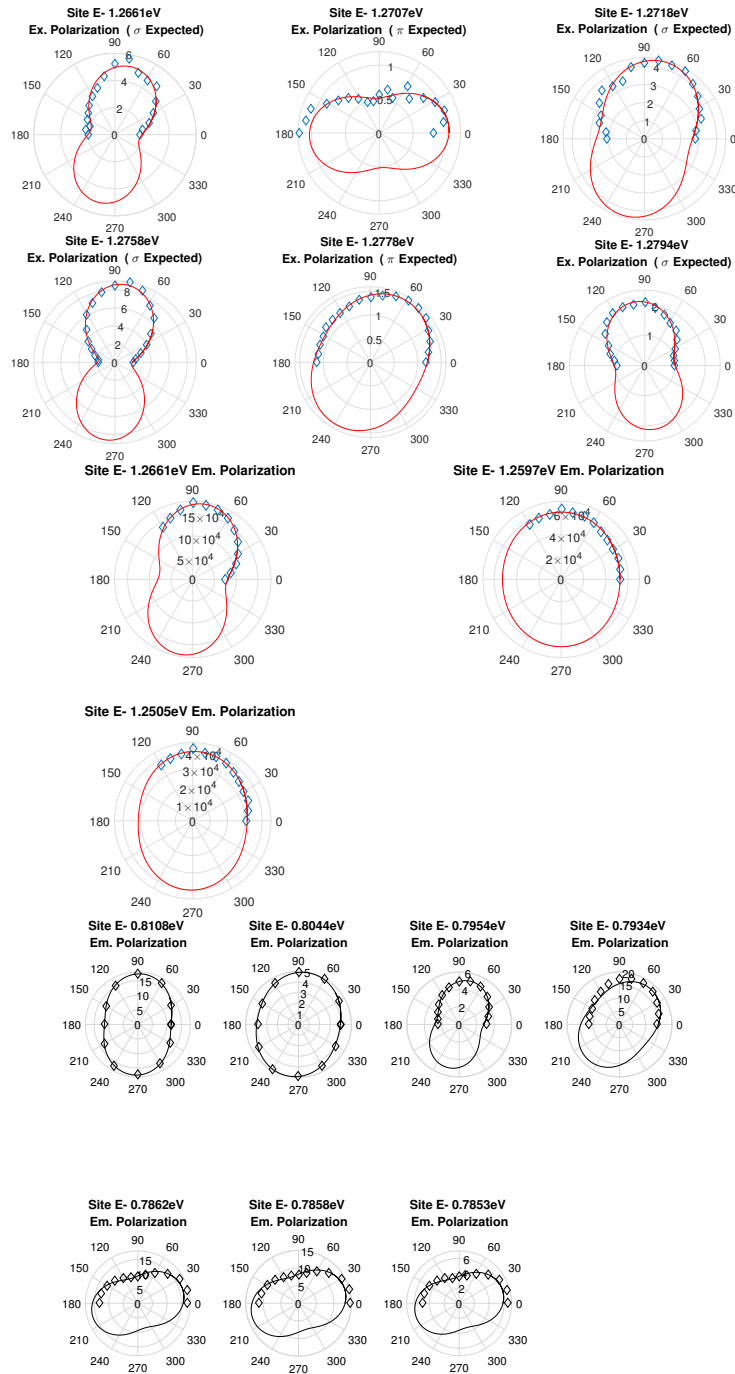


Figure 5.18: Fitted amplitudes as a function of polarization for several transitions for site E. 0 degrees corresponds to π polarization, assuming correct angling of the sample and setup.

Comparison of Scaled Polarization Plots for Second Excitation Energy

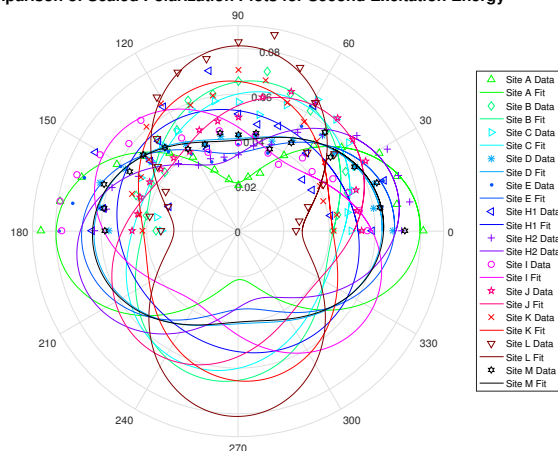


Figure 5.19: These show scaled intensity as a function of excitation polarization angle for a transition believed to be the same transition for all identified sites. 0 degrees corresponds to π polarization, assuming correct angling of the sample and setup.

differences correspond to particular breakings of symmetry. This approach showed, for example, that site E has the third greatest degree of π polarization (out of 12) for one expected π polarized excitation peak, but had the least degree for the other such excitation peak. However, this does indicate that site A is clearly distinguishable from the other sites, and that site B and C appear to be sites with significant departures from the symmetry of site A.

Table 5.2: Ratios of π to σ polarization for two excitation peaks (involving the ground state and levels of ${}^4I_{\frac{11}{2}}$) found to be predominantly π polarized for site A.

Site	Ratio (C2 to A1)	Rank	Ratio(C5 to A1)	Rank
A	$3.75 \pm .25$	1	$4.60 \pm .33$	1
B	$.638 \pm .028$	10	$.349 \pm .006$	9
C	$.770 \pm .050$	9	$.404 \pm .004$	7
D	$1.554 \pm .058$	6	$.380 \pm .017$	8
E	$2.00 \pm .21$	3	$.229 \pm .006$	10
H1	$1.00 \pm .14$	7		
H2	$2.06 \pm .11$	2	$.552 \pm .020$	5
I	$1.76 \pm .19$	4	$.520 \pm .014$	6
J	$.923 \pm .032$	8	$.827 \pm .033$	4
K	$.633 \pm .024$	11	$.888 \pm .035$	2
L	$.346 \pm .029$	12	$.888 \pm .045$	2
M	$1.600 \pm .083$	5		

5.3.3 Magnetic Splittings

As mentioned earlier, a crystal-field number of $\frac{3}{2}$ for C_{3v} symmetry suggests the level should not split under a magnetic field applied perpendicular to the c-axis of the crystal, assuming no higher order terms. For symmetry determination then, the perpendicular field results are likely more important. However, also having the parallel field splittings permits determination of effective g factors for the levels as a function of field angle, and can give insight into the makeup of the states in terms of m_j labeled states. This, in turn, can give insight into the crystal-field numbers. For example, a parallel effective g factor of roughly 15 for a doubly degenerate level in a multiplet with $J = \frac{15}{2}$ suggests that the two levels must be primarily states of $m_j = \pm \frac{15}{2}$, if the Landé g factor for this multiplet is one. However, it is roughly 1.09, suggesting that if the effective g factor is measurably greater than 14.2 (for $\pm \frac{13}{2}$) this reasoning still suggests the state contains $m_j = \pm \frac{15}{2}$. This would also suggest that this level must have a crystal-field number of $\frac{3}{2}$ for C_{3v} symmetry (because $m_j = \pm \frac{15}{2}$ states are only included in the makeup of $\frac{3}{2}$ crystal-field number levels).

As discussed in Chapter 2, the splittings are expected to have the following behavior as a function of angle between the c-axis and the applied magnetic field:

$$g_{eff}(\theta) = \sqrt{g_{\parallel}^2 \cos^2(\theta) + g_{\perp}^2 \sin^2(\theta)}$$

$$\Delta E = \mu_B g_{eff} B$$

In order to fit these splittings, a number of techniques were used. For most of the results, spectra were extracted from CEES data, and fitted, applying a few restrictions. Transitions splitting from the same original transition were forced to have identical widths. Initial examinations of individual split peaks were used to help confirm the level assignments already discussed. Having done this, the splittings were fitted using the splittings of the original levels as parameters, reducing the number of parameters. For example, if three transitions share a level, rather than having two parameters describing each of the three peaks, for a total of six, only four are needed, describing splittings of each of the original doubly degenerate levels. In some cases, to handle issues of overlapping peaks, a simple model for

describing portions of CEES data was used. In this model, the data is modeled as a product of functions describing the peaks along the excitation and emission axes, with the addition of a parameter approximating the relation between the emission and excitation energies as linear (handling the case of peaks that "tilt" in the CEES data). Issues of signal to noise ratio, especially in the case of overlapping peaks from different sites, and peak widths, limited the amount of data which could be extracted, and much of the fitting was individually adjusted for each case.

A large number of splittings for a variety of sites, field angles, and energy levels were determined, and are presented in Appendix A. For some levels, a series of splittings were determined for each of five angles between the c-axis and the magnetic field. Effective g factors listed in the tables in this chapter were determined from direct measurement, rather than interpolating. It is difficult to discern between a level that does not split and a level with a small splitting. Even with perfect ability to discern this from spectra, errors in angles and higher-order interactions may cause splittings in a level expected to have no splittings from C_{3v} symmetry.

Site A

Following the same idea as in the previous portion on polarization, site A is first examined in an attempt to determine what might constitute a typical site. Recall that the polarization data suggested that this site is a good candidate for exhibiting C_{3v} symmetry. Unfortunately, this site has the issue of what appears to be an energy transfer with site B. Specifically, when either site A or site B is excited, a less intense emission is observed for the other site. While this can be managed for determining which transition is from which site (by observing which emission is stronger for a given excitation), it is not easy to remove the closely spaced peaks from the site of less interest for fitting individual spectra. Thus, plots in this section show sites A and B simultaneously fitted.

For a parallel field, it is apparent that sharp peaks seem to split quite visibly. There are issues in resolving splittings for broader, dimmer peaks. For the perpendicular field case, it is difficult to identify any peaks sufficiently split to enable

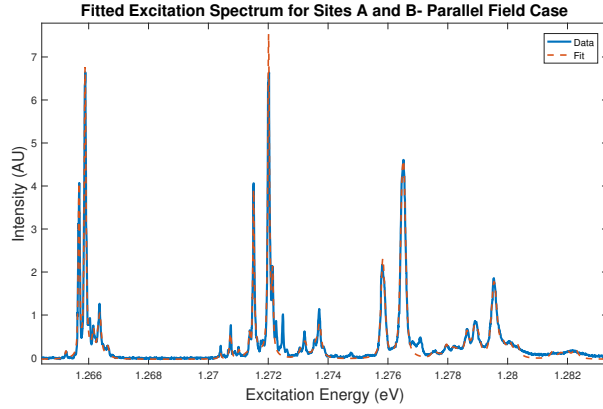


Figure 5.20: Fitted Zeeman split peaks from an excitation spectrum for sites A and B.

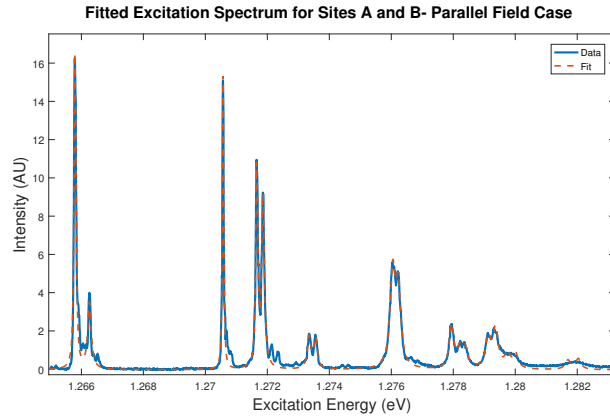


Figure 5.21: Fitted Zeeman split peaks from an excitation spectrum for sites A and B.

determination of the splittings for several levels. As discussed in Appendix A, an additional data set from a run with a higher field magnitude (estimated to be roughly 1.25T) yielded similar difficulties in determining a splitting for the ground state.

There was originally an intent to determine some of these levels by fitting splittings as a function of magnetic field angle. However, for levels for which splittings could be found for all the field angles selected, it was found that issues of field magnitude may render this difficult to perform with much precision. As discussed

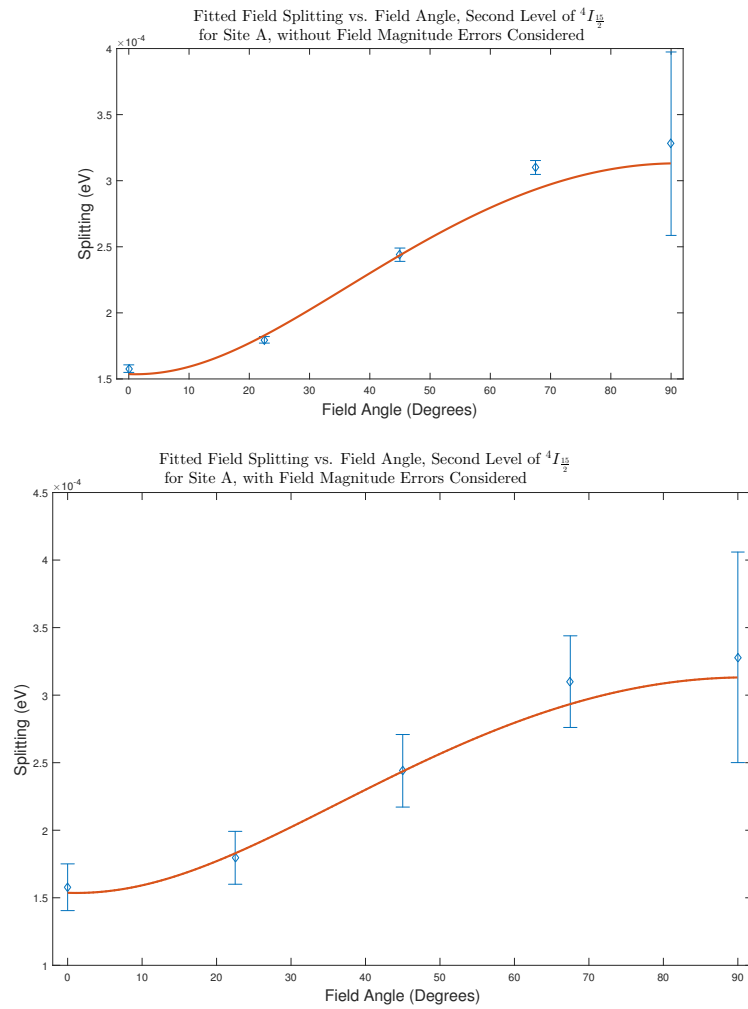


Figure 5.22: Fitting of splitting of a level for site A as a function of magnetic field angle relative to the c -axis. Error bars represent a 95 percent confidence interval from the fitting algorithms used, and in the second case, an inclusion of an estimate of possible field magnitude error.

in Chapter 6, nonlinear effects would also affect this, meaning that trying to solve these issues with larger magnetic field strengths may lead to other issues.

All Sites

To summarize the data obtained for all the sites, rather than presenting figures of plots, a table of determined effective g factors is given. Errors given are derived from 95 percent confidence intervals from the fitting algorithms used. It can be seen that many of the effective g factors for the same level from different sites are within the listed error of one another. This suggests similar levels for all the sites. It can be argued that the error within the same measurement set is less than the errors presented here (which includes an estimate of 8mT error in the magnetic field). It is suggested that if the reader wishes to examine these differences more closely, the appendix includes splittings in units of meV, without this extra source of error considered.

Generally, the splittings observed seem to confirm the crystal-field number assignments suggested by the polarization, but there are significant shortcomings due to the incompleteness of the data. For example, no splittings for the ground state were found in the data for the perpendicular field orientation for any site. Visually, they were all similar to the plots shown for site A, in that no splittings could be seen by eye. Ideally, if this state, as suggested by results so far, has a $\frac{3}{2}$ crystal-field number, its splitting may give a good measure of the deviation from C_{3v} symmetry. Interestingly, it appears that the lowest energy levels in each of the lowest three multiplets are predominantly of the character of the largest m_j states for each multiplet. This is in contrast to the majority site for erbium in gallium nitride, whose effective g factors are discussed in Chapter 6.

Table 5.3: Shown are fitted g factors for sites A-D.

Site		A	B	C	D
Ground ($A1$)	g_{\parallel}	15.04 ± 0.64	15.04 ± 0.64	14.67 ± 0.64	14.75 ± 0.64
	g_{\perp}	0?	0?	0?	0?
Second ${}^4I_{\frac{15}{2}}$ ($A2$)	g_{\parallel}	3.60 ± 0.44	4.12 ± 0.38	3.52 ± 0.33	3.85 ± 0.33
	g_{\perp}	7.67 ± 0.94	7.56 ± 0.56		7.8 ± 2.0
First ${}^4I_{\frac{13}{2}}$ ($B1$)	g_{\parallel}	12.65 ± 0.59	13.26 ± 0.62	12.31 ± 0.60	12.44 ± 0.59
First ${}^4I_{\frac{11}{2}}$ ($C1$)	g_{\parallel}	10.20 ± 0.82	10.10 ± 0.64	10.08 ± 0.85	
	g_{\perp}				
Second ${}^4I_{\frac{11}{2}}$ ($C2$)	g_{\parallel}			5.6 ± 1.3	
	g_{\perp}			2.05 ± 0.65	
Third ${}^4I_{\frac{11}{2}}$ ($C3$)	g_{\parallel}	3.32 ± 0.30	3.51 ± 0.31	2.76 ± 0.31	
	g_{\perp}	4.87 ± 0.36		4.46 ± 0.67	
Forth ${}^4I_{\frac{11}{2}}$ ($C4$)	g_{\parallel}		1.34 ± 0.23		
	g_{\perp}	4.12 ± 0.36	4.05 ± 0.68	4.58 ± 0.76	
Fifth ${}^4I_{\frac{11}{2}}$ ($C5$)	g_{\parallel}		2.90 ± 0.88	3.1 ± 1.2	
	g_{\perp}				
Sixth ${}^4I_{\frac{11}{2}}$ ($C6$)	g_{\parallel}		1.6 ± 2.1	1.3 ± 2.5	
	g_{\perp}	6.56 ± 0.44		4.29 ± 0.93	

Table 5.4: Shown are fitted g factors for sites E, H1, H2, and I.

Site		E	H1	H2	I
Ground ($A1$)	g_{\parallel}	14.39 ± 0.62	14.05 ± 0.64	14.91 ± 0.82	15.21 ± 0.82
	g_{\perp}	0?			0?
Second ${}^4I_{\frac{15}{2}}$ ($A2$)	g_{\parallel}	3.92 ± 0.48	3.71 ± 0.35	3.70 ± 0.49	3.66 ± 0.33
	g_{\perp}				
First ${}^4I_{\frac{13}{2}}$ ($B1$)	g_{\parallel}	12.01 ± 0.60	12.03 ± 0.60	12.93 ± 0.78	12.14 ± 0.61
	g_{\perp}	1.69 ± 0.23			
First ${}^4I_{\frac{11}{2}}$ ($C1$)	g_{\parallel}	10.42 ± 0.83			
	g_{\perp}				
Second ${}^4I_{\frac{11}{2}}$ ($C2$)	g_{\parallel}				
	g_{\perp}				
Third ${}^4I_{\frac{11}{2}}$ ($C3$)	g_{\parallel}				
	g_{\perp}	4.28 ± 0.36			4.28 ± 0.43
Forth ${}^4I_{\frac{11}{2}}$ ($C4$)	g_{\parallel}				
	g_{\perp}	3.92 ± 0.36			4.2 ± 1.1
Fifth ${}^4I_{\frac{11}{2}}$ ($C5$)	g_{\parallel}				
	g_{\perp}				
Sixth ${}^4I_{\frac{11}{2}}$ ($C6$)	g_{\parallel}				
	g_{\perp}	5.75 ± 0.92			

Table 5.5: Shown are fitted g factors for sites J-M.

Site	J	K	L	M
Ground ($A1$)	g_{\parallel}	13.68 ± 0.93	15.17 ± 0.78	15.31 ± 0.65
	g_{\perp}		0?	0?
Second ${}^4I_{\frac{15}{2}}$ ($A2$)	g_{\parallel}	5.43 ± 0.41	4.02 ± 0.95	4.2 ± 1.8
	g_{\perp}	7.39 ± 0.45	7.32 ± 0.99	4.61 ± 0.36
First ${}^4I_{\frac{13}{2}}$ ($B1$)	g_{\parallel}	11.10 ± 0.66	11.20 ± 0.91	12.47 ± 0.91
	g_{\perp}			
First ${}^4I_{\frac{11}{2}}$ ($C1$)	g_{\parallel}		11.62 ± 0.61	
	g_{\perp}			
Second ${}^4I_{\frac{11}{2}}$ ($C2$)	g_{\parallel}			
	g_{\perp}			
Third ${}^4I_{\frac{11}{2}}$ ($C3$)	g_{\parallel}			
	g_{\perp}	4.74 ± 0.69		
Forth ${}^4I_{\frac{11}{2}}$ ($C4$)	g_{\parallel}			
	g_{\perp}	4.20 ± 0.59		
Fifth ${}^4I_{\frac{11}{2}}$ ($C5$)	g_{\parallel}			
	g_{\perp}			
Sixth ${}^4I_{\frac{11}{2}}$ ($C6$)	g_{\parallel}			
	g_{\perp}			

5.3.4 Polarization of Zeeman Split Peaks

Before continuing, some discussion of polarizations of transitions under the influence of an applied magnetic field is merited.

5.3.5 Expected Behavior

Recall the results derived for the half-integer J case for C_{3v} symmetry for electric dipole allowed transitions.

	$E_{\frac{3}{2}}$	$E'_{\frac{3}{2}}$	$E_{\frac{1}{2}}$
$E_{\frac{3}{2}}$	π		σ
$E'_{\frac{3}{2}}$		π	σ
$E_{\frac{1}{2}}$	σ	σ	$\pi\sigma$

If the $E_{\frac{3}{2}}$ and $E'_{\frac{3}{2}}$ representations are truly treated as components of a single representation, nothing in the above suggests polarizations should change. However, if the addition of a magnetic field is treated as a perturbing symmetry, the symmetry group, C_{3v} , becomes more and more incorrect as the effects of the magnetic field become more significant than those of the crystal-field. Thus, whether these polarization rules still apply after application of a magnetic field is dependent on the relative magnitudes of the crystal-field and magnetic field terms in the Hamiltonian.

Site A in Erbium Doped Lithium Tantalate

Only the site which seemed to best obey selection rules for C_{3v} symmetry was considered, on the grounds that the selection rules for the others are less well understood.

Somewhat unsurprisingly, the polarization plots for the split peaks appear very similar to the plots before the splitting, which were discussed earlier in this chapter. The magnetic fields are believed to be the same as the fields used for calculating Zeeman splittings for this material earlier in this chapter (0.75T). If anything, some of the transitions under the influence of a magnetic field appear more polarized than was the case without a magnetic field. Unfortunately, because the setup for this

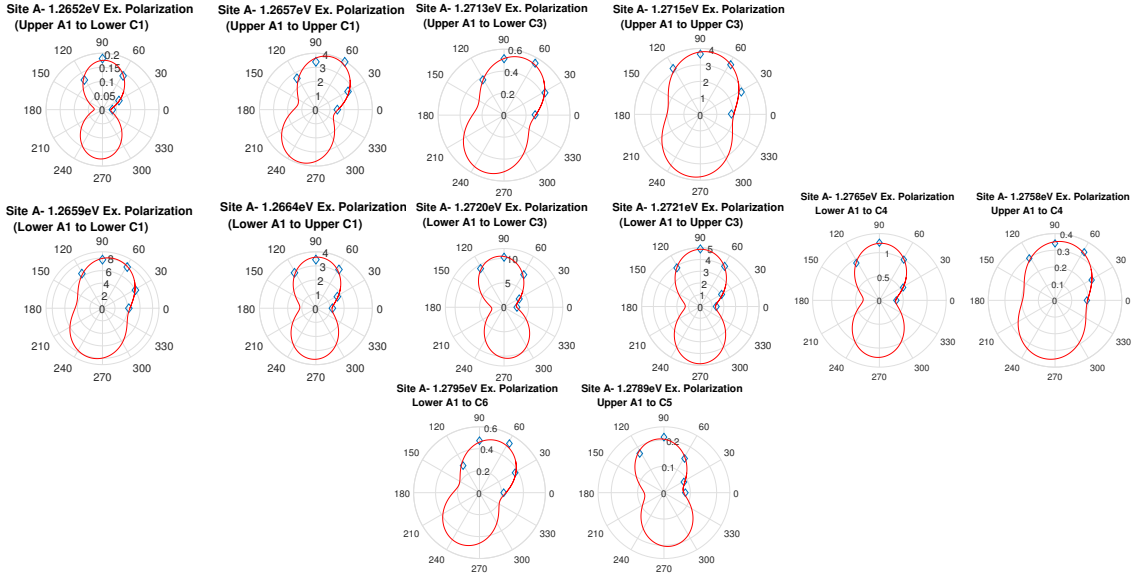


Figure 5.23: Fitted excitation polarizations for the Zeeman split transitions for a field parallel to the c -axis. This is for the lowest doubly degenerate level of ${}^4I_{15/2}$ to the lowest doubly degenerate level of ${}^4I_{11/2}$. The shown transitions were σ polarized in the zero magnetic field case.

experiment and the experiments which produced the plots in the previous chapter may be slightly different, a true comparison may be flawed. There were difficulties in correctly normalizing for variations in power as a function of excitation polarization angle.

The transitions shown here were selected for their having a clear π or σ bias in the zero field data. Some levels did not split appreciably, and so only two, rather than four peaks are shown. If anything, some of the peaks appear more strongly polarized than in the zero field case.

It should be pointed out that for the magnetic fields used for this portion, there should not be significant mixing of the states considered here. The data appears to confirm that the character of the states is roughly the same. This implies that for this magnetic field magnitude, the C_{3v} symmetry of the crystal-field term is still a dominating influence on the selection rules.

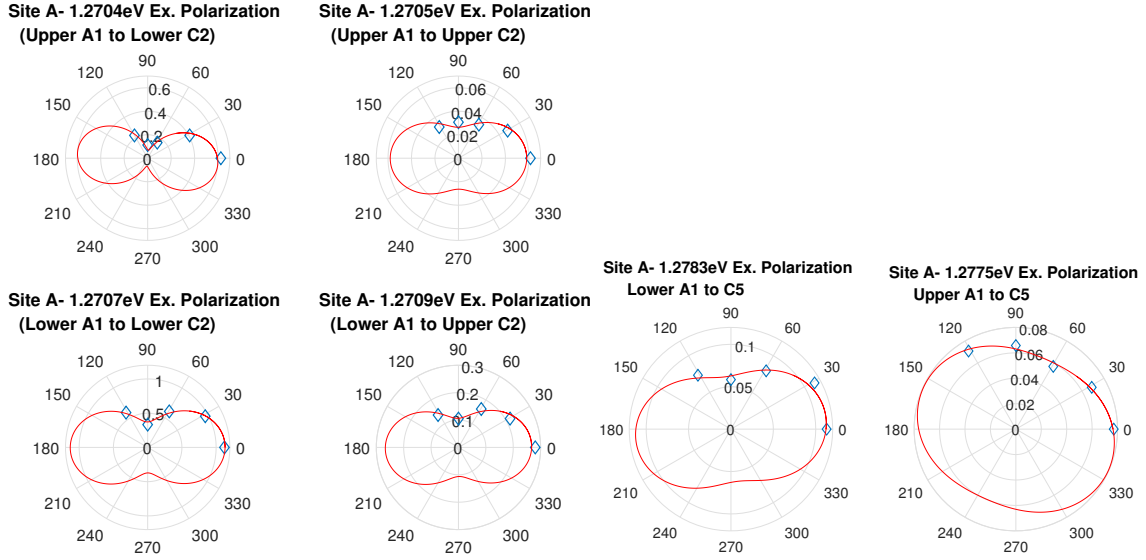


Figure 5.24: Fitted excitation polarizations for the Zeeman split transitions for a field parallel to the c-axis. This is for the lowest doubly degenerate level of ${}^4I_{\frac{15}{2}}$ to the second lowest doubly degenerate level of ${}^4I_{\frac{11}{2}}$. The shown transitions were π polarized in the zero magnetic field case.

5.3.6 Conclusions

Based on the polarization and magnetic splitting results, a table of crystal-field numbers was developed. If a level showed appreciable magnetic splitting, it was inferred that that level was assigned to $\pm\frac{1}{2}$. If the parallel effective g factor for a level suggested the level was mostly made up of an m_j state with $m_j = \pm j$ for the multiplet, the assignment that would be given for that m_j state was used. C_{3v} symmetry was assumed correct. The polarization results were already discussed. It should be noted that site A was used in particular to develop these assignments.

Imperfect polarization results may suggest that none of the sites has perfect C_{3v} symmetry, but evidence suggests site A is possibly the site that adheres best to this symmetry. As suggested in prior work, charge compensation, balancing the +3 charge of the erbium ion in the host crystal, likely prevents perfect symmetry. [45] Differences in symmetry are likely due to whether this compensation occurs in a

way that preserves C_{3v} symmetry, such as a change along the c-axis of the crystal immediately next to the dopant.

Table 5.6: Shown are suggested crystal-field number assignments

Level	μ
Ground (A1)	$\frac{3}{2}$
Second ${}^4I_{\frac{15}{2}}$ (A2)	$\pm\frac{1}{2}$
First ${}^4I_{\frac{13}{2}}$ (B1)	$\pm\frac{1}{2}$
First ${}^4I_{\frac{11}{2}}$ (C1)	$\pm\frac{1}{2}$
Second ${}^4I_{\frac{11}{2}}$ (C2)	$\frac{3}{2}$
Third ${}^4I_{\frac{11}{2}}$ (C3)	$\pm\frac{1}{2}$
Forth ${}^4I_{\frac{11}{2}}$ (C4)	$\pm\frac{1}{2}$
Fifth ${}^4I_{\frac{11}{2}}$ (C5)	$\frac{3}{2}$
Sixth ${}^4I_{\frac{11}{2}}$ (C6)	$\pm\frac{1}{2}$

5.4 Erbium in Lithium Niobate

The sample was provided by Dr. László Kovács of the Wigner Research Centre for Physics in Budapest, Hungary. It is a stoichiometric lithium niobate sample doped with 2 molar percent erbium.

The results presented here are mainly to compare whether a similar crystal-field number assignment is applicable to this similar host. Therefore, not all sites are considered, only a select few for which a fairly complete level assignment was found. Prior work exists for classifying sites for erbium in lithium niobate. [9] [65] Only a select few sites (2,3,4,7, and 9) were analyzed, due to difficulty in separating out and identifying said sites.

5.4.1 Polarization without a Magnetic Field

Reviewing the polarization data for excitation from ${}^4I_{\frac{15}{2}}$ to ${}^4I_{\frac{11}{2}}$, it appears that the data for site 4 bears close resemblance to the data for site A in lithium tantalate, that is, the second and fifth excitations appear to be π polarized, and the rest σ polarized. It appears that the other sites for which a fairly complete identification of these excitations seems possible, the fifth excitation appears σ polarized, to varying degrees. This feature also appeared in the other sites in lithium tantalate. As was the case for lithium tantalate, the emission polarization for ${}^4I_{\frac{13}{2}}$ to ${}^4I_{\frac{15}{2}}$ transitions do not seem as dramatically polarized.

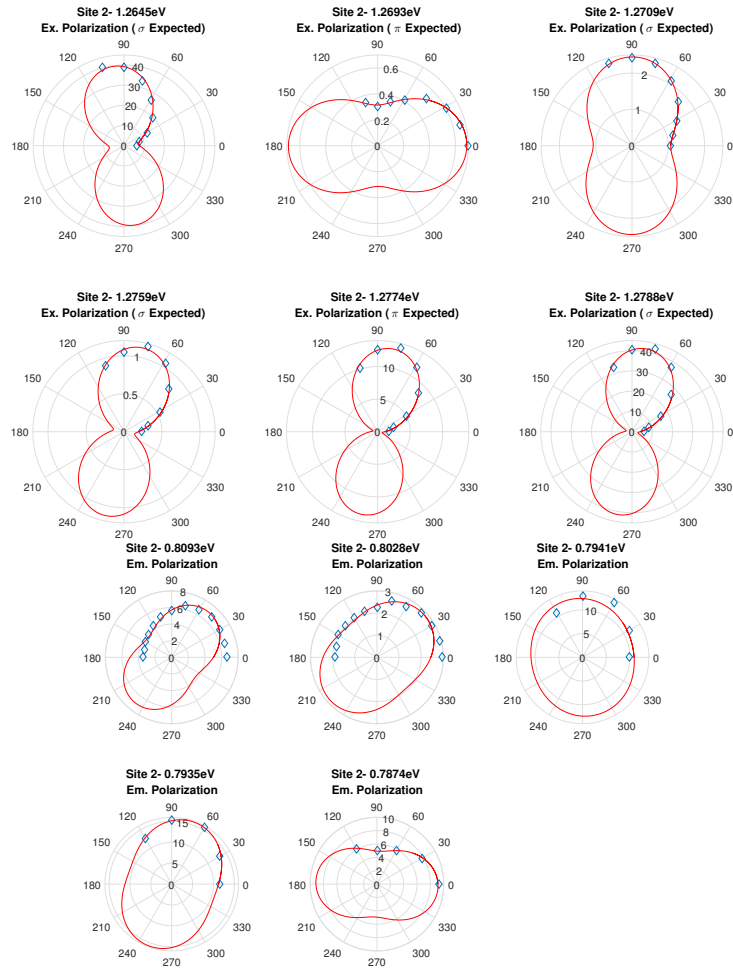


Figure 5.25: Fitted amplitudes as a function of polarization for several transitions for site 2. 0 degrees corresponds to π polarization, assuming correct angling of the sample and setup.

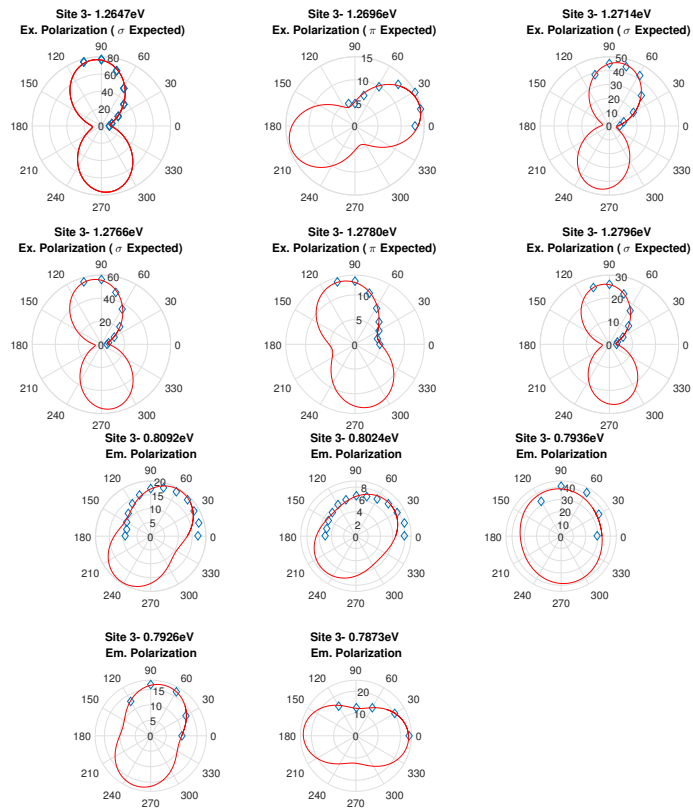


Figure 5.26: Fitted amplitudes as a function of polarization for several transitions for site 3. 0 degrees corresponds to π polarization, assuming correct angling of the sample and setup.

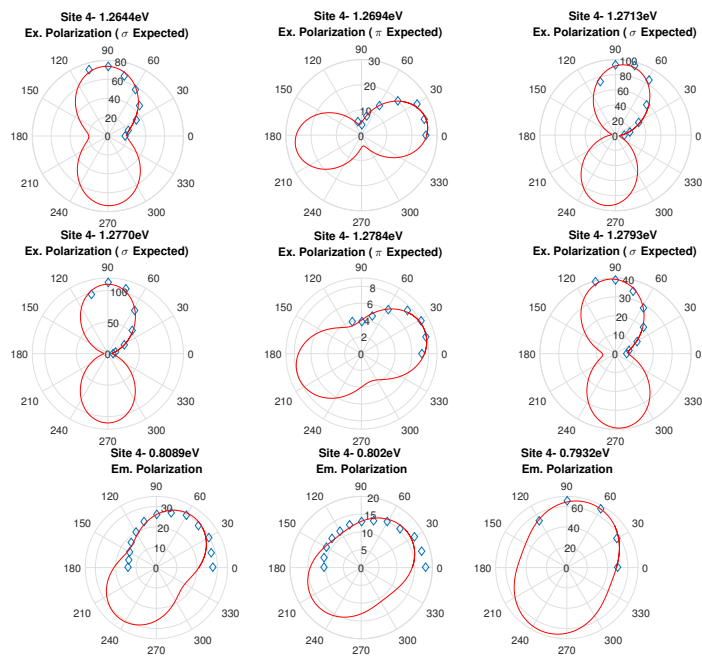


Figure 5.27: Fitted amplitudes as a function of polarization for several transitions for site 4. 0 degrees corresponds to π polarization, assuming correct angling of the sample and setup.

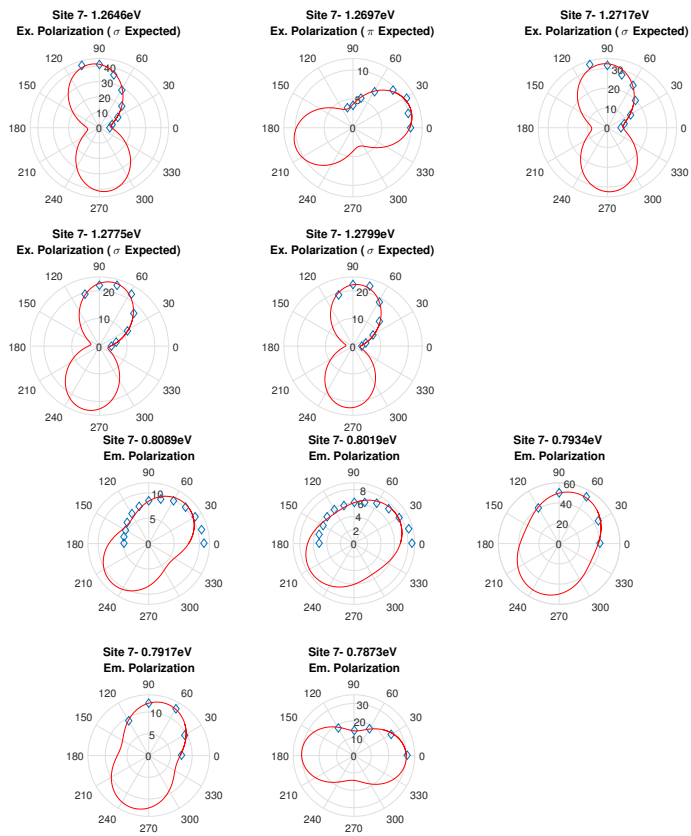


Figure 5.28: Fitted amplitudes as a function of polarization for several transitions for site 7. 0 degrees corresponds to π polarization, assuming correct angling of the sample and setup.

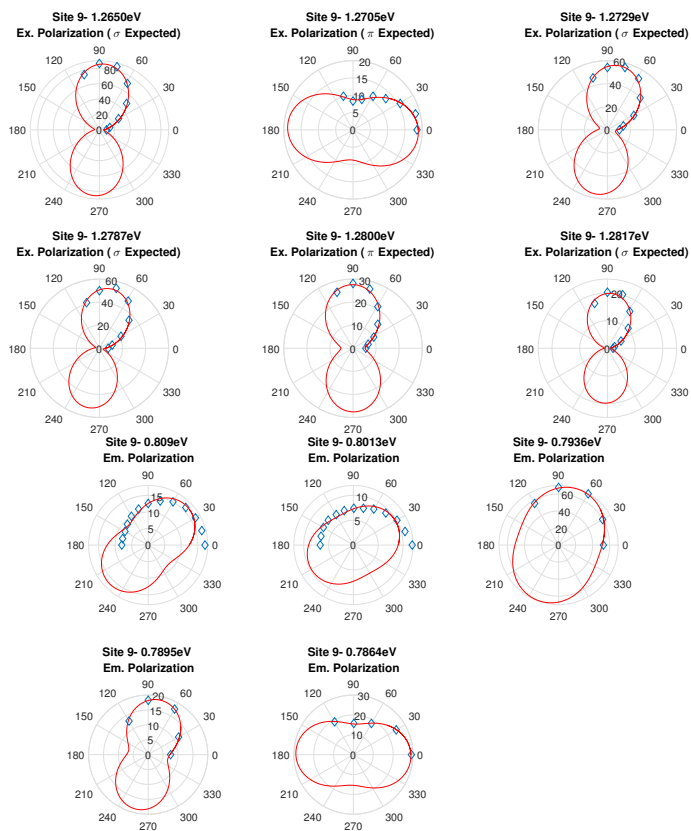


Figure 5.29: Fitted amplitudes as a function of polarization for several transitions for site 9. 0 degrees corresponds to π polarization, assuming correct angling of the sample and setup.

5.4.2 Polarization with a Magnetic Field

As for lithium tantalate, only the site which seemed to best adhere to C_{3v} selection rules was considered, site 4.

The results for site 4 in lithium niobate are essentially identical to the results for site A in lithium tantalate, in line with the observation that the two seem to have similar polarization and magnetic splitting behavior. Only the excitation transitions from the lowest level of ${}^4I_{\frac{15}{2}}$ (A1) to the levels of ${}^4I_{\frac{11}{2}}$ were considered, because these appeared to have more definitive results. All the polarizations which were examined appear to be unchanged by the application of a magnetic field. Unfortunately, it was difficult to isolate the A1 to C5 transition, but all the other excitation transitions from A1 to C levels seemed to indicate the same polarization behavior under the influence of a magnetic field.

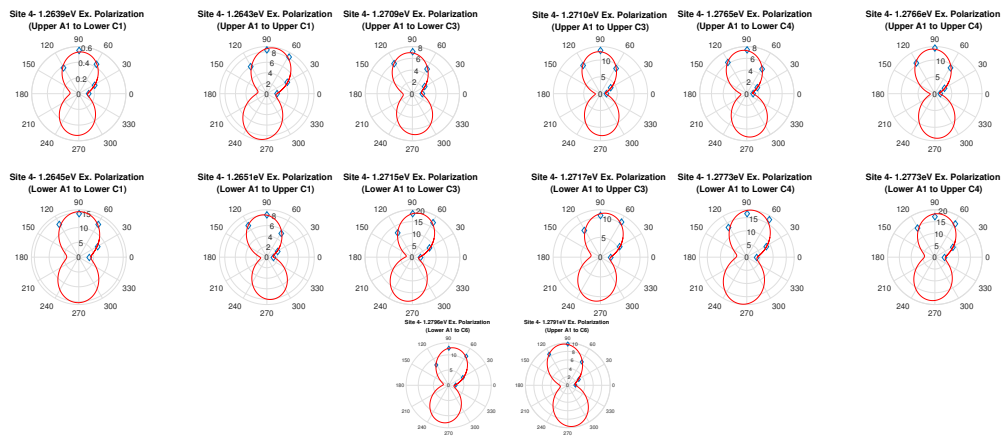


Figure 5.30: Fitted excitation polarizations for the Zeeman split transitions for a field parallel to the c-axis. These are the transitions which were σ polarized for the zero magnetic field case. This is for the lowest doubly degenerate level of ${}^4I_{\frac{15}{2}}$ to the lowest doubly degenerate level of ${}^4I_{\frac{11}{2}}$

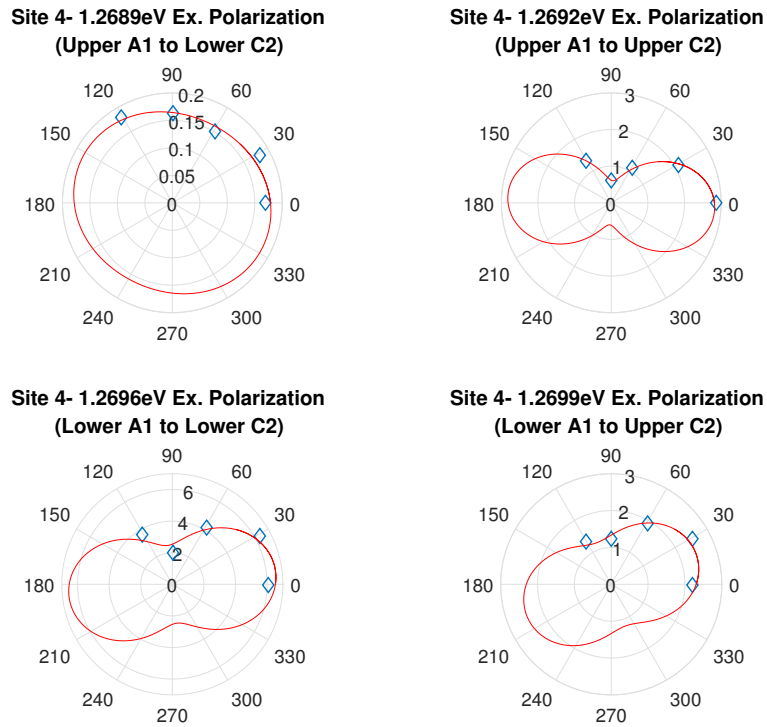


Figure 5.31: Fitted excitation polarizations for the Zeeman split transitions for a field parallel to the c-axis. These are transitions which were π polarized for the zero magnetic field case. This is for the lowest doubly degenerate level of ${}^4I_{\frac{15}{2}}$ to the second lowest doubly degenerate level of ${}^4I_{\frac{11}{2}}$

5.4.3 Magnetic Splittings

Appendix B contains more information regarding the splittings measured for the sites. The analysis was less complete than for erbium doped lithium tantalate, but the results appear very similar. Shown here is the list of effective g factors for site 4, the site thought to best correspond to C_{3v} symmetry.

5.4.4 Conclusions

As was done for site A in lithium tantalate, site 4 was used to develop a list of crystal-field numbers. The two are essentially identical, which seems reasonable, given that the two hosts are themselves similar.

Imperfect polarization results may suggest that none of the sites has perfect C_{3v} symmetry, but evidence suggests site 4 is possibly the site that adheres best to this symmetry. As suggested in prior work, charge compensation, balancing the +3 charge of the erbium ion in the host crystal, likely prevents perfect symmetry. [45] Differences in symmetry are likely due to whether this compensation occurs in a way that preserves C_{3v} symmetry, such as a change along the c -axis of the crystal immediately next to the dopant.

Table 5.7: Fitted effective g factors for site 4, magnetic field parallel to c-axis.

Site		4
Ground (A1)	g_{\parallel}	15.51 ± 0.66
Second ${}^4I_{\frac{15}{2}}$ (A2)	g_{\parallel}	4.57 ± 0.34
First ${}^4I_{\frac{13}{2}}$ (B1)	g_{\parallel}	10.69 ± 0.55
First ${}^4I_{\frac{11}{2}}$ (C1)	g_{\parallel}	10.01 ± 0.66
Second ${}^4I_{\frac{11}{2}}$ (C2)	g_{\parallel}	7.28 ± 0.46
Forth ${}^4I_{\frac{11}{2}}$ (C4)	g_{\parallel}	2.10 ± 0.45

Table 5.8: Suggested crystal-field number assignments for erbium-doped lithium tantalate

Level	μ
Ground (A1)	$\frac{3}{2}$
Second ${}^4I_{\frac{15}{2}}$ (A2)	$\pm\frac{1}{2}$
First ${}^4I_{\frac{13}{2}}$ (B1)	$\pm\frac{1}{2}$
First ${}^4I_{\frac{11}{2}}$ (C1)	$\pm\frac{1}{2}$
Second ${}^4I_{\frac{11}{2}}$ (C2)	$\frac{3}{2}$
Third ${}^4I_{\frac{11}{2}}$ (C3)	$\pm\frac{1}{2}$
Forth ${}^4I_{\frac{11}{2}}$ (C4)	$\pm\frac{1}{2}$
Fifth ${}^4I_{\frac{11}{2}}$ (C5)	$\frac{3}{2}$
Sixth ${}^4I_{\frac{11}{2}}$ (C6)	$\pm\frac{1}{2}$

5.5 Suggested Future Work

As was stated already, a less complete analysis of the erbium doped lithium niobate system was completed here. However, what was done suggests that this and the same dopant in lithium tantalate result in erbium sites with essentially identical levels in terms of crystal-field numbers and zeeman splittings.

This cataloging of erbium sites in lithium tantalate also aids future work of other types, such as how the distribution of these sites changes from sample to sample, or attempts to establish a direct correspondence between these sites and those in lithium niobate.

This process can also be applied to other systems to identify comparatively higher symmetry sites, as well as to characterize the states of the dopant in a site-specific way.

Chapter 6

Transitions in Erbium Doped Gallium Nitride

6.1 Experimental Measurements of Zeeman Splittings as a Function of Applied Field in Erbium Doped Gallium Nitride

6.1.1 Introduction

Past work on energy levels for the majority site in erbium doped gallium nitride has yielded some interesting features and results. First, there is some disagreement regarding the effective g factor for the ground state. [57] [30] Second, there exist prior results in Ref. [44] seeming to yield curvature in the transition energies as a function of magnetic field strength. This led to the question of whether the latter could explain the former. In order to do so, ultimately, energy levels as a function of magnetic field must be extracted from optical spectra.

6.1.2 Motivation

As discussed in the second chapter, it is reasonable to expect nonlinear effects, like avoided crossings, to occur between crystal-field split levels when an additional perturbation is applied. It is also of interest to determine at what point linear approximations for Zeeman splittings break down, and to what degree. This informs what experimental parameters produce data in this regime. CEES is well-suited to examining a range of energy levels (and separating them by site) via their transitions, and should be a useful tool for examining details of level interactions experimentally. As discussed in Chapter 2, crystal-field splitting (at least for C_{3v} symmetry) is also expected to produce some doubly degenerate levels which do not split under a field applied perpendicular to the symmetry axis (the c -axis of the crystal) for odd half integer values of J . A detailed analysis of splittings would also give insight into the nature of the levels. All of this information is potentially useful for confirming incorporation site symmetry.

Our group has produced large data sets showing emission spectra as a function of applied magnetic field magnitude over a period of years. In this chapter, detailed information on the energy levels is extracted from these spectra, creating data on energy level positions as a function of applied field.

Objectives

- Confirm or correct existing level assignments for the transitions
- Determine the energy levels as a function of applied magnetic field for fields both parallel and perpendicular to the c -axis
- Use this information to assign effective g factors
- Investigate nonlinearities in Zeeman splitting using this information
- Determine whether such nonlinearities can explain or cause discrepancies in the literature

6.1.3 Approach

The basic process is to create a model using input parameters describing energy levels, rather than peak positions, then fit the spectra using a least-squares fitting algorithm, such as Levenberg-Marquardt. [41] The advantage in describing energy levels rather than individual peak positions is redundancy in information, allowing for situations in which individual transitions may be difficult to pick out from one another, but transitions sharing an energy level may not be overlapping.

This approach has a weakness in that it is required that one have a very good understanding of the origins of every peak in the emission spectrum being fitted, in terms of the energy levels that produce them. It is also required that one have good estimates for starting parameters for successful fitting. To accomplish this, a spectrum without any applied field is examined. Differences in energy levels produce the transitions, and the correct differences in transition energies should produce energy level spacings. Using other data, such as CEES, one obtains information on transitions between other multiplet sets, and finding transitions sharing a multiplet with the same differences in transition energies suggests that those differences correspond to energy level spacings in the shared multiplet.

Once this is done, a spectrum without any applied perturbations should be possible to fit using only the energy levels involved, labeling the lowest energy as zero. After this, portions of the spectra set are examined to develop starting parameters for effective g factors. It should be noted that depending on the choice of system, some of this work in developing initial estimates may already have been done, and one merely needs to check the result.

6.1.4 ${}^4I_{\frac{13}{2}}$ to ${}^4I_{\frac{15}{2}}$ Emission

A Note on Samples

All the data in this chapter were obtained using a sample labeled A2373, whose growth conditions are described in [73]. It is a thin film (0.5 μm) of erbium doped

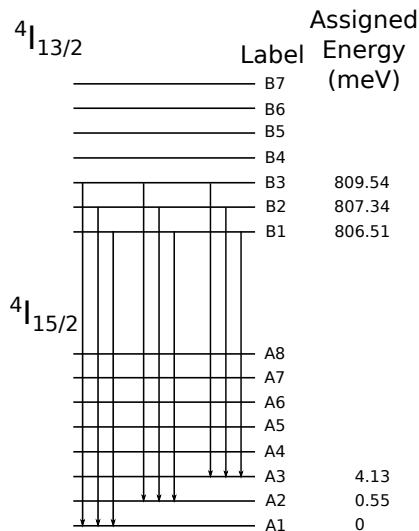


Figure 6.1: Emission transitions for Er^{+3} observed in the data used for this work.

gallium nitride on a layer of undoped gallium nitride, grown by Metal-Organic Chemical Vapor Deposition (MOCVD) on 0001 polished sapphire. Of the samples available to our group, this one produces the sharpest transition peaks, making detailed analysis of small changes in energy levels feasible.

Developing Initial Estimates

Previous similar work on this particular system has been completed for the same levels. [44] However, only a single number was recorded to characterize the splittings. This system is of particular interest with regards to possible level interactions because of a small splitting between the doubly degenerate ground state and the doubly degenerate state immediately above it (roughly 0.55 meV, as opposed to splittings of a few meV). This refers to A1 and A2 in the diagram of transitions indicated in Figure 6.1. This could mean that measurements for the magnetic properties of the ground state could be influenced by interactions with this next level at comparatively low fields.

Existing level assignments appear to reproduce the emission spectra rather well,

Multiplet	[75]	[44]	[39]	Field Data	⊥ Field Data
${}^4I_{\frac{15}{2}}$ (meV)	0	0	0	0	0
	0.63	0.62	0.56	$0.556 \pm .021$	0.546 ± 0.005
	4.3	4.3	4.20	$4.144 \pm .025$	4.123 ± 0.006
${}^4I_{\frac{13}{2}}$ (eV)	0.8063	0.8063	0.80649	$0.806504 \pm .000019$	0.806519 ± 0.00005
	0.8072	0.8072	0.80736	$0.807341 \pm .000023$	0.807347 ± 0.00005
	0.8094	0.8094	0.80954	$0.809532 \pm .000036$	0.809548 ± 0.00008

Table 6.1: Results for the energy levels of the main site in Er doped GaN from various sources. The last two columns are from two different sets of data fitted for this work. The errors in those columns are from estimated 95 percent confidence intervals from the fitting algorithm used, and do not take into account errors from sources such as calibration of the emission axis.

and values obtained here. This enables the next portion of the work, which is to estimate Zeeman splitting parameters. Each of nine transitions is thought to be a transition between two doubly degenerate levels. This means that each transition can become four new transitions. Fitting a relatively isolated transition on its own yields two splittings, one for each level. Assigning each splitting to one of two doubly degenerate levels requires comparison of transitions with only one doubly degenerate level in common. By repeating this, one can determine initial guesses for effective g factors for each level. To reduce the number of free parameters for fitting, it was assumed that the widths of the split peaks are identical. The model to predict the centers of peaks used three parameters. The first was the difference in energy between the centers of the two split levels. The other two were the differences in energy from the center of each split level to each level (or, half the total splitting).

It is worth noting that the center of the transitions would sometimes shift in what appeared to be a nonlinear way even while the splittings of each level involved would appear to remain linear with field, as shown in Figure 6.3 for one transition, suggesting that curvature in the transitions as a function of applied field may not correspond to significant curvature in splittings (at least at the level of precision achievable by this approach and equipment).

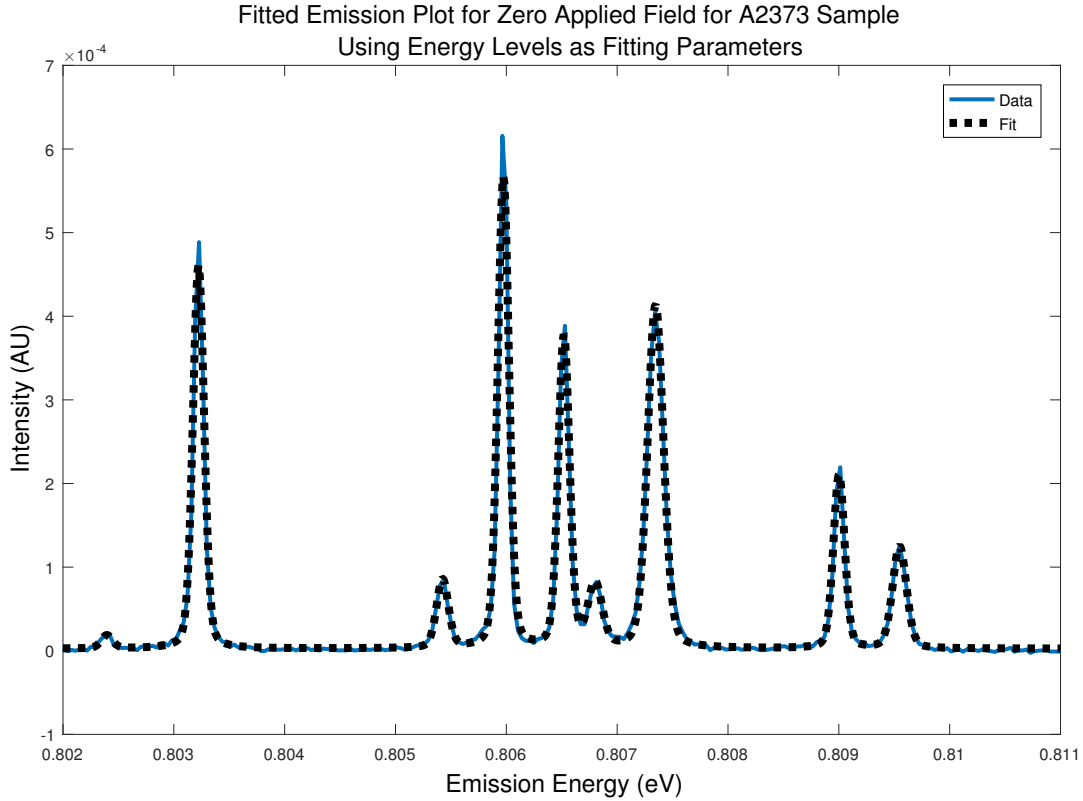


Figure 6.2: Fitting of an emission spectrum from the majority site in erbium doped gallium nitride. Five parameters are used to describe the positions of nine emission peaks.

An Avoided Crossing

The most notable feature observed in the available data sets was a discernible avoided crossing in the parallel field data set. The involved transitions shared one level in common in the ${}^4I_{\frac{13}{2}}$ multiplet, but had as their other levels the lowest two observed levels of the ${}^4I_{\frac{15}{2}}$ multiplet (A1 and A2). To examine this, this portion of the spectra was fitted using two peaks for each field. The result was that the peaks appear to show signs of an avoided crossing. The result of this is shown in

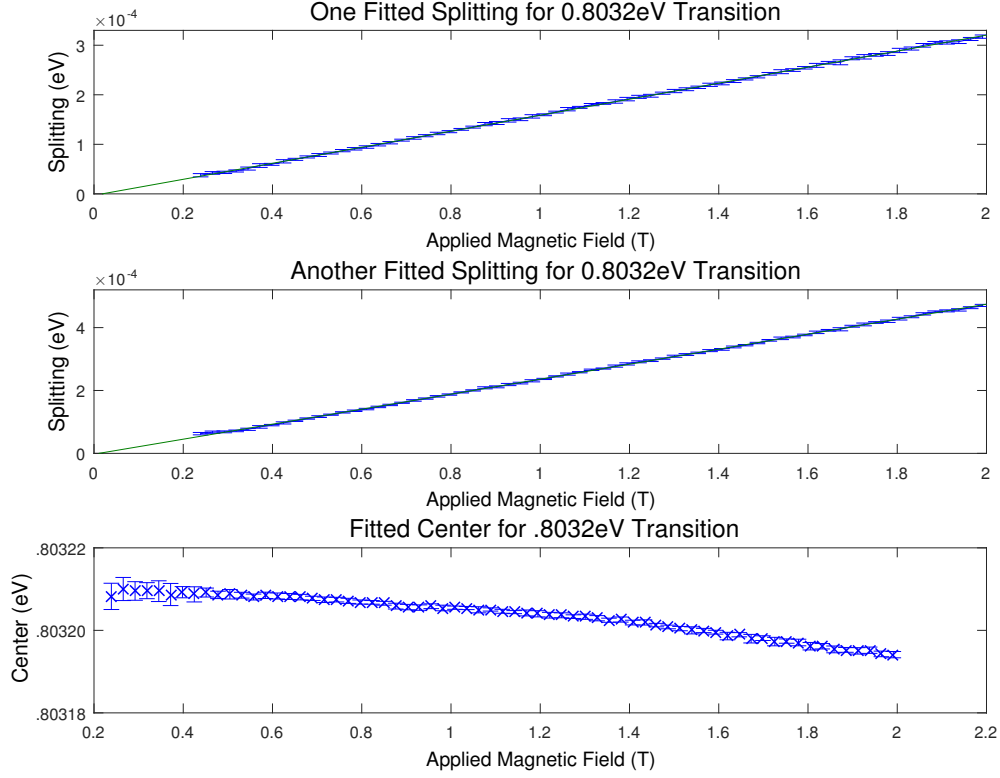


Figure 6.3: Result of fitting the splitting of a transition near 0.8032eV. In this case, the field was applied parallel to the c-axis. The linear fits shown in green for the splittings were not forced to have a particular intercept. Error bars are from 95 percent confidence intervals from the fitting algorithm.

Figure 6.4. Fitting the peaks in this way also allowed for an estimate of a cross-term for the levels involved to describe the avoided crossing. This feature was added to the initial guess model.

Specifically, if the crystal-field splitting is viewed as a mixing of sets of levels (of the same crystal-field quantum number) with distinct m_j values, if two crystal-field levels Φ_1 and Φ_2 share component m_j states, $\langle \Phi_1 | H_z | \Phi_2 \rangle$ may contain terms like $c_1 c_2^* \langle m_j | H_z | m_j \rangle = c_1 c_2^* m_j g_J \mu_B B$. This implies that there may be terms linear in the

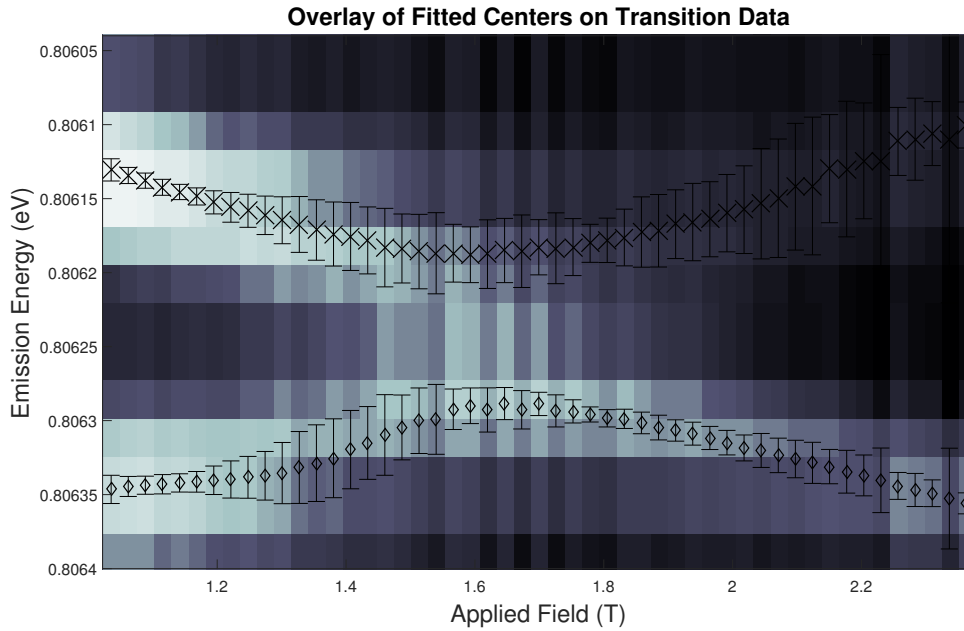


Figure 6.4: Spectra for a parallel applied field in the vicinity of what is believed to be an avoided crossing. Portions of spectra in this region were fitted using two peaks for each field. The results of that fitting are overlaid here. Error bars are from 95 percent confidence intervals from the fitting algorithm.

applied field between different crystal-field states without much added complication in the theoretical model. The new method for calculating energy levels, then, is to create a matrix containing terms corresponding to effective g factors on its diagonal, with the cross term mentioned added to that. Then, the matrix is diagonalized. While, in principle, there may be nonzero terms for many pairs of levels, here, only one cross term is known, so only the diagonalization of a 2×2 matrix is required.

The Actual Fitting

After determining estimates for parameters, and successfully fitting the zero field case, the next step is to fit each spectrum individually, allowing the parameters to vary. Unfortunately, there were some issues with this approach in certain regimes.

Spectra for Ramping of a Magnetic Field Applied Parallel to the c-axis with an Overlay of a Model with Initial Parameter Estimates

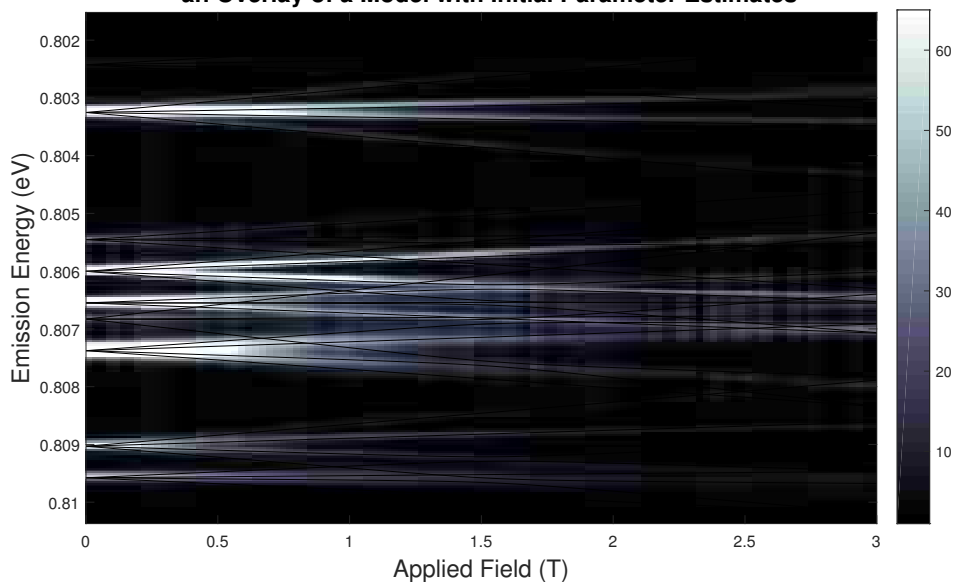


Figure 6.5: This is data for A2373 showing spectra as a function of applied field, with lines indicating the transitions centers as predicted by the initial guesses obtained to this point.

At low fields, both changes in widths and changes in splittings produce a similar result in the model, increasing error in splittings at lower fields. The cross term used for fitting the avoided crossing has much less effect far from the avoided crossing, and error in that becomes large far from the avoided crossing. The former problem cannot be easily resolved without finding means of improving resolution and sharpness of the lines, or forcing peak widths to a static value. The latter problem is made more difficult because within the context of an individual spectrum, parameters given for the splitting and centers of lines can duplicate the effects of a cross term. Thus, the initial parameter for this cross term is used as a fixed value in fitting. It can be recalculated from the resulting fitted energy levels later, and stating a fixed value for this allows for better initial guesses for other parameters.

For the data set for a perpendicular field, the range of the applied field was

Level	[44]	From Fitting	[57] (around 90mT)	[30] (around 65mT)
A1	$6.94 \pm .35$	$7.58 \pm .16$	$7.645 \pm .003$	$8.806 \pm .005$
A2	0	$3.03 \pm .12$		
A3	$4.83 \pm .24$	$1.86 \pm .13$		
B1	$5.70 \pm .29$	$5.79 \pm .25$		
B2	0	$4.91 \pm .08$		
B3	$4.52 \pm .23$	$5.64 \pm .18$		

Table 6.2: Effective g factors for a magnetic field applied perpendicular to the c-axis. The values in the column corresponding to results obtained here were determined by averaging the g factors determined from each spectrum, using the errors from the fitting algorithm for weighting. Listed errors in that column correspond to one standard deviation.

limited to $1T$, and no such avoided crossing was observed. No level was observed to have zero splitting, implying at least one of several things is likely true: none of the levels are of crystal-field number $\frac{3}{2}$, the symmetry group is not C_{3v} , the sample was not well angled relative to the applied field, or higher order terms are present to allow significant splitting of levels of crystal-field number $\frac{3}{2}$.

The results of these fittings for the energy levels as a function of applied magnetic field are shown in Figures 6.6 and 6.7. The parallel field case, due to the avoided crossing, and higher resolution, is promising for further analysis. Using the fitted results, it is reasonable to examine features like small curvatures in the transitions and the avoided crossings, but in terms of the actual levels producing those transitions.

Effective g Factors- Perpendicular Field Case

Note that the data used in Ref. [44] for the perpendicular field case is the same as the data used in this analysis. That work suggested that the large discrepancies between results reported in Ref. [57] and Ref. [30] for the ground state g factor could be explained by a substantial nonlinear interaction. This was argued because it appeared that the results in those works suggested a trend in which the effective

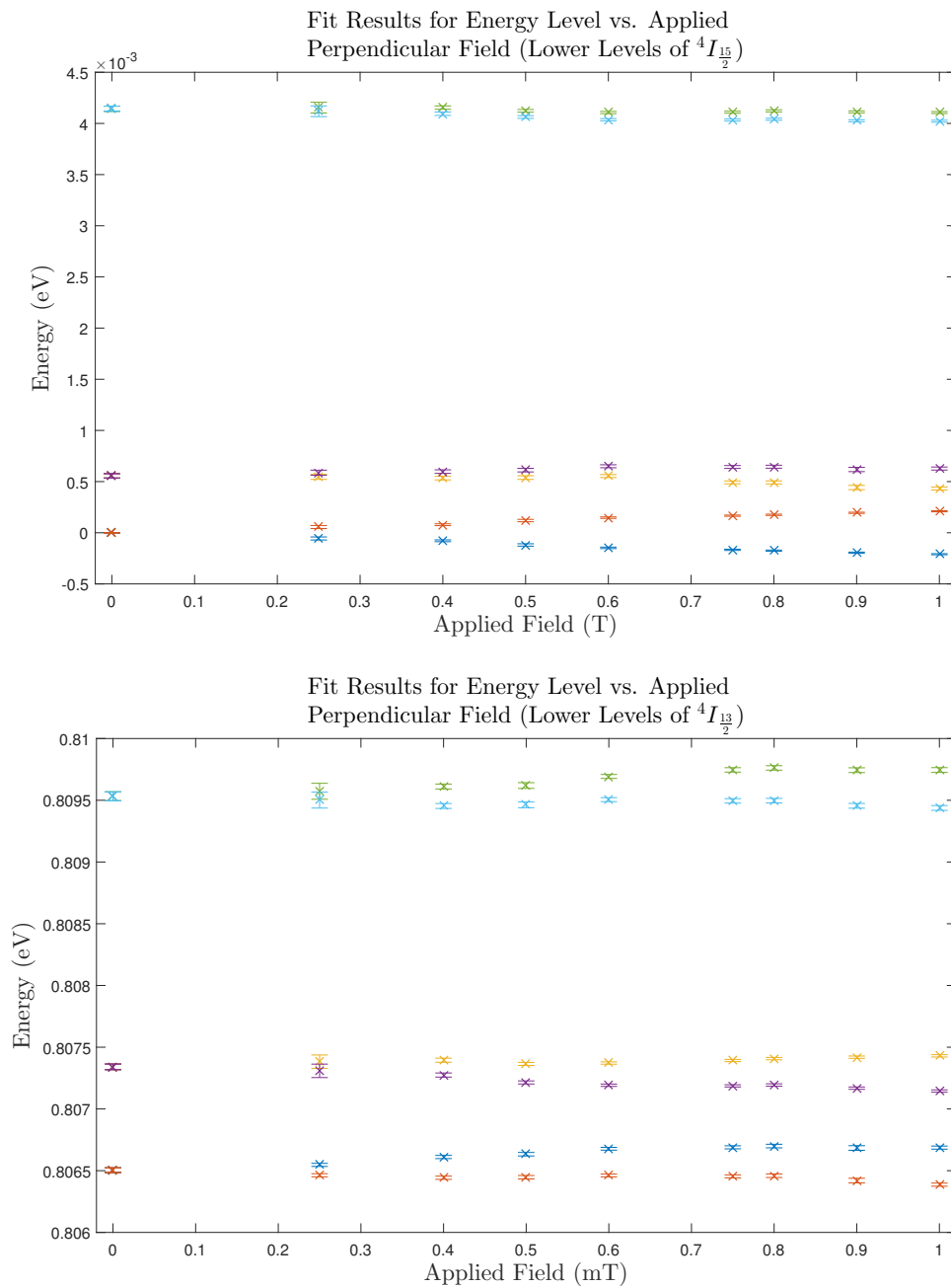


Figure 6.6: Fitted energy levels for A2373 with a magnetic field applied perpendicular to the c axis. Error bars correspond to a 95 percent confidence interval, using values from the fitting algorithm.

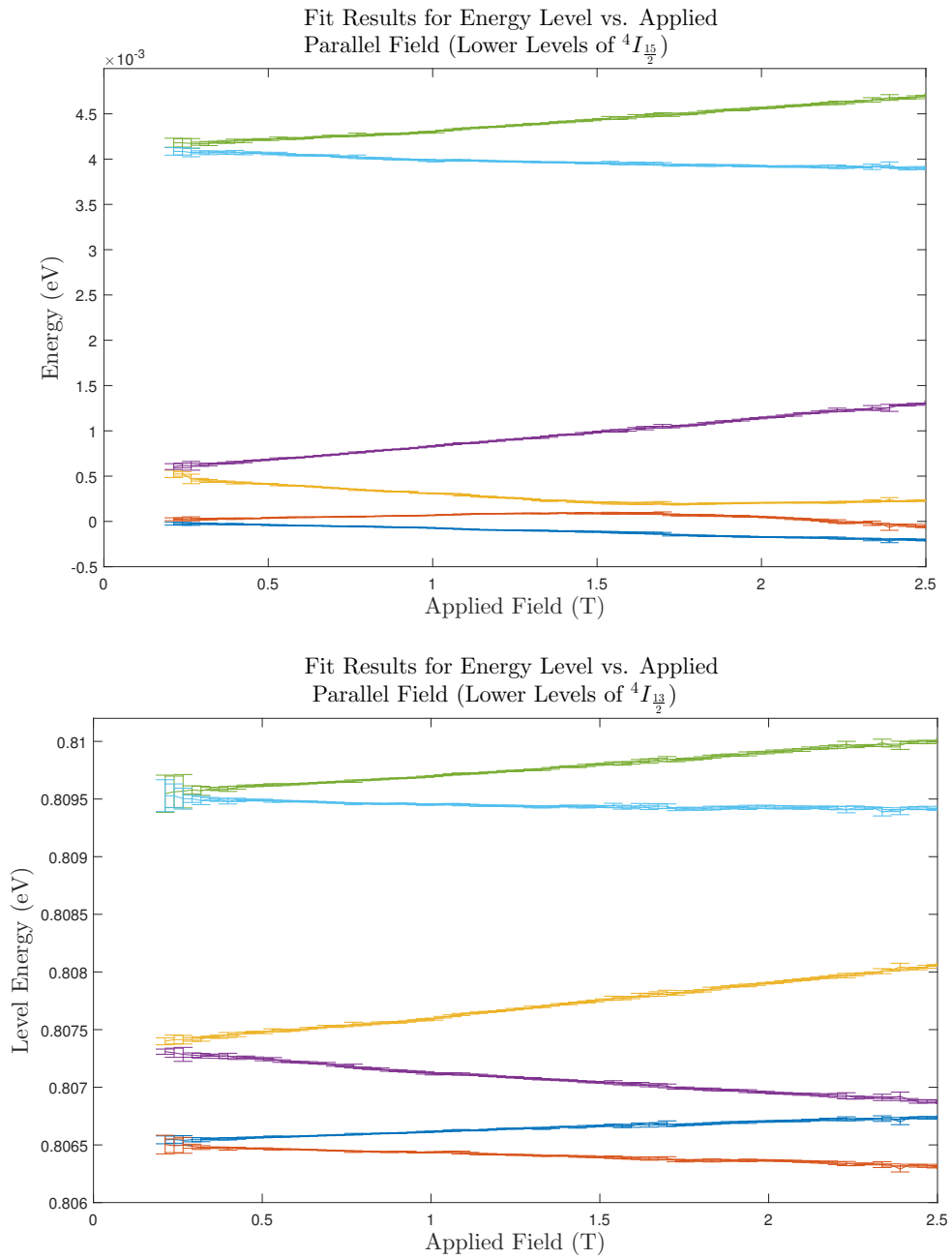


Figure 6.7: Fitted energy levels for A2373 with a magnetic field applied parallel to the c axis. Error bars shown correspond to a 95 percent confidence interval, using values from the fitting algorithm.

g factor decreased with applied field. However, the result obtained in this analysis strongly favors one of those two values. However, if a large nonlinear effect were to be present at values below 100 mT, it might be experimentally difficult to determine a g factor without an attempt to extrapolate to zero field, and it would call into question all values determined here, taken at field magnitudes of 200mT and above.

While one effective g factor for the perpendicular field case is notably smaller than the other five determined here, it is certainly nonzero. There are certainly enough levels in each multiplet left undetermined that it could be that C_{3v} symmetry is applicable, there are no significant higher order effects causing Zeeman splitting in levels not expected to split, and the sample was correctly angled relative to the applied field. This suggests that determination of other g factors in the ground multiplet is of interest.

Supposing that all of the levels which can be observed from this emission scheme are of the same crystal-field number (at least in the sense that each doubly degenerate level contains both a $+\frac{1}{2}$ and a $-\frac{1}{2}$ crystal-field quantum number state), this implies that all of these levels could conceivably have a cross term between one another from simply sharing m_j labeled states in common, as described earlier.

Effective g Factors- Parallel Field Case

Before continuing, it is important to make abundantly clear that although several times in this chapter, it is implied that effective g factors are changing with the applied magnetic field, the correct framework in which to consider these results is such that plots in this portion might be more accurately labeled, “number which might naïvely be thought to be the effective g factor, if one assumed that all magnetic splittings were perfectly linear and only one data point from a level splitting at a particular magnetic field magnitude and orientation were considered in order to calculate this number”. Here, it will be called the apparent effective g factor.

The parallel field case is complicated by the presence of an avoided crossing. Otherwise, the comparatively high resolution of the parallel field data set allows for a more interesting analysis for obtaining the effective g factors. There is visible

curvature in the level splittings as a function of applied field. The correct effective g factor should be the value obtained infinitely close to zero applied field, for which direct measurement is clearly not possible with this approach. Fitting cannot be handled in a correct manner without developing a matrix involving cross terms (which may involve more terms than can easily be calculated from the data). A simple solution is to consider the effective g factor as corresponding to the first nonzero term in a Taylor expansion for the energy level splitting. The next term for the magnetic splitting in the field would be proportional to the square of the applied field.

$$\Delta E_B \approx g_{eff}\mu_B B + g_2\mu_B B^2$$

Here, the quantity labeled g_2 would correspond to the ratio of the change in the apparent effective g factor (assuming one were not aware of nonlinearities) calculated to the applied field. If this approximation is accepted, then the desired g factor in the limiting case of small applied field is the g_{eff} term. So, using the fitted energy levels, one merely fits pairs of split levels to second order polynomials, forcing identical values for doubly degenerate values at zero applied field which agree with the zero field results obtained earlier (within error). Then, the differences in coefficients must correspond to the differences in the coefficients of B in the above equation.

This approach, however, runs into some problems for the levels experiencing an observed avoided crossing, because the quadratic term can replace some of the features of the matrix diagonalization, but may not exactly replace its functional form. Results presented here for the lowest two doubly degenerate levels of ${}^4I_{\frac{15}{2}}$ to extrapolate to zero field use an alternate fitting approach, effectively setting g_2 equal to zero and relying on the cross terms to model the nonlinear behavior. This g_2 approach is applied to other levels, which still gives some indication of how apparent effective g factors vary with applied field. It is important to note that while much of this analysis ultimately depends on the linearity of the magnetic field with time (as the field was continuously ramped in the parallel field data set) produced by the magnet, such an effect would not explain shifts in the center of gravity of transitions.

Level	[44]	0T Extrapolated	[57] (around 230mT)	[30] (around 240mT)
A1	$2.88 \pm .14$	$2.77 \pm .12$	$2.861 \pm .003$	$2.952 \pm .005$
A2	$9.28 \pm .46$	$9.17 \pm .20$		
A3	$5.27 \pm .26$	$5.48 \pm .12$		
B1	$2.88 \pm .14$	$3.335 \pm .059$		
B2	$7.96 \pm .40$	$8.13 \pm .14$		
B3	$4.52 \pm .23$	$4.332 \pm .095$		

Table 6.3: Effective g factors for a field applied parallel to the c-axis. Only levels appearing in transitions in the data set used are included. Listed errors in the extrapolated and interpolated columns correspond to a 95 percent confidence interval calculated from a covariance matrix from the fitting algorithm.

Level	0T Extrapolated	1T Interpolated	2T Interpolated	3T Extrapolated
A1	$2.77 \pm .12$	$2.588 \pm .058$	$3.153 \pm .020$	$3.203 \pm .026$
A2	$9.17 \pm .20$	$9.14 \pm .13$	$9.434 \pm .051$	$9.286 \pm .056$
A3	$5.48 \pm .12$	$5.488 \pm .066$	$5.496 \pm .045$	$5.503 \pm .089$
B1	$3.335 \pm .059$	$3.148 \pm .035$	$2.960 \pm .026$	$2.771 \pm .044$
B2	$8.13 \pm .14$	$8.138 \pm .081$	$8.143 \pm .051$	$8.149 \pm .081$
B3	$4.332 \pm .095$	$4.222 \pm .052$	$4.110 \pm .055$	$4.00 \pm .10$

Table 6.4: Values for apparent effective g factors determined using fits of the fitted energies as a function of fields for the parallel field case (with a small fitted offset for the zero field). Listed errors in the extrapolated and interpolated columns correspond to a 95 percent confidence interval calculated from a covariance matrix from the fitting algorithm.

If this were an issue, it is expected that a similar effect would appear for all the levels (that is, fitted values for this g_2 parameter of the same sign, and of similar value when scaled by g_{eff}).

Even when simply using this fit to interpolate energy levels, it appears that some levels, which were not observed to have an avoided crossing in this range of fields, may have statistically significant changes in apparent effective g factor as function of

Level	Fitted g_2 Parameter
A1	
A2	
A3	$.008 \pm .064$
B1	$-.187 \pm .020$
B2	$.007 \pm .062$
B3	$-.111 \pm .058$

Table 6.5: Values for the g_2 parameters described in this chapter from fits of the fitted energies as a function of fields for the parallel field case (with a small fitted offset for the zero field). Listed errors in the extrapolated and interpolated columns correspond to a 95 percent confidence interval calculated from a covariance matrix from the fitting algorithm.

field. Of course, this may be an indication that these levels experience similar anti-crossings at higher fields. Some levels appear not to have a statistically significant change in apparent effective g factor as a function of applied field, but this may be slightly affected by the ability of the fitting algorithm to offset the zero field point (an attempt to handle the problem of imperfect synchronizing of the taking of spectra and the start of the field ramping in this particular experimental setup). This g_2 idea and the parameters given here should probably only be considered as a tool to demonstrate that measurable changes of a particular magnitude in apparent effective g factors are present, rather than a specific value to use in further analysis.

As was the case for the perpendicular data, the data shown here from two other sources involving electron spin/paramagnetic resonance results appear to disagree with one another, despite using similar field magnitudes to make their measurements. [57] [30] It seems unlikely that differences of a few hundredths of a tesla would be sufficient to cause such a discrepancy, comparing to fluctuations seen in data here. The data fitted here seems to favor the results in Ref. [57]. The reason for this discrepancy could be due to nonlinear splittings, but it is not entirely clear that this is the case.

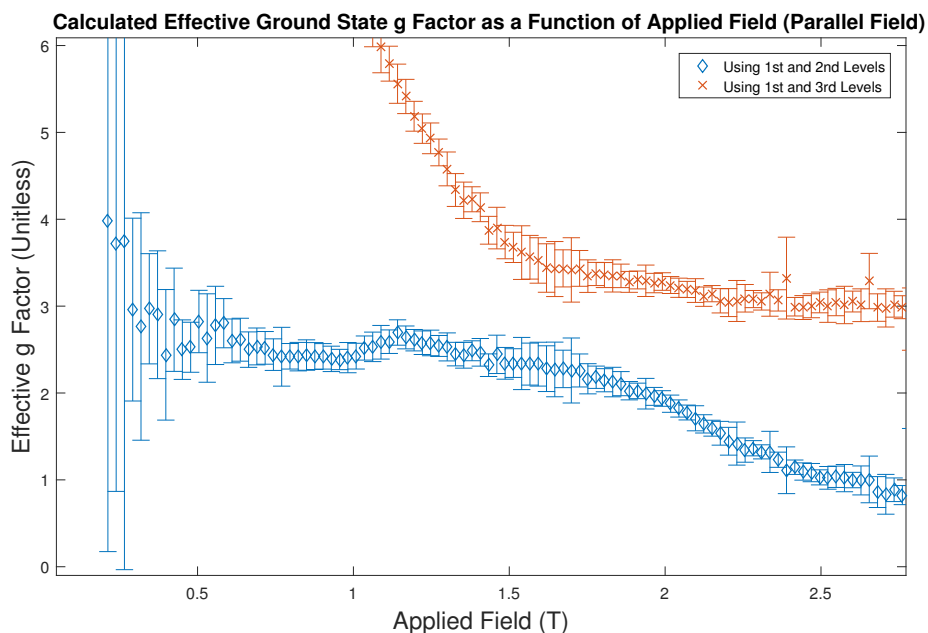


Figure 6.8: Calculated apparent effective g factors for the ground state of the majority site, using a linear dependence for the splitting on the applied field magnitude, depending on which levels are used for the calculation. The errors are from 99 percent confidence intervals derived from Monte Carlo error estimation, using a covariance matrix from the fitting algorithm, as well as an estimate for the error in field magnitude.

Complications for Measuring the Ground State Effective g Factor

Avoided crossings raise complications for measurement of the ground state. At a sufficiently high applied magnetic field, the two lowest energy states may not correspond to the doubly degenerate ground level in the absence of an applied field. Near an avoided crossing involving the ground state, the levels involving the ground state are mixed with other states, and the separations may not reflect the effective g factor of the ground state. The numeric consequences of this ambiguity are demonstrated in Figure 6.8. While this technique of measuring g factors does not give precisions comparable to electron spin resonance type experiments at lower field magnitudes,

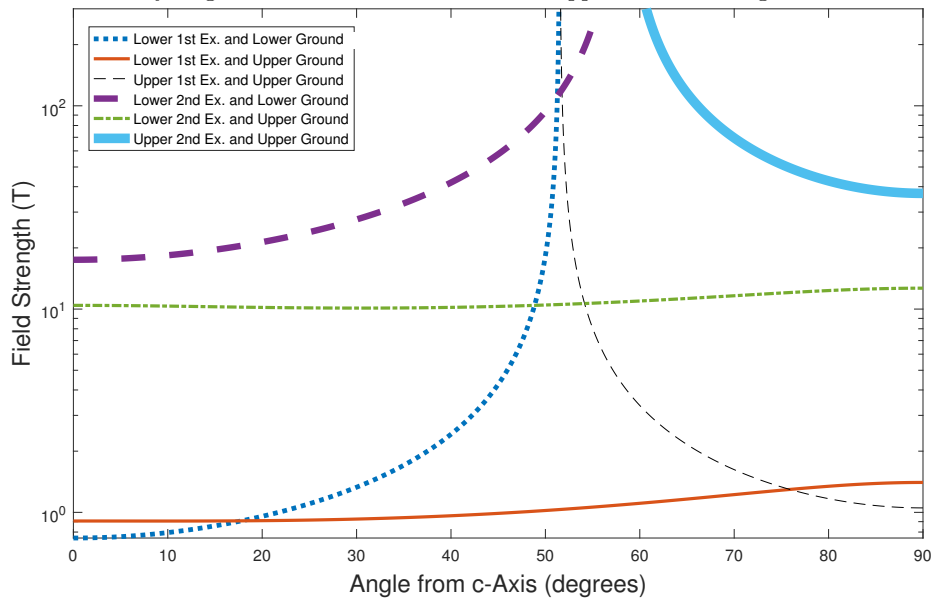
as in Refs. [57] and [30], it does shed light on the cases in which these problems occur, due to its giving information on several (presumably) adjacent levels, and how splittings vary with applied field magnitude.

An attempt to calculate the apparent ground state effective g factor as a function of field using the fittings for the parallel field case reveals several interesting features. First, it appears that there is an offset on the order of parts in ten in the apparent effective g factor on both sides of the avoided crossing that persists for a significant fraction of a tesla. If correct, this implies that an avoided crossing might still have an effect on measurements with comparatively much larger step sizes in the applied field. Second, the closest approach of the two possible calculations for the apparent effective g factor (depending on the level used) in the region of the avoided crossing is quite large. Unfortunately, while it appears that the apparent effective g factor is increasing to a value closer to values reported by others [57] [30], the errors in the technique used here increase too quickly as the field decreases to make a meaningful comment on disagreements between previously measured values at magnetic fields of 0.1T or less. Of course, it is still possible to fit the values already obtained using the simple matrix diagonalization model to attempt to extrapolate to the zero field case.

Using the determined effective g factors for the three lowest observed doubly degenerate levels for the main site, it is possible to plot as a function of magnetic field strength and angle relative to the c-axis approximately where these intersections occur. Note that since not all avoided crossings are known, this assumes a simple linear model for Zeeman splitting. It is advised that any experiment measuring the Zeeman splitting of the ground state either avoid these regions (ideally, by staying in a low field magnitude regime), or be aware of them when analyzing data.

This exercise reveals several interesting things. First, the only reason that these crossings are relevant is because of the close spacing of the first two doubly degenerate levels. The next (third) doubly degenerate level is not expected to have any such crossings until the applied field exceeds 10T. Also, the expected point of the crossing from assuming this simplified linear model appears to predict crossings at lower fields than actually is the case, so this threshold is likely higher. Next, there

Approximate Locations of Expected Intersections with the Ground State and the Next Two Doubly Degenerate Levels as a Function of Applied Field Strength and Orientation



Approximate Locations of Expected Intersections with the Ground State and the Next Doubly Degenerate Level as a Function of Applied Field Strength and Orientation

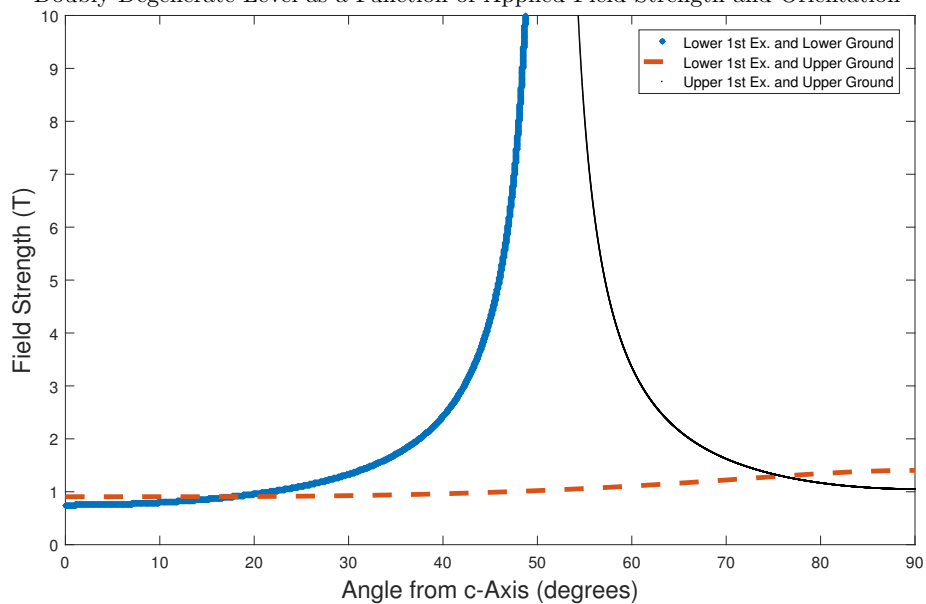


Figure 6.9: This is an illustrative example showing approximately where level (anti)crossings including the ground state are expected to occur. Note that the first plot has a logarithmic scale while the second does not.

exists a pair of crossings that corresponds to one set of levels having a higher value for the effective g factor than the other, which presumably does not take place if their effective g factors are equal. Only one of these crossings would appear if for all angles, one g factor were greater than the other. Because this crossing is expected to occur for the ground state and the first excited doubly degenerate level, and a crossing of this type occurs, there is a potential problem for measurements involving fairly continuous rotation of the sample. If a threshold field magnitude is exceeded, there will always be a field angle at which there is a level crossing, due to both crossing points tending to infinite field magnitude as the field angle approaches the angle at which the g factors are equal. Inspection of the fitting results for individual levels suggests that this threshold is probably around or above $3T$.

Still, it must be noted that the question of how relevant this is to an experiment cannot be answered without knowing the precision associated with that experiment, and the specific values for the crossing. Since only one such level crossing for one field angle has been observed here, it may be misleading to assume all such crossings behave similarly to the one observed.

Shifts in Centers of Transitions

By visual inspection, the transitions in the original data set show curvature, which often appears similar for all of the magnetically split lines from one original transition between doubly degenerate levels. This likely implies that the centers of energy levels are shifting. The previous analysis discussed nonlinear effects in splittings of transitions, corresponding to differences in levels. The logical next step for analyzing this data is to consider nonlinear effects (or even linear shifts) in averages (sums) of split levels.

This is complicated by levels being determined relative to the ground state, which is itself undergoing nonlinear effects, due to an avoided crossing, as already discussed. Subtracting out the lowest energy level from the fit results obtained earlier would effectively add an increasing term to all the other level centers. So, it may be preferable to compare differences in centers of levels to one another. This

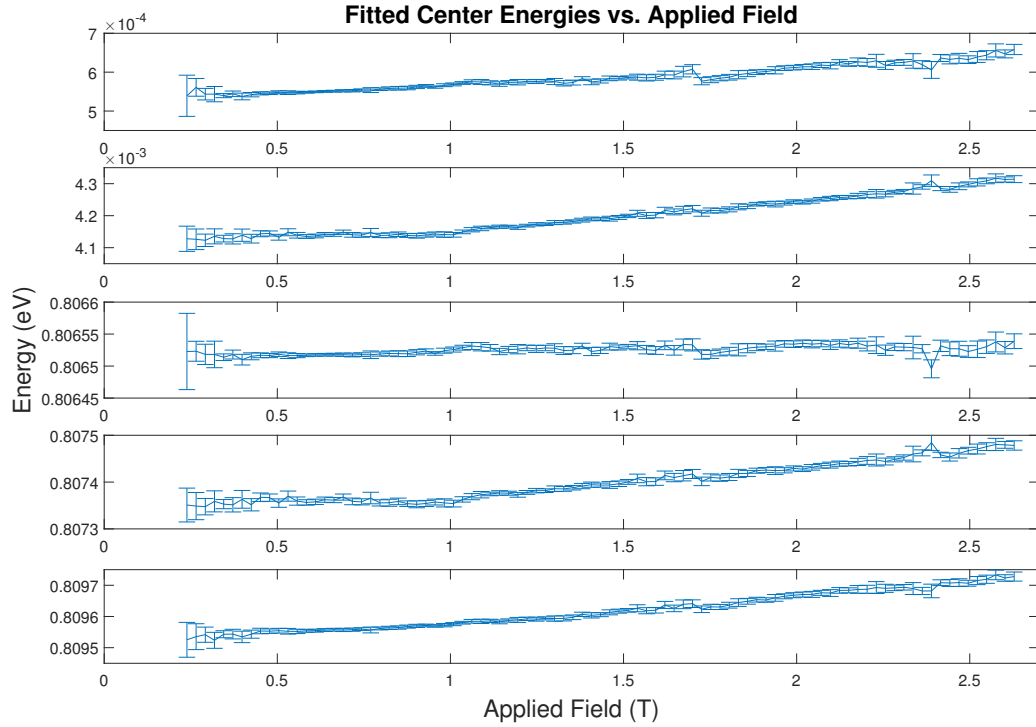


Figure 6.10: Fitted center energies as a function of applied field strength. Note that the ground state center is fixed to be zero.

ultimately means comparing shifts in sets of split transitions, of which we have nine.

As was done in the previous sections, only the data for the parallel field case will be considered, due to higher resolution, higher maximum field, and readily apparent nonlinear effects. Since all the energies shown here appear to move in the same direction, and the value for the ground state center energy is fixed at zero, this data may be taken to mean that this avoided crossing is decreasing the energy of the ground state relative to all the other states. Of course, variations in the degree of this shift also imply additional processes are in effect.

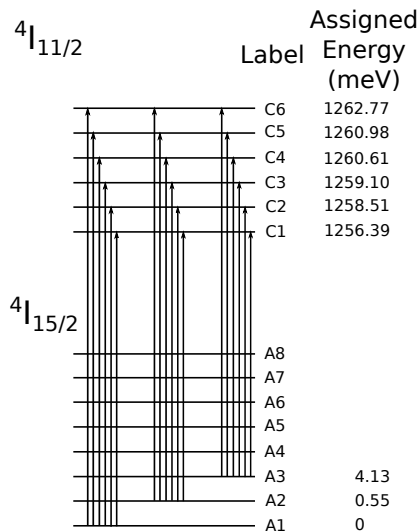


Figure 6.11: The transitions which were observed in this data set are indicated, with corresponding levels. The level scheme corresponds to the one used in this work.

6.1.5 ${}^4I_{15/2}$ to ${}^4I_{11/2}$ Excitation

Assignment of Levels

Level assignments for the ${}^4I_{11/2}$ multiplet were initially less certain. Three sources of level assignments based on experimental data [75] [44] [17] have conflicting assignments which all claim to have identified all six crystal-field split energy levels. While there are some conflicts regarding the level assignment for the emission of the majority site, [15], the level assignment which will be discussed here appears to fit data well, and agrees with the level assignments for the ${}^4I_{15/2}$ multiplet used in the previous portion.

The author of Ref. [44] claims not to observe a peak corresponding to what is here labeled as C2. However, in data collected by that author, and additional data collected for this work, the level assignment used fails to assign a rather sharp peak near 1.2579eV, shown in Figure 6.12. In Ref. [75], this particular peak is assigned its own level in the crystal-field multiplet, but this assignment omits a peak near

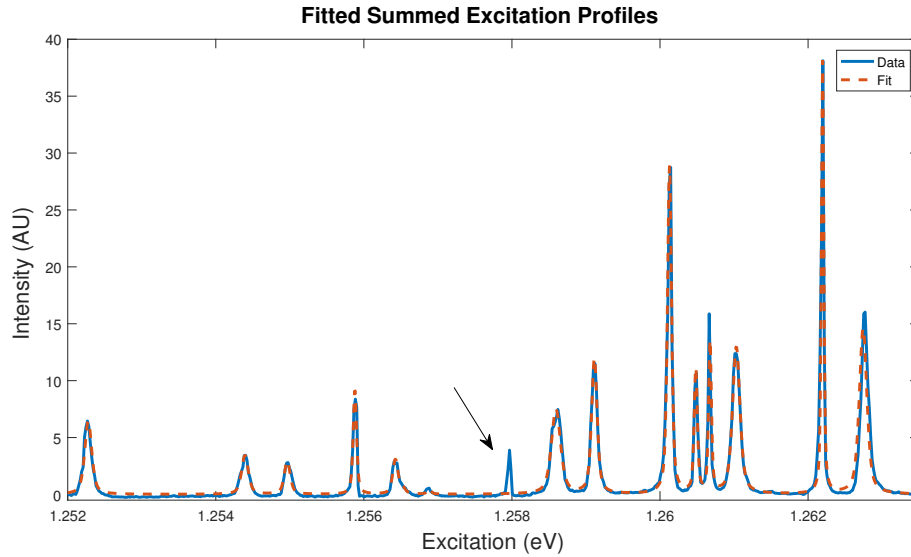


Figure 6.12: Excitation profile taken from CEES data collected by the author of [44], believed to be from sample A2373, using the level scheme suggested in that work. The arrow indicates the peak not assigned.

1.2550eV.

Subsequent experiments are believed to have been conducted at a lower temperature. This is due to the added use of a heat shield and the absence or severe relative reduction of peaks associated with the third doubly degenerate level of ${}^4I_{15/2}$, A3. They also showed that a peak assigned to an excitation from A1 to the lowest of the C levels (1.2550eV) in Ref.[44] disappears from the excitation data at lower temperatures, as shown in Figure 6.13. For transitions starting from the ground state, a decrease in temperature is not expected to cause a such decrease in intensity. Such a decrease however, appears typical of transitions involving A3 whose assignment is not in conflict.

This suggests that the 1.2550eV peak is associated with a thermally excited level in the ${}^4I_{15/2}$ multiplet. Noting this, and the similar decay in intensity with decreasing temperature for levels thought to involve A3, inspired an assignment in which the

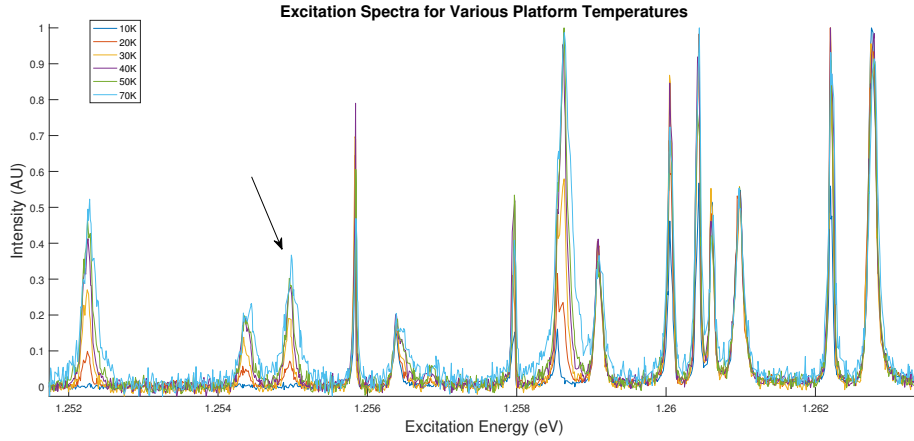


Figure 6.13: Excitation spectra as a function of platform temperature. The 1.2550eV peak is marked with an arrow. Scaling is accomplished by dividing by the amplitude of the highest intensity peak.

energy corresponding to the A1 to C2 nearly overlaps with the A2 to C3 transition. This explains why the author of [44] was not able to observe a separate transition for this level using the same sample. Subsequent fitting using the energy levels as parameters shows that this assignment allows fitting of all the observed peaks in this data using only six levels for the ${}^4I_{\frac{11}{2}}$ multiplet, and the same three levels of the ${}^4I_{\frac{15}{2}}$ used in the previous section. A plot showing this fitting and the level assignments is shown in Figure 6.14.

The fact that this assignment assigns all the peaks seen in this data without issues in assigning too many levels to the ${}^4I_{\frac{11}{2}}$ multiplet, contradicting results already obtained for the ${}^4I_{\frac{15}{2}}$ multiplet, or having to rely on more exotic mechanisms, such as phonons or transfers of energy between sites, suggests that this is probably the correct assignment.

Comparison of Level Assignment with Literature

This assignment appears to resolve issues with Refs. [75] and [44], but not with Refs. [17] and [18]. The last two initially appear to be a mystery. However, if an

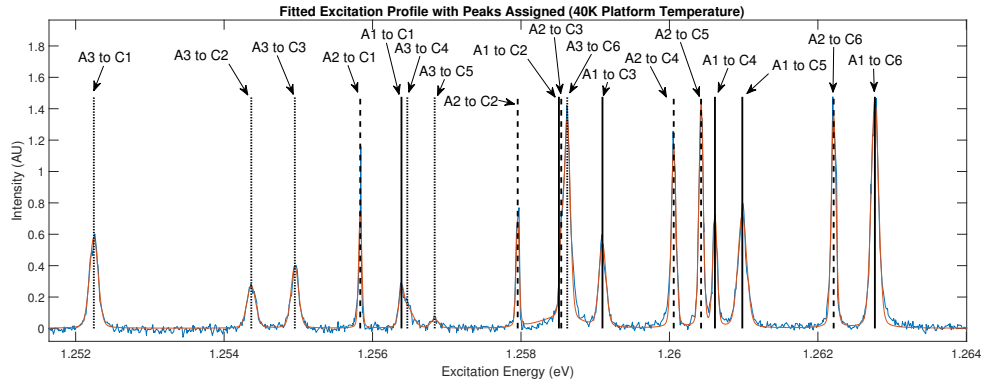


Figure 6.14: Fitted excitation spectrum with transition assignments labeled. Solid lines involve A1, dashed lines involve A2, and dotted lines involve A3.

offset value is added to the values from these two papers for this multiplet, the levels can be made to match levels presented here. Comparison of spectra presented in Ref. [18] using this offset reveal that their results and assignments are essentially identical to the ones presented here. This, and the inconsistency between the two papers with the same first author suggests an axis calibration issue for this particular range of energies.

After adding offsets, those two works appear to have no conflict with the assignments given here, or with each other. This also implies that the level assignment proposed here is not new. It can also be seen in these papers that the thermal behavior of the 1.2550eV peak has been reported previously. A comparison of assignments and levels is shown in Table 6.6.

Temperature Dependence of Peak Centers

The temperature dependence data also permits the analysis of changes in peak centers as a function of temperature, which will give an indication of the relative importance of temperature. Fitting these profiles and plotting the fitted energies as a function of temperature resulted in Figure 6.15. It appears that most of the energies

[75]	[44]	As given [18]	As given [17]	Offset [18]	Offset [17]	This Work
1.2564	1.2550	1.25417	1.25318	1.25631	1.25636	1.25639
1.2579	1.2564					
		1.25632	1.25530	1.25846	1.25848	1.25851
1.2592	1.2592	1.25704	1.25605	1.25918	1.25923	1.25911
1.2607	1.2607	1.25850	1.25742	1.26064	1.26060	1.26062
1.2611	1.2611	1.25881	1.25773	1.26095	1.26091	1.26098
1.2628	1.2628	1.26068	1.25961	1.26283	1.26279	1.26277

Table 6.6: Comparison of values (in eV) for the assignment of the levels of ${}^4I_{\frac{11}{2}}$.

do not fluctuate with more than random noise at the lower end of the temperature range here. There also seems to be some evidence of the energies changing over the whole range. It is likely that additional error is introduced by factors like small power fluctuations and imperfect precision of the wavelength meter. Errors on the order of a few hundredths of a meV appear to be typical, and should be considered when reviewing data presented here.

For the most part, however, it appears that comparing data at slightly different temperatures in the Montana Instruments Cryostation should not significantly impact the energies measured in this range.

If a Boltzmann distribution is assumed for the relative amplitudes of the peaks involving A3, with an associated energy of 4.13meV, one can make a rough estimate of the actual temperature of the point being measured. By interpolating by eye, at around 30K for the platform temperature, the relative amplitude appears to attain about half of its maximum value. This corresponds to $T = \frac{4.13 \times 10^{-3} \text{ eV}}{(\ln 2)(8.617 \times 10^{-5} \frac{\text{eV}}{\text{K}})} = 69 \text{ K}$. Of course, it is not unreasonable that the temperature at a point farther from the cooling apparatus than the platform thermometer (and with a laser focused on it) has a significantly higher temperature than that thermometer reads.

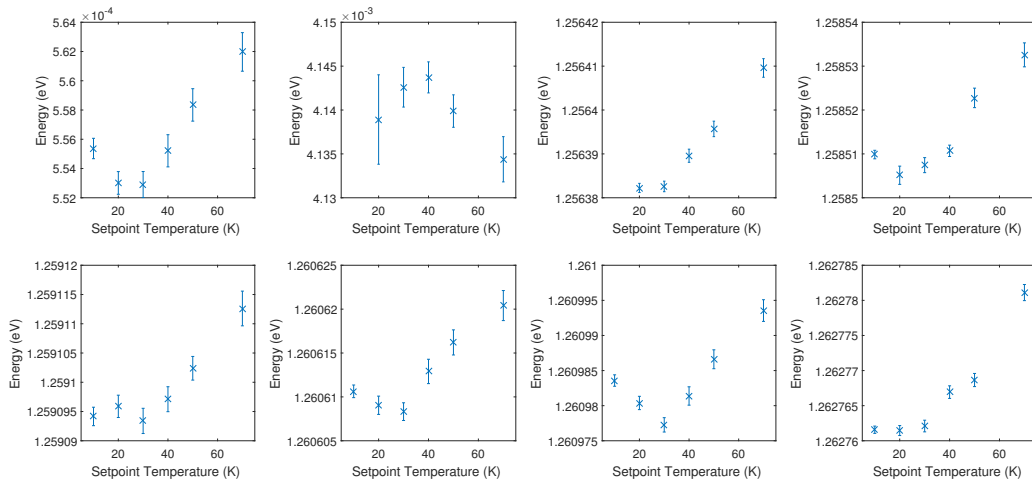


Figure 6.15: Fitted energies vs. platform setpoint temperature, with errors taken from the fitting algorithms used

Fitting Results- Parallel Field Case

In order to prevent issues arising from broader peaks, the fitting was conducted at the lowest possible temperature, which prevented observation of transitions from the A3 level.

The data were collected by ramping the magnetic field using the Montana Instrument Cryostation’s Magneto-Optic option magnet at each excitation wavelength. Unfortunately, this could create issues involving hysteresis, as discussed in Chapter 4. Of course, this ideally should produce a similar nonlinearity for all levels, and should be detectable. Fitting the apparent effective g factors using the scheme mentioned for the emission case, it appears that only one level in the upper multiplet may potentially have detectable nonlinearity, but this may have more to do with errors in the fitting than a real nonlinearity, given the similar magnitude of the error. The lowest two states do not seem to show appreciable nonlinearity, but this may be due to issues in field-step resolution, fluctuations in magnetic field values over time while using an electromagnet, and the comparatively low magnetic field

magnitude. Non-linearity, however, was observed in emission, as already discussed. It should be noted that not all spectra were used to calculate these values for each level. Some were excluded due to large errors or inconsistency with the rest of the fitted values.

It is worth noting that one effective g factor is close to 11 in this multiplet, implying that if C_{3v} symmetry applies, and since the Landé g factor for this multiplet is close to unity, this level would almost certainly need to be of crystal-field number $\frac{1}{2}$, as this level would need to be mostly of the character of the $m_j = \frac{11}{2}$ state for this result. Similar reasoning suggests that the level with the second highest effective g factor, nearly 9, would be a likely candidate for $\frac{3}{2}$. These possible crystal-field number assignments will be discussed later in this chapter.

Slight disagreements in the fitted effective g factor for the lowest two doubly degenerate levels may also reveal issues in calibrating the magnetic field between the two experiments, with differences on the order of ten percent. It should be noted that the hysteresis effects mentioned in the Chapter 4 would slightly increase calculated effective g factors for intermediate field values for this set of data, but not the emission data previously discussed (because of the different magnets used for each). The existence, however, of small discrepancies, implies that these measurements are unlikely to be able to determine which of two close values for an effective g factor is correct.

Fitting Results- Perpendicular Field Case

Generally, effective g factors were much smaller for this field orientation. The g_2 parameters described earlier were not fitted, partly for this reason. The fitted g factors for the lowest two doubly degenerate states of ${}^4I_{\frac{15}{2}}$ matches the emission results shown earlier reasonably well, but it is worth pointing out that both experiments were conducted with the same cryostat and magnet. If correct, the results imply issues for the validity of C_{3v} symmetry, in that two of these levels should have an effective g factor close to zero. Some of the levels did not appear to show significant splittings upon visual inspection, implying that this method is using restrictions

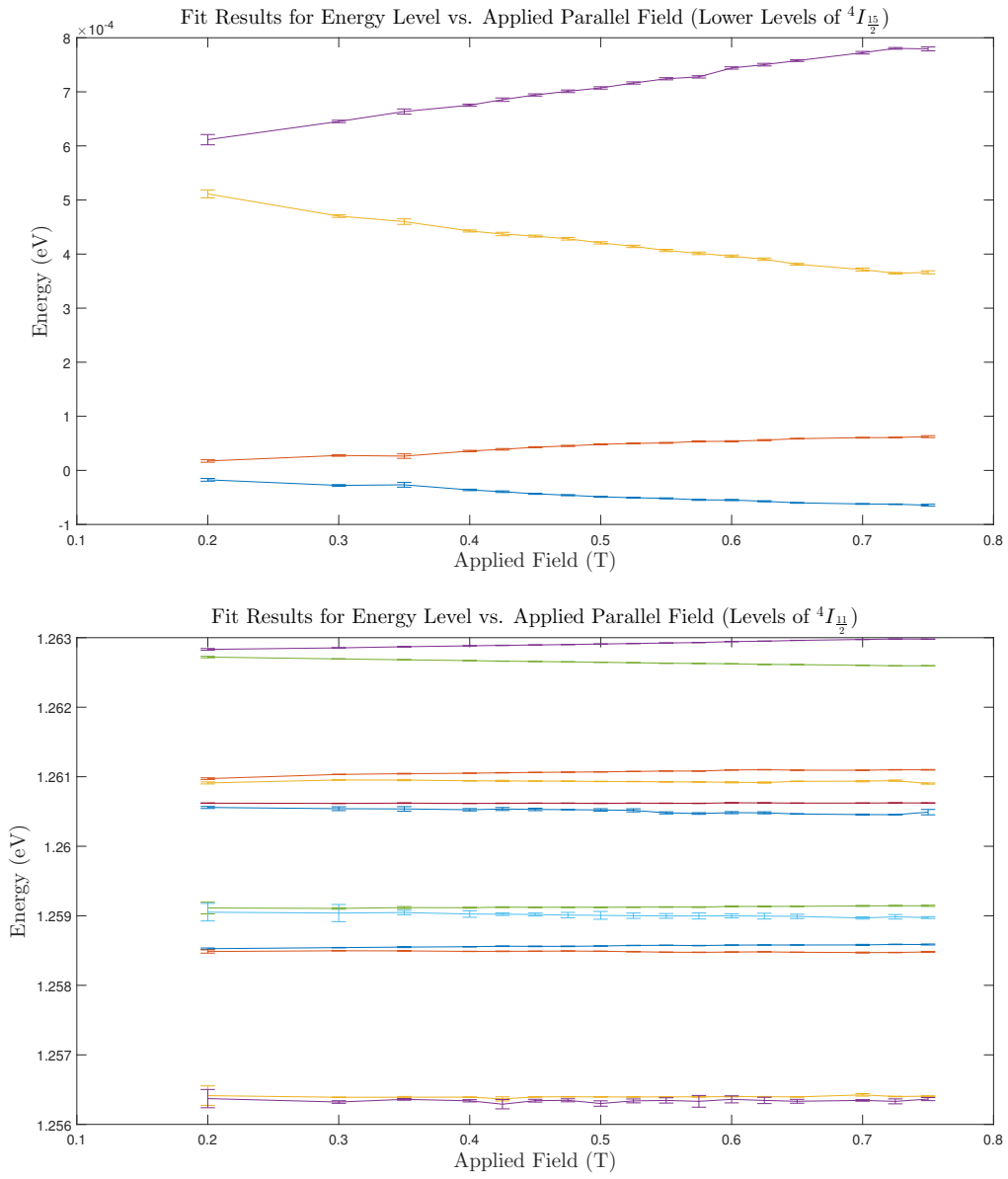


Figure 6.16: Fitted energy levels for A2373 with a magnetic field applied parallel to the c axis. Error bars correspond to a 95 percent confidence interval, using values from the fitting algorithm.

Multiplet	Energy (eV)	Fitted g Parameter	Fitted g_2 Parameter
${}^4I_{\frac{15}{2}}$	0	$3.10 \pm .08$	
	$0.0005614 \pm .0000006$	$9.97 \pm .05$	$-.22 \pm .36$
${}^4I_{\frac{11}{2}}$	$1.2563899 \pm .0000018$	$2.19 \pm .35$	-2.34 ± 2.4
	$1.2585213 \pm .0000014$	$2.81 \pm .10$	$.40 \pm .33$
	$1.2591095 \pm .0000018$	$4.10 \pm .30$	$.47 \pm 3.5$
	$1.2606201 \pm .0000008$	$3.76 \pm .19$	
	$1.2609935 \pm .0000009$	$4.72 \pm .10$	$0 \pm .72$
	$1.2627745 \pm .0000005$	$9.14 \pm .05$	$.38 \pm .34$

Table 6.7: These are fittings for the effective g factors, energy levels, and g_2 parameters for the parallel field case for excitation from ${}^4I_{\frac{15}{2}}$ to ${}^4I_{\frac{11}{2}}$. g_2 factors which seemed unrealistic are not included here. While fitting g factors given here, it was assumed g_2 values were zero. Errors are 95 percent confidence intervals derived from fitting algorithms.

Multiplet	Energy (eV)	Fitted Effective g Factor
${}^4I_{\frac{15}{2}}$	0	$7.65 \pm .28$
	$0.0005511 \pm .0000004$	$3.67 \pm .25$
${}^4I_{\frac{11}{2}}$	$1.2563870 \pm .0000007$	$1.65 \pm .28$
	$1.2584822 \pm .0000084$	*
	$1.2590971 \pm .0000008$	$4.81 \pm .79$
	$1.2606116 \pm .0000004$	$2.33 \pm .16$
	$1.2609795 \pm .0000008$	$1.54 \pm .30^{**}$
	$1.2627602 \pm .0000005$	$1.60 \pm .19^{**}$

Table 6.8: Fittings for the effective g factors, energy levels, and g_2 parameters for the perpendicular field case for excitation from ${}^4I_{\frac{15}{2}}$ to ${}^4I_{\frac{11}{2}}$. Errors are 95 percent confidence intervals derived from fitting algorithms. * For this level (the 1.2585eV peak), while a number with a nonzero error was returned by the fitting, it appeared to be fitting noise for this peak, due to low signal as the field magnitude increased. ** For these levels, visible splittings were not readily apparent in the spectra.

from other peaks to fit these peaks.

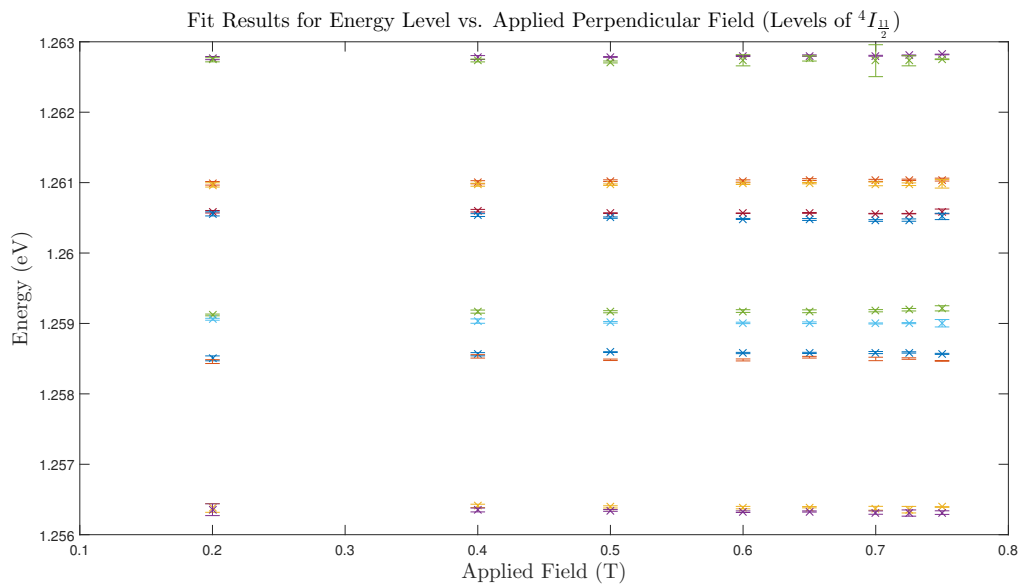
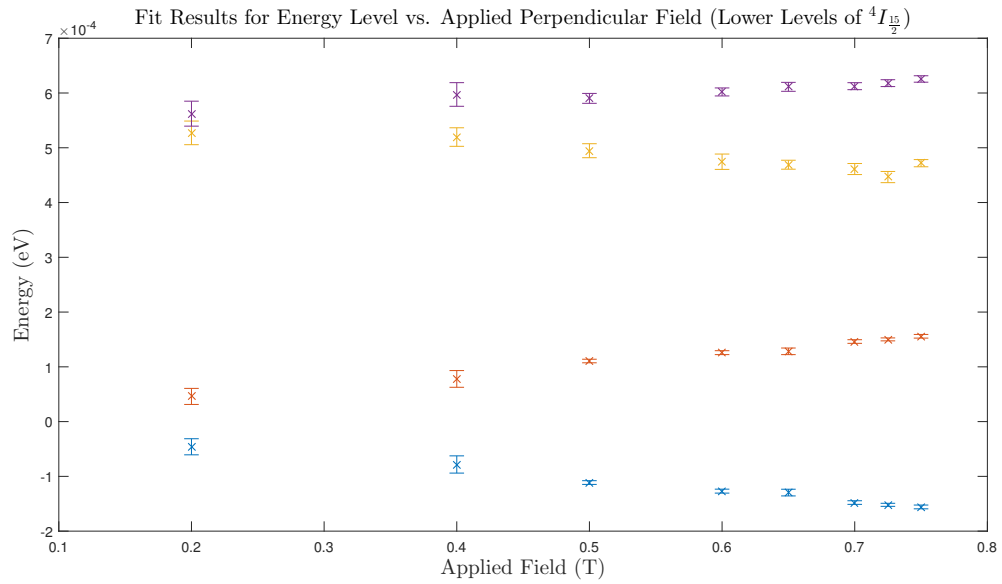


Figure 6.17: Fitted energy levels for A2373 with a magnetic field applied perpendicular to the c axis. Error bars correspond to a 95 percent confidence interval, using values from the fitting algorithm.

6.2 Polarizations

The majority site for Er doped GaN has already been investigated, some of which result in disagreements in the levels of the ${}^4I_{\frac{11}{2}}$ multiplet, as was discussed earlier in this chapter.[75] [44] Also earlier in this chapter, it was found that a level claimed in Ref. [44] not to split under a magnetic field applied perpendicular to the c-axis of the crystal, did, in fact, split substantially. This calls into question the crystal-field numbers presented in that work. This uncertainty makes polarization measurements in this material of importance.

It has now been shown that the levels do not have effective g factors similar to the erbium doped materials discussed in Chapter 5, implying that the ordering and character of individual levels may be significantly different. There could be a different degree of mixing of m_j states with the same crystal-field number.

6.2.1 Without a Magnetic Field

The emission transitions for ${}^4I_{\frac{13}{2}}$ to ${}^4I_{\frac{15}{2}}$ show no especially strong polarization, as seen in Figure 6.18, which appears to be typical in these measurements. The most striking results for the ${}^4I_{\frac{15}{2}}$ to ${}^4I_{\frac{11}{2}}$ polarizations, as seen in in Figure 6.19, are the two transitions involving A2 which appear to be strongly π polarized. given that two out of six levels of the upper multiplet have this behavior, it seems reasonable that this means that C2 and C5 should be assigned crystal-field numbers of $\frac{3}{2}$, while the other four should be assigned $\pm\frac{1}{2}$. Of course, this reasoning also implies that A2 also has this crystal-field number (despite a large perpendicular effective g factor). If it is considered for the moment that perhaps C_{3v} symmetry is broken to some degree, the assignment can continue on the basis of these polarizations. Since A1 does not seem to have this behavior for the excitation transitions, it is assigned $\pm\frac{1}{2}$.

The emission polarizations seem to suggest that A2 and A3 have similar behavior, but A1 and A2 do not. If the crystal-field number assignments suggested earlier are continued, and the slight biases in the emission polarization results are considered as the result of imperfect selection rules, this implies a crystal-field number assignment

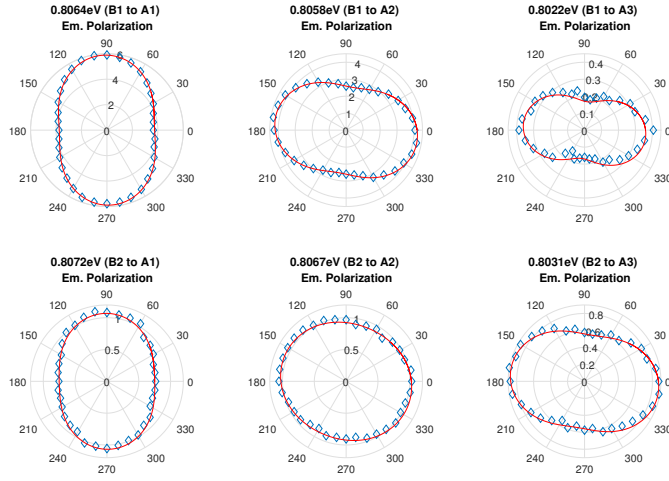


Figure 6.18: Emission polarizations for some of the transitions observed in Er doped GaN. Labels indicate assigned transitions. σ polarization corresponds to 90 degrees, and π to 0 degrees.

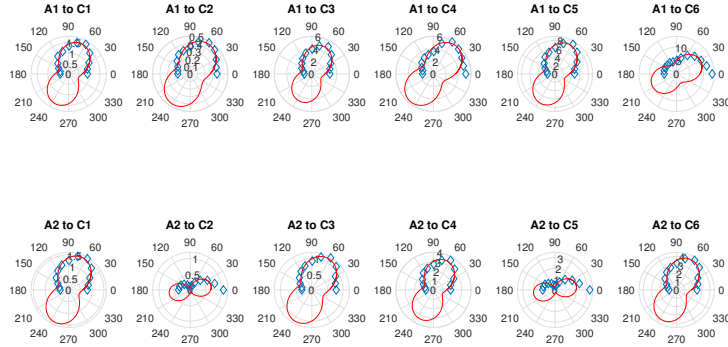


Figure 6.19: Excitation polarizations for some of the transitions observed in Er doped GaN. Labels indicate assigned transitions. σ polarization corresponds to 90 degrees, and π to 0 degrees.

of $\frac{3}{2}$ for A3, B1, and B2. As already mentioned, all of these levels have non-zero effective g factors for a field applied perpendicular to the c-axis.

It is still somewhat unclear what the correct crystal-field number assignments are, largely because of magnetic splitting results for the lowest energy multiplet which seem at odds with the assignments arrived at by polarization measurements.

The next subsection discusses polarization measurements for Zeeman split peaks, and provides more convincing evidence suggesting that the ground state must be assigned as $\pm\frac{1}{2}$.

As discussed earlier in this chapter, there is an avoided crossing between A1 and A2 between 1 and 2 tesla. If this is treated as a first order effect due to overlap in states (that is, shared states labeled with m_j quantum numbers) between these two levels, this implies the symmetry cannot be perfect. Near that magnetic field, of course, it is expected that these selection rules would break down, as the two states (A1 and A2) would mix, and the pure version of each state has differing selection rules.

6.2.2 With a Magnetic Field

Whereas the two materials in Chapter 5 produced sharp peaks which could be easily separated at relatively low magnetic field magnitudes, erbium doped gallium nitride presents difficulties in that regard. Thus, for the data presented here, spectra were fitted to obtain amplitudes. To accomplish this, four spectra for each of four polarization angles were fitted with parameters pertaining to peak centers, shapes, and widths shared in common, but unique amplitudes for each peak in each spectrum. While some peaks (A1 to C2, for example), appear not to fit well due to low signal to noise ratios, others (such as A1 to C6) appear to fit very well. The result of this fitting is shown in Figure 6.20.

The peak assigned to A1 to C6 in particular seems to have an interesting behavior, shown in Figures 6.21 and 6.22, with the peaks appearing to exhibit differing polarization behaviors. This is already visible in the raw data, without performing any fitting of amplitudes. It is not alone in this regard. A1 to C1 shows a similar result in the fitted data, also shown in Figure 6.22. A1 to C3 shows something similar, shown in Figure 6.23, but with different pairings. A1 to C5 shows all the peaks as σ polarized, shown in Figure 6.25. A1 to C4 is probably of this type of transition, but shows three π and one σ transition at face value, seen in Figure 6.24.

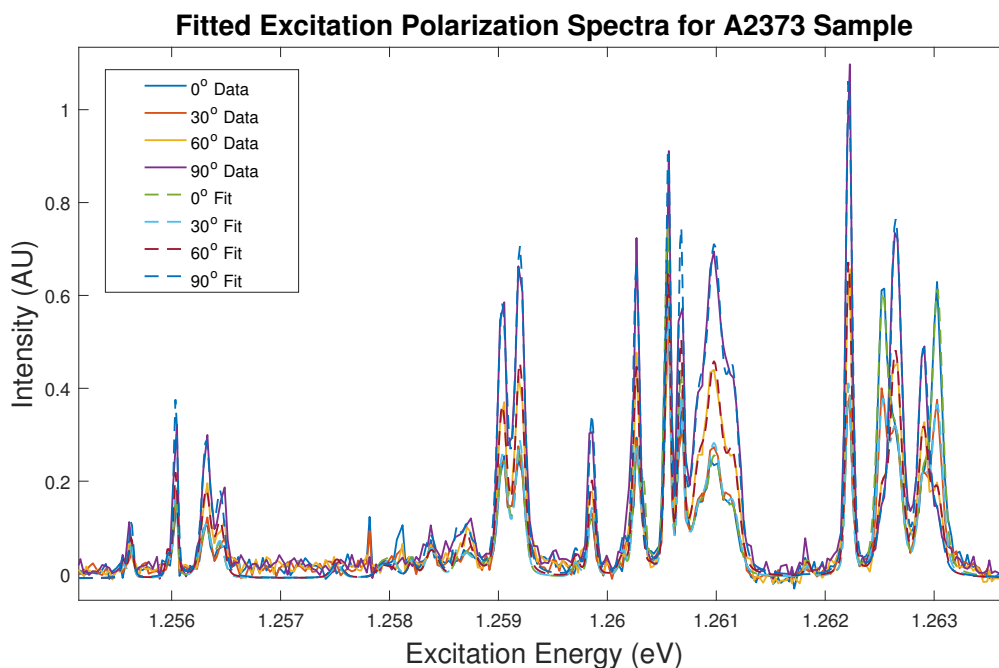


Figure 6.20: Fitted spectra for four excitation polarization angles for the A2373 sample. The magnetic field is parallel to the c-axis. This shows transitions involving from the lower levels of ${}^4I_{\frac{15}{2}}$ to the levels of ${}^4I_{\frac{11}{2}}$.

It is important to note that errors in closely spaced peaks may still adversely affect amplitude measurements, even with peak fitting in use. Two peaks for A1 to C2 were not judged sufficiently greater than noise to merit including, but the two remaining appear π polarized, also shown in Figure 6.25.

This raises a few questions. First, for the zero field case, this peak seemed to be somewhat more biased towards π polarization. Some sense could be made of the result if it is accepted that a crystal-field number of $\pm\frac{1}{2}$ describes both A1 and C6, and changes involving opposite vs. same sign crystal-field numbers produce different polarizations. Strictly speaking, this result is not disallowed for such a crystal-field number assignment under C_{3v} symmetry for electric dipole transitions. This difference in crystal-field number assignment between this and the previous two materials would justify why this phenomenon did not occur in those materials.

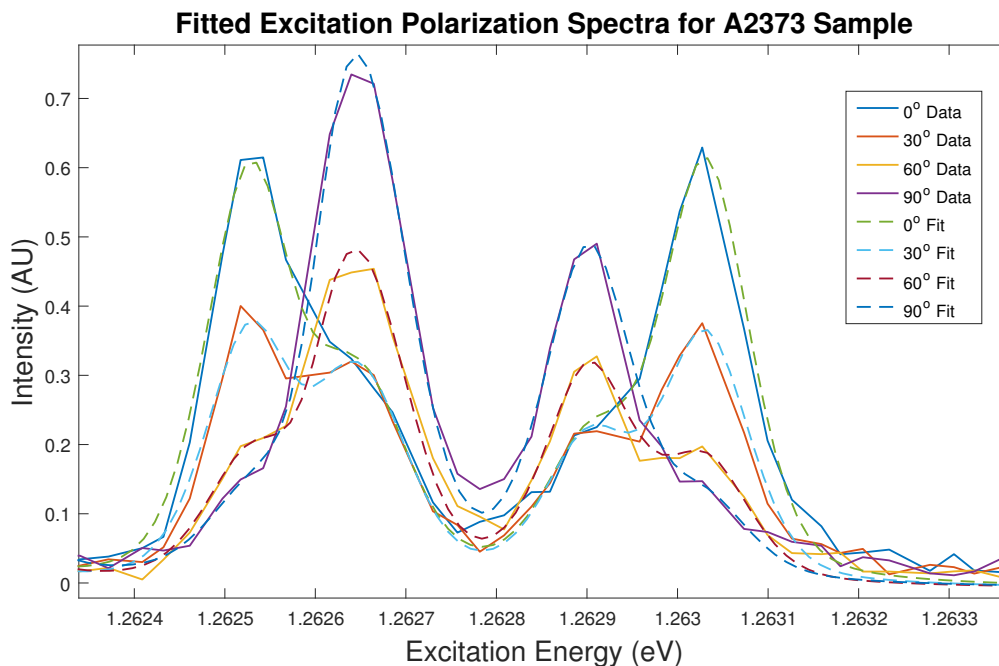


Figure 6.21: Fitted spectra for four excitation polarization angles for the A2373 sample. The magnetic field is parallel to the *c*-axis. This shows four split peaks from the level assigned as A1 to C6.

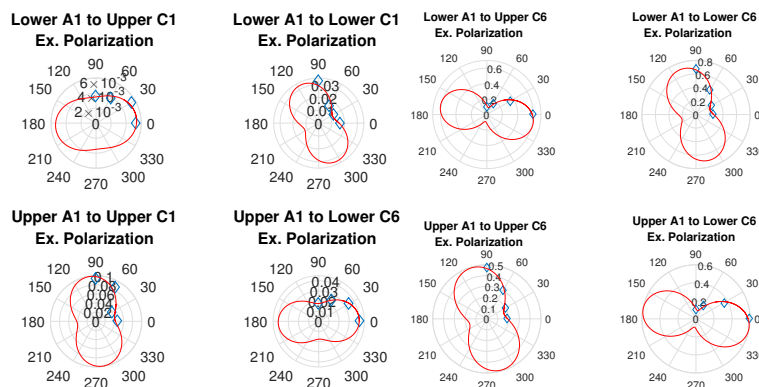


Figure 6.22: Excitation polarizations for the four peaks originating from magnetic splitting of the A1 to C6 and A1 to C1 transitions for the majority site for Er in GaN. These are expected to be π and σ polarized.

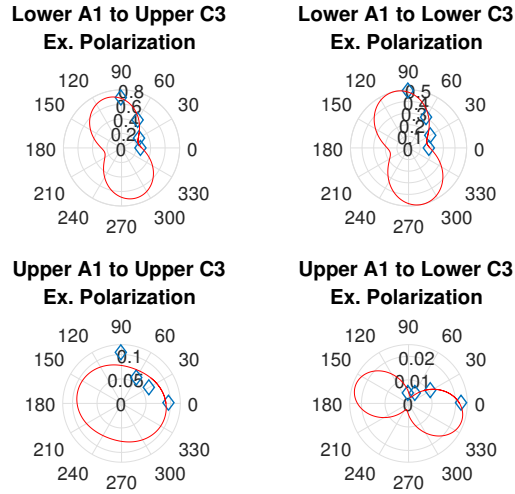


Figure 6.23: Excitation polarizations for the four peaks originating from magnetic splitting of the A1 to C3 transition for the majority site for Er in GaN. These are expected to be π and σ polarized.

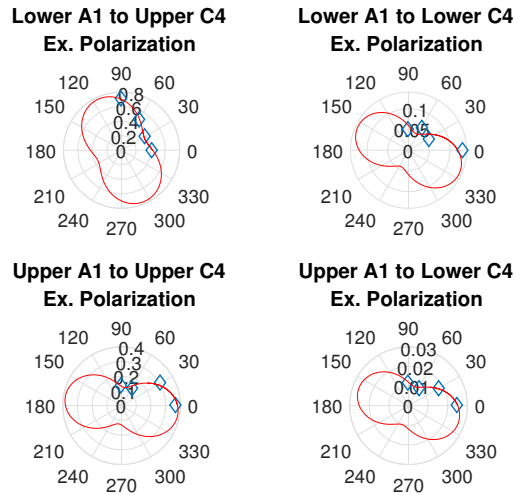


Figure 6.24: Excitation polarizations for the four peaks originating from magnetic splitting of the A1 to C4 transition for the majority site for Er in GaN. These are expected to be π and σ polarized.

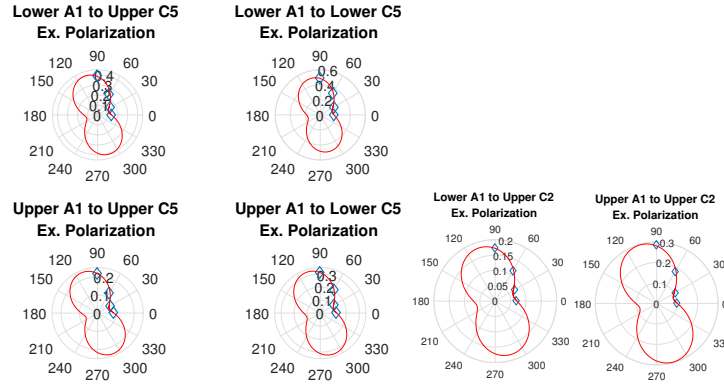


Figure 6.25: Excitation polarizations for the four peaks originating from magnetic splitting of the A1 to C5 and A1 to C2 transitions for the majority site for Er in GaN. These are expected to be π polarized.

This may simply suggest that the portion of the selection rules corresponding to transitions between crystal-field numbers $\pm\frac{1}{2}$ ought to be expanded to separate these into $+\frac{1}{2}$ and $-\frac{1}{2}$ under the influence of a magnetic field. Requiring that the representation for z , corresponding to the dipole operator for π polarization, still acts like the identity operator in multiplication, transitions between levels of the same crystal-field number must be π allowed. It should be noted that since in this case, the rotation axes for the magnetic field and the crystal-field match, the irreducible representation for z acts in this way for both $SO(2)$ symmetry of the magnetic field and C_{3v} symmetry of the crystal-field. This would imply for the above transition that the upper (lower) level of C6 and the lower (upper) level of A1 are of the same sign of crystal-field number, whereas the lower (upper) level of C6 and the lower (upper) level of A1 are of different signs of crystal-field number.

Following through, the σ polarization of all the split levels for A1 to C5 (the latter of which was assigned a crystal-field number of $\frac{3}{2}$), and the argument above strongly suggest the ground state must have crystal-field number $\pm\frac{1}{2}$. This also suggests that the selection rules for C_{3v} symmetry are still valid at this magnetic field.

It appears that the selection rules predicted for C_{3v} symmetry generally continue

to describe the polarization results at an applied magnetic field of about 0.75T to a degree comparable to the zero magnetic field case. There was also some additional insight into the polarizations involving A1 for erbium in gallium nitride which seemed to confirm a crystal-field number of $\pm\frac{1}{2}$.

6.3 Conclusions and Future Work

6.3.1 Nonlinear Zeeman Splittings

This work suggests that several avoided crossings may be present at higher fields, and provides starting parameters that should enable similar analysis of higher resolution (in magnetic field) data, and data going to higher magnitude applied magnetic field. It is suggested that a high quality sample (in the sense of having sharp, discernible transitions) be used. A similar approach could also be applied to other multiplets as a means of confirming energy level assignment.

So far, however, it appears that the apparent nonlinearity described qualitatively in Refs. [44] and [75] may be predominantly due to shifting of centers of levels rather than significant changes in the effective g factors. Of course, while this could be indicative of other interesting interactions, it does not successfully explain differences in measured effective g factors. Even the avoided crossing involving the ground state does not seem to be sufficient to account for the discussed discrepancies in the ground state effective g factors. It also appears that it is difficult for this method to measure these g factors at field magnitudes less than a few tenths of a tesla, suggesting that if significant nonlinearities appear between 60 and 90mT, this setup likely would not be able to identify them.

The observed avoided crossing involving the ground state also gives potentially useful restrictions (in terms of field magnitude) for measuring the ground state effective g factor in a valid way. In addition, this process has also provided strong verification for the assignments of the levels discussed in this section, specifically, the lowest three doubly degenerate levels of ${}^4I_{\frac{15}{2}}$ and ${}^4I_{\frac{13}{2}}$, and all the levels of ${}^4I_{\frac{11}{2}}$.

From the point of view of someone seeking to determine the exact properties of

the ground state, these avoided crossings might be highly advantageous, as fittings of these avoided crossings could be used to determine or at least restrict how m_j states might be shared between crystal-field split levels.

6.3.2 Level Assignments and Properties

The success in fitting spectra confirms that the energy levels listed in this chapter are likely to be correct. It appears possible to assign crystal-field numbers consistent with the polarization data. However, there seem to be conflicts with assigning a crystal-field number of $\frac{3}{2}$ to A2 and A3, because while the polarization data appears to require this, the magnetic splitting data suggests a significant, non-zero effective g factor for a magnetic field applied perpendicular to the c -axis of the crystal. This may suggest either some breaking of C_{3v} symmetry, or an unusual case in which the comparatively small spacing between A1 and A2 (0.55meV, compared to a typical value of about 7meV for the same levels in the other two systems) causes higher order effects to be more relevant.

This has an important ramification, if correct, that the perpendicular effective g factor being nonzero is not sufficient evidence for a crystal-field number of $\pm\frac{1}{2}$ for closely spaced levels.

Table 6.9: Suggested crystal-field number assignments for the majority site for erbium in gallium nitride. A * indicates that the assignment is in apparent conflict with the effective g factors measured for a magnetic field perpendicular to the c-axis.

Level	μ
Ground (A1)	$\pm\frac{1}{2}$
Second ${}^4I_{\frac{15}{2}}$ (A2)	$\frac{3}{2}^*$
Third ${}^4I_{\frac{15}{2}}$ (A3)	$\frac{3}{2}^*$
First ${}^4I_{\frac{13}{2}}$ (B1)	$\frac{3}{2}^*$
Second ${}^4I_{\frac{13}{2}}$ (B2)	$\frac{3}{2}^*$
First ${}^4I_{\frac{11}{2}}$ (C1)	$\pm\frac{1}{2}$
Second ${}^4I_{\frac{11}{2}}$ (C2)	$\frac{3}{2}$
Third ${}^4I_{\frac{11}{2}}$ (C3)	$\pm\frac{1}{2}$
Fourth ${}^4I_{\frac{11}{2}}$ (C4)	$\pm\frac{1}{2}$
Fifth ${}^4I_{\frac{11}{2}}$ (C5)	$\frac{3}{2}$
Sixth ${}^4I_{\frac{11}{2}}$ (C6)	$\pm\frac{1}{2}$

Chapter 7

Investigation into an Asymmetry in Zeeman Split Peaks

7.1 What is this Asymmetry?

It was previously observed that reversing the direction of an applied magnetic field oriented parallel to the *c*-axis of some samples led to differences in amplitudes of observed emission spectral lines. Since this reversal amounts to running time backwards, this was not expected unless some other source of asymmetry is present (presumably, one which would also change sign with time-reversal, preserving that symmetry overall). This was observed in both Nd and Er doped GaN epitaxial films. A figure from [75] demonstrates this result.

To give a short description of the effect, it is the change of relative amplitudes of Zeeman split spectroscopic peaks when only the sign of an applied magnetic field is changed. Ultimately, this implies a change in transition probabilities.

So far, it appears that no other research group has reported the same effect. It is not obvious how it could arise. Magnetic fields, arising from the motion of electrons, reverse direction when the direction of time is reversed. A CPT symmetry operation, a reversal of signs of charges, parity of particles, and the direction of flow of time, is required to be a symmetry. Reversing the signs of charges does not

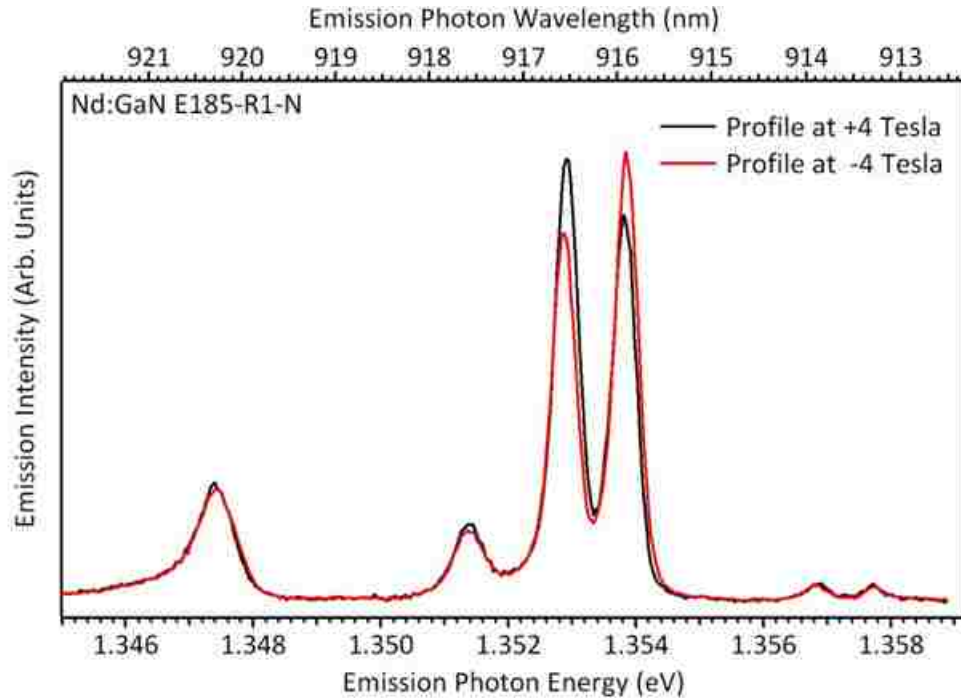


Figure 7.1: Comparison of spectra taken for a Nd doped GaN sample with a magnetic field applied parallel and antiparallel to the c-axis. The figure is taken from Ref. [75].

appear to change whether an electric field is attractive or repulsive, because both the charges producing and experiencing a field change sign, so this operation is not quite equivalent to simply reversing the signs of electric fields. It also does not change the relative positions of ions in the crystal. One solution is that the root cause of the asymmetry also changes sign with time-reversal, such as an intrinsic magnetic field. In short, the effect initially looks like a potential violation of T symmetry, and one possible solution would be an interesting discovery.

The initial thinking was that this may have something to do with ferromagnetism, such as a linear magnetostriction mechanism, or perhaps some special property derived from the samples being strained films. The latter was suspected due to a result suggesting that the degree of strain in the epitaxial film correlated with

the degree of difference in the spectra for Er doped GaN. [74]

Several new results were obtained which suggest a reexamination of these ideas is merited.

7.2 Theoretical Difficulties

7.2.1 Transition Probabilities

Ultimately, calculating a change in amplitude of a peak requires a calculation of transition probabilities. As was suggested in the previous chapters, electric dipole moments were thought to be the primary contributions to several transitions, particularly those which obey the electric dipole selection rules for the associated symmetry group. Since the transitions discussed in this work all involve 4f electrons with the same parity, in vacuum, electric dipole moments are expected to be zero. This implies that the transition probabilities must be largely due to the perturbing terms associated with the crystal-field.

A framework for these calculations does exist, Judd-Ofelt Theory, which ties relative intensities to three parameters (in addition to parameters used to calculate energy levels discussed in Chapter 2). [24] Some drastic assumptions are made in order to calculate the dipole moments, including that all sublevels of a given even parity state have the same energy. It comes to the following result for the oscillator strength of an electric dipole transition.

$$f_{ED}^{abs} = \frac{8\pi^2 m_e}{3h} \frac{\nu}{2J+1} \frac{\chi_{ED}^{abs}}{n} \sum_{\lambda=2,4,6} \Omega_{(\lambda)} (\langle l^N SLJ || U^{(\lambda)} || l^N S' L' J' \rangle)^2$$

χ_{ED}^{abs} is a constant, ν is the frequency corresponding to the transition, n is the number of electrons, the Ω values are the intensity parameters mentioned, and the reduced matrix elements for U were discussed in the second chapter. Notice that the above does not give any clear insight into what happens when a magnetic field is added or reversed. The situation is similar for the magnetic dipole moment. Here, g is the gyromagnetic ratio for the electron, roughly equal to two.

$$f_{MD}^{abs} = \frac{h\nu}{6m_e c^2} \frac{n}{2J+1} (\langle l^N SLJ || L + gS || l^N S' L' J' \rangle)^2$$

The framework is considered largely successful, with a handful of problem cases, such as Pr^{+3} . Extensions often attempt to add terms, perhaps at the cost of physical meaning of the parameters. [24]

Still, it would be surprising to find that a basic theory of oscillator strengths produces different values depending on the sign of an applied magnetic field. Note that the energy levels themselves are determined by whether the magnetic moments associated with the electrons have a particular angle relative to an applied field, so an explanation based on such a breaking being due to reversed relative angles of magnetic fields would not work either. This implies a source of symmetry breaking that is not expected to appear in this framework.

7.2.2 Crystal-Field Distortions

One possible approach is to assume that something happens to change the crystal host structure in such a way that there are essentially two configurations of the local environment for the dopant ion for each sign of the magnetic field. This is, however, not straightforward to establish. To do so, one would need to identify a quantity that changes with magnetic field which is likely to correlate with changes in the structure, such as strain. The use of Raman spectroscopy to identify strain will be discussed later.

Magnetostriction

Magnetostriction has been known for well over a century, an effect in which applying a magnetic field causes physical deformation in a material. [27] The effect is a property of ferromagnetic materials, and typically proportional to the square of a magnetic field. [33] Both of those points raise potential issues. For the former, as will be seen, a variety of host materials appear to exhibit this effect, and it would be surprising if all of them exhibit ferromagnetism with comparatively high Curie temperatures (in excess of 120K for the erbium doped lithium tantalate sample

used). For the latter, an effect proportional to the square of the magnetic field would not cause a difference for different signs of an applied field.

Effects can be envisioned which depend on the magnetic field, but what is ultimately required is an effect which depends on the sign of the magnetic field. It is known that materials which are antiferromagnetic and belonging to one of 35 magnetic crystal classes can exhibit magnetostriction with a linear term. [2] These classes include the symmetry groups associated with the crystal hosts used in this chapter. Of course, this also implies that a type of ferromagnetic ordering is required to be present in all these materials .

This inspired an investigation into how the effect varies as a function of the applied magnetic field.

Piezoelectrics and Ferroelectrics

If some mechanism like magnetostriction is in fact present, it is possible to establish that this can couple with changes in electric fields via piezoelectricity or ferroelectricity. This inspired an investigation into whether the c-axis of a ferroelectric has some special importance with regard to this effect.

7.2.3 Numeric Measure

To adequately answer questions about dependence on other variables, a numeric measure of the degree of the effect is required. It was observed in erbium doped lithium tantalate that the effect seemed to occur in pairs of the four peaks magnetically split from an original peak. This inspired the following measure.

First, identify the aforementioned four peaks from one original transition for the same site. Next, subtract their spectra, and fit the difference using 4 peaks, which can have negative amplitude (using only three parameters to describe their centers, as was done in chapters 5 and 6). Then, subtract the sum of the amplitudes of one pair of peaks with similar behavior from the sum of the amplitudes of the other pair of peaks. Scale this number by the average intensity of the original peaks.

Of course, one has to select a convention which may reverse the sign of the

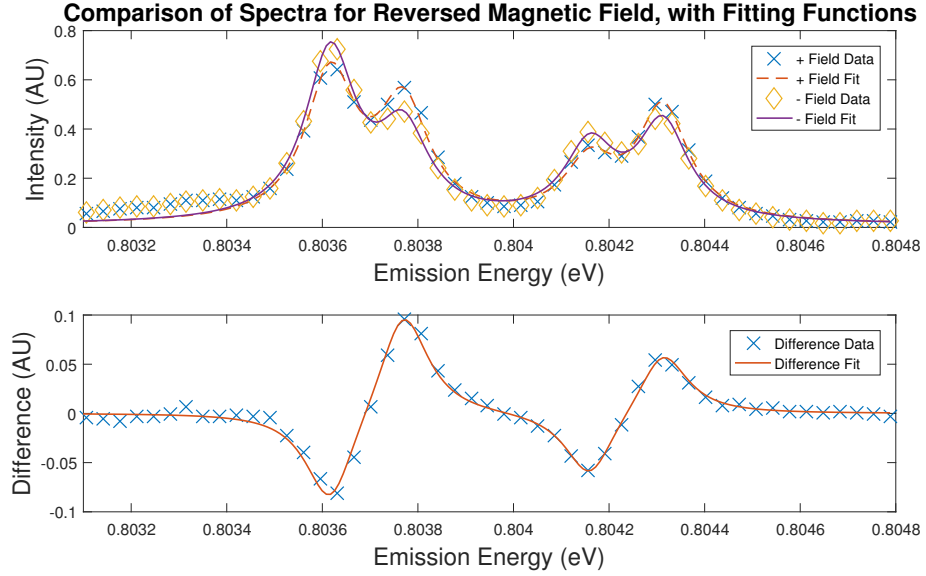


Figure 7.2: Typical difference in spectra for a field applied in one direction, and then reversed. Data fitted to determine a measure of the asymmetry. Spectra from Site A in erbium doped lithium tantalate.

measure. In the example shown here, if the second and fourth peaks (numbering starting from the lowest energy peak) give a positive value for the difference, the first and third give a negative difference. If a positive value is desired, using the results of fitting this data (and for the moment, ignoring questions of exact precision),

$$\frac{(\Delta A_2 + \Delta A_4) - (\Delta A_1 + \Delta A_3)}{A_1 + A_2 + A_3 + A_4} = \frac{(.111 + .066) - (-.099 + -.070)}{0.636 + 0.405 + 0.261 + 0.423} = 0.200$$

In the above, A refers to a peak's amplitude, and ΔA to the difference in amplitudes when the two spectra are subtracted. Thus, for this particular peak in this spectrum, a value of 0.2 would be used to describe the degree of asymmetry. This combines the behavior of several peaks. If the ratios of the difference to the average amplitude of each peak are considered separately, one obtains -0.156, 0.244, -0.268, 0.156, in order of increasing energy. It was decided that combining behaviors of

several peaks was advantageous in determining what other variables might correlate with the overall effect.

7.3 Results to Date

Investigation into this effect led to a large number of specific measurements and results. Lacking a definitive reason for the asymmetry to appear at all, some of these were attempted simply to determine whether or not they played a role. Others were attempted with a particular potential mechanism in mind, such as determining whether the asymmetry was somehow tied to the c-axis for the crystal hosts used.

Unless otherwise noted, all experiments using the Montana Instruments Cryostation with Magneto-Optic option were conducted at the lowest temperature achievable at the time of the experiment, which typically corresponded to temperatures measured on the platform thermometer between 4K and 15K, with the complication that different thermal shielding, sample mounts, and remounting of the platform thermometer over the course of years may mean that some differences in this measured temperature may not be particularly meaningful in terms of the actual temperature of the sample.

7.3.1 Consistency Issues with Neodymium doped Gallium Nitride

A large, obvious instance of the effect was observed in emission in [75]. Originally, it was hoped to use this material in order to determine a number of additional properties of the effect.

The samples used for this work are the same as those used in [75], grown by Plasma Assisted Molecular Beam Epitaxy (PA-MBE), as described in [62]. They are all $1\mu m$ thick layers of GaN:Nd of varying concentration, on a $200nm$ undoped GaN layer on c-plane sapphire.

This material presented a stubborn problem of inconsistency in the asymmetry results. Possible reasons for this will be discussed later, but include a temperature

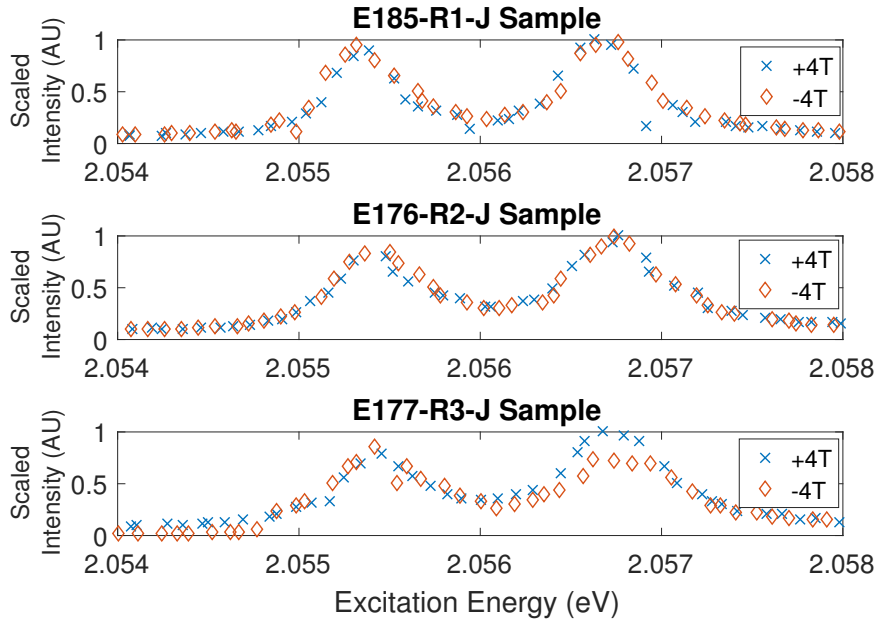


Figure 7.3: Comparison of scaled excitation profiles taken from CEES data for +4T and -4T magnetic fields applied parallel to the c-axis, using the the Janis brand cryostat and helium immersion superconducting magnet, thought to be at helium vapor temperatures (tens of K). Samples are Nd doped GaN epitaxial films. Emission energy was 1.355eV. Data shown was taken from three different samples in the same run of the experiment on the same day.

dependence for the effect, variations in angling of the sample relative to the applied magnetic field, and a possible aging of the sample.

Consider the ratio of the difference in the peaks to their sum. The results reported in Ref. [75] are quite large, with changes of tens of percent. Some runs conducted for this work showed no detectable asymmetry in emission, but significant asymmetry in excitation. This can be seen in Figure 7.5 and Figure 7.6. Some runs with multiple samples in the same run showed some samples had this effect, while others did not. This last point is shown in Figure 7.3, in which only one of the three samples showed what appeared to be a significant asymmetry effect in the excitation axis.

Recent results obtained using a Janis brand cryostat with an Oxford brand helium immersion superconducting magnet never showed the emission asymmetry, but often showed the excitation asymmetry. In one run with multiple samples, some samples which had previously shown an excitation axis effect showed neither effect, while other samples did show the excitation axis effect. In a result using the Montana Instruments Cryostation with Magneto-Optic option, emission axis asymmetry was observed, but of lesser degree than shown in Ref. [75], perhaps a few percent.

Unfortunately, a simple subtraction of spectra may be misleading for a small result, due to inhomogeneous line broadening, discussed earlier. If the center of an emission peak varies with excitation wavelength, it may be difficult to discern the difference between asymmetries resulting in small differences in amplitude of only slightly split peaks. and small shifts in the peaks relative to one another. This should not be much of an issue in the case of the Montana Instruments Cryostation results, in which changes in the sign of the magnetic field are conducted in seconds, rather than tens of minutes. However, the magnet used for that cryostat has limitations on field magnitude (not much more than 1-2T).

Although excitation axis asymmetry was not explicitly considered and measured in those past results showing strong emission axis asymmetry, it can be seen from a portion of a CEES under the influence of a magnetic field that it appears there may be one present. This can be seen clearly in a comparison of excitation profiles shown in Figure 7.5. There appears to be a trend where the split peaks decrease and increase together along the emission and excitation axes in a region with four split peaks in the CEES data, as shown in Figure 7.7. Of course, this is not definitive, but there does seem to be a similar behavior in data taken later.

Polarization control is probably not as significant in explaining the inconsistencies in the Janis cryostat results, because the geometry for these experiments was typically such that only σ polarized excitations and emissions should be possible. The result shown at the beginning of this chapter is thought to have been conducted in this way as well. Relative temperature can be compared by examining relative transitions involving thermally excited peaks. By this measure, results from the Janis brand cryostat I obtained are generally at higher temperature than the results

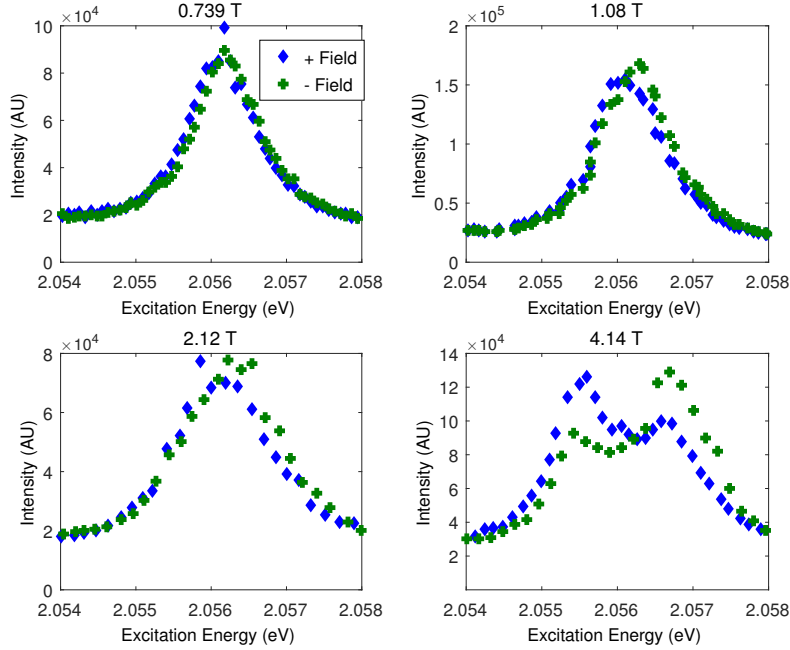


Figure 7.4: Excitation profiles from CEES data for sample E185-R1-N, for fields applied both parallel and anti-parallel to the c-axis with the indicated magnitudes. The two sets with lower field values were conducted on the Montana Instruments Cryostation setup, and the remaining two with the Janis brand cryostat setup.

in Ref. [75], but results I obtained using the Montana Instruments Cryostation are lower in temperature than either. Thus, a single threshold temperature for the effect cannot explain the absence of the emission axis effect.

One suggested idea for explaining this lack of emission axis asymmetry was a spatial dependence. If this were the case, it would be expected that the magnetically split emission peaks near 1.353eV would change in relative amplitude as the focal point of the confocal microscope moved across the sample. To test this, Attocube brand linear steppers were installed in the Janis cryostat system. A laser was kept at a fixed wavelength while a magnetic field was applied. The experiment had two components. First, a few lines across each sample were traversed, and the

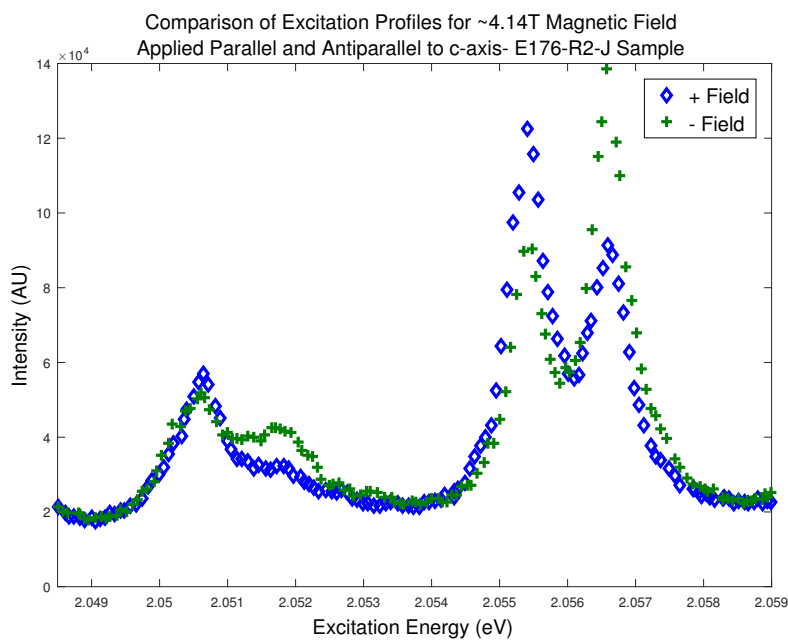
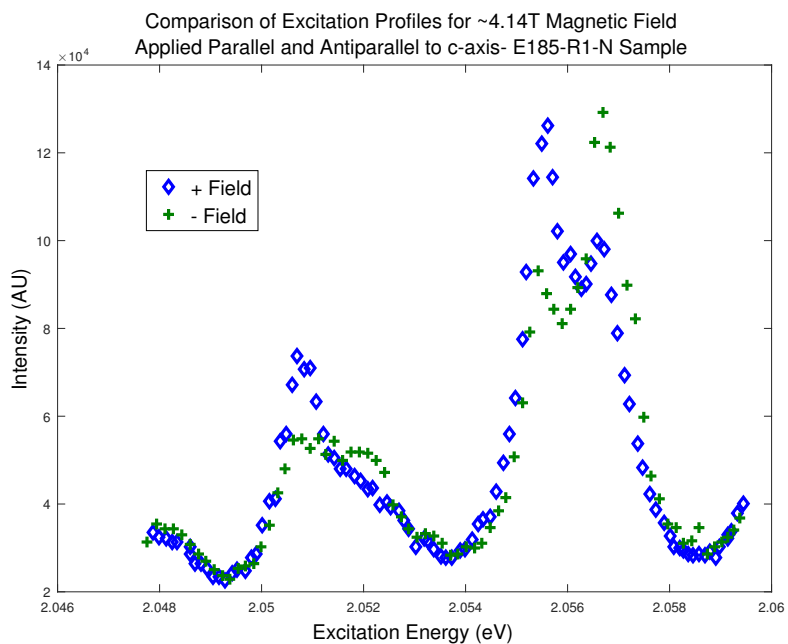


Figure 7.5: Comparisons of the asymmetry effect in excitation profiles from CEES data for two GaN:Nd samples.

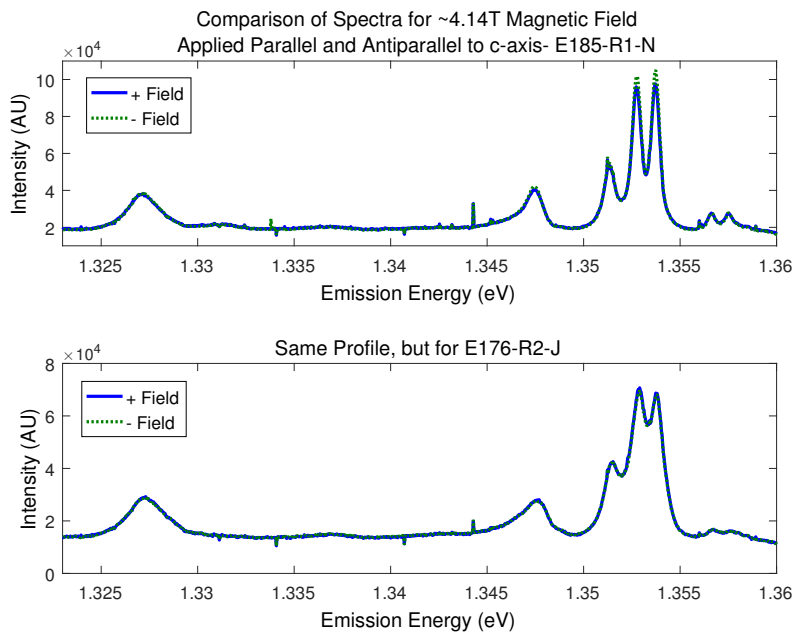


Figure 7.6: Comparisons of the asymmetry effect in emission profiles, taken from the same CEES data as the excitation profiles in Figure 7.5.

spectra were inspected visually. No discernible difference in relative amplitudes in the spectra was seen for any sample tried. Second, a small range spatial scan was conducted. It is estimated that the increment size used was at least one micron, and likely much more, but this is not known definitively. Then, the amplitudes of these peaks were determined by fitting them, and their ratios for each spatial point were examined. It appears that any fluctuations observed are likely random noise. Unfortunately, if both on a large and small scale, no discernible changes are evident, it would seem likely that there either is no significant spatial variation, or there exist small special spots which were not found.

This could be explained rather neatly if one posits that some sort of aging of the samples occurred over years, such as a relaxation of strain. The temperature differences in my own results may affect how well slight differences in spectra can

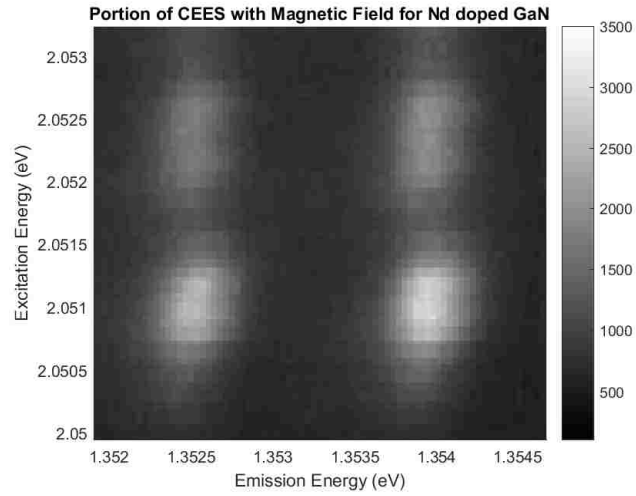


Figure 7.7: Portion of CEES under applied magnetic field from data taken by the author of [75]. Emission axis is approximate. Neodymium doped gallium nitride, but specific sample unknown.

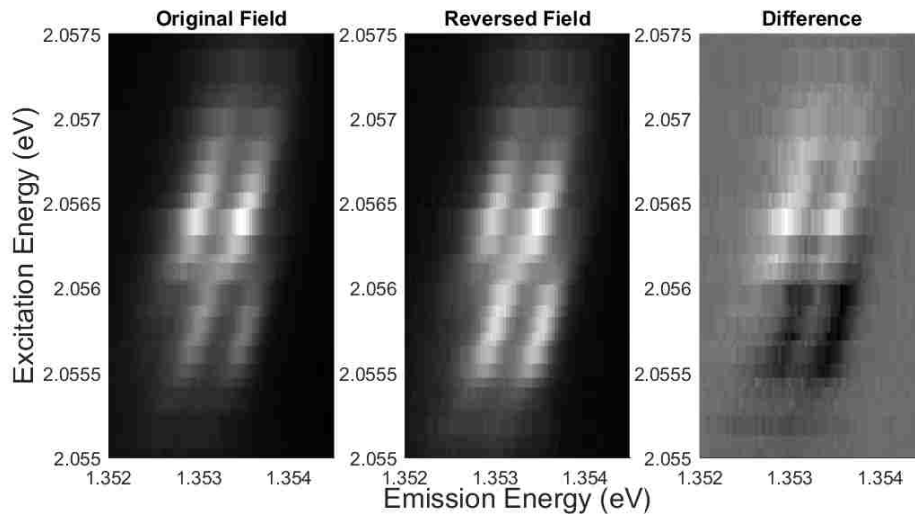


Figure 7.8: Comparison of portion of CEES for magnetic field applied parallel and antiparallel to the c-axis for sample E176-R2-J.

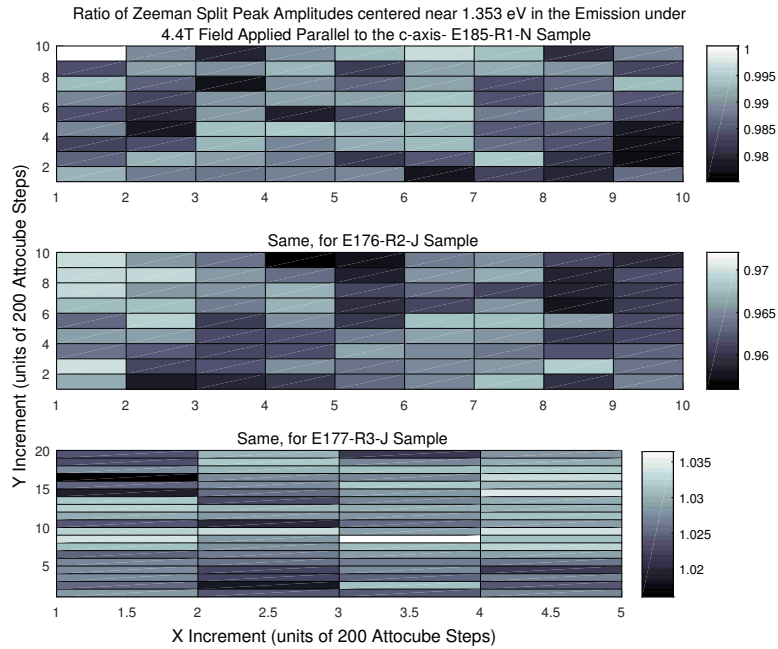


Figure 7.9: Comparison ratios of amplitudes of magnetically split emission peaks expected to experience changes in relative amplitude due to the previously observed asymmetry effect, as a function of approximate relative spatial location on the sample.

be detected. If the former is the case, this may be further evidence that strain plays a role.

7.3.2 Different Effects in Erbium Doped Gallium Nitride Samples

As already mentioned, previous results had shown this asymmetry in Er doped GaN, and noted a correlation between strain and the degree of asymmetry observed. Continuing on these observations, it was found that the asymmetry effect appears not only in the emission, but also in the excitation. There were some inconsistencies in

the excitation effect measurement, until equipment to control the excitation polarization was added, finding that this changed the asymmetry observed. Polarization dependence will be discussed in more detail later. The primary result was that different excitation and emission schemes exhibited the effect in different samples to different degrees.

It should be noted that some of the data shown here were generated in a regime (significantly above 1T, and sometimes above values mentioned as possible by the manufacturer) in which spatial variations in magnetic field produced by the Magneto-Optic module of the Montana Instruments Cryostation may cause some noticeable discrepancies between the magnetic field magnitude values shown here and the actual values of the magnetic field. It is in general thought to be the case that the actual magnetic field magnitudes were smaller than the values shown here. This should not be an issue with regards to comparing spectra for two signs of the same magnitude of field.

Samples used were the same as the samples used in Ref. [74], a set of epitaxial films of GaN:Er on various substrates, allowing differing strains. Results from experiments shown here were conducted differently from the results shown in prior works. In prior works, a particular applied field was first selected, and then a CEES map was taken at that field. This was repeated for the reverse field. Here, the steps in CEES described earlier were modified. At each excitation wavelength step, an emission spectrum was taken at each of the two applied magnetic fields. This was made possible by the use of a non-superconducting magnet for the Montana Instruments Cryostation. The advantage of this is that the same excitation wavelength steps (and ideally, laser power) should be used in comparing the two resulting CEES maps, permitting direct subtraction of emission spectra for comparison, without interpolation.

It should be noted that two particular forms of the asymmetry appear in CEES maps. One is along the emission axis, and the other is along the excitation axis. Curiously, while the [111] Si substrate showed very little in the way of changes in emission, it still showed significant changes in the excitation. The sapphire substrate sample, however, showed evidence of emission axis asymmetry in both situations,

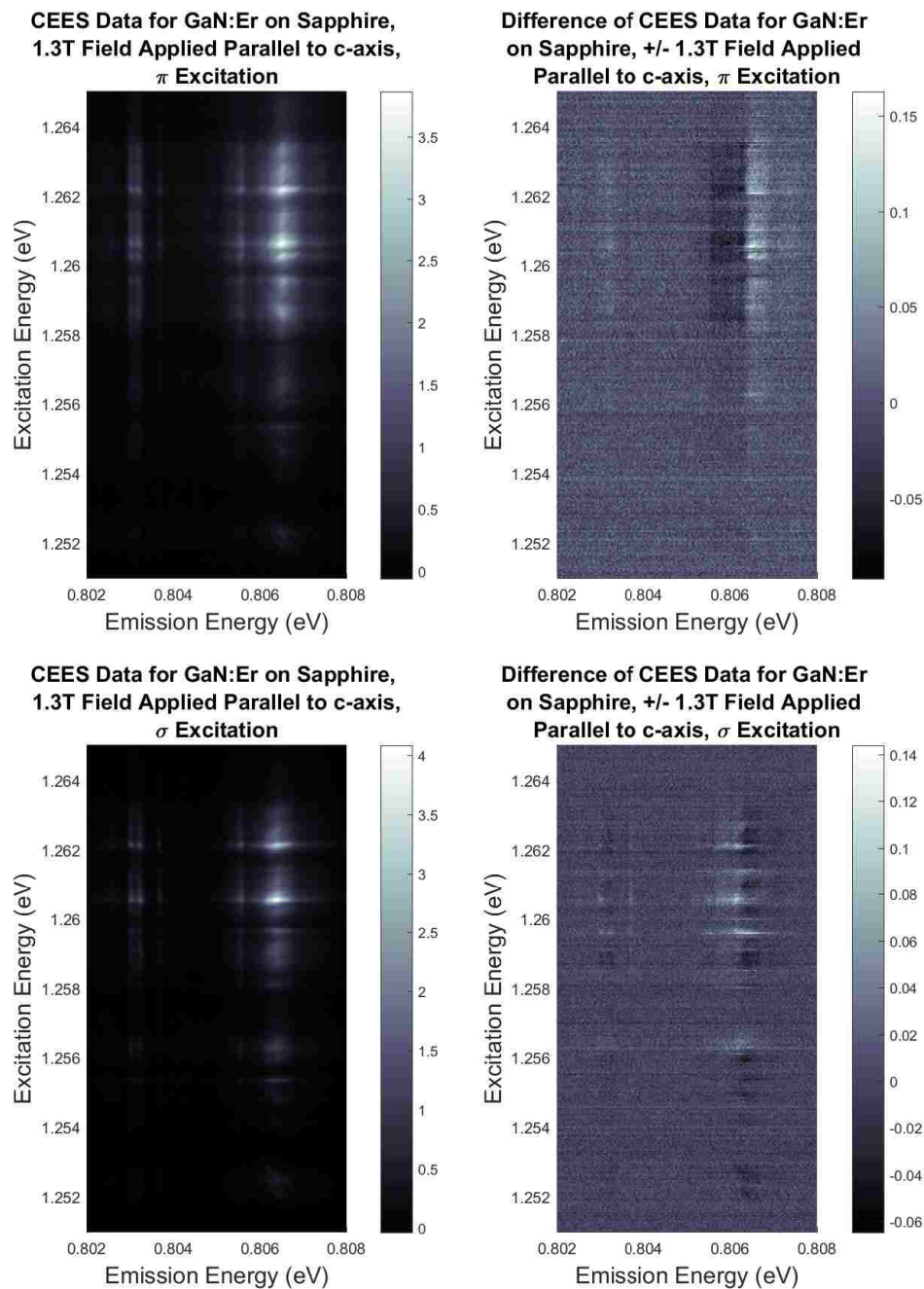


Figure 7.10: CEES data differences of CEES data for application of a magnetic field parallel and antiparallel to the c-axis. The sample used is the GaN:Er on sapphire substrate sample used in Ref. [74].

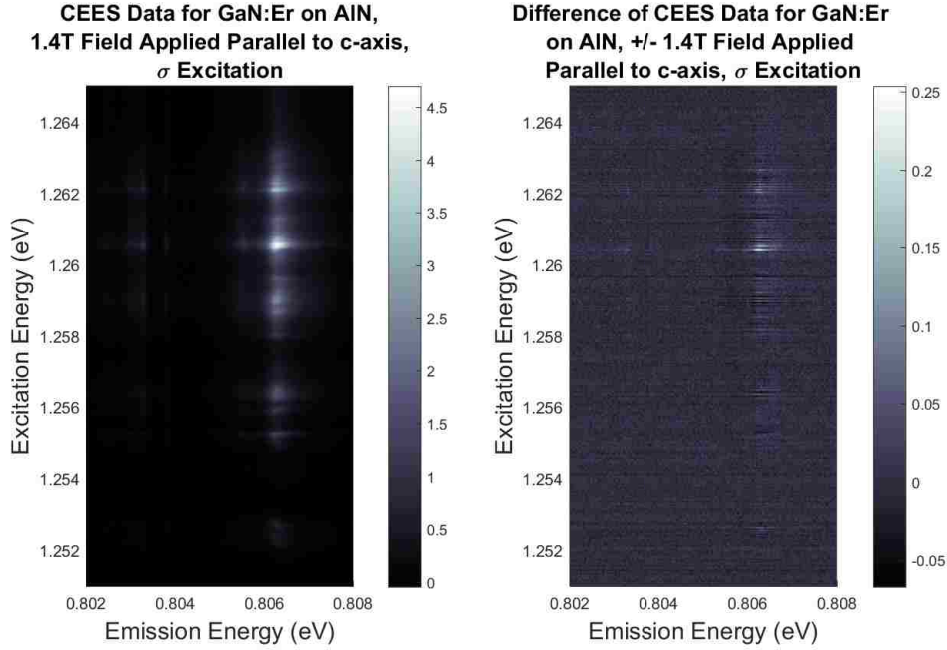


Figure 7.11: CEES data differences of CEES data for application of a magnetic field parallel and antiparallel to the c -axis. The sample used is the GaN:Er on AlN substrate sample used in Ref. [74].

and what appears to be an additional excitation axis effect for σ excitation. The results for the AlN substrate sample were similar to those for the sapphire substrate sample. It is difficult to say much definitively from the results shown here for the GaN substrate sample, owing to a much lower signal to noise ratio. These experiments were conducted with the beam path from the microscope to the sample orthogonal to the c -axis, which should allow both π and σ emissions to be collected. Emission polarization was not controlled at this point, but may have been affected by bias in the system.

These results can be examined in individual spectra as well. These comparisons of slight changes in field led to a question of whether these changes might be ascribed to small differences in maximum field intensity for each field direction. This was addressed by conducting a similar experiment, in which the applied field remained

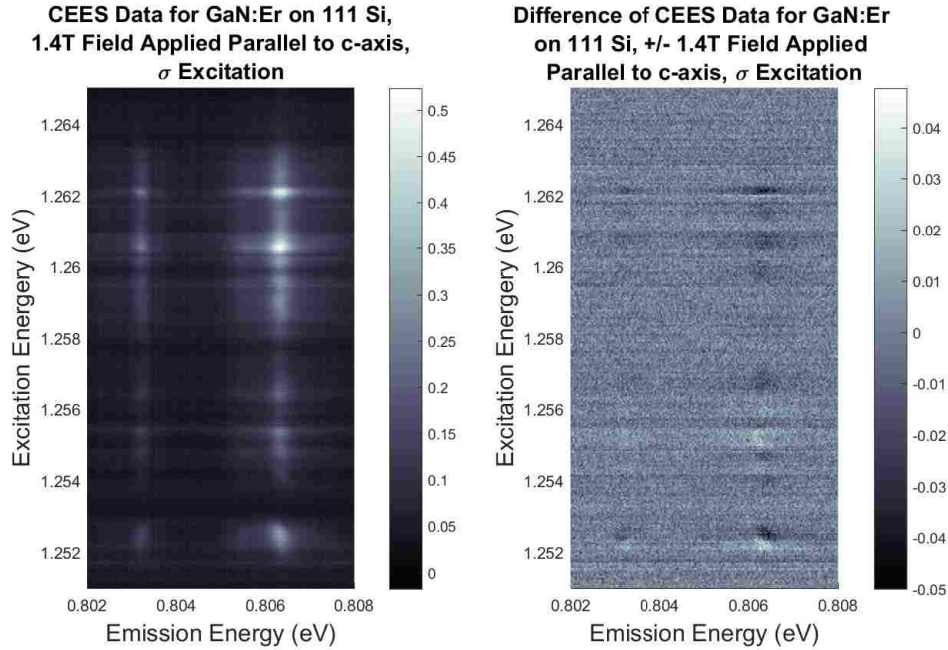


Figure 7.12: CEES data and differences of CEES data for application of a magnetic field parallel and antiparallel to the c-axis. The sample used is the GaN:Er on 111 plane Si substrate sample used in Ref. [74].

of the same sign, but its magnitude was changed by an amount thought to be larger than the precision of the magnet used. CEES were conducted for 1300mT and 1250mT on the [111] Si substrate sample. While no similar features appeared for this, signal was not especially high. Results shown later for other materials are far more convincing.

Results were also taken for the sample A2373, which was the sample used elsewhere in this work for measuring nonlinearities in magnetic splittings. This sample was used in that case for its sharp spectral lines. The fact that it displays this effect suggests that this appears even in samples thought to be of high quality.

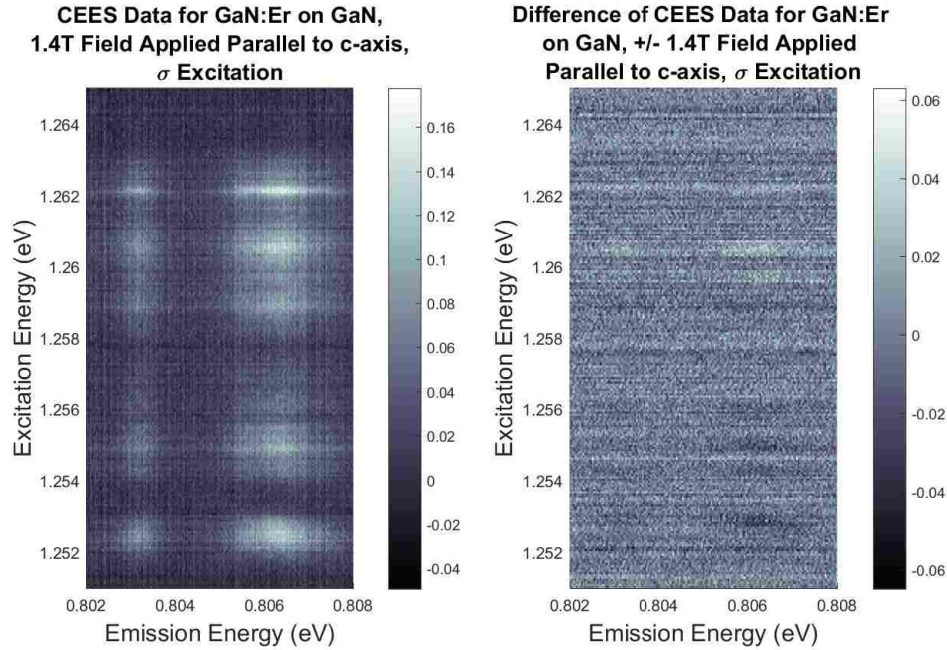


Figure 7.13: CEES data and differences of CEES data for application of a magnetic field parallel and antiparallel to the c-axis. The sample used is the GaN:Er on GaN substrate sample used in Ref. [74].

7.3.3 Bulk Crystal Hosts

The samples just discussed and which were used for prior measurements were thin films of gallium nitride grown on substrates. Other erbium doped host materials which were bulk single crystal also displayed the effect.

Er doped LiTaO_3

Lithium tantalate (and lithium niobate, to be discussed next) was chosen as a host material for this work for a few reasons. First, the samples available resulted in very sharp peaks, enabling the use of smaller magnetic fields. Second, the samples available were bulk crystals, giving insight into whether strained films are needed to observe the effect. Third, as a ferroelectric, the c-axis can be inverted by poling.

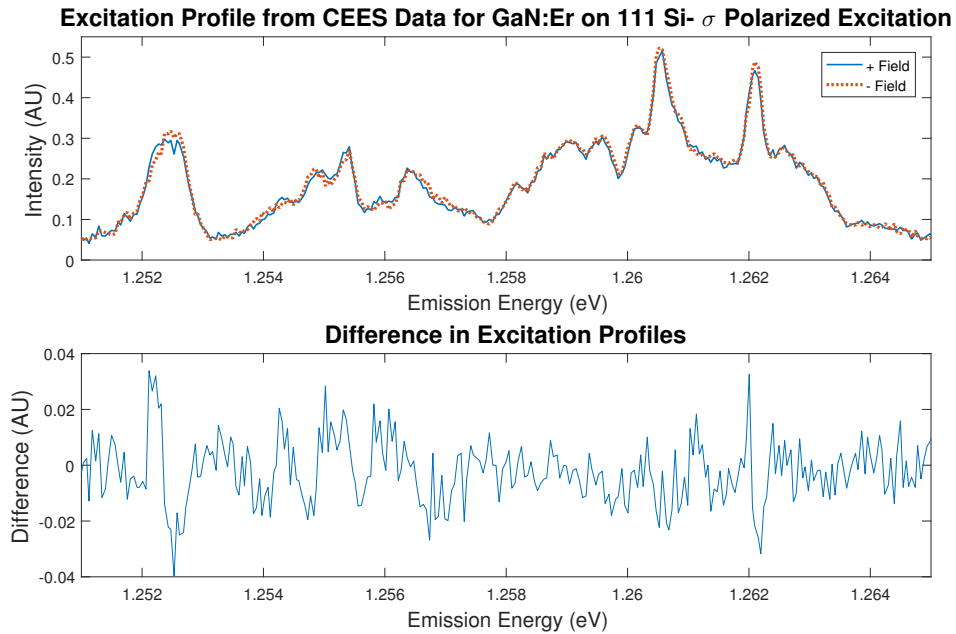


Figure 7.14: Comparison of excitation profiles from CEES data for GaN:Er on [111] Si sample

Fourth, the presence of a large number of sites enables comparison of the degree of local site symmetry with the degree of the asymmetry.

Samples for this material, erbium doped stoichiometric lithium tantalate, were purchased from the OXIDE Corporation. Data for this material was all obtained with the Montana Instruments Cryostation with Magneto-Optic option, using a process in which spectra for both positive and negative magnetic field values were obtained for each excitation wavelength step in a CEES measurement.

Initially, results seemed to show that Er doped LiTaO_3 did not have much of this asymmetry. However, once polarization was controlled, in both the emission and excitation axes, it was found that this material not only had this effect, but relative changes in peak amplitudes could be reversed by examining polarizations both parallel and perpendicular to the c -axis.

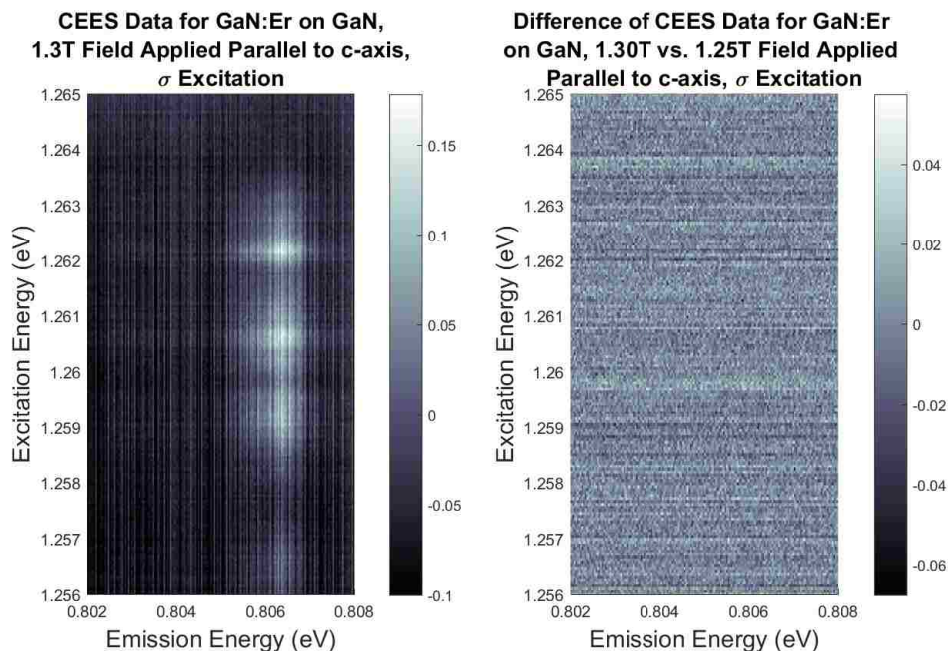


Figure 7.15: Comparison of two sets of CEES data for GaN:Er on [111] Si sample, with difference of 50mT in applied field magnitude, in same direction

Having found a system which appeared to exhibit these effects in a reproducible way, one of the first concerns was to definitively address whether the observed asymmetries were attributable to some sort of asymmetry in the setup, rather than an asymmetry in the sample itself. To do so, experiments were done to examine asymmetries for a sample in two orientations, such that the *c*-axis was reversed, as well as for two emission polarizations. The result was that the asymmetry flipped with the sample being flipped, reducing the number of possible external causes, and that the polarization dependence appeared to persist in both cases.

Er doped LiNbO₃

This material seemed a natural next step after Er doped LiTaO₃, changing only one element in the host crystal, and keeping similar properties. The key result for

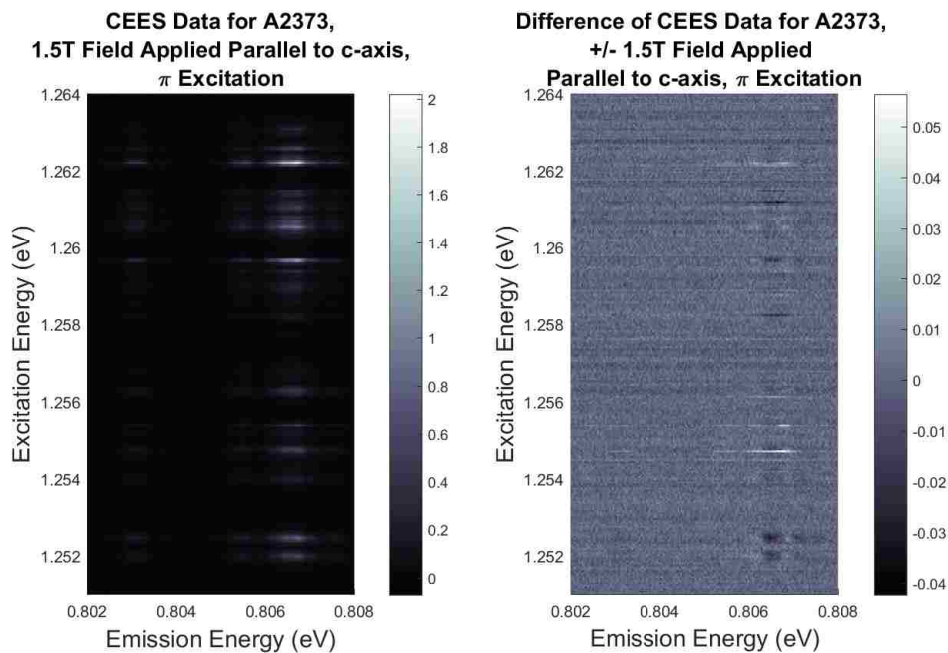


Figure 7.16: CEES data and differences of CEES data for application of a magnetic field parallel and antiparallel to the c-axis. The sample used is A2373, also a GaN:Er epitaxial film on a sapphire substrate.

this material was that the measurements made indicated that this material was essentially identical to Er doped LiTaO₃, in that there is a similar polarization behavior, and all sites seem to show the same sort of result. The sample used is the same as the one in chapter 5.

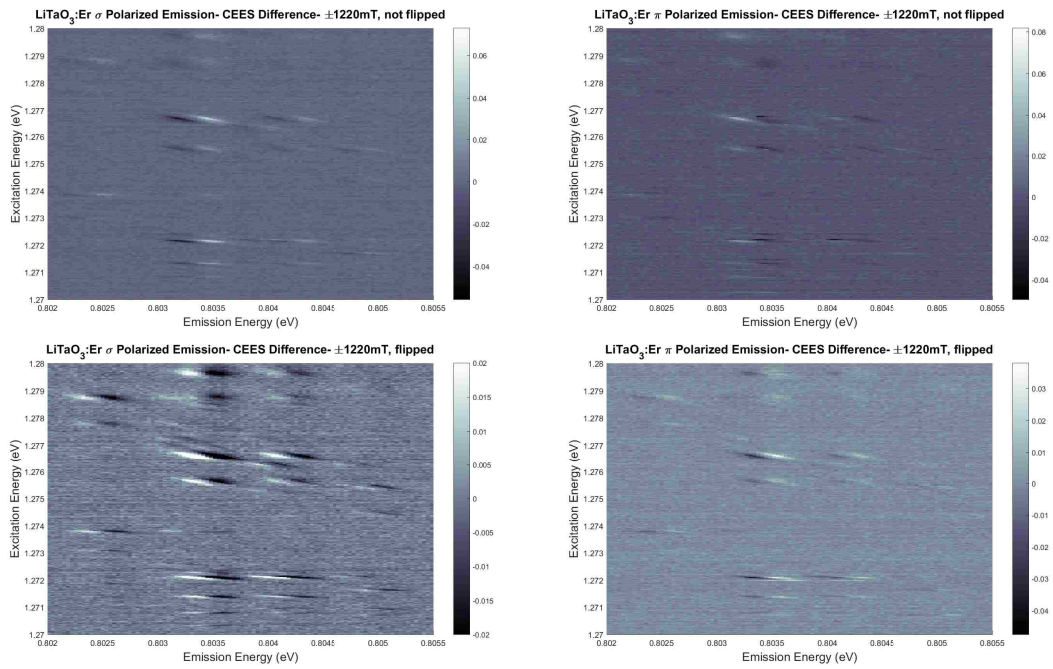


Figure 7.17: Differences in CEEs data for a magnetic field applied parallel and antiparallel to the c-axis for σ and π emission polarizations, and for flipping of the sample in the mount relative to the the magnetic field for LiTaO₃:Er

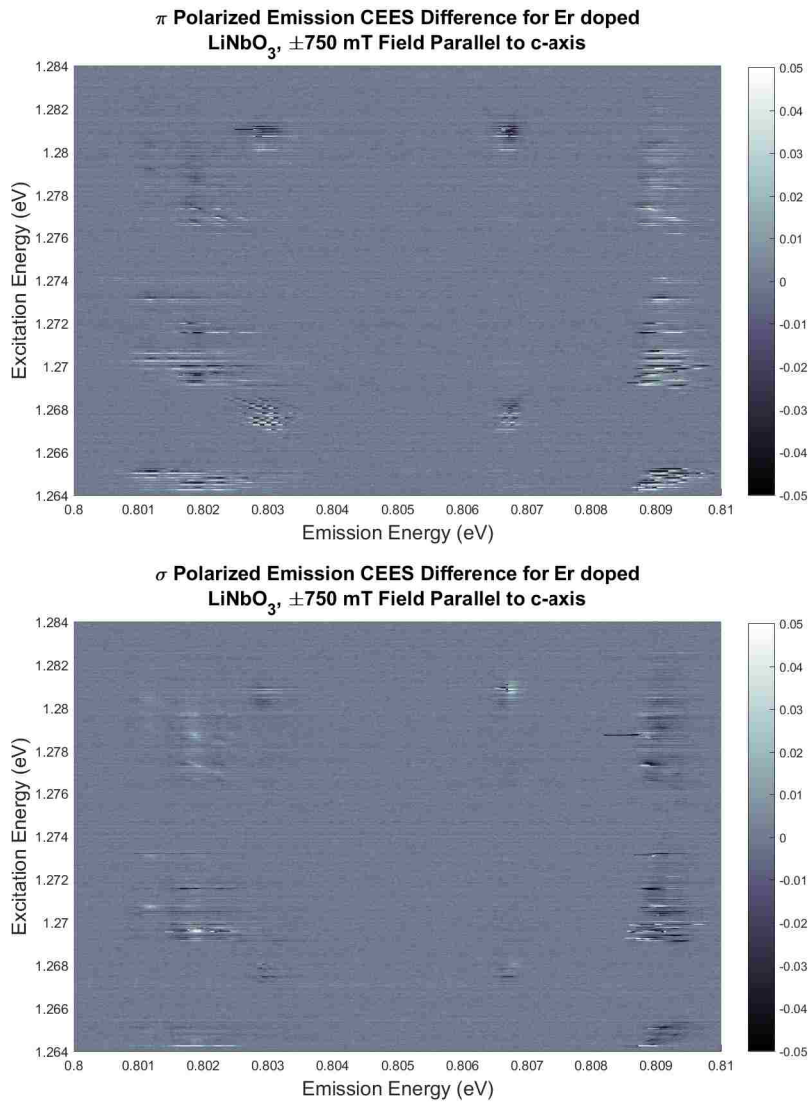


Figure 7.18: Differences in CEES data for a magnetic field applied parallel and antiparallel to the c-axis for π and σ polarized emission in erbium doped lithium niobate.

7.3.4 Local Symmetry

Lithium tantalate has a large number of distinguishable incorporation sites for erbium, [45] and all the sites for which a reliable comparison in spectra could be made appeared to show this same feature. This includes site A, thought to be the site best conforming to C_{3v} symmetry selection rules, based on measurements presented in Chapter 5, and to a similar degree. Results in the same chapter suggested that sites B and C appear to conform least to C_{3v} symmetry. If anything, site A appears to have nearly double the effect of that of the (presumed) lower symmetry sites, as shown in Figure 7.19. This suggests the specifics of the site symmetry are not crucial to the appearance of the asymmetry, and if anything, greater symmetry may increase the degree to which it appears.

To compare the three sites, CEES measurements were conducted in a small excitation range. The technique was combined with polarization control and magnetic field control to develop a series of data as a function of emission polarization, excitation energy, emission energy, and the designation of positive or negative magnetic field. Then, spectra corresponding to excitation showing the best signal and separation from other sites for each site were used for analysis with the asymmetry measure described earlier.

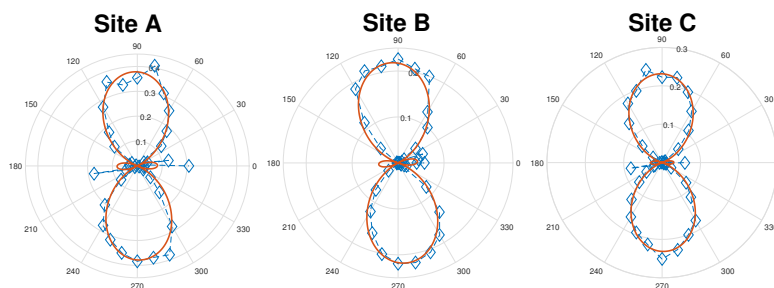


Figure 7.19: Comparison of asymmetry effect for three different sites (A, B, and C) for Er in LiTaO_3 . Results were obtained by comparing the Zeeman split transitions corresponding to the assigned transition from B1 to A2.

7.3.5 Magnetic Field Magnitude Dependence

A result for erbium doped lithium tantalate indicated that the angle of the magnetic field relative to the c -axis seems not to affect the presence of the asymmetry. The logical next question is whether the magnitude of the field matters.

For the excitation peak exhibiting the asymmetry in Nd doped GaN, it was decided to attempt to determine the field magnitude dependence. This was done by modifying the aforementioned measure for the asymmetry for use with only two peaks (as one effective g factor was small, so only two split peaks were clearly separated). The result was that there was no obvious dependence on the field magnitude. Note that if certain measures are used, such as sums of differences of spectra, for peaks which overlap, some of the effect from the two peaks cancel, creating the appearance of an increase in the measure until the peaks are clearly separated.

This would seem to imply that two Zeeman split levels are not equivalent at any magnetic field, which seems questionable. Still, it is possible that whatever mechanism is responsible for the effect saturates at a low magnetic field. However, this yields difficulties similar to those discussed in previous chapters, that it is extremely difficult to conduct high precision measurements at low magnetic fields on Zeeman split peaks, due to peak overlap in optical spectra. Thus, if such a

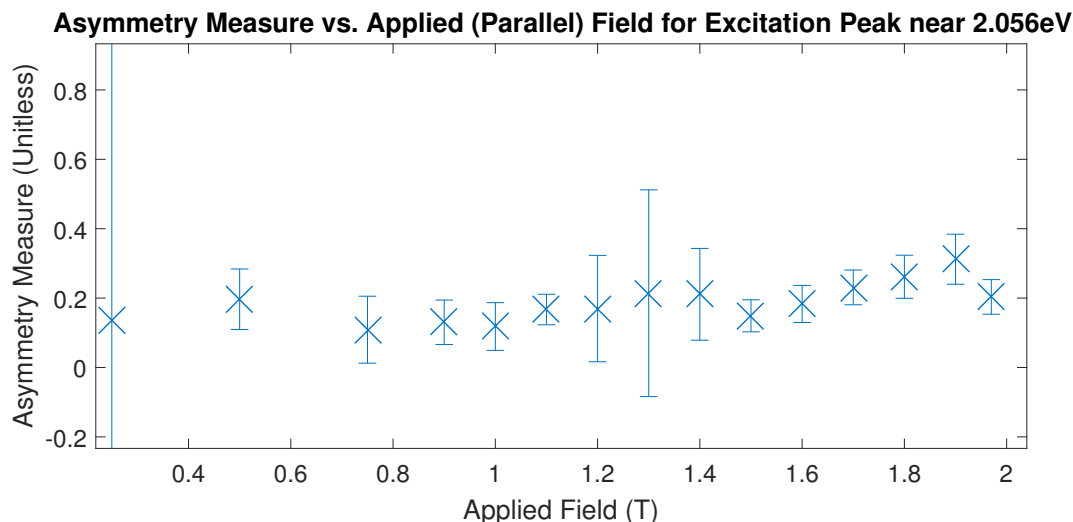


Figure 7.20: Numeric measure of asymmetry vs. applied field magnitude for an excitation peak for the E176-R2-J sample, which is a neodymium doped gallium nitride sample. Error bars correspond to one standard deviation.

mechanism were to saturate at 10mT or so, it may be impossible to determine this using this equipment and method.

Fortunately, ramping data was available from the author of [75], which shows far more significant emission axis asymmetry than was recently observed. This also allowed comparison of multiple runs. Since it is difficult to establish the precise magnetic field, the axes are unfortunately approximate. Lacking precise ability to compare positive and negative fields, it was decided to examine relative amplitudes as a function of applied field. To analyze this data, the two split peaks shown at the beginning of the chapter (an emission near 1.353eV) were fitted, and the ratio of the difference in amplitudes to the sum of their amplitudes was calculated. Multiple data sets were available.

Initially, this analysis appears to support the notion that there is some measurable dependence of the asymmetry effect on the field magnitude, if only one sign of

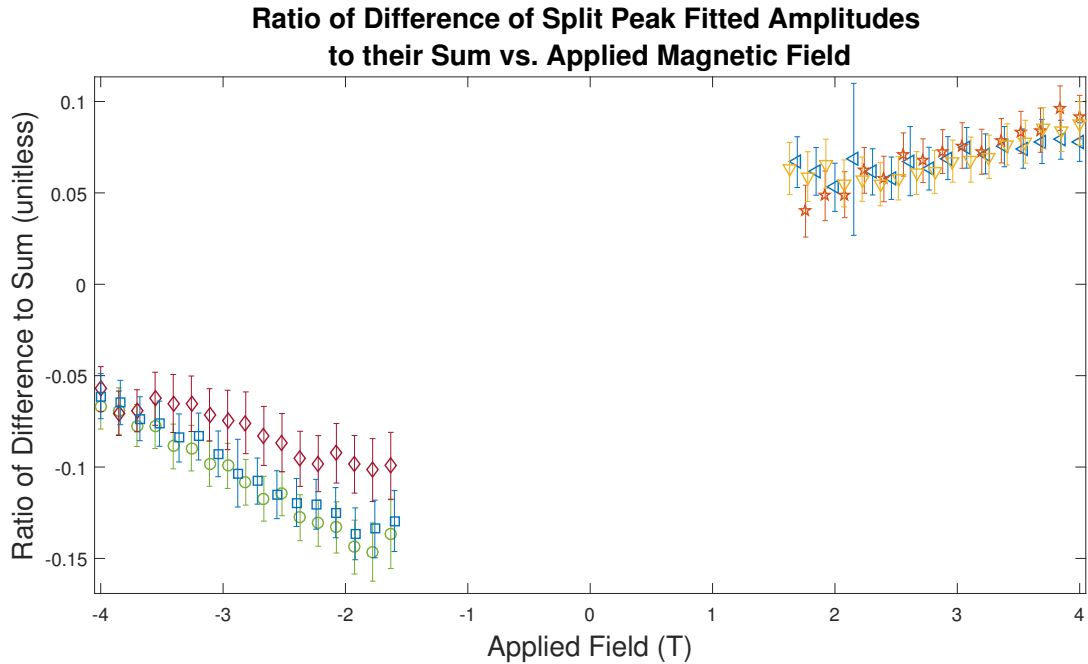


Figure 7.21: Modified numeric measure of asymmetry vs. applied field magnitude for an emission peak for an unknown Nd doped GaN sample. Error bars correspond to one standard deviation.

the field is considered. However, this analysis did not take into account an approximate thermal population of the starting state. This did not affect direct comparison of spectra with positive and negative fields of the same magnitude, because the relative spacings of energy levels remain the same in that comparison. If a temperature of about 70K is estimated, this dependence essentially vanishes.

So far, it appears that it is likely that whatever causes this effect saturates at a magnetic field which is smaller than the fields at which reliable comparisons can be made easily. It is also important to note that different scaling and saturation behaviors could conceivably occur for each particular transition and host material.

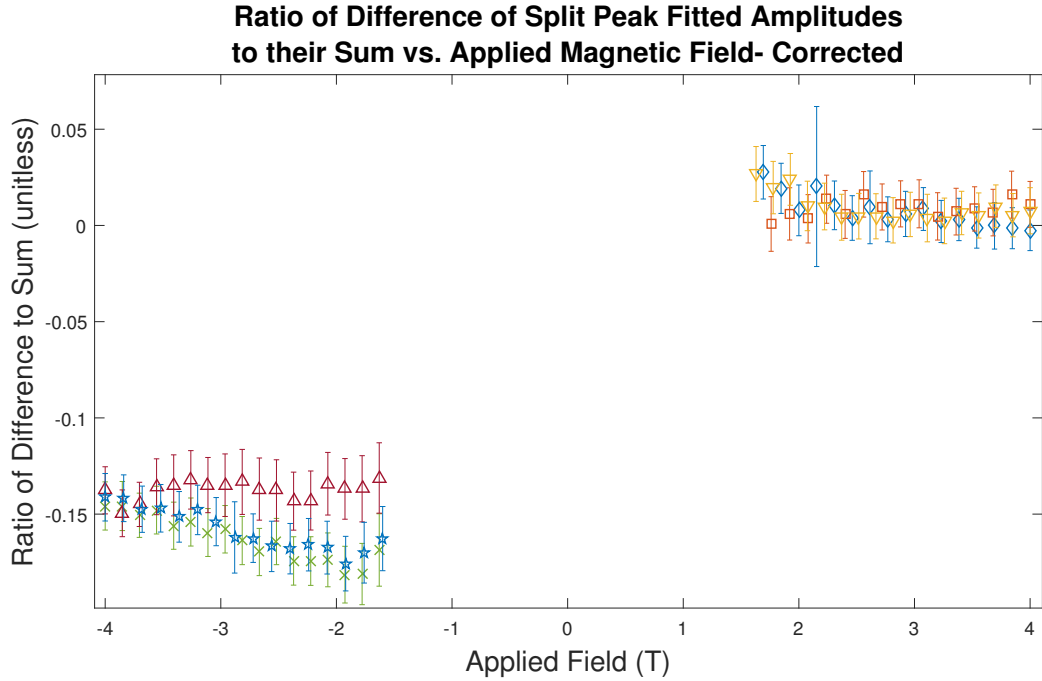


Figure 7.22: Modified numeric measure of asymmetry vs. applied field magnitude for an emission peak for an unknown Nd doped GaN sample. Error bars correspond to one standard deviation.

7.3.6 Polarization Dependence and Magnetic Field Angle Dependence

A dependence of the effect on polarization angle was found which resembled the sum of a constant and a squared sine or cosine function, suggesting that the split peaks have different degrees of π and σ polarization. Polarization dependence experiments were analyzed by fitting this measure of asymmetry to a function of the following form:

$$f(\theta) = A + B \cos^2(\theta - \theta_0)$$

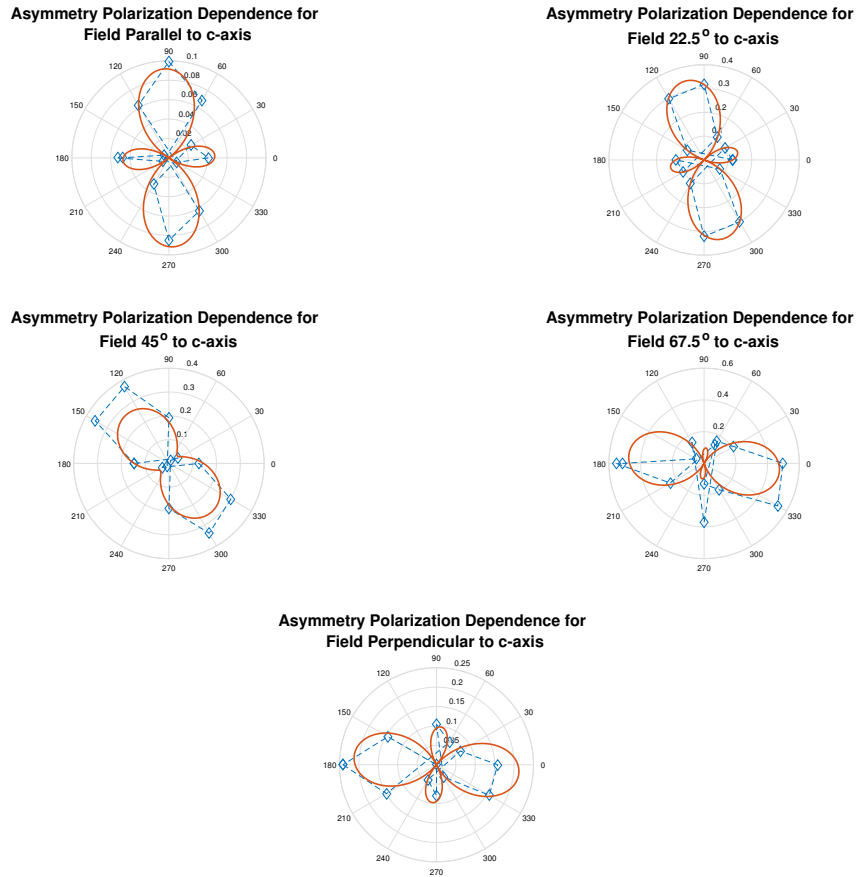


Figure 7.23: Numeric measure of asymmetry vs. polarization angle for several orientations of the magnetic field relative to the c-axis for the B1 to A2 transition for site A in $\text{LiTaO}_3:\text{Er}$. Dotted lines are added to give an indication of the change in sign of the data. The angle axes indicate the angle of the linear polarizer, and the magnetic field is always applied at an angle corresponding to zero degrees. The sample is rotated relative to these for each experiment. Thus, in the parallel case, the c-axis of the crystal is also along zero degrees (with some error), and in the perpendicular case, the c-axis of the crystal is along 90 degrees.

Erbium doped lithium tantalate was used for these experiments, owing to convenience resulting from its sharp peaks, and a transition with relatively high effective g factors for both parallel and perpendicular magnetic fields, and clear results for asymmetry in emission. Results were obtained by examining the split peak corresponding to the assigned transition from B1 to A2 for site A. Similar results are present for other sites, but site A was selected for its relatively higher intensity. This particular transition was selected for ease in identifying all four split peaks, relatively high intensity, and experimental ease in controlling emission polarization rather than excitation polarization. Results are shown in Figure 7.23. In a deviation from what might be implied by the earlier description of the numeric measure, the added and subtracted peaks were followed as the rotation in field moved these peaks. That is, signs in the numeric measure for the asymmetry were kept the same for a peak involving the same two levels, even if this changed the ordering of the peaks in terms of energy.

Several important results came from these polarization experiments. First, the asymmetry seems somehow intrinsically linked to the c -axis of the crystal. Note how rotating the c -axis relative to the magnetic field results in the polarizations giving the maximum and minimum asymmetry rotating with the c -axis, not the magnetic field. Second, it appears that these asymmetries may be present for any field orientation relative to the crystal, not just fields parallel and antiparallel to the c -axis. If anything, it appears that the maximum values for the asymmetry measure appear at neither the parallel nor the perpendicular orientation. Third, as shown in previous data for the case of a magnetic field parallel to the c -axis, the fitting function which appears appropriate for the asymmetry measure seems to be a Malus' Law type of function, [23] rather than some complicated form which explicitly takes into account the relative angles of the magnetic field and the c -axis.

This last point led to an alternative method for determining these asymmetry measures which would ideally be less subject to problems of noise. Rather than fit each spectrum for each polarization angle individually, a series of spectra are fit simultaneously, with the amplitudes for the peaks being described by a Malus' Law type form. A visual display of the data and the fit is shown in Figure 7.24.

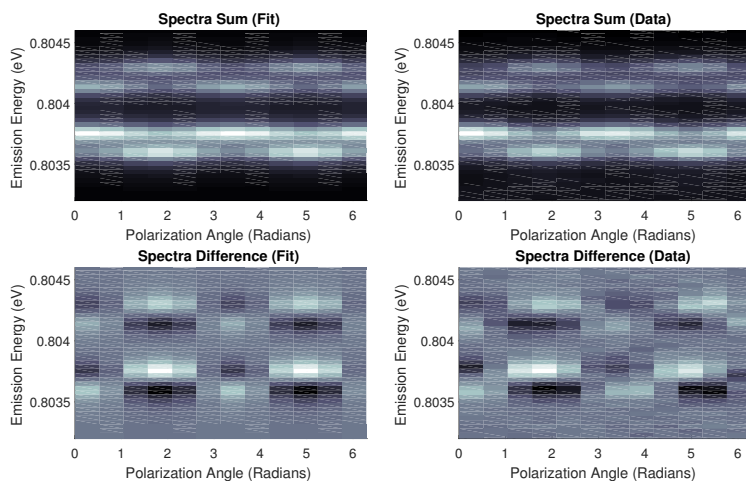


Figure 7.24: Example fitting of sums and differences of spectra for one Zeeman split peak, using a Malus' Law type form to describe amplitudes and differences for positive and negative magnetic fields. The data is identical to the data used to produce the plot for the parallel case in Figure 7.23. The sums and differences refer to combining spectra for positive and negative magnetic fields.

This permitted fitting of individual polarization parameters for each of the four split peaks, and a straightforward method of determining errors in the results. For an individual Zeeman split peak, the measure was simply defined as the ratio of the difference in peak amplitudes to the average peak amplitudes.

The results, shown in Figure 7.23, suggest that although the measure does vary with field angle, it does not appear to ever reach a value of zero. They also suggest that maximum values can be obtained for angles around 45 degrees, which may be useful for examining the role of other variables. An example fitted spectrum for this angle is shown in Figure 7.26, from the same data set and transition used for the figures presented here.

It must be noted that in order to perform the above experiments, for angles of 45, 67.5, and 90 degrees, a different heat shield was used (due to issues regarding sample mounting), which makes it likely that the temperatures for these measurements are

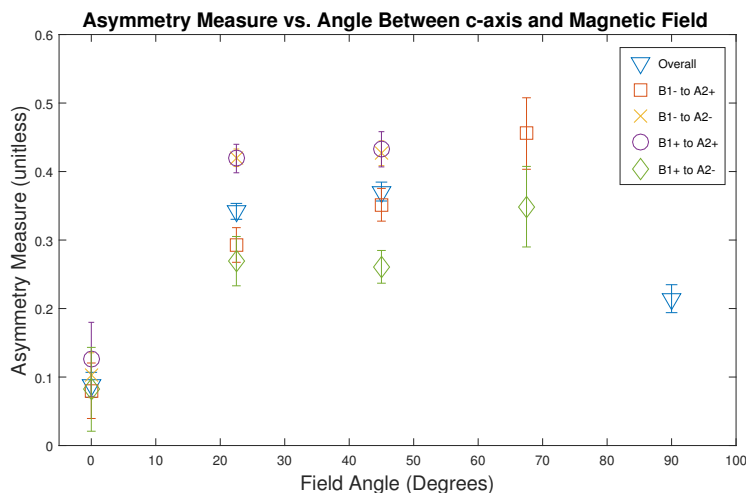


Figure 7.25: Maximum magnitude (signs removed) of asymmetry measure for both overall asymmetry numerical measure and measures for individual peaks as a function of applied field angle. Values with unusually high errors in the fitting are omitted. Error bars correspond to a 95 percent confidence interval.

not the same as those for 0 and 22.5 degrees. Further, there may be issues involving the relative alignment of the magnetic field axis, the crystal c-axis, and the polarizer axis. Still, even if these relative alignments allow for a magnetic field perpendicular to the c-axis to result in no effect, it is still puzzling why a maximum would appear for an angle near 45° between the c-axis and the magnetic field.

The data shown here for an angle of 45° between the c-axis and the magnetic field allows for a great enough difference between the amplitudes for the two peaks to easily demonstrate changes in polarization behavior of each individual peak. See Figure 7.28. It is worth noting that in this case, the primary change is in σ polarized emission, with little change in π polarization (which, as was shown in Figure 7.23, is not always the case, at least to this relative degree). The summed data, if anything, appears somewhat more even in polarization than the data for the case without a magnetic field applied, shown in Figure 7.27. Of course, a more valid comparison

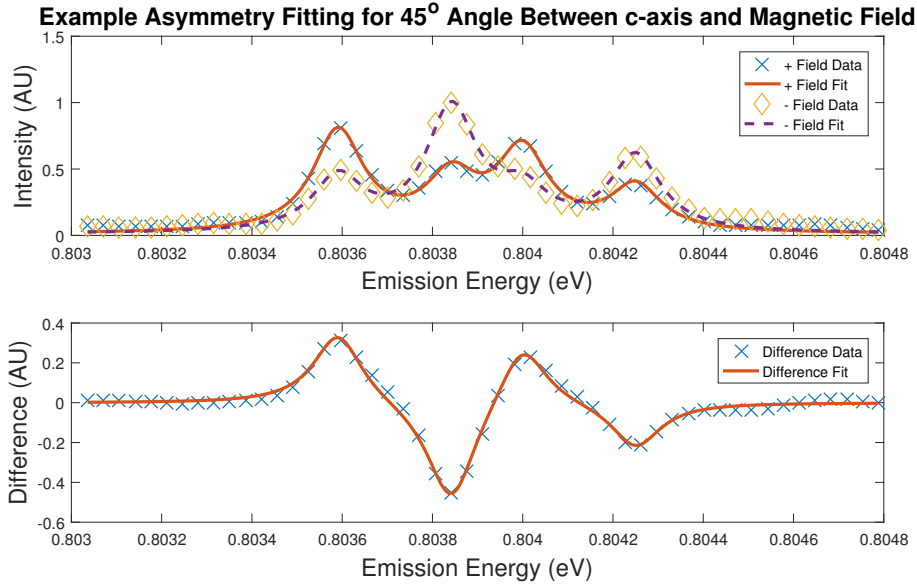


Figure 7.26: Example fitting of +/- magnetic field spectra and their difference for 45 degrees between the c-axis and the magnetic field. Note the rather large effect.

would involve measuring polarizations with and without an applied magnetic field in the same experiment and run.

7.3.7 Crystal-Field Numbers

A comparison of the effect for different crystal-field numbers requires a number of sharp transitions involving levels with known crystal-field numbers exhibiting the effect. Ideally, this would be the ${}^4I_{\frac{15}{2}}$ to ${}^4I_{\frac{11}{2}}$ transitions in erbium doped lithium tantalate or lithium niobate, but no experimental data for those systems has yet indicated an effect for that transition.

The transition which seems to be most useful for those two systems for evaluating the dependence on other variables, is the transition from B1 to A2. All four split peaks can be easily seen (refer to data shown earlier), and there is a clear behavior

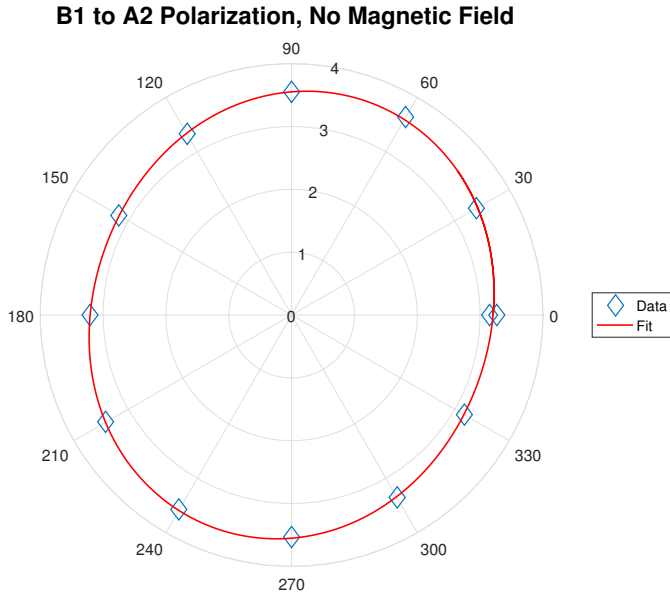


Figure 7.27: Fitted emission polarization for the B1 to A2 transition for site A in erbium doped lithium tantalate without an applied magnetic field. Here, 0° corresponds to the c-axis of the crystal.

for each split peak. Both of these levels have been assigned as $\pm\frac{1}{2}$. Further, the increase and decrease in the pairs of peaks seems to depend on whether the energy is associated with a higher or lower level of B1. However, the transition assigned to B1 to A1 seems to have a similar behavior in lithium tantalate, with A1 being assigned $\frac{3}{2}$. This would suggest that the effect can occur for emissions starting from $\pm\frac{1}{2}$ levels.

The emission peak for neodymium doped gallium nitride which exhibited a large effect was assigned to a transition between two levels of crystal-field number $\pm\frac{1}{2}$ [75], and the two visible split peaks corresponded to a difference in energy from the lower level. The two excitation peaks in that system, near 2.056eV and 2.051eV, which exhibited the effect, involved the same lower level assigned $\pm\frac{1}{2}$, and the two upper levels were not assigned any crystal-field number in Ref. [75]. For both of those, there were also two visible split peaks whose splitting was due to the lower

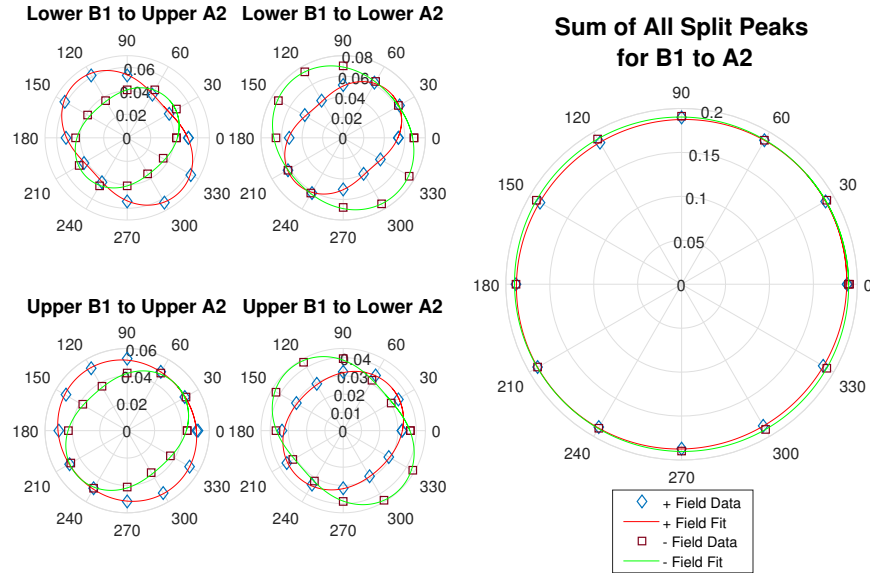


Figure 7.28: Comparison of polarizations of Zeeman split peaks for the B1 to A2 transition for site A in erbium doped lithium tantalate for an angle of 45° between the c-axis and the magnetic field. Here, 0° corresponds to the orientation of the magnetic field, and the c-axis of the crystal is oriented along 45° . The angles show data as a function of polarization angle.

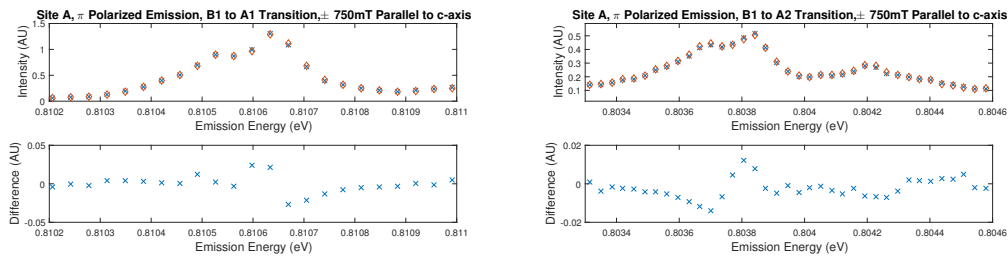


Figure 7.29: Plots demonstrating asymmetry effect for site A in LiTaO3 for the transitions assigned as B1 to A1 and B1 to A2, with an overlapping pair of peaks from site B appearing to the right in the former.

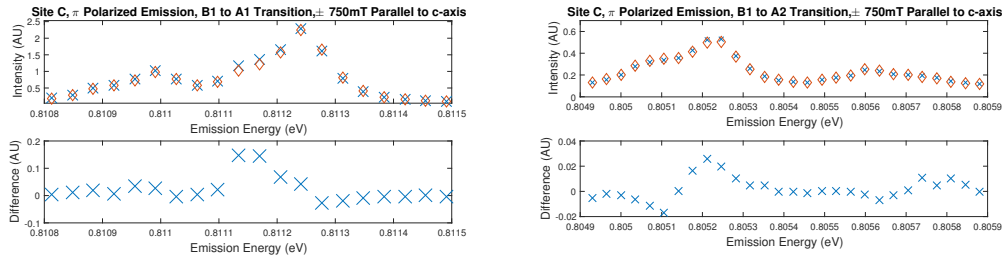


Figure 7.30: Plots demonstrating asymmetry effect for site C in LiTaO₃ for the transitions assigned as B1 to A1 and B1 to A2

level.

It is not yet certain whether the crystal-field numbers have a significant role to play, owing to a small number of transitions for which high quality data showing the effect is available. Even comparing the degree of the effect for just two transitions may fail to account for other differences between them than just the crystal-field number assignment. This is also complicated by the already discussed possibility of a much more symmetric symmetry group (O_h) giving rise to the same effect. How the crystal-field numbers influence the effect is currently considered an open question.

7.3.8 Raman Spectroscopy

As mentioned earlier, one possible mechanism proposed to explain this effect was magnetostriction. However, since magnetostriction typically depends on the square of the magnetic field, a particular type, linear magnetostriction, would be required. Linear magnetostriction, a linear relation between an applied magnetic field and strain in a material, is known to be possible in antiferromagnetic material. [5] This effect is specifically a property of ferromagnetic materials, so its existence would hint at ferromagnetic semiconductors.

Raman spectroscopy was conducted on a sample of Er doped LiTaO₃ with no applied magnetic field, and magnetic fields applied with a positive and negative

amplitude. It was expected that strain might be detectable using peak shifts in these spectra, due to changes in phonon energies as the crystal lattice changed. No such peak shifts were detected, in comparing either the reversed field direction spectra, or in comparing those to the zero field spectrum. The width of a pixel in this data corresponds to roughly 1.5 cm^{-1} . The spectra can be seen in Figure 7.31.

Using data from Ref. [26], an estimate for the Young's modulus of about 100GPa, and grossly oversimplifying issues of directionality for the purpose of an order of magnitude estimate, one can make an estimate that 10^3 cm^{-1} is a feasible strain shift for peaks for this material. This would suggest any strains involved in this material as a result of the application of a magnetic field would need to be on the order of 10^{-3} or less. This is comparable to the amount of strain which results from growing GaN films on various substrates. Data for lithium niobate suggest that this estimate, while not unreasonable, may be an upper estimate for the detection threshold. [71] It was found that strains of about 2 parts in a thousand correlated with nearly an order of magnitude enhancement in photoluminescence efficiency. [14] Thus, while this particular experiment failed to show the presence of strain, its existence at a level which could affect transition probabilities significantly has not been definitively ruled out.

7.3.9 Temperature Dependence

Since ferromagnetism has been suggested as part of a possible mechanism, there should exist a phase transition temperature above which the effect ceases to appear. Such a temperature should be the same for all instances of the asymmetry effect, since it would be a property of the overall material.

First, note that the temperatures discussed here refer to the platform thermometer temperature in the Montana Instruments Cryostation, which may be a lower value than the sample temperature, owing to the sample being more distant from the cooling stages than this thermometer, or, if the thermal contact of this thermometer is poor, perhaps a higher value.

To examine temperature dependence, the Montana Instruments Cryostation was

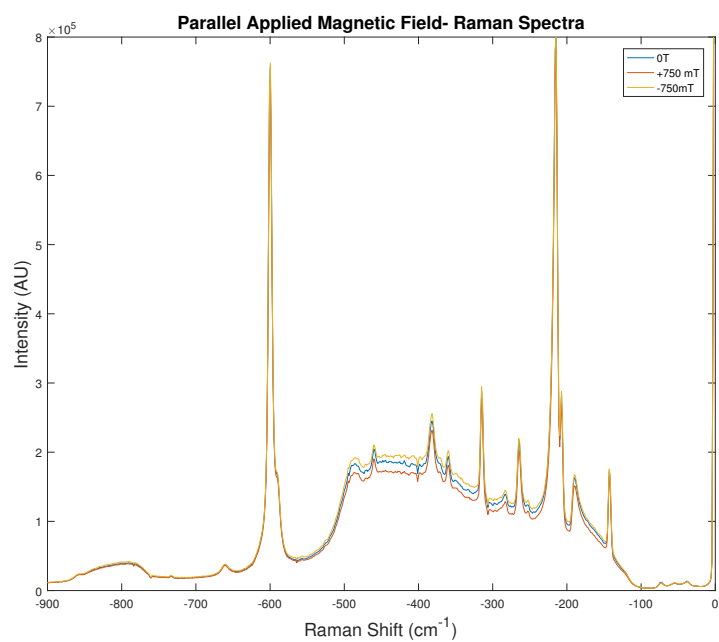
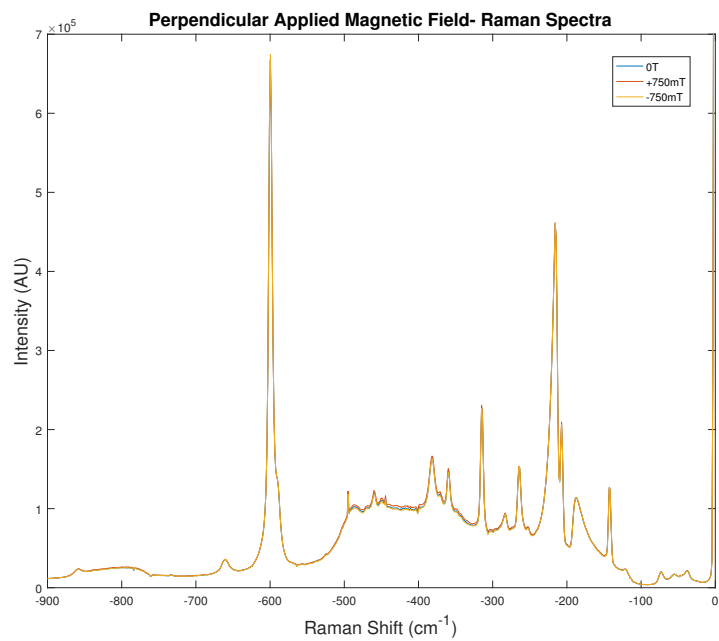


Figure 7.31: Comparison of Raman spectra for an applied magnetic field parallel and perpendicular to the c-axis, as well as without an applied magnetic field, for erbium doped lithium tantalate.

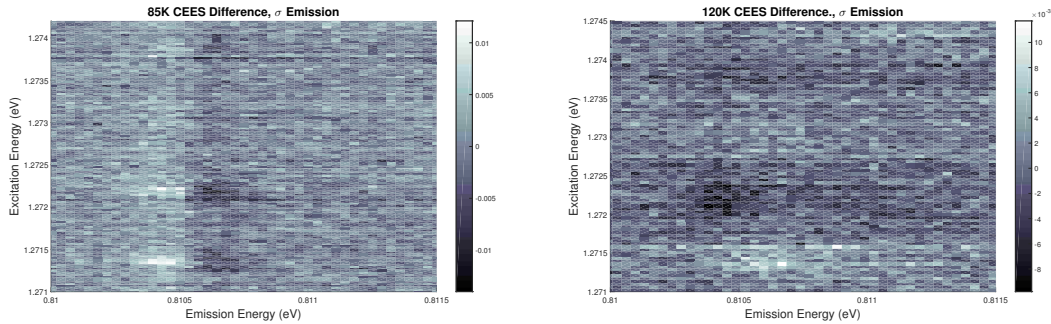


Figure 7.32: Differences in CEES for applied magnetic fields parallel and antiparallel to the c-axis for higher temperatures.

set to various platform temperatures. It should be noted that the temperature of the sample at the laser focus is expected to be higher than this set value, especially for insulating sample materials. It was found that the effect definitively persisted with a very similar appearance to 85K, and it is possible that a small excitation axis effect appeared at 120K, which suggests a similar situation to that mentioned for some results in GaN:Nd. A comparison for those two temperatures with a fixed emission polarization is shown in Figure 7.32. Ultimately though, higher temperatures lead to lower signals, wider peaks, and more peaks, and this reduces signal to noise ratio.

A more thorough investigation was performed after noting that the asymmetry appeared to be greater for a 45° angle between the c-axis and the applied magnetic field than for a parallel orientation. There was still an issue involving poor signal to noise ratio while conducting CEES spectroscopy above a platform temperature of about 120K. To address this, a non-tunable laser (ThorLabs CLD 1015 with a laser diode outputting about 974nm light) with higher power output (hundreds of milliwatts) was used. This potentially created an analysis issue, in that emissions from a large number of incorporation sites were measured simultaneously. In practice, what appeared to be a single pair of Zeeman split peaks in the spectra was identified and used to calculate the asymmetry measures. The result of this, as shown for a few select temperatures in Figure 7.33, is that it appears that the asymmetry persists to

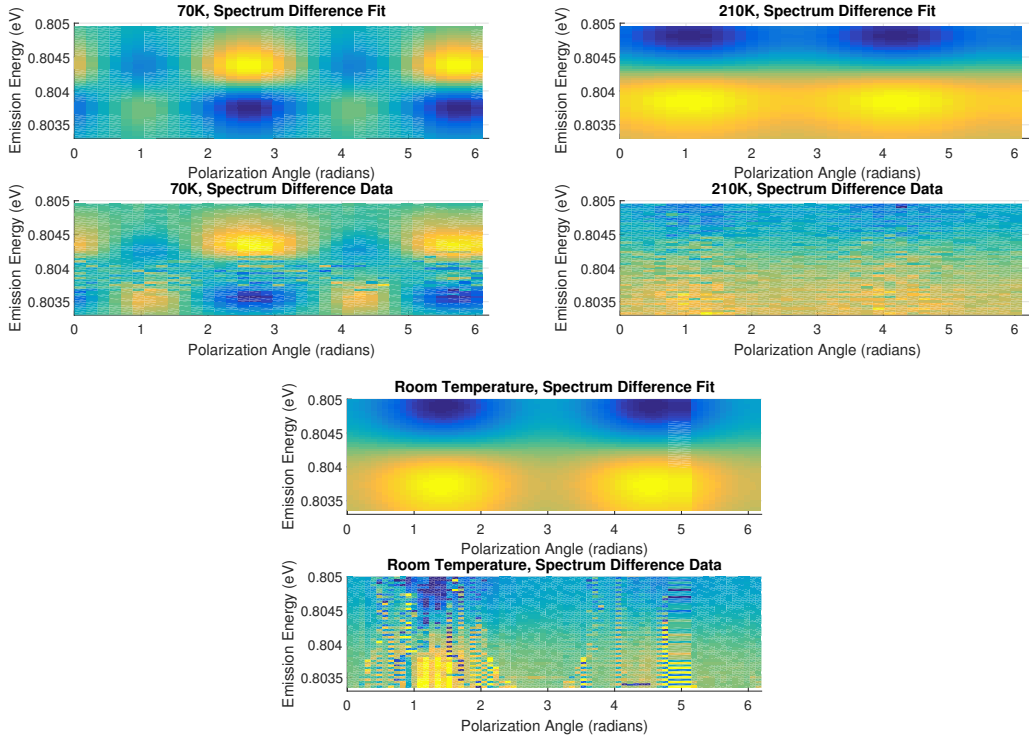


Figure 7.33: Fitted differences in emission spectra of erbium lithium tantalate as a function of emission polarization angle for select temperatures. The magnetic field was applied along 0° , while the c-axis was aligned along 45° . The fitting model assumes that the amplitudes of the peaks can be described using a Malus' law type dependence, with the same offset angle for both peaks. This also assumes this portion of the spectra can be accurately modeled with only two peaks.

room temperature, but differently for π and σ polarized light. The fitting procedure here attempts to fit all of the spectra for each polarization angle together, as was done for the magnetic field angle dependence data.

Combining the data from this technique for higher temperatures with data from CEES maps for lower temperatures results in Figure 7.34. This plot shows a few interesting features. Most importantly, it appears that the effect persists to high temperatures. Second, the degree of the effect appears to change dramatically from

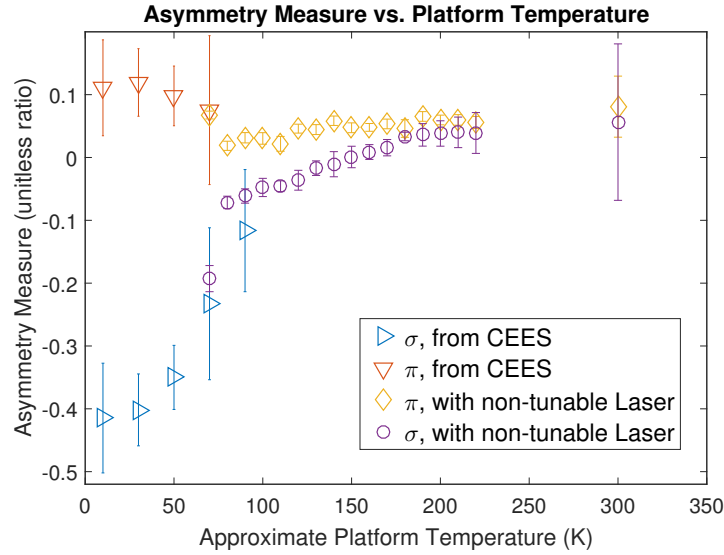


Figure 7.34: Values of the asymmetry measure for π and σ polarized emission from erbium doped lithium tantalate as a function of platform temperature. Error bars correspond to 95% confidence intervals.

low (10K) to high (about 300K) temperatures, particularly for the σ polarized emission light. This was also visible in the data shown in Figure 7.33. Finally, there is an appearance of phase-transition like behavior, in that there is a sharp change in the measure of the effect near 70K which seems to be supported by data from both experimental methods. This last point probably requires additional verification, because it is possible that factors like temperature dependent conductivity and uncertainty in biases of the platform thermometer temperature in this mounting configuration are making this change seem more dramatic than it actually is.

If there is a phase transition, it could be a sign of a ferromagnetic critical temperature mentioned earlier. However, this would also be problematic, as the implication of this would be that while ferromagnetism can contribute to the asymmetry, the asymmetry is still present without ferromagnetism.

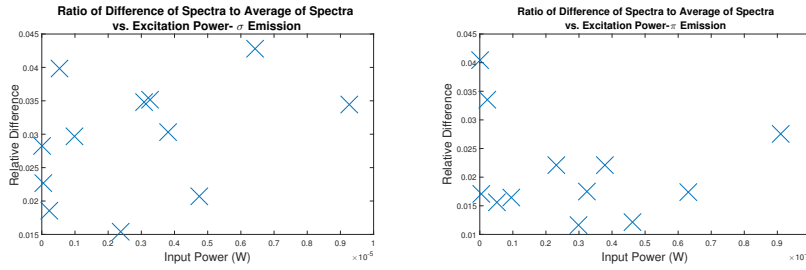


Figure 7.35: A measure of the asymmetry vs. excitation power for two emission polarizations.

7.3.10 Laser Power Dependence

While attempting to determine the reason for inconsistency in the Nd doped GaN data, one suggestion was to examine whether the input laser power had any effect on the emission axis asymmetry. To test this, neutral density filters were used to vary the power for a system which showed this effect consistently, erbium doped lithium tantalate. Comparisons of the emission asymmetry for the same emission peak as a function of excitation power suggested that there was no obvious trend.

7.4 Additional Preliminary Results

7.4.1 Appearance in a Crystal with Cubic Symmetry

This effect seems to be present in Er doped Cs_2NaYF_6 . This material was obtained mostly by a chance opportunity, and was studied because it represents a different material entirely. These samples were provided by Dr. Henk Vrielinck of Ghent University. The sample used here had 3 percent nominal doping of erbium.

The previous materials are thought likely to have C_{3v} symmetry for the majority incorporation site for the rare-earth ions. The erbium incorporation site for this material is expected to have O_h symmetry, perhaps with some perturbations from cubic symmetry.[40] While fewer results have been obtained for this material, one

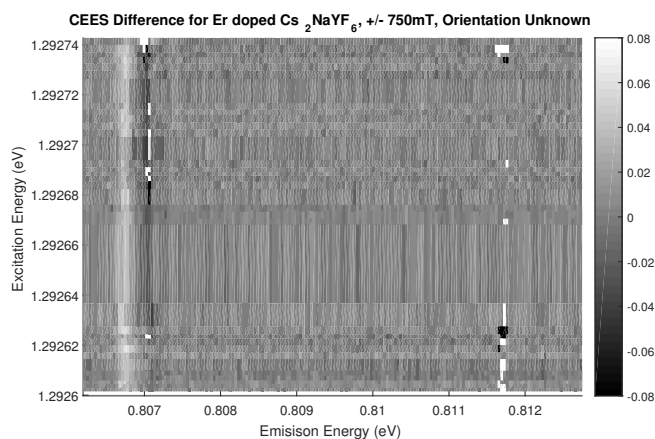


Figure 7.36: Difference in CEES data for an applied magnetic field and an applied magnetic field in the opposite direction, for erbium doped Cs_2NaYF_6 , with unknown orientation.

measurement showed that asymmetry is present in this material as well. This suggests that C_{3v} symmetry (or a slightly broken version of it) is not particularly vital to the presence of the asymmetry effect.

Unlike for the other materials discussed here, other results to determine specific sites and levels in detail were not collected, the orientation of the crystal was not known during the experiment, and a cubic symmetry adds complications. If, for example, a particular incorporation site breaks from this symmetry due to some change along an axis, the same defect could occur along three axes, presumably resulting in the same energy levels in the absence of a magnetic field. However, the addition of a magnetic field to such a system would add the complication of the relative angle of the magnetic field and the broken symmetry axis. This could potentially lead to what is essentially one site exhibiting magnetic splittings as if there are multiple sites with the same energy level. Thus, such work is expected to be more difficult than for the other materials discussed in this work.

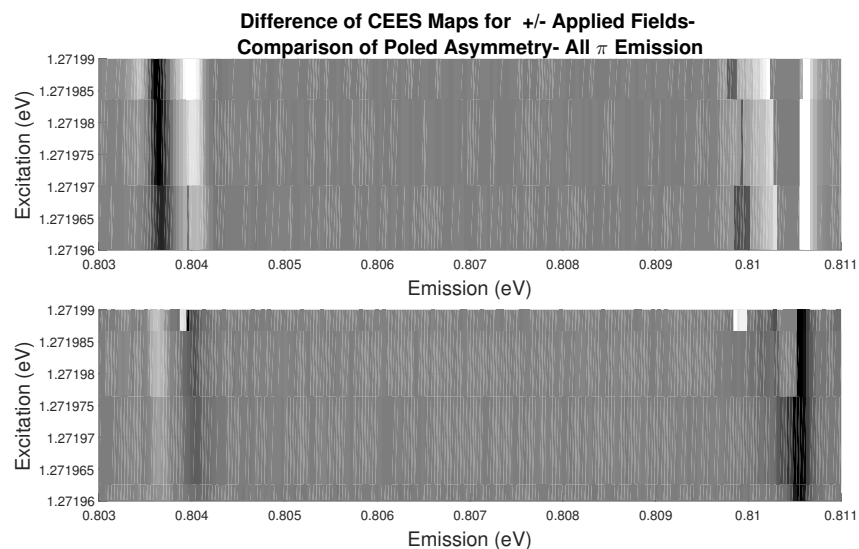


Figure 7.37: Difference in CEES data for an applied magnetic field parallel and antiparallel to the c -axis of erbium doped lithium tantalate, for what are believed to be two differently ferroelectric poled regions of erbium doped lithium tantalate.

7.4.2 Reversing the c -axis in a Ferroelectric

Preliminary results suggest that reversing the polarity of Er doped LiTaO_3 also reverses the direction of the asymmetry. If correct, this would strongly suggest the importance of an electric field in establishing the direction of the asymmetry. This is perhaps one of the more interesting lines of reasoning to pursue for future experiments, and in principle, some such experiments should be relatively easy to perform.

7.5 Possible Mechanisms

7.5.1 Faraday Effect

There is a known effect in which left and right polarized light are transmitted with different refractive indices in a material with a magnetic field applied parallel to the direction of travel of the light. This results in rotation of linearly polarized light. This has been considered as a possible explanation. It is not entirely satisfying. In some of the experiments (all those conducted with the Montana Instruments Cryostation), the magnetic field is applied perpendicular to the path of the emission and excitation light. Similar magnitudes of degree of asymmetry were seen in excitation in experiments done in the Janis brand cryostat (field parallel to light propagation) and the Montana Instruments Cryostation (field perpendicular to light propagation). In the case of emission, this would imply that the optical setup is sensitive to circularly polarized light in a consistent way, in that experiments done several times over the course of months show a consistent result. It seems surprising that epitaxial films with a thickness of a micron would allow enough distance traveled in a material to cause differences of tens of percent as would have to be the case in Nd doped GaN.

For the purpose of developing a Fermi-type estimate, suppose that a difference of ten percent in intensity corresponds in some way to a rotation in polarization angle at which the square of a cosine function is equal to 0.9. This angle is about 0.32 radians. This corresponds to results taken at 4T on samples in which the signal comes from epitaxial films about one micron thick, so dividing this out, the obtained Verdet constant is on the order of $8 \times 10^5 \frac{\text{rad}}{\text{T}\cdot\text{m}}$, orders of magnitude higher than for terbium gallium garnet ($\sim 2 \times 10^2 \frac{\text{rad}}{\text{T}\cdot\text{m}}$), a material used for its unusually high Verdet constant. [6] This makes this explanation seem highly implausible, at least for the case of earlier results in epitaxial films of neodymium doped gallium nitride. The bulk crystal samples, however, are millimeters thick. However, most of the bulk crystal results presented involved the direction of light propagation as perpendicular to the magnetic field, yielding further difficulties. Definitive refutation of this idea

would require more thorough polarimetry.

7.5.2 Thermal Gradient

One considered possible cause for the effect in the bulk crystal ferroelectrics was the existence of a thermal gradient. This was not suggested with an explanation for how this could occur. To test this, an attempt was made to make a symmetric mounting, in the sense that the mounting was roughly symmetric about the plane perpendicular to the *c*-axis in the middle of the crystal for Er doped LiTaO₃. This was accomplished though applying copper tape to each of two sides of the sample which was in contact with the heat sink. Roughly the same degree of asymmetry was observed as when the sample was mounted on only one side, suggesting this was not the cause.

Furthermore, the results shown earlier for erbium in lithium tantalate showed that remounting the sample in a flipped orientation resulted in the reversal of the asymmetry effect, suggesting that the effect tracks some orientation of the crystal itself.

7.5.3 Strain and Magnetostriction

Strain alone appears insufficient as an explanation for the origin of this asymmetry, as ferroelectric bulk crystals believed to be of high quality exhibit the effect to a similar degree.

The Raman spectroscopy results suggest that the application of a magnetic field sufficient to observe this effect does not cause a detectable amount of additional strain, let alone a difference in strain for opposite field directions. However, as discussed earlier, it is reasonable that an amount of added strain below the limits of detection could cause significant changes in peak amplitudes.

7.5.4 Role of an Additional Electric Field

The presence of the effect in ferroelectric bulk crystals (LiTaO_3 and LiNbO_3) and strained piezoelectric crystals (GaN), [38] with a correlation between strain and the effect, suggests that an electric field may play some role in the mechanism leading to this effect. Furthermore, the aforementioned behavior in which the polarization angles which give maximum asymmetry rotate with the c-axis of the crystal, rather than with rotation of a magnetic field, suggests that this asymmetry is closely tied to some asymmetry in the crystal itself. Additional experiments are suggested to examine this. Initial results involving poling the lithium tantalate samples seem to support this idea.

Of course, this is not in and of itself a complete explanation, but thus far seems the most promising hypothesis of the ones considered here upon which to base further work. It would likely be tied to another effect, such as the previous one discussed.

7.6 Suggested Future Work

The ferroelectric poling result should be confirmed. If correct, it suggests an important relationship between electric fields in the host material and the magnetic field.

There is still the issue of inconsistency in the neodymium doped gallium nitride samples. Suggested reasons for this, temperature dependence and aging effects, should be investigated for this material to see if these can explain this. For the former, data for temperature dependence in erbium doped lithium tantalate suggests this is a very realistic explanation. For the latter, if the samples age over time, this may indicate that whatever is responsible for the effect may decrease over time in epitaxial films. Testing this would require obtaining new samples exhibiting the effect, and testing them periodically over the course of years. Additionally, one could attempt anneal samples we already possess, performing measurements of the effect before and after the annealing, to determine whether this tends to remove the

effect further.

One possible hypothesis is that larger scale defects in the host crystal may be present, such as spiral discontinuities. It is not entirely clear, however, what advantages this has over ascribing a root cause of the asymmetry to ferroelectricity or strain. Still, this is advanced as another possible source of asymmetry. It is feasible that the rotation in Czochralski crystal growth could introduce a left or right handed bias of some kind in crystal growth in bulk samples. This suggests a search for these defects in bulk crystals.

In order to determine whether the crystal as a whole rather than specific locations with rare-earth dopants shows signs of asymmetry, a search for effects such as changes in index in refraction for left and right circularly polarized light in one of the materials exhibiting this effect are suggested. Measurements which may identify evidence of specific defects in the host crystal, such as atomic force microscopy of the surface, are suggested for the bulk crystals exhibiting the effect. A variety of defects may be expected in strained thin film samples, so defects in the bulk crystal samples may be more likely to be relevant to the problem.

The results for whether the sample becomes strained as a result of applying a magnetic field, and strained differently for reversed orientations of the magnetic field were not entirely conclusive. To rule out a magnetostriction mechanism, it is suggested that an alternate method for determining strain be found and applied.

The temperature dependence effect for erbium doped lithium tantalate suggests two additional experiments. First, it should be determined whether or not these samples are ferromagnetic at room temperature. If not, ferromagnetism and magnetostriction are poor candidates for a complete explanation. Second, an alternate means of measuring temperatures should be employed while performing similar experiments to verify the appearance of a sharp change at a critical temperature. One suggestion is to add a thermometer closer to the sample itself. Another, potentially much more accurate approach, would be to identify a laser which can be used for both Raman spectroscopy, and exciting the dopant in such a way that this asymmetry can be identified in some emission peak. This would allow measurement of the temperature at the laser focus without changing variables like the laser power

and wavelength used to perform the associated asymmetry measurements.

7.7 Conclusions

First and foremost, the effect is highly reproducible in erbium doped lithium tantalate, which seems to suggest that it is not merely an artifact of the way the experiment is conducted. Second, it is present at room temperature in at least one sample.

The effect clearly has polarization dependence, and an interesting temperature dependence. So far, the most convincing result is that the effect is somehow tied to the *c*-axis of the crystals (ignoring the cubic crystal host for the moment, for which results to examine this were not obtained). It does not appear that a specific type of symmetry or crystal-field number is required for the effect.

At the moment, the most promising (but still very much unproven) explanation considered here seems to be that some sort of coupling involving an electric field in the crystal and the magnetic field (possibly via a piezoelectricity and a linear magnetostriction-like mechanism) is responsible for a difference in the local environments of the rare-earth dopants, which gives rise to these differences in transition probability. A simple scalar product term of the magnetic field and the electric field would likely be inadequate, given the earlier results which suggested the effect is present for angles from 0 to 90 degrees between the *c*-axis and the magnetic field, and seems greatest near 45 degrees. Something of that type, however, would potentially explain how reversing magnetic and electric fields changed the result. Assuming that the transition probabilities become zero in the limit of zero applied magnetic field, any effect must saturate at low fields compared to the fields used in this work (less than hundreds of mT).

Results suggest that the effect may be greater for a site with greater adherence to selection rules for C_{3v} symmetry, which implies a need to explain how a magnetic field perpendicular to the *c*-axis can cause a difference between two magnetic field directions. This is still unresolved. It is recommended that future work involve

measuring angular position with higher precision and smaller angle step size to determine the form of the angular dependence.

Chapter 8

Summary

8.1 Major Points

Progress or genuine success was made on each of the objectives of this work.

- While it has now been demonstrated that the presence of magnetic hysteresis curves can be observed spectroscopically using Zeeman splitting of emissions from rare earth dopants, its detection threshold is probably not anywhere near what what is needed for the samples of interest here.
- Some discrepancies for energy level assignments for the majority site in erbium doped gallium nitride have now been clarified, especially for the $^4I_{11/2}$ multiplet. While the crystal field number assignments given here are not entirely certain, results as a whole for the material confirm that the energy levels are very different in nature from those in erbium doped lithium niobate or erbium doped lithium tantalate.
- While a convincing explanation for the asymmetry effect discussed in Chapter 7 is still lacking, a number of additional results have been obtained which constrain any future attempts at explanation, and may help to explain some discrepancies.

- A technique for analyzing energy levels as a function of magnetic field magnitude was developed which appears to be rather successful in providing insight into nonlinear behaviors in Zeeman splittings, and also sheds light on an avoided crossing between the two lowest energy doubly degenerate levels for the majority site for erbium in erbium doped gallium nitride.
- An experimental technique and data analysis were successfully developed to determine crystal field numbers, effective g factors, and some sense of relative degrees of symmetry for several sites in erbium doped lithium tantalate and erbium doped lithium niobate. This was also applied to the majority site in erbium doped gallium nitride.

8.2 Peak Fitting vs. Method of Moments

Several projects in this work, such as the fitting of energy levels as a function of applied magnetic field, employed peak fitting, and would likely have been more difficult or impossible with the method of moments approach suggested by prior work in this research group [75]. It is suggested that peak fitting, including with an approximated Voigt profile, should be considered as an important tool in continuing this work in the future.

8.3 Uniqueness of Erbium Doped Gallium Nitride

Whereas erbium doped lithium niobate and lithium tantalate seemed to show a tendency for the lowest doubly degenerate state in each of the multiplets studied to have an effective g factor similar to that of the j value for the multiplet, the ground state for the majority site in erbium doped gallium nitride appears to have an effective g factor somewhat less than three for a magnetic field parallel to the c-axis.

The spacing between the two lowest energy doubly degenerate levels in the latter system of about 0.58 meV also seems unusual compared to the other systems studied.

This close spacing has consequences for measurements of the ground state as a function of magnetic field, as the presence of an avoided crossing between the ground state and the next higher energy level means that state mixing with other energy levels occurs as a function of applied magnetic field.

Taken together, this implies some care must be taken in examining erbium doped gallium nitride which may not have been warranted in systems like erbium doped lithium tantalate and lithium niobate.

8.4 The Asymmetry Effect

The results for the asymmetry effect suggest that in at least one system (erbium doped lithium tantalate), it is highly reproducible, and appears not to be easily dismissed as an artifact. Since this effect does not appear to have been reported by other groups, it may be an interesting, new research problem for the future. A number of specific properties of the effect were identified, and some analysis techniques were developed which should be considered for future work. Of particular note is the finding that the effect persists to room temperature in erbium doped lithium tantalate, which may restrain mechanisms relying on ferromagnetic properties.

While the goal of identifying crystal-field quantum numbers was to determine whether these numbers played a role in the asymmetry effect, not enough specific transitions exhibiting the effect were found to allow this sort of analysis. Still, this work does provide a basis for pursuing that goal in the future.

Appendix A

Additional Data for Erbium Doped Lithium Tantalate

The erbium doped lithium tantalate project, by its very nature, resulted in large lists of numbers. Tables thought to be less immediately relevant, but still important to report, are displayed here. It should be noted that the rated accuracy of the wavelength meter used to measure these energies was 3 ppm, so any error less than that should be questioned.

A.1 Energy Levels

Errors in energies listed here are derived from fitting algorithms, and may be smaller than systematic errors associated with the equipment used to measure them. Specifically, the wavelength meter used to measure the excitation wavelengths reported in this section has a rated accuracy of about 3 ppm.

In the tables giving energy levels for sites, only some of the levels for the ${}^4I_{15/2}$ multiplet which could be derived from the observed transitions are given. The reasoning for this a combination of a lack of data, and a concern about avoiding the possibility of phonon-assisted transitions when examining especially broad transition peaks.

Table A.1: Fitted transitions observed for sites A-D. All values are given in eV. Errors are 95 percent confidence intervals derived from the fitting algorithm used.

Site	A	B	C	D
${}^4I_{\frac{9}{2}}$ to	$1.534655 \pm .000008$	$1.534552 \pm .00001$	$1.534031 \pm .000005$	$1.536213 \pm .000004$
${}^4I_{\frac{15}{2}}$	$1.535612 \pm .000002$		$1.534786 \pm .000007$	
${}^4I_{\frac{15}{2}}$ to	$1.265782 \pm .000037$	$1.266270 \pm .000001$	$1.266106 \pm .000006$	$1.265924 \pm .000007$
${}^4I_{\frac{11}{2}}$	$1.270577 \pm .000067$	$1.271726 \pm .000005$	$1.270497 \pm .000003$	$1.270838 \pm .000002$
	$1.271748 \pm .000002$	$1.273457 \pm .000001$	$1.271298 \pm .000054$	$1.272246 \pm .000002$
	$1.276134 \pm .000003$	$1.278279 \pm .000002$	$1.274953 \pm .000005$	$1.274540 \pm .000006$
	$1.277939 \pm .000017$	$1.279938 \pm .000021$	$1.277022 \pm .000006$	$1.276764 \pm .000003$
	$1.279229 \pm .000004$	$1.281842 \pm .000008$	$1.278669 \pm .000005$	$1.279753 \pm .000026$
${}^4I_{\frac{11}{2}}$ to	$1.265816 \pm .000006$	$1.266283 \pm .000002$	$1.266108 \pm .000004$	$1.265937 \pm .000003$
${}^4I_{\frac{15}{2}}$	$1.259218 \pm .000010$	$1.258686 \pm .000003$	$1.260347 \pm .000006$	$1.259059 \pm .000013$
	$1.24975 \pm .00018$	$1.25022 \pm .00014$	$1.25141 \pm .00051$	$1.250053 \pm .000036$
	$1.24875 \pm .00019$			$1.24792 \pm .00030$
	$1.241211 \pm .000016$			
${}^4I_{\frac{13}{2}}$ to	$0.810424 \pm .000003$	$0.810456 \pm .000004$	$0.811080 \pm .000008$	$0.810411 \pm .000007$
${}^4I_{\frac{15}{2}}$	$0.80380 \pm .00034$	$0.802834 \pm .000004$	$0.805315 \pm .000005$	$0.803568 \pm .000010$
	$0.79444 \pm .00066$	$0.794529 \pm .000004$	$0.796494 \pm .000010$	$0.794763 \pm .000026$
	$0.793354 \pm .000017$	$0.79062 \pm .00065$	$0.795455 \pm .000023$	$0.792554 \pm .000037$
	$0.78686 \pm .00012$	$0.785550 \pm .000007$	$0.793749 \pm .000011$	$0.790554 \pm .000042$
	$0.786029 \pm .000009$	$0.785221 \pm .000006$	$0.78585 \pm .00030$	$0.785372 \pm .000029$
	$0.785000 \pm .000010$	$0.784864 \pm .000010$	$0.785749 \pm .000008$	
			$0.785328 \pm .000016$	

Table A.2: Fitted transitions observed for sites E, H1, H2, and I. All values are given in eV. Errors are 95 percent confidence intervals derived from the fitting algorithm used.

Site	E	H1	H2	I
${}^4I_{\frac{9}{2}}$ to	$1.534464 \pm .000002$	$1.535402 \pm .000054$		$1.533905 \pm .000002$
${}^4I_{\frac{15}{2}}$	$1.535603 \pm .000003$			
${}^4I_{\frac{15}{2}}$	$1.266092 \pm .000005$	$1.266425 \pm .000011$	$1.266151 \pm .000007$	$1.266175 \pm .000058$
to	$1.270737 \pm .000013$		$1.270716 \pm .000006$	$1.270227 \pm .000006$
${}^4I_{\frac{11}{2}}$	$1.271802 \pm .000003$	$1.272028 \pm .000002$	$1.272006 \pm .000004$	$1.270495 \pm .000007$
	$1.273305 \pm .000016$		$1.274439 \pm .000004$	$1.273992 \pm .000016$
	$1.275785 \pm .000002$	$1.276535 \pm .000010$	$1.276464 \pm .000005$	
	$1.277767 \pm .000019$	$1.279526 \pm .000020$		$1.277464 \pm .000019$
${}^4I_{\frac{11}{2}}$	$1.266105 \pm .000007$	$1.266409 \pm .000010$		$1.266153 \pm .000006$
to	$1.259668 \pm .000006$	$1.259759 \pm .000076$		$1.613528 \pm .000015$
${}^4I_{\frac{15}{2}}$	$1.250464 \pm .000089$			
${}^4I_{\frac{13}{2}}$	$0.810828 \pm .000008$	$0.810301 \pm .000003$	$0.810640 \pm .000007$	$0.811353 \pm .000004$
to	$0.804375 \pm .000008$	$0.803437 \pm .000005$	$0.803827 \pm .000008$	$0.806606 \pm .000011$
${}^4I_{\frac{15}{2}}$	$0.795409 \pm .000017$		$0.794831 \pm .000013$	$0.797438 \pm .000023$
	$0.793369 \pm .000060$		$0.792753 \pm .000015$	$0.794780 \pm .000014$
	$0.786199 \pm .000010$			$0.786342 \pm .000041$
	$0.785755 \pm .000009$			$0.785746 \pm .000019$
	$0.785265 \pm .000015$			

Table A.3: Fitted transitions observed for sites J-M. All values are given in eV. Errors are 95 percent confidence intervals derived from the fitting algorithm used.

Site	J	K	L	M
${}^4I_{\frac{9}{2}}$ to ${}^4I_{\frac{15}{2}}$	1.534011 ± .000057		1.534031 ± .000011	1.535482 ± .000004
${}^4I_{\frac{15}{2}}$ to ${}^4I_{\frac{11}{2}}$	1.266433 ± .000004	1.267014 ± .000005	1.266646 ± .000006	1.266526 ± .000021
	1.270722 ± .000011	1.270015 ± .000001	1.270431 ± .000003	1.274525 ± .000002
	1.271346 ± .000002	1.270768 ± .000008	1.270933 ± .000002	1.279683 ± .000015
	1.274692 ± .000014	1.272934 ± .000003	1.273710 ± .000007	
	1.276852 ± .000017		1.27462 ± .00020	
	1.27869 ± .00016		1.27790 ± .00017	
${}^4I_{\frac{11}{2}}$ to ${}^4I_{\frac{15}{2}}$	1.266424 ± .000007		1.266613 ± .000015	1.266540 ± .000003
	1.26086 ± .00032		1.262116 ± .000030	1.258244 ± .000008
			1.253168 ± .000046	1.245769 ± .000054
${}^4I_{\frac{13}{2}}$ to ${}^4I_{\frac{15}{2}}$	0.811543 ± .000011	0.812470 ± .000003	0.812021 ± .000025	0.810403 ± .000007
	0.806006 ± .000020	0.808931 ± .000017	0.807591 ± .000008	0.80209 ± .00024
		0.799346 ± .000033	0.79337 ± .00029	0.79338 ± .00023
		0.79660 ± .00013	0.789804 ± .000010	0.789832 ± .000021
		0.785579 ± .000036	0.786010 ± .000014	
			0.785356 ± .000007	

Table A.4: Fitted energy levels for sites A-D. All values are given in eV. Errors are 95 percent confidence intervals derived from the fitting algorithm used.

Site	A	B	C	D
	0	0	0	0
${}^4I_{\frac{15}{2}}$	0.00662 ± 0.00015	0.007611 ± 0.000008	0.006872 ± 0.000026	0.006872 ± 0.000016
	0.01601 ± 0.00034	0.015997 ± 0.000079	0.01463 ± 0.00028	0.015779 ± 0.000026
	0.01707 ± 0.00010	0.01983 ± 0.00033	0.015624 ± 0.000012	0.01794 ± 0.00017
${}^4I_{\frac{13}{2}}$	0.81043 ± 0.00012	0.810476 ± 0.000029	0.81109 ± 0.00010	0.810473 ± 0.000017
	1.265792 ± 0.000064	1.266266 ± 0.000014	1.266100 ± 0.000051	1.265900 ± 0.000025
	1.270577 ± 0.000068	1.271725 ± 0.000005	1.270498 ± 0.000003	1.270838 ± 0.000002
${}^4I_{\frac{11}{2}}$	1.271748 ± 0.000002	1.273457 ± 0.000001	1.271305 ± 0.000052	1.272247 ± 0.000002
	1.276133 ± 0.000003	1.278279 ± 0.000002	1.274954 ± 0.000006	1.274541 ± 0.000005
	1.277937 ± 0.000018	1.279939 ± 0.000023	1.277022 ± 0.000006	1.276764 ± 0.000006
	1.279229 ± 0.000004	1.281842 ± 0.000008	1.278669 ± 0.000005	1.279753 ± 0.000005
${}^4I_{\frac{9}{2}}$	1.534655 ± 0.000007	1.534552 ± 0.000001	1.534031 ± 0.000005	1.536213 ± 0.000004
	1.535612 ± 0.000002		1.534786 ± 0.000007	

Table A.5: Fitted energy levels for sites E, H1, H2, and I. All values are given in eV. Errors are 95 percent confidence intervals derived from the fitting algorithm used.

Site	E	H1	H2	I
	0	0	0	0
${}^4I_{\frac{15}{2}}$	0.006452 ± 0.000008	0.00665 ± 0.00011	0.006812 ± 0.000011	0.004785 ± 0.000021
	0.015541 ± 0.000056		0.015809 ± 0.000015	0.013915 ± 0.000012
	0.017459 ± 0.000061		0.017886 ± 0.000017	0.016573 ± 0.000015
${}^4I_{\frac{13}{2}}$	0.810868 ± 0.000020	0.810301 ± 0.000003	0.810640 ± 0.000007	0.811371 ± 0.000010
	1.266079 ± 0.000064	1.266417 ± 0.000007	1.266151 ± 0.000007	1.266155 ± 0.000024
	1.270739 ± 0.000068		1.270712 ± 0.000007	1.270228 ± 0.000005
${}^4I_{\frac{11}{2}}$	1.271802 ± 0.000002	1.272028 ± 0.000002	1.272006 ± 0.000004	1.270495 ± 0.000007
	1.275785 ± 0.000003		1.274438 ± 0.000008	1.273990 ± 0.000006
	1.277776 ± 0.000021	1.276535 ± 0.000010	1.276464 ± 0.000005	1.275528 ± 0.000016
	1.279430 ± 0.000013	1.279526 ± 0.000020	1.279384 ± 0.000012	1.277462 ± 0.000017
${}^4I_{\frac{9}{2}}$	1.534655 ± 0.000007	1.535402 ± 0.000054		1.533905 ± 0.000002
	1.535612 ± 0.000002			

Table A.6: Fitted energy levels for sites J-M. All values are given in eV. Errors are 95 percent confidence intervals derived from the fitting algorithm used.

Site	J	K	L	M
	0	0	0	0
${}^4I_{\frac{15}{2}}$	0.00553 ± 0.00019	0.003583 ± 0.000017	0.004483 ± 0.000020	0.008306 ± 0.000014
		0.013124 ± 0.000033	0.013444 ± 0.000025	0.017023 ± 0.00022
		0.01587 ± 0.00013	0.01865 ± 0.00012	0.02067 ± 0.00014
${}^4I_{\frac{13}{2}}$	0.811541 ± 0.000097	0.812470 ± 0.000003	0.812043 ± 0.000020	0.810403 ± 0.000007
	1.266429 ± 0.000048	1.267014 ± 0.000051	1.266619 ± 0.000010	1.266525 ± 0.000012
	1.270721 ± 0.000013	1.27001 ± 0.00070	1.270431 ± 0.000003	1.270837 ± 0.000002
${}^4I_{\frac{11}{2}}$	1.271346 ± 0.000002	1.270771 ± 0.000006	1.270932 ± 0.000002	
	1.274692 ± 0.000015	1.272934 ± 0.000008	1.273709 ± 0.000008	1.274526 ± 0.000005
	1.276854 ± 0.000016	1.27509 ± 0.00043		
	1.27869 ± 0.00016	1.277719 ± 0.000032	1.27792 ± 0.00018	1.279686 ± 0.000028
${}^4I_{\frac{9}{2}}$	1.534011 ± 0.000057		1.534031 ± 0.000011	1.535482 ± 0.000004

A.2 Magnetic Splittings

Magnetic splittings had the complication of possibly different maximum field magnitudes from experiment to experiment. Thus, each excitation/emission scheme, and each mounting angle relative to the magnetic field has associated splittings listed separately in the tables shown here. For all data shown in this section, the target magnetic field was set to $750mT$, and subsequent measurements suggested that this field tended to stabilize around $740mT$ as the magnet reached an equilibrium temperature, with an error due to spatial variation and fluctuations over time likely less than $10mT$.

For the tables in this section, all values are given in meV, except for the energy levels themselves, which are in eV. Errors are 95 percent confidence intervals derived from the fitting algorithm used. The columns correspond to the expected angle in degrees between the c-axis of the crystal and the applied magnetic field. The rows give results for each associated energy level. Splittings which were not clearly identified or resulted in very high fitted errors were omitted. If a level is marked 0?, there was no visible splitting of the associated transition in the data, which should simply be taken as implying it is likely smaller than some detection threshold.

For reasons discussed in Chapter 6 describing nonlinearities in magnetic splittings of levels in erbium in gallium nitride, ideally, lower magnetic field strengths are generally preferable in the determination of g factors. However, in an effort to improve the ability to measure splittings for the perpendicular field case for the ground state, an additional data set with a higher field strength (but initially unknown magnitude) was collected. However, splittings for the ground state were not observed in this data set, despite a significantly higher field strength (estimated about 1.25T from comparison). Thus, that data is not used to generate the numbers here, but does suggest that the ground states are not splitting appreciably.

Table A.7: Fitted level splittings for site A.

Field Angle	0°	22.5°	45°	67.5°	90°
${}^4I_{\frac{15}{2}}$ to ${}^4I_{\frac{11}{2}}$					
Ground	0.322 ± 0.001	0.302 ± 0.001	0.239 ± 0.001	0.136 ± 0.001	0?
1.2658	0.221 ± 0.001		0.161 ± 0.001	0.090 ± 0.001	0?
1.2706				0.066 ± 0.006	
1.2718	0.071 ± 0.001	0.071 ± 0.001	0.085 ± 0.001	0.091 ± 0.001	0.104 ± 0.001
1.2761	0.036 ± 0.002	0.033 ± 0.001	0.061 ± 0.003	0.086 ± 0.001	0.088 ± 0.001
1.2779					
1.2793					0.141 ± 0.005
${}^4I_{\frac{13}{2}}$ to ${}^4I_{\frac{15}{2}}$					
Ground	0.323 ± 0.003				0?
0.0066	0.079 ± 0.001	0.090 ± 0.001	0.124 ± 0.003	0.155 ± 0.003	0.164 ± 0.035
0.8104	0.271 ± 0.003	0.254 ± 0.001	0.201 ± 0.002	0.117 ± 0.002	0?
${}^4I_{\frac{11}{2}}$ to ${}^4I_{\frac{15}{2}}$					
Ground					
0.0066	0.075 ± 0.002				
1.2658	0.216 ± 0.002				

Table A.8: Fitted level splittings for site B.

Field Angle	0°	22.5°	45°	67.5°	90°
${}^4I_{\frac{15}{2}}$ to ${}^4I_{\frac{11}{2}}$					
Ground	0.322 ± 0.002	0.319 ± 0.001	0.238 ± 0.001	0.141 ± 0.001	0?
1.2663	0.212 ± 0.003				0?
1.2718		0.156 ± 0.008	0.130 ± 0.012	0.119 ± 0.037	0?
1.2734	0.075 ± 0.003	0.088 ± 0.001	0.083 ± 0.001	0.093 ± 0.001	
1.2783	0.029 ± 0.006	0.037 ± 0.003	0.061 ± 0.003	0.083 ± 0.002	
1.2799	0.062 ± 0.035				
1.2818					
${}^4I_{\frac{13}{2}}$ to ${}^4I_{\frac{15}{2}}$					
Ground	0.334 ± 0.006				0?
0.0076	0.088 ± 0.008	0.098 ± 0.001	0.128 ± 0.005	0.149 ± 0.004	0.162 ± 0.014
0.8105	0.284 ± 0.006	0.260 ± 0.002	0.218 ± 0.008	0.116 ± 0.004	

Table A.9: Fitted level splittings for site C.

Field Angle	0°	22.5°	45°	67.5°	90°
${}^4I_{\frac{15}{2}}$ to ${}^4I_{\frac{11}{2}}$					
Ground	0.314 ± 0.006	0.295 ± 0.001	0.233 ± 0.002	0.136 ± 0.001	0?
1.2661	0.212 ± 0.006	0.202 ± 0.002		0.094 ± 0.001	0?
1.2705	0.119 ± 0.052		0.104 ± 0.006	0.070 ± 0.030	0.044 ± 0.025
1.2713	0.059 ± 0.006	0.066 ± 0.001	0.078 ± 0.002	0.091 ± 0.001	0.096 ± 0.024
1.2750			0.062 ± 0.008	0.086 ± 0.001	0.098 ± 0.028
1.2770			0.058 ± 0.026		
1.2786					0.092 ± 0.036
${}^4I_{\frac{13}{2}}$ to ${}^4I_{\frac{15}{2}}$					
Ground	0.314 ± 0.007			0.136 ± 0.001	0?
0.0058	0.075 ± 0.004		0.112 ± 0.020	0.161 ± 0.004	0.164 ± 0.010
0.8111	0.264 ± 0.007		0.192 ± 0.012	0.111 ± 0.003	0?
${}^4I_{\frac{11}{2}}$ to ${}^4I_{\frac{15}{2}}$					
Ground					
0.0058	0.076 ± 0.007				
1.2661	0.220 ± 0.008				

Table A.10: Fitted level splittings for site D.

Field Angle	0°	22.5°	45°	67.5°	90°
${}^4I_{\frac{13}{2}}$ to ${}^4I_{\frac{15}{2}}$					
Ground	0.316 ± 0.004				0?
0.0068	0.082 ± 0.004	0.110 ± 0.003	0.119 ± 0.006	0.137 ± 0.009	0.167 ± 0.083
0.8104	0.266 ± 0.004	0.256 ± 0.004	0.205 ± 0.005	0.129 ± 0.008	0?

Table A.11: Fitted level splittings for site E.

Field Angle	0°	22.5°	45°	67.5°	90°
${}^4I_{\frac{15}{2}}$ to ${}^4I_{\frac{11}{2}}$					
Ground	0.308 ± 0.001	0.297 ± 0.002	0.232 ± 0.001	0.141 ± 0.001	0?
1.2661	0.211 ± 0.001	0.201 ± 0.002			0?
1.2707		0.143 ± 0.012	0.112 ± 0.005	0.074 ± 0.006	
1.2718	0.060 ± 0.001	0.068 ± 0.002	0.079 ± 0.001	0.091 ± 0.001	0.092 ± 0.006
1.2757			0.067 ± 0.003	0.090 ± 0.006	0.094 ± 0.006
1.2778			0.082 ± 0.012		
1.2794			0.110 ± 0.007		0.123 ± 0.035
${}^4I_{\frac{13}{2}}$ to ${}^4I_{\frac{15}{2}}$					
Ground	0.310 ± 0.007	0.297 ± 0.030			0?
0.0065	0.077 ± 0.005	0.093 ± 0.007	0.116 ± 0.001	0.153 ± 0.002	0.143 ± 0.007
0.8109	0.257 ± 0.007	0.255 ± 0.009	0.199 ± 0.001	0.113 ± 0.002	0?
${}^4I_{\frac{11}{2}}$ to ${}^4I_{\frac{15}{2}}$					
Ground					
0.0065	0.091 ± 0.003				
1.2661	0.235 ± 0.003				

Table A.12: Fitted level splittings for site H1.

Field Angle	0°	22.5°	45°	67.5°	90°
${}^4I_{\frac{13}{2}}$ to ${}^4I_{\frac{15}{2}}$					
Ground	0.301 ± 0.008				
0.0069	0.080 ± 0.006				
0.8103	0.247 ± 0.008				

Table A.13: Fitted level splittings for site H2.

Field Angle	0°	22.5°	45°	67.5°	90°
${}^4I_{\frac{13}{2}}$ to ${}^4I_{\frac{15}{2}}$					
Ground	0.319 ± 0.022				
0.0068	0.079 ± 0.016				
0.8106	0.277 ± 0.022				

Table A.14: Fitted level splittings for site I.

Field Angle	0°	22.5°	45°	67.5°	90°
${}^4I_{\frac{15}{2}}$ to ${}^4I_{\frac{11}{2}}$					
Ground		0.295 ± 0.005		0.132 ± 0.004	0?
1.2662		0.199 ± 0.010			
1.2702		0.102 ± 0.019			0?
1.2705				0.087 ± 0.002	0.092 ± 0.011
1.2740				0.089 ± 0.007	0.091 ± 0.042
1.2755					
1.2775					
${}^4I_{\frac{13}{2}}$ to ${}^4I_{\frac{15}{2}}$					
Ground	0.326 ± 0.022				
0.0047	0.078 ± 0.004	0.092 ± 0.002	0.125 ± 0.002		
0.8114	0.257 ± 0.007	0.240 ± 0.003	0.191 ± 0.002		

Table A.15: Fitted level splittings for site J.

Field Angle	0°	22.5°	45°	67.5°	90°
${}^4I_{\frac{15}{2}}$ to ${}^4I_{\frac{11}{2}}$					
Ground		0.293 ± 0.005		0.143 ± 0.006	0?
1.2664		0.201 ± 0.005			0?
1.2707					
1.2713				0.104 ± 0.006	0.102 ± 0.025
1.2747					0.090 ± 0.021
1.2768					
1.2787					
${}^4I_{\frac{13}{2}}$ to ${}^4I_{\frac{15}{2}}$					
Ground					
0.0056	0.077 ± 0.005	0.091 ± 0.008		0.153 ± 0.002	
0.8115	0.238 ± 0.016				

Table A.16: Fitted level splittings for site K.

Field Angle	0°	22.5°	45°	67.5°	90°
${}^4I_{\frac{15}{2}}$ to ${}^4I_{\frac{11}{2}}$					
Ground	0.288 ± 0.002	0.290 ± 0.006	0.201 ± 0.002	0.110 ± 0.003	0?
1.2670	0.249 ± 0.038	0.236 ± 0.008			0?
1.2700					
1.2708					
1.2729					
1.2751					
1.2772					
${}^4I_{\frac{13}{2}}$ to ${}^4I_{\frac{15}{2}}$					
Ground	0.298 ± 0.014				
0.0035	0.086 ± 0.038	0.102 ± 0.009	0.117 ± 0.015		
0.8125	0.240 ± 0.031	0.229 ± 0.010	0.187 ± 0.018		

Table A.17: Fitted level splittings for site L.

Field Angle	0°	22.5°	45°	67.5°	90°
${}^4I_{\frac{15}{2}}$ to ${}^4I_{\frac{11}{2}}$					
Ground		0.283 ± 0.004	0.222 ± 0.004	0.122 ± 0.004	0?
1.2667		0.192 ± 0.008			
1.2704				0.081 ± 0.011	
1.2709				0.092 ± 0.005	
1.2737				0.086 ± 0.008	
1.2745					
1.2779			0.195 ± 0.058		
${}^4I_{\frac{13}{2}}$ to ${}^4I_{\frac{15}{2}}$					
Ground	0.324 ± 0.019				
0.0044	0.090 ± 0.075	0.100 ± 0.014	0.115 ± 0.007	0.149 ± 0.007	
0.8120	0.267 ± 0.030	0.249 ± 0.021	0.189 ± 0.009	0.095 ± 0.006	

Table A.18: Fitted level splittings for site M.

Field Angle	0°	22.5°	45°	67.5°	90°
${}^4I_{\frac{15}{2}}$ to ${}^4I_{\frac{11}{2}}$					
Ground			0.235 ± 0.031		
1.2665					
1.2708					
1.2745			0.083 ± 0.053		
1.2797					
${}^4I_{\frac{13}{2}}$ to ${}^4I_{\frac{15}{2}}$					
Ground	0.328 ± 0.005	0.276 ± 0.006	0.229 ± 0.009		
0.0083	0.099 ± 0.003	0.114 ± 0.005	0.134 ± 0.009		
0.8104					

Appendix B

Additional Data for Erbium Doped Lithium Niobate

As was the case for the erbium doped lithium tantalate project, tables thought to be less immediately relevant, but still important to report, are displayed here. Less extensive data was taken for this material. Note that sites 1 and cluster were not clearly identified, and that additional peaks not assigned to a site are present in the original data. Data shown is that which could be related to previously studied sites. It should be noted that the rated accuracy of the wavelength meter used to measure these energies was 3 ppm, so any error less than that should be questioned.

B.1 Energy Levels

The comments in the previous corresponding portion on erbium doped lithium tantalate are relevant.

Table B.1: Fitted transitions for sites 2-5. All values are given in eV. Errors are 95 percent confidence intervals derived from the fitting algorithm used.

Site	2	3	4	5
	1.264540 ± 0.000006	1.264676 ± 0.000005	1.264425 ± 0.000006	
${}^4I_{\frac{11}{2}}$	1.269253 ± 0.000004	1.269593 ± 0.000053	1.269425 ± 0.000008	
to	1.270856 ± 0.000002	1.271377 ± 0.000003	1.271287 ± 0.000003	1.271191 ± 0.000009
${}^4I_{\frac{15}{2}}$	1.275861 ± 0.000004	1.276574 ± 0.000003	1.278352 ± 0.000003	
	1.277392 ± 0.000007	1.278038 ± 0.000010	1.278352 ± 0.000007	
	1.278833 ± 0.000029	1.279615 ± 0.000003	1.279336 ± 0.000004	
	0.809280 ± 0.000016	0.809203 ± 0.000015	0.808857 ± 0.000004	0.809055 ± 0.000025
${}^4I_{\frac{13}{2}}$	0.802850 ± 0.000001	0.802392 ± 0.000016	0.802046 ± 0.000004	0.802343 ± 0.000002
to	0.794063 ± 0.000016	0.793604 ± 0.000053	0.793216 ± 0.000011	
${}^4I_{\frac{15}{2}}$	0.793460 ± 0.000036	0.792616 ± 0.000023		
	0.787375 ± 0.000012	0.787312 ± 0.000021		

Table B.2: Fitted transitions for sites 6-9. All values are given in eV. Errors are 95 percent confidence intervals derived from the fitting algorithm used.

Site	6	7	8	9
		1.264595 ± 0.000005		1.264980 ± 0.000002
${}^4I_{\frac{11}{2}}$	1.270328 ± 0.000010	1.269732 ± 0.000003		1.270539 ± 0.000002
to	1.271777 ± 0.000009	1.271733 ± 0.000003	1.272854 ± 0.000002	1.272854 ± 0.000002
${}^4I_{\frac{15}{2}}$	1.275343 ± 0.000013			1.278749 ± 0.000006
		1.277485 ± 0.000008		1.280007 ± 0.000005
		1.279907 ± 0.000012		1.281657 ± 0.000010
	0.809279 ± 0.000009	0.808920 ± 0.000005	0.809332 ± 0.000022	0.809018 ± 0.000012
${}^4I_{\frac{13}{2}}$	0.802404 ± 0.000042	0.801929 ± 0.000007	0.802110 ± 0.000005	0.801342 ± 0.000003
to	0.793977 ± 0.000006	0.793376 ± 0.000020		0.793612 ± 0.000006
${}^4I_{\frac{15}{2}}$		0.791660 ± 0.000010		0.789548 ± 0.000018
		0.787304 ± 0.000021		0.786433 ± 0.000020

Table B.3: Fitted transitions for sites 10-11. All values are given in eV. Errors are 95 percent confidence intervals derived from the fitting algorithm used.

Site	10	11
${}^4I_{\frac{11}{2}}$		1.265298 ± 0.000003
to		
${}^4I_{\frac{15}{2}}$	1.273742 ± 0.000013	1.273848 ± 0.000010
${}^4I_{\frac{13}{2}}$	0.809149 ± 0.000006	0.809060 ± 0.000013
to	0.801175 ± 0.000014	0.800863 ± 0.000008
${}^4I_{\frac{15}{2}}$		0.792668 ± 0.000018

B.2 Magnetic Splittings

Splittings were determined only for some levels of sites 2, 3, 4, and 9, and only for field orientation parallel to the c-axis of the crystal. The expected field is expected to match that for the erbium doped lithium tantalate data. The result of this data was that the states generally seem to show agreement with splittings and effective g factors for the erbium doped lithium tantalate data.

Table B.4: Fitted splittings for sites 2, 3, 4 and 9, for a magnetic field applied parallel to the c-axis, with an expected magnitude of 740mT. All values are given in meV. Errors are 95 percent confidence intervals derived from the fitting algorithm used.

Site	2	3	4	9
Ground		0.327 ± 0.006	0.332 ± 0.005	0.322 ± 0.006
2nd ${}^4I_{\frac{15}{2}}$	0.091 ± 0.009	0.103 ± 0.005	0.098 ± 0.003	0.114 ± 0.004
1st ${}^4I_{\frac{13}{2}}$	0.282 ± 0.009	0.289 ± 0.008	0.229 ± 0.005	0.234 ± 0.004
1st ${}^4I_{\frac{11}{2}}$		0.221 ± 0.007	0.214 ± 0.005	
2nd ${}^4I_{\frac{11}{2}}$		0.164 ± 0.007	0.156 ± 0.004	
3rd ${}^4I_{\frac{11}{2}}$		0.092 ± 0.006		
4th ${}^4I_{\frac{11}{2}}$			0.045 ± 0.016	

Bibliography

- [1] H Bang, J Sawahata, G Piao, M Tsunemi, H Yanagihara, E Kita, and K Akimoto. Magnetic properties of rare-earth-doped gan. *physica status solidi (c)*, 0(7):2874–2877, 2003.
- [2] R R Birss and J C Anderson. Linear magnetostriction in antiferromagnetics. *Proceedings of the Physical Society*, 81(6):1139, 1963.
- [3] A Bonanni. Ferromagnetic nitride-based semiconductors doped with transition metals and rare earths. *Semiconductor Science and Technology*, 22(9):R41, 2007.
- [4] A. T. Boothroyd. Spectre a program for calculating spectroscopic properties of rare earth ions in crystals, 1990-2014.
- [5] A. S. Borovik-romanov. Piezomagnetism, linear magnetostriction and magneto-optic effect. *Ferroelectrics*, 162(1):153–159, 1994.
- [6] DJ Dentz, RC Puttback, and RF Belt. Terbium gallium garnet for faraday effect devices. In *AIP Conference Proceedings*, volume 18, pages 954–958. AIP, 1974.
- [7] S. Dhar, O. Brandt, M. Ramsteiner, V. F. Sapega, and K. H. Ploog. Colossal magnetic moment of gd in gan. *Phys. Rev. Lett.*, 94:037205, Jan 2005.
- [8] S Dhar, L Perez, O Brandt, A Trampert, KH Ploog, J Keller, and B Beschoten. Gd-doped gan: A very dilute ferromagnetic semiconductor with a curie temperature above 300 k. *Physical Review B*, 72(24):245203, 2005.

- [9] V. Dierolf and M. Koerdt. Combined excitation-emission spectroscopy of er^{3+} ions in stoichiometric linbo_3 : the site selectivity of direct and up conversion excitation processes. *Phys. Rev. B*, 61:8043–8052, Mar 2000.
- [10] T. Dietl, H. Ohno, F. Matsukura, J. Cibert, and D. Ferrand. Zener model description of ferromagnetism in zinc-blende magnetic semiconductors. *Science*, 287(5455):1019–1022, 2000.
- [11] M. S. Dresselhaus. Applications of group theory to the physics of solids, 2002. <http://web.mit.edu/course/6/6.734j/www/group-full02.pdf>.
- [12] Avanish Kumar Dubey and Vinod Yadava. Laser beam machininga review. *International Journal of Machine Tools and Manufacture*, 48(6):609 – 628, 2008.
- [13] P.N. Favennec, H. L’Haridon, M. Salvi, D. Moutonnet, and Y. Le Guillou. Luminescence of erbium implanted in various semiconductors: Iv, iii-v and ii-vi materials. *Electronics Letters*, 25(11):718–719, May 1989.
- [14] I-Wen Feng, Jing Li, Ashok Sedhain, JY Lin, HX Jiang, and John Zavada. Enhancing erbium emission by strain engineering in gan heteroepitaxial layers. *Applied Physics Letters*, 96(3):031908, 2010.
- [15] DK George, MD Hawkins, HX Jiang, JY Lin, JM Zavada, and NQ Vinh. Optical excitation of er centers in gan epilayers grown by mocvd. In *SPIE OPTO*, pages 97440V–97440V. International Society for Optics and Photonics, 2016.
- [16] D. M. Gill, L. McCaughan, and J. C. Wright. Spectroscopic site determinations in erbium-doped lithium niobate. *Phys. Rev. B*, 53:2334–2344, Feb 1996.
- [17] V. Glukhanyuk, H. Przybyliska, A. Kozanecki, and W. Jantsch. High resolution site-selective studies of erbium-centers in gan and gan:mg. *MRS Proceedings*, 866, 2005.

- [18] V. Glukhanyuk, H. Przybyliska, A. Kozanecki, and W. Jantsch. Optical properties of a single er center in gan. *Optical Materials*, 28(67):746 – 749, 2006. Rare earth doped photonic materials. Proceedings of the European Materials Research Society 2005 Spring Meeting Symposium {CEuropean} Materials Research Society 2005 Spring Meeting.
- [19] T Gog, P Schotters, J Falta, G Materlik, and M Grodzicki. The lattice position of fe in fe-doped linbo 3. *Journal of Physics: Condensed Matter*, 7(35):6971, 1995.
- [20] Th. Gog, M. Griebenow, and G. Materlik. X-ray standing wave determination of the lattice location of er diffused into linbo3. *Physics Letters A*, 181(5):417 – 420, 1993.
- [21] Kazuo Hagimoto, Yuuzou Miyagawa, Yutaka Miyamoto, Masaharu Ohashi, Masanobu Ohhata, Kazuo Aida, and Kiyoshi Nakagawa. A 10 gbit/s long-span fiber transmission experiment employing optical amplification technique and monolithic ic technology. *IEICE TRANSACTIONS (1976-1990)*, 73(1):27–30, 1990.
- [22] Morton Hamermesh. *Group Theory and its Application to Physical Problems*. Dover Publications, Inc., 1989.
- [23] E. Hecht. *Optics*. Pearson education. Addison-Wesley, 2002.
- [24] Markus P. Hehlen, Mikhail G. Brik, and Karl W. Krmer. 50th anniversary of the juddofelt theory: An experimentalist’s view of the formalism and its application. *Journal of Luminescence*, 136:221 – 239, 2013.
- [25] U Hoemmerich, Ei Ei Nyein, D.S Lee, J Heikenfeld, A.J Steckl, and J.M Zavada. Photoluminescence studies of rare earth (er, eu, tm) in situ doped gan. *Materials Science and Engineering: B*, 105(1):91 – 96, 2003. EMRS 2003 Symposium J, Rare Earth Doped Materials for Photonics.

- [26] A Jayaraman and AA Ballman. Effect of pressure on the raman modes in linbo_3 and lita_3 . *Journal of applied physics*, 60(3):1208–1210, 1986.
- [27] JP Joule. On the effects of magnetism upon the dimensions of iron and steel bars. london. *Philadelphia Magazine & Journal of Science*, 1847.
- [28] P. Kielanowski, S.T. Ali, P. Bieliavsky, A. Odziejewicz, M. Schlichenmaier, and T. Voronov. *Geometric Methods in Physics: XXXIV Workshop, Białowieża, Poland, June 28 – July 4, 2015*. Trends in Mathematics. Springer International Publishing, 2016.
- [29] S. Kim, S. J. Rhee, X. Li, J. J. Coleman, and S. G. Bishop. Selective enhancement of 1540 nm er^{3+} emission centers in er-implanted gan by mg codoping. *Applied Physics Letters*, 76(17):2403–2405, 2000.
- [30] A. Konopka, S. Greulich-Weber, V. Dierolf, H.X. Jiang, U. Gerstmann, E. Rauls, S. Sanna, and W.G. Schmidt. Microscopic structure and energy transfer of vacancy-related defect pairs with erbium in wide-gap semiconductors. *Optical Materials*, 33(7):1041 – 1044, 2011. Rare earth doped materials for optical based technologies Symposium K of the 2010 {EMRS} Spring Meeting.
- [31] George F. Koster, John O. Dimmock, Robert G. Wheeler, and Hermann Statz. *The Properties of the Thirty-Two Point Groups (Research Monograph)*. The MIT Press, 1963.
- [32] Hendrik Antoon Kramers. Théorie générale de la rotation paramagnétique dans les cristaux. *Proc. Acad. Amst*, 33:959–972, 1930.
- [33] Eric W Lee. Magnetostriction and magnetomechanical effects. *Reports on progress in physics*, 18(1):184, 1955.
- [34] Albert K Levine and Frank C Palilla. A new, highly efficient red-emitting cathodoluminescent phosphor ($\text{yvo}_4: \text{Eu}$) for color television. *Applied Physics Letters*, 5(6):118–120, 1964.

- [35] Yuyan Liu, Jieli Lin, Guangming Huang, Yuanqing Guo, and Chuanxi Duan. Simple empirical analytical approximation to the voigt profile. *JOSA B*, 18(5):666–672, 2001.
- [36] HJ Lozykowski and WM Jadwisienczak. Thermal quenching of luminescence and isovalent trap model for rare-earth-ion-doped aln. *physica status solidi (b)*, 244(6):2109–2126, 2007.
- [37] Melvyn Oliver Luen, Neeraj Nepal, Pavel Frajtag, John Zavada, Ei Brown, Uwe Hommerich, Salah M. Bedair, and Nadia El-Masry. Ferromagnetism and near-infrared luminescence in neodymium and erbium doped gallium nitride via diffusion. *MRS Proceedings*, 1183, 2009.
- [38] C. M. Lueng, H. L. W. Chan, C. Surya, and C. L. Choy. Piezoelectric coefficient of aluminum nitride and gallium nitride. *Journal of Applied Physics*, 88(9):5360–5363, 2000.
- [39] K. Makarova, M. Stachowicz, V. Glukhanyuk, A. Kozanecki, C. Ugolini, J.Y. Lin, H.X. Jiang, and J. Zavada. Spectroscopic studies of er-centers in {MOCVD} grown gan layers highly doped with er. *Materials Science and Engineering: B*, 146(13):193 – 195, 2008. {EMRS} 2007, Symposium C, Rare Earth Ion Doping for Photonics: Materials, Mechanisms and Devices.
- [40] B. Z. Malkin, D. S. Pytalev, M. N. Popova, E. I. Baibekov, M. L. Falin, K. I. Gerasimov, and N. M. Khaidukov. Random lattice deformations in rare-earth-doped cubic hexafluoroelpasolites: High-resolution optical spectroscopy and theoretical studies. *Phys. Rev. B*, 86:134110, Oct 2012.
- [41] Donald W Marquardt. An algorithm for least-squares estimation of nonlinear parameters. *Journal of the society for Industrial and Applied Mathematics*, 11(2):431–441, 1963.
- [42] A L McKenzie. Physics of thermal processes in laser-tissue interaction. *Physics in Medicine and Biology*, 35(9):1175, 1990.

- [43] A Meftah, S Ait Mammar, JF Wyart, W-Ü L Tchang-Brillet, N Champion, C Blaess, D Deghiche, and O Lamrous. Analysis of the free ion spectrum of er^{3+} (er^{iv}). *Journal of Physics B: Atomic, Molecular and Optical Physics*, 49(16):165002, 2016.
- [44] Brandon Mitchell. *The Role of Defect Complexes in the Magneto-Optical Properties of Rare Earth Doped Gallium Nitride*. PhD thesis, Lehigh University, 2014.
- [45] K Miyahara, A Toulouse, N Woodward, P Capek, and V Dierolf. Site selective spectroscopy on erbium ions in stoichiometric lithium tantalate. *Journal of Physics: Conference Series*, 249(1):012011, 2010.
- [46] TD Myers and JD McDaniel. The pulsed nd: Yag dental laser: review of clinical applications. *Journal of the California Dental Association*, 19(11):25–30, 1991.
- [47] N Nepal, JM Zavada, R Dahal, C Ugolini, A Sedhain, JY Lin, and HX Jiang. Optical enhancement of room temperature ferromagnetism in er-doped gan epilayers. *Applied Physics Letters*, 95(2):022510, 2009.
- [48] EA Nesbitt. New permanent magnet materials containing rare-earth metals. *Journal of Applied Physics*, 40(3):1259–1265, 1969.
- [49] AJ Neuhalfen and BW Wessels. Thermal quenching of er^{3+} -related luminescence in in_1-xga_xp . *Applied physics letters*, 60(21):2657–2659, 1992.
- [50] D.J. Newman and B. Ng. *Crystal Field Handbook*. Cambridge University Press, 2007.
- [51] A. Ney. 6 - gadolinium-doped gallium-nitride: Synthesis routes, structure, and magnetism. In V. Dierolf, I.T. Ferguson, and J.M. Zavada, editors, *Rare Earth and Transition Metal Doping of Semiconductor Materials*, pages 195 – 223. Woodhead Publishing, 2016.
- [52] C.W. Nielson and G.F. Koster. *Spectroscopic coefficients for the pn , dn and fn configurations*. M. I. T. Press, 1963.

- [53] K.P. O'Donnell and V. Dierolf. *Rare-Earth Doped III-Nitrides for Optoelectronic and Spintronic Applications*. Topics in Applied Physics. Springer Netherlands, 2010.
- [54] O'Donnell, K. P. and Hourahine, B. Rare earth doped iii-nitrides for optoelectronics. *Eur. Phys. J. Appl. Phys.*, 36(2):91–103, 2006.
- [55] Y. Ohno, D. K. Young, B. Beschoten, F. Matsukura, H. Ohno, and D. D. Awschalom. Electrical spin injection in a ferromagnetic semiconductor heterostructure. *Nature*, 402:790–792, 1999.
- [56] W. Opechowski. Sur les groupes cristallographiques doubles. *Physica*, 7(6):552 – 562, 1940.
- [57] M Palczewska, A Wolos, M Kaminska, I Grzegory, M Bockowski, S Krukowski, T Suski, and S Porowski. Electron spin resonance of erbium in gallium nitride. *Solid State Communications*, 114(1):39 – 42, 2000.
- [58] C. Perez-Rojas. Fitting saturation and hysteresis via arctangent functions. *IEEE Power Engineering Review*, 20(11):55–57, Nov 2000.
- [59] Giulio Racah. Theory of complex spectra. ii. *Phys. Rev.*, 62:438–462, Nov 1942.
- [60] Giulio Racah. Theory of complex spectra. iii. *Phys. Rev.*, 63:367–382, May 1943.
- [61] Giulio Racah. Theory of complex spectra. iv. *Phys. Rev.*, 76:1352–1365, Nov 1949.
- [62] E. D. Readinger, G. D. Metcalfe, H. Shen, and M. Wraback. Gan doped with neodymium by plasma-assisted molecular beam epitaxy. *Applied Physics Letters*, 92(6):061108, 2008.
- [63] Y. Repelin, E. Husson, F. Bennani, and C. Proust. Raman spectroscopy of lithium niobate and lithium tantalate. force field calculations. *Journal of Physics and Chemistry of Solids*, 60(6):819 – 825, 1999.

- [64] W. A. Runciman. Stark-splitting in crystals. *Philosophical Magazine*, 1(11):1075–1077, 1956.
- [65] Christian Sandmann. *Confocal luminescence microscopy study of defect-domain wall interaction in LiNbO₃ and its application to light-induced domain engineering*. PhD thesis, Lehigh University, 2004.
- [66] Simone Sanna, W. G. Schmidt, Th. Frauenheim, and U. Gerstmann. Rare-earth defect pairs in gan: LDA + u calculations. *Phys. Rev. B*, 80:104120, Sep 2009.
- [67] K. Sato, L. Bergqvist, J. Kudrnovský, P. H. Dederichs, O. Eriksson, I. Turek, B. Sanyal, G. Bouzerar, H. Katayama-Yoshida, V. A. Dinh, T. Fukushima, H. Kizaki, and R. Zeller. First-principles theory of dilute magnetic semiconductors. *Rev. Mod. Phys.*, 82:1633–1690, May 2010.
- [68] K. Sato, W. Schweika, P. H. Dederichs, and H. Katayama-Yoshida. Low-temperature ferromagnetism in (ga, mn)n: Ab initio calculations. *Phys. Rev. B*, 70:201202, Nov 2004.
- [69] RG Smith, K Nassau, and MF Galvin. Efficient continuous optical second-harmonic generation. *Applied Physics Letters*, 7(10):256–258, 1965.
- [70] Andrew J Steckl and John M Zavada. Optoelectronic properties and applications of rare-earth-doped gan. *MRS Bulletin*, 24(09):33–38, 1999.
- [71] Matias R Tejerina, Daniel Jaque, and Gustavo Adrián Torchia. μ -raman spectroscopy characterization of linbo₃ femtosecond laser written waveguides. *Journal of Applied Physics*, 112(12):123108, 2012.
- [72] Michael Tinkham. *Group Theory and Quantum Mechanics*. Dover Publications, Inc., 2003.
- [73] C. Ugolini, N. Nepal, J. Y. Lin, H. X. Jiang, and J. M. Zavada. Erbium-doped gan epilayers synthesized by metal-organic chemical vapor deposition. *Applied Physics Letters*, 89(15):151903, 2006.

- [74] N. T. Woodward, N. Nepal, B. Mitchell, I. W. Feng, J. Li, H. X. Jiang, J. Y. Lin, J. M. Zavada, and V. Dierolf. Enhanced magnetization in erbium doped gan thin films due to strain induced electric fields. *Applied Physics Letters*, 99(12):122506, 2011.
- [75] Nathaniel T. Woodward. *Optical and Magneto-Optical Studies of Rare Earth Doped Gallium Nitride*. PhD thesis, Lehigh University, 2011.
- [76] Jean-François Wyart, Ali Meftah, Annik Bachelier, Jocelyne Sinzelle, Wan-Ü Lydia Tchang-Brillet, Norbert Champion, Nissan Spector, and Jack Sugar. Energy levels of 4f3 in the nd3+ free ion from emission spectra. *Journal of Physics B: Atomic, Molecular and Optical Physics*, 39(5):L77, 2006.
- [77] Brian G. Wybourne. *Spectroscopic properties of rare earths*. Wiley, 1965.
- [78] J.M. Zavada and Duhua Zhang. Luminescence properties of erbium in iiiv compound semiconductors. *Solid-State Electronics*, 38(7):1285 – 1293, 1995.
- [79] Guohua Zhong, Kang Zhang, Fan He, Xuhang Ma, Lanlan Lu, Zhuang Liu, and Chunlei Yang. Ga vacancy induced ferromagnetism enhancement and electronic structures of re-doped gan. *Physica B: Condensed Matter*, 407(18):3818 – 3827, 2012.

Vita

Andrew J. Helbers was born in East Stroudsburg, PA on April 30, 1990 to Dale and Patricia Helbers. He is the eldest of four sons. He obtained a Bachelor's degree in Applied Physics from New Jersey Institute of Technology in 2012, and a Master's Degree in Physics from Lehigh University in 2014. He has been conducting research under the supervision of Dr. Volkmar Dierolf for the previous four years, and has presented at two conferences.